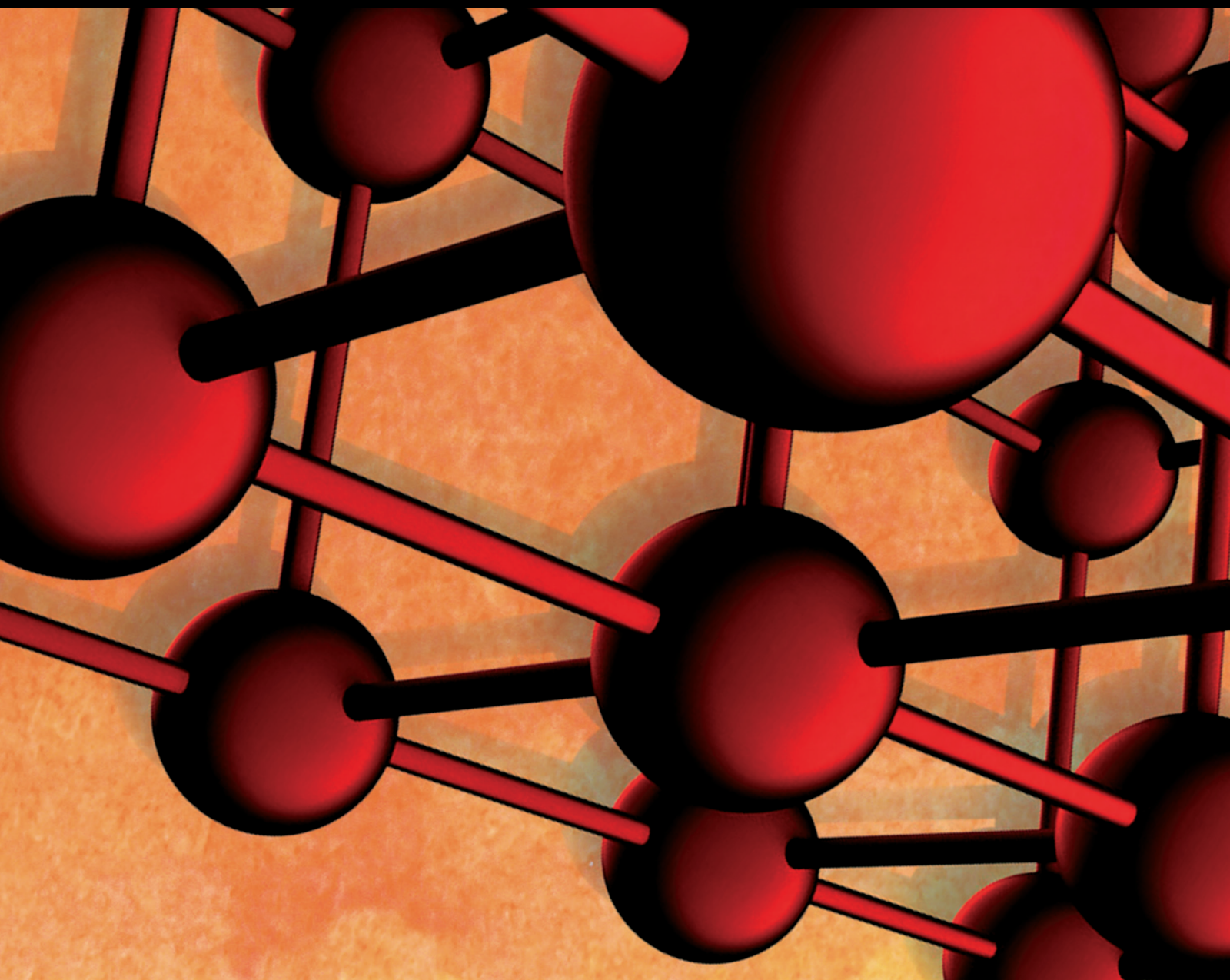


Advances in Materials Science and Engineering

Micromechanical Properties of Construction and Building Materials

Lead Guest Editor: Junjie Wang

Guest Editors: Engui Liu and Rotana Hay





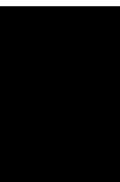
Micromechanical Properties of Construction and Building Materials

Advances in Materials Science and Engineering

**Micromechanical Properties of
Construction and Building Materials**

Lead Guest Editor: Junjie Wang


Guest Editors: Engui Liu and Rotana Hay



Copyright © 2023 Hindawi Limited. All rights reserved.

This is a special issue published in "Advances in Materials Science and Engineering." All articles are open access articles distributed under the Creative Commons Attribution License, which permits unrestricted use, distribution, and reproduction in any medium, provided the original work is properly cited.

Chief Editor










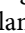



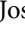



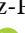


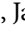



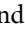
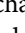
Amit Bandyopadhyay , USA

Associate Editors

Vamsi Balla , India
Mitun Das , USA
Sandip Harimkar, USA
Ravi Kumar , India
Peter Majewski , Australia
Enzo Martinelli , Italy
Luigi Nicolais , Italy
Carlos R. Rambo , Brazil
Michael J. Schütze , Germany
Kohji Tashiro , Japan
Zhonghua Yao , China
Dongdong Yuan , China
Wei Zhou , China

Academic Editors

Antonio Abate , Germany
Hany Abdo , Saudi Arabia
H.P.S. Abdul Khalil , Malaysia
Ismael Alejandro Aguayo Villarreal , Mexico
Sheraz Ahmad , Pakistan
Michael Aizenshtein, Israel
Jarir Aktaa, Germany
Bandar AlMangour, Saudi Arabia
Huaming An, China
Alicia Esther Ares , Argentina
Siva Avudaiappan , Chile
Habib Awais , Pakistan
NEERAJ KUMAR BHOI, India
Enrico Babilio , Italy
Renal Backov, France
M Bahubalendruni , India
Sudharsan Balasubramanian , India
Markus Bambach, Germany
Irene Bavasso , Italy
Stefano Bellucci , Italy
Brahim Benmokrane, Canada
Jean-Michel Bergheau , France
Guillaume Bernard-Granger, France
Giovanni Berselli, Italy
Patrice Berthod , France
Michele Bianchi , Italy
Hugo C. Biscaia , Portugal

Antonio Boccaccio, Italy
Mohamed Bououdina , Saudi Arabia
Gianlorenzo Bussetti , Italy
Antonio Caggiano , Germany
Marco Cannas , Italy
Qi Cao, China
Gianfranco Carotenuto , Italy
Paolo Andrea Carraro , Italy
Jose Cesar de Sa , Portugal
Wen-Shao Chang , United Kingdom
Qian Chen , China
Francisco Chinesta , France
Er-Yuan Chuang , Taiwan
Francesco Colangelo, Italy
María Criado , Spain
Enrique Cuan-Urquiza , Mexico
Lucas Da Silva , Portugal
Angela De Bonis , Italy
Abílio De Jesus , Portugal
José António Fonseca De Oliveira
Correia , Portugal
Ismail Demir , Turkey
Luigi Di Benedetto , Italy
Maria Laura Di Lorenzo, Italy
Marisa Di Sabatino, Norway
Luigi Di Sarno, Italy
Ana María Díez-Pascual , Spain
Guru P. Dinda , USA
Hongbiao Dong, China
Mingdong Dong , Denmark
Frederic Dumur , France
Stanislaw Dymek, Poland
Kaveh Edalati , Japan
Philip Eisenlohr , USA
Luis Evangelista , Norway
Michele Fedel , Italy
Francisco Javier Fernández Fernández , Spain
Spain
Isabel J. Ferrer , Spain
Massimo Fresta, Italy
Samia Gad , Egypt
Pasquale Gallo , Finland
Sharanabasava Ganachari, India
Santiago Garcia-Granda , Spain
Carlos Garcia-Mateo , Spain

Achraf Ghorbal , Tunisia
Georgios I. Giannopoulos , Greece
Ivan Giorgio , Italy
Andrea Grilli , Italy
Vincenzo Guarino , Italy
Daniel Guay, Canada
Jenő Gubicza , Hungary
Xuchun Gui , China
Benoit Guiffard , France
Zhixing Guo, China
Ivan Gutierrez-Urrutia , Japan
Weiwei Han , Republic of Korea
Simo-Pekka Hannula, Finland
A. M. Hassan , Egypt
Akbar Heidarzadeh, Iran
Yi Huang , United Kingdom
Joshua Ighalo, Nigeria
Saliha Ilican , Turkey
Md Mainul Islam , Australia
Ilia Ivanov , USA
Jijo James , India
Hafsa Jamshaid , Pakistan
Hom Kandel , USA
Kenji Kaneko, Japan
Rajesh Kannan A , Democratic People's
Republic of Korea
Mehran Khan , Hong Kong
Akihiko Kimura, Japan
Ling B. Kong , Singapore
Pramod Koshy, Australia
Hongchao Kou , China
Alexander Kromka, Czech Republic
Abhinay Kumar, India
Avvaru Praveen Kumar , Ethiopia
Sachin Kumar, India
Paweł Kłosowski , Poland
Wing-Fu Lai , Hong Kong
Luciano Lamberti, Italy
Fulvio Lavecchia , Italy
Laurent Lebrun , France
Joon-Hyung Lee , Republic of Korea
Cristina Leonelli, Italy
Chenggao Li , China
Rongrong Li , China
Yuanshi Li, Canada




Guang-xing Liang , China
Barbara Liguori , Italy
Jun Liu , China
Yunqi Liu, China
Rong Lu, China
Zhiping Luo , USA
Fernando Lusquiños , Spain
Himadri Majumder , India
Dimitrios E. Manolakos , Greece
Necmettin Maraşlı , Turkey
Alessandro Martucci , Italy
Roshan Mayadunne , Australia
Mamoun Medraj , Canada
Shazim A. Memon , Kazakhstan
Pratima Meshram , India
Mohsen Mhadhbi , Tunisia
Philippe Miele, France
Andrey E. Miroshnichenko, Australia
Ajay Kumar Mishra , South Africa
Hossein Moayedi , Vietnam
Dhanesh G. Mohan , United Kingdom
Sakar Mohan , India
Namdev More, USA
Tahir Muhmood , China
Faisal Mukhtar , Pakistan
Dr. Tauseef Munawar , Pakistan
Roger Narayan , USA
Saleem Nasir , Pakistan
Elango Natarajan, Malaysia
Rufino M. Navarro, Spain
Miguel Navarro-Cia , United Kingdom
Behzad Nematollahi , Australia
Peter Niemz, Switzerland
Hiroschi Noguchi, Japan
Dariusz Oleszak , Poland
Laurent Orgéas , France
Togay Ozbakkaloglu, United Kingdom
Marián Palcut , Slovakia
Davide Palumbo , Italy
Gianfranco Palumbo , Italy
Murlidhar Patel, India
Zbyšek Pavlík , Czech Republic
Alessandro Pegoretti , Italy
Gianluca Percoco , Italy
Andrea Petrella, Italy

Claudio Pettinari , Italy
Giorgio Pia , Italy
Candido Fabrizio Pirri, Italy
Marinos Pitsikalis , Greece
Alain Portavoce , France
Simon C. Potter, Canada
Ulrich Prah, Germany
Veena Ragupathi , India
Kawaljit Singh Randhawa , India
Baskaran Rangasamy , Zambia
Paulo Reis , Portugal
Hilda E. Reynel-Avila , Mexico
Yuri Ribakov , Israel
Aniello Riccio , Italy
Anna Richelli , Italy
Antonio Riveiro , Spain
Marco Rossi , Italy
Fernando Rubio-Marcos , Spain
Francesco Ruffino , Italy
Giuseppe Ruta , Italy
Sachin Salunkhe , India
P Sangeetha , India
Carlo Santulli, Italy
Fabrizio Sarasini , Italy
Senthil Kumaran Selvaraj , India
Raffaele Sepe , Italy
Aabid H Shalla, India
Poorva Sharma , China
Mercedes Solla, Spain
Tushar Sonar , Russia
Donato Sorgente , Italy
Charles C. Sorrell , Australia
Damien Soulat , France
Adolfo Speghini , Italy
Antonino Squillace , Italy
Koichi Sugimoto, Japan
Jirapornchai Suksaeree , Thailand
Baozhong Sun, China
Sam-Shajing Sun , USA
Xiaolong Sun, China
Yongding Tian , China
Hao Tong, China
Achim Trampert, Germany
Tomasz Trzepieciński , Poland
Kavimani V , India

Matjaz Valant , Slovenia
Mostafa Vamegh, Iran
Lijing Wang , Australia
Jörg M. K. Wiezorek , USA
Guosong Wu, China
Junhui Xiao , China
Guoqiang Xie , China
YASHPAL YASHPAL, India
Anil Singh Yadav , India
Yee-wen Yen, Taiwan
Hao Yi , China
Wenbin Yi, China
Tetsu Yonezawa, Japan
Hiroshi Yoshihara , Japan
Bin Yu , China
Rahadian Zainul , Indonesia
Lenka Zaji#c#kova# , Czech Republic
Zhigang Zang , China
Michele Zappalorto , Italy
Gang Zhang, Singapore
Jinghuai Zhang, China
Zengping Zhang, China
You Zhou , Japan
Robert Černý , Czech Republic

Contents

Study on Mechanical Properties of Concrete-Filled Steel Tubular Members under Axial Tension

Huaguo Gao, Lingxin Zhang , Xiuchun Wang , Renjie Sun, Qingli Wang, and Lu Yang 

Research Article (18 pages), Article ID 3232992, Volume 2023 (2023)



Thermal and Waterproof Properties of Foamed Concrete with Nano SiO₂ Aerogel and Organosilicon

Waterproofing Agent

Baojun Cheng, Xiaowei Gu , Yuxin Gao, Pengfei Ma, and Shengrong Kang

Research Article (8 pages), Article ID 3054214, Volume 2022 (2022)

Bond Slip Behavior of Grout-Filled Concrete Members with Different Interface Materials

Eryu Zhu , Teng Li , Lei Liu, Li Zhu, and Yuanyuan Tian


Research Article (17 pages), Article ID 1235843, Volume 2022 (2022)

Experimental Analysis of Recycled Aggregate Concrete Beams and Correction Formulas for the Crack Resistance Calculation

Xuyong Chen, Zhixin Zhang, Zhifeng Xu , Qiaoyun Wu , Jianping Fan, and Xuri Zhao

Research Article (13 pages), Article ID 1466501, Volume 2022 (2022)

Analysis of Stress-Strain Relationship of Earthen Soil Based on Molecular Dynamics

Jianwei Yue, Xuanjia Huang, Peng Li , and Tingting Yue





Research Article (13 pages), Article ID 8591973, Volume 2022 (2022)

Hysteresis Behavior and Design of the New Autoclaved Lightweight Concrete (ALC) External Panel Connector with the Steel Frame

Kewei Ding , Chikun Zhang , Shulin He , and Yunlin Liu 

Research Article (18 pages), Article ID 8319044, Volume 2022 (2022)

An Empirical Model for Geopolymer Reactions Involving Fly Ash and GGBS

Beulah M , MR Sudhir , Shen Chen , Sasha Rai, and Deekshith Jain 

Research Article (13 pages), Article ID 8801294, Volume 2022 (2022)

Seismic Behavior of Elliptical Concrete-Filled Steel Tubular Columns under Combined Axial Compression and Cyclic Lateral Loading

YouWu Xu , Jian Yao , Feng Hu , Ying Zhou , and Shuai Jiang 

Research Article (14 pages), Article ID 5892788, Volume 2021 (2021)

The Normal Force Characteristic of a Novel Magnetorheological Elastomer Based on Butadiene Rubber Matrix Compounded with the Self-Fabricated Silly Putty

Fei Guo, Chengbin Du , and Guojun Yu


Research Article (13 pages), Article ID 5831721, Volume 2021 (2021)

Mechanical Properties of Full-Scale Prestressed Concrete Beams with Thin Slab after Exposure to Actual Fire

Chaowei Hao , Yanjiang Chen , Yu Tang, and Laiyong Wang

Research Article (13 pages), Article ID 2211413, Volume 2021 (2021)

Pretreatment of Crumb Rubber with a Silane Coupling Agent to Improve Asphalt Rubber Performance

Li Liu , Zhaohui Liu, and Chengcheng Yang

Research Article (9 pages), Article ID 1828145, Volume 2021 (2021)

Early Age Hydration Characteristics of Calcium Sulphoaluminate Cement Mortar Cured at a Temperature Range from –10 to 20°C

Zhongyu Chen, Jianhong Fang , Feng Ming , and Yuhang Liu

Research Article (13 pages), Article ID 4494056, Volume 2021 (2021)

Damage Evolution of Sandstone under Constant-Amplitude Cyclic Loading Based on Acoustic Emission Parameters and Resistivity

Kui Wang , Zhengting Xia , Zhen Huang , and Xue Li 

Research Article (10 pages), Article ID 7057183, Volume 2021 (2021)

Research Article

Study on Mechanical Properties of Concrete-Filled Steel Tubular Members under Axial Tension

Huaguo Gao,^{1,2,3} Lingxin Zhang ,^{1,2} Xiuchun Wang ,³ Renjie Sun,³ Qingli Wang,³ and Lu Yang ⁴

¹Institute of Engineering Mechanics, China Earthquake Administration, Harbin 150080, China

²Key Laboratory of Earthquake Engineering and Engineering Vibration of China Earthquake Administration, Harbin 150080, China

³University of Science and Technology Liaoning, Anshan 114051, China

⁴Shenyang University of Technology, Shenyang 110000, China

Correspondence should be addressed to Lingxin Zhang; civilengineering@ustl.edu.cn

Received 19 November 2021; Revised 7 July 2022; Accepted 13 July 2022; Published 24 April 2023

Academic Editor: Junjie Wang

Copyright © 2023 Huaguo Gao et al. This is an open access article distributed under the Creative Commons Attribution License, which permits unrestricted use, distribution, and reproduction in any medium, provided the original work is properly cited.

At present, the concrete-filled steel tube structure has been widely used in various practical projects. Due to the low tensile strength of the core concrete of round steel tube concrete (CFST) specimens, the axial tensile performance of CFST specimens is far from superior to its compressive performance. However, in practical projects, the concrete-filled steel tube members bearing tensile load often appear. In order to study the axial tensile properties of CFST specimens, the axial tensile tests of 5 CFST specimens and 1 pure steel tube specimen were carried out with steel tube diameter and concrete strength as variation parameters. The results show that the bearing capacity of CFST specimens is increased by 7.5%–16.3% compared with that of pure steel tube specimens with the same cross-sectional area, mainly because the core concrete limits the circumferential shrinkage of the outer steel tube. The larger the cross-sectional area of CFST specimens is, the higher the bearing capacity is. In this paper, the stress-strain relationship and the overall failure mode of CFST members under tensile force are studied, and the deformation characteristics and stress of steel pipe and core concrete are analyzed, which is expected to provide a reference for the application of CFST specimens in practical engineering.

1. Introduction

The essence of the concrete-filled steel tube (CFST) component is the restraining effect of the outer steel tube on the core concrete, which produces an excellent combination effect between the two materials, thus showing many advantages. Because the compressive capacity of concrete materials is much higher than its tensile capacity, it is mainly used as compression members in actual projects, it is rarely used in tension members, and there are relatively few related studies. However, when it is used as the bottom side column of high-rise building under wind load or earthquake load, the base and bracket of a large structure under horizontal wind load, and the tie rod in a truss structure, the member is in the tension state. At the same time, the stress mode of

concrete-filled steel tubular members in eccentric tension is similar to that of compression bending members. The study on the tensile bending performance of CFST members has certain reference significance for us to understand the compression bending performance of concrete-filled steel tubular members. The axial tensile and eccentric tensile properties of concrete-filled steel tubular (CFST) are one of the most basic mechanical properties. Since the research team will also carry out the tensile performance test of CFRP concrete-filled steel tubular (CFST) in the later stage, the research on the axial tensile properties of ordinary CFST is also to lay a foundation for the later research on a series of related properties of CFRP concrete-filled steel tubular (CFST). Therefore, it is very important to study the mechanical properties of CFST components under tensile load.

Compared with previous studies, this paper finds that the bearing capacity of CFST will be improved, and the ductility will be reduced.

Han [1] made a systematic study about the concrete-filled steel tubular structures theory. Some scholars have studied the axial tensile properties of concrete-filled steel tubular specimens, and the authors of [2] conducted an experimental study on the tensile properties of concrete-filled square steel tubular and proposed that the improvement of tensile stiffness was the comprehensive result of finite stiffness effect and tensile stiffness effect. The design formula and analysis were a model of circular CFST under axial tension put forward by Xu et al. [3]. Hua et al. [4], Ying [5], Wang et al. [6], Han et al. [7] conducted detailed research and analysis on the axial tensile properties of concrete-filled steel tube members through experimental research and finite element analysis. The effects of material properties, steel content, cross-sectional form, concrete shrinkage, and carbon fibre reinforced plastics (CFRP) reinforcement on the axial tensile properties of the specimens were discussed. Li et al. [8] have studied the performance of concrete-filled steel tubes subjected to eccentric tension. Wang et al. [9] did some research on the behavior of CFRP externally reinforced circular CFST members under combined tension and bending. Experimental research and finite element analysis were carried out on the axial tension and tension-bending performance of hollow sandwich steel tube concrete and reinforced steel tube concrete, and the corresponding calculation methods of bearing capacity and stiffness were proposed [10, 11]. Ye et al. [12] evaluated the variation of tensile strength and studied the tensile properties of circular CFST members with small gaps. Han et al. [13] and Zhou et al. [2] studied the mechanical behavior of concrete-filled steel tubes (CFST) under axial tension, established the finite element model of axial tension of concrete-filled steel tubular, and carried out mechanical analysis and parameter research. Chen et al. [14] carried out a series of axial tensile tests on concrete-filled steel tubular with reinforcement or angle steel. The properties and strength of concrete-filled steel tubular with reinforcement or angle steel under axial tension were studied. Zhou et al. [15] studied the mechanical behavior of circular concrete-filled steel tubular (CCFTS) under axial tension. The test results showed that the tensile strength of CCFTS was approximately 10.2% larger than that of hollow tubes. This stiffness and strength enhancement should be considered in typical static and dynamic analyses of structures using CCFT members subjected to tension to provide more accurate results. Qiao et al. [16] studied the seismic behavior of specially shaped concrete-filled tube (CFT) columns with multiple cavities under axial tension or axial compression. The results showed that the compression-flexure test specimen showed lower yield damage, higher bearing capacity, and superior seismic performance relative to the tension-flexure test specimen. Han et al. [13] carried out the axial tension test study of 18 concrete-filled steel tube specimens, established the relevant finite element analysis model, then deeply analyzed the axial tension force mechanism of the concrete-filled steel tube member, and summarized the

formula for calculating the bearing capacity of the shaft in relation to the steel rate.

$$N_u = (1.1 - 0.4\alpha)f_y A_s, \quad (1)$$

where N_u is the axial tension capacity, α is the steel content, f_y is the yield strength of steel tube, and A_s is the cross-sectional area of steel tube.

Through the above literature research, compared with the mechanical properties of other CFST members, there are few studies on its axial tensile properties, and the constitutive relationship curve of the steel used in the finite element simulation is different from the relationship curve obtained by the actual tension of the steel pipe. The calculation of steel content in formula (1) is complicated. Therefore, on the basis of the existing research, this paper analyzes in detail the deformation and stress characteristics of the outer steel pipe and the core concrete during the test, and adjusts the existing steel constitutive relationship on the basis of the actual tensile curve of the steel pipe, and adopts finite element method for parameter analysis. Finally, a simplified calculation formula for the axial tension bearing capacity related to the wall thickness and outer diameter ratio is proposed. It is expected to provide a reference for quickly calculating the bearing capacity of this type of member in engineering practice.

2. Test Overview

2.1. Specimen Design. In this experiment, a total of 1 pure steel tube and 5 circular steel tube concrete members was designed and manufactured. The detailed parameters of the test piece are shown in Table 1, where α is the steel content, which can be calculated according to formula (2). The length of the test piece is 460 mm. The detailed dimensions of the end plates and stiffeners of the test piece are shown in Figure 1. The front number in the serial number is the outer diameter of the steel tube, the back number represents the strength grades of the core concrete of the specimen as C30, C40, and C50, and the number 0 represents that the specimen is a pure steel pipe specimen.

$$\alpha = \frac{A_s}{A_c}, \quad (2)$$

where A_s is the cross-sectional area of the steel, and A_c is the cross-sectional area of the concrete.

2.2. Material Properties Experiment

2.2.1. Steel Performance. The model of the steel used in the production of the test piece is Q235 according to the relevant regulations in "Tensile Test of Metallic Materials Part 1: Room Temperature Test Method" GB/T 228.1 [17]. Three test specimens are cut out from the steel used in the test piece. Tensile specimens were tested for the material properties of the steel, and the relevant material properties of the steel are measured in Table 2. In the table, f_y is the yield strength, f_u is the ultimate strength, E_s is the modulus of elasticity, ν_s is the Poisson's ratio, and δ' is the elongation. The tensile specimen is shown in Figures 2(a) and 2(b).

TABLE 1: Specimen parameter.

Number	Diameter (mm)	Tube thickness (mm)	α	$f_{cw,k}$ (MPa)
1	89	3.5	0.178	40
2	114	3.5	0.135	40
3	139	3.5	0.109	40
4	114	3.5	0.135	30
5	114	3.5	0.135	50
6	114	3.5	—	—

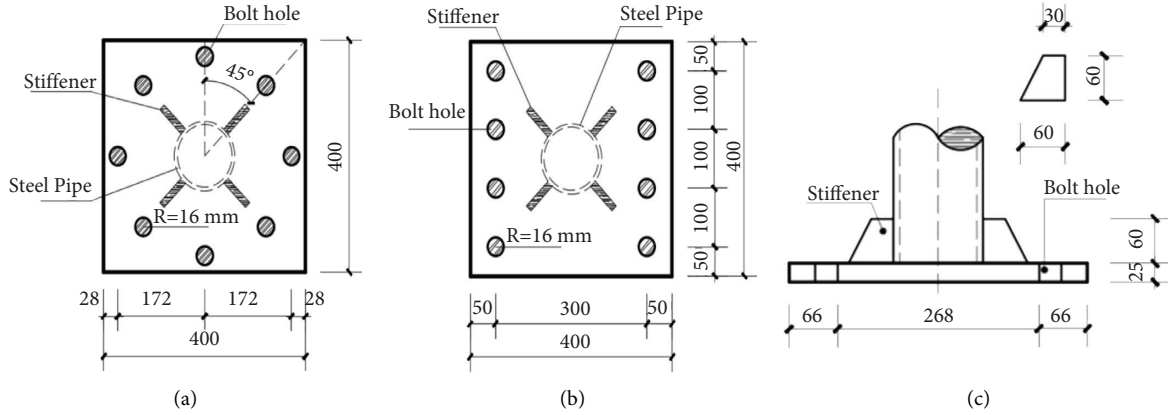


FIGURE 1: Sizes of specimens (unit: mm): (a) upper end plate, (b) lower end plate, and (c) stiffener.

TABLE 2: Properties of steel tube.

f_y (MPa)	f_u (MPa)	E_s (GPa)	ν_s	$\delta'(\%)$
305.6	447	199.67	0.29	29.7

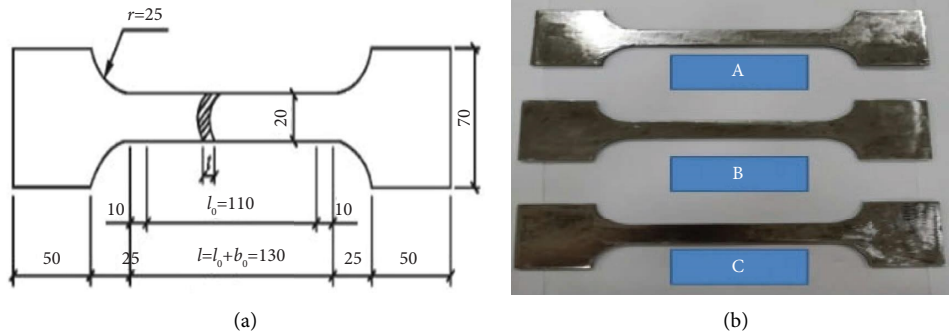


FIGURE 2: Steel tensile test piece production: (a) tensile specimen size and (b) tensile specimen.

According to the relevant regulations in the “Standard for Test Methods for Physical and Mechanical Properties of Concrete” GB/T50081 [18], the compressive strength test of standard concrete test blocks is carried out, and the compressive strength of three strength concretes is measured. The elastic modulus E_c can be calculated by formula (3), and Poisson’s ratio ν_c is 0.2. The relevant material properties of concrete can be gotten from Table 3.

$$E_c = 4700\sqrt{f'_c} \quad (3)$$

where f_c is the standard value of the compressive strength of the concrete cylinder, which can be taken according to the literature.

2.2.2. *Concrete Performance.* In order to prevent the internal strain gauge from falling off, the method of manual mixing is used in the mixing process, that is, placing a vibrator inside while pouring concrete, and hammering it outside the steel pipe with a leather hammer, and the mix proportion is shown in Table 4. In the table, C is grade 42.5 ordinary Portland cement, G is natural medium sand, the fineness

TABLE 3: Properties of concrete.

Strength level	C30	C40	C50
f_{cu-k} (MPa)	31.3	39.6	52.0
E_c (GPa)	23.50	26.96	30.28

modulus is 2.5, S is gravel coarse aggregate with the maximum particle size of 25 mm, W is tap water, and SP is hydroxy acid water reducing agent. The water-cement ratio of three strength concrete is 0.487, 0.395, and 0.349, respectively.

In this paper, a total of 10 standard concrete test blocks are made, 3 test blocks are configured for each strength of concrete, and another test block with a strength grade of C40 is made. The configuration of test block is shown in Figure 3(a). After the test block is demoulded, the test block is placed in the same environment as the concrete-filled steel tube, that is, the test block is watered, and the same watering frequency is used for curing until the test is carried out, and the press is used to test each test block.

The concrete test blocks were tested for compressive strength, as shown in Figure 3(b). Now, the compressive strength of each test block is listed in Table 5. Since the test was carried out immediately after the 28 d curing period of concrete, the concrete strength before the test was not measured. The relevant data of 28 d concrete in Table 5 can be used directly.

2.3. Test Piece Production. Cut the steel tube, end plate, and stiffener according to the design size of the test piece. First, complete the welding of the steel pipe and the lower end plate, and paste the horizontal and vertical strain gauges on the inner wall of the steel pipe at a position $1/3L$ from the upper port. Drill a 5 mm hole between the ribs to connect the strain gauge. Connect the wires throughout. The internal strain gauge treatment is shown in Figure 4. After the concrete is poured, the port is ground flat, and the upper-end plate and the stiffener are welded. A small hole with a radius of 15 mm is reserved at the center of the upper-end plate for water injection curing of the concrete.

After the test piece is made, in order to prevent the corrosion of the steel pipe, the outside of the test piece shall be painted. Before the test, in order to solve the void phenomenon of the end plate caused by the shrinkage of the concrete, after the concrete curing period, epoxy is injected into the water injection hole of the upper-end plate resin fills the gap between the concrete shrinkage and the end plate. The sample before loading is shown in Figure 5.

2.4. Test Device and Measurement. The test was carried out on a 3000 kN electro-hydraulic servo short column eccentric compression testing machine in the structural engineering laboratory of University of Science and Technology Liaoning, and the manufacturer of the equipment is Jilin Jinli Test Technology Co., LTD. During the test, place the test piece on the operating platform of the testing machine, and align the centers of the upper and lower end plates with the centroids of the test device base and the force sensor, and

TABLE 4: Concrete material consumption table.

Strength grade	Material consumption per cubic meter (kg/m^3)				
	C	S	G	W	SP
C30	380	1198	648	185	3.9
C40	460	1210	590	182	4.2
C50	510	1220	545	178	4.5

place them vertically to ensure that the bolt holes are aligned. The upper and lower end plates are connected with the testing machine through $8 * 12.9$ grade high-strength bolts. The boundary conditions are approximately completely fixed, and the test loading device is shown in Figure 6.

In order to accurately measure the deformation of the test specimen, 3 measuring points are arranged at the mid-span section with an interval of 120° . Each measuring point is pasted with two strain gauges in the horizontal and vertical directions. The steel pipe is at a position $1/3L$ from the upper and lower end plates. Two measuring points are set on the outer wall, and each measuring point is pasted with two horizontal and vertical strain gauges to measure the strain at $1/3L$ of the test piece. In order to study the difference in strain at the same point on the inner and outer surfaces of the steel pipe, paste two horizontal and vertical strain gauges on the inner wall of the $1/3L$ section. Finally, paste two horizontal and vertical strain gauges on the stiffeners at both ends to study the strain at the stiffener. The layout of the strain gauges is shown in Figure 7.

Axial force is measured by a spoke force sensor. The overall displacement of the test piece is measured by a 100 mm range thimble displacement meter at the loading end plate. Two sizes are spot welded at the upper and lower $1/3L$ of the test piece before the test. It is a steel sheet of $20 \text{ mm} \times 40 \text{ mm}$ (spot welding is only for fixing the steel sheet, and the influence on the steel pipe is negligible), and two thimble type displacement meters with a range of 50 mm are arranged on the two steel sheets, respectively, and the measurement is on the middle $1/3L$ of the test piece. The layout of the displacement meter is shown in Figure 8(a).

2.5. Acquisition System and Loading System. Displacement loading was adopted in the test with a loading rate of 1 mm/min. During the test, the tension was measured by a spokes force sensor with a range of 3000 kN, and the stress, strain, and displacement were simultaneously collected by the DH3816H static stress and strain tester produced by Donghua Testing Company, as shown in Figure 8(b). Using the same acquisition device to collect experimental data can ensure that different data are collected at the same time and maintain a one-to-one correspondence relationship. The data acquisition frequency is set to 1 Hz.

3. Analysis of Test Results

3.1. Test Phenomenon and Failure Mode. At the beginning of loading, the specimen is the elastic range, and the deformation of the specimen is small, so the experimental



FIGURE 3: Concrete test block configuration diagram: (a) block configuration and (b) compression test.

TABLE 5: Test block compressive strength measured table.

Configuration grade	f_{cu} (MPa)			Average value
	Block 1	Block 2	Block 3	
C30	34	31	29	31.3
C40	42	39	38	39.6
C50	49	52	55	52.0

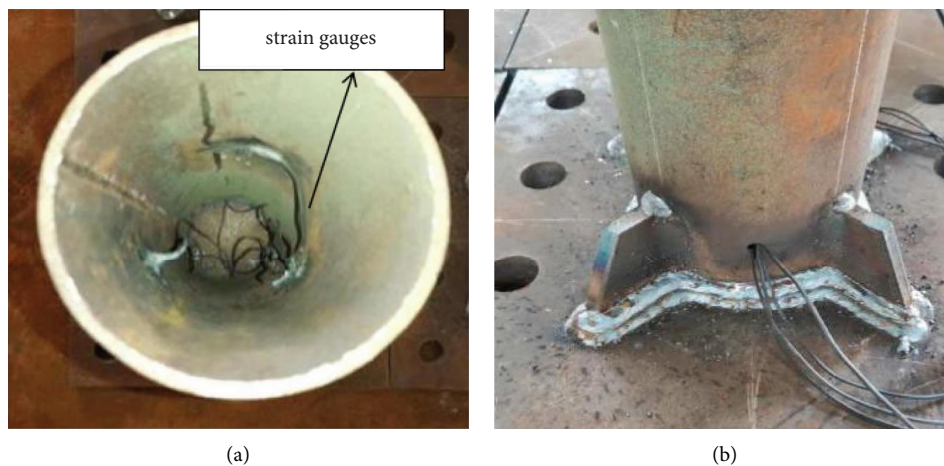


FIGURE 4: Sticking of strain gauges on inner wall: (a) arrangement of inner strain gauges and (b) wire handling method.

phenomenon is not obvious. As the axial force increases, the specimen has a slight “snapping” sound, and the spray paint on some areas of the outer surface is torn. When the axial tensile force reaches about 80% of the ultimate bearing capacity of the specimen (the 114-40 specimen reaches 37.1 t at this time, and the ultimate bearing capacity of the specimen is 47.6 T), the growth rate of specimen displacement is accelerated, and the specimen enters the elastic-plastic stage. The accelerated deformation results in cracks of AB glue attached to the outer surface of strain gauge. As the load increases, the test piece enters the strengthening stage, and the longitudinal deformation of the test piece is large, and the outer steel pipe shrinks laterally, causing some strain gauges to fall off. When the specimen is damaged, cracks appear at one point of the outer steel pipe, and the bearing capacity decreases, and the cracks gradually extend along the

circumferential direction. Finally, the specimen fractures and the test end. The damage of the specimen after the test is shown in Figure 9.

Through comparative analysis, it is concluded that there are three types of failures of the specimen: 1. the midspan section damages (114-0). Due to the absence of the restraint effect of the core concrete, the midspan section of the specimen exhibits obvious diameter shrinkage, and then damage occurs. 2. The junction between the top of the stiffener and the steel pipe is damaged (139-40). Due to the increase in pipe diameter but the same wall thickness, the stress concentration at this position is more obvious, and the steel pipe outside the section is weaker due to welding, so damage occurs. 3. Damage section is near to the 1/3L section (89-40, 114-30, 114-40, 114-50). Since the transverse deformation of the



FIGURE 5: Specimens before loading.

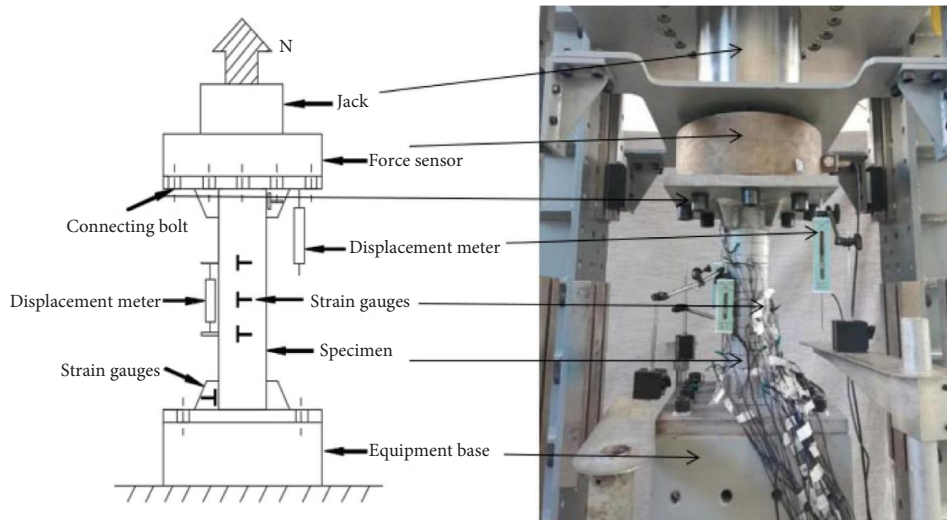


FIGURE 6: Experimental setup.

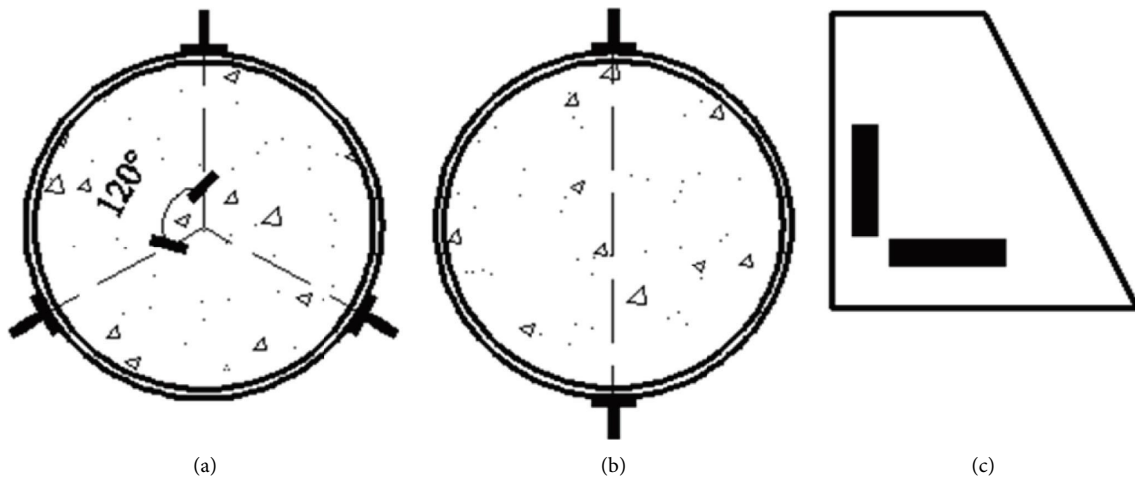


FIGURE 7: Distribution of strain gauge: (a) 1/2L section, (b) 1/3L section, and (c) stiffener.

specimen is constrained by the core concrete, the fracture position should be related to the damage position of the concrete, and the concrete appears after the crack, and the

position of the crack no longer provides hoop restraint, resulting in stress concentration of the outer steel pipe at this position and subsequent failure.

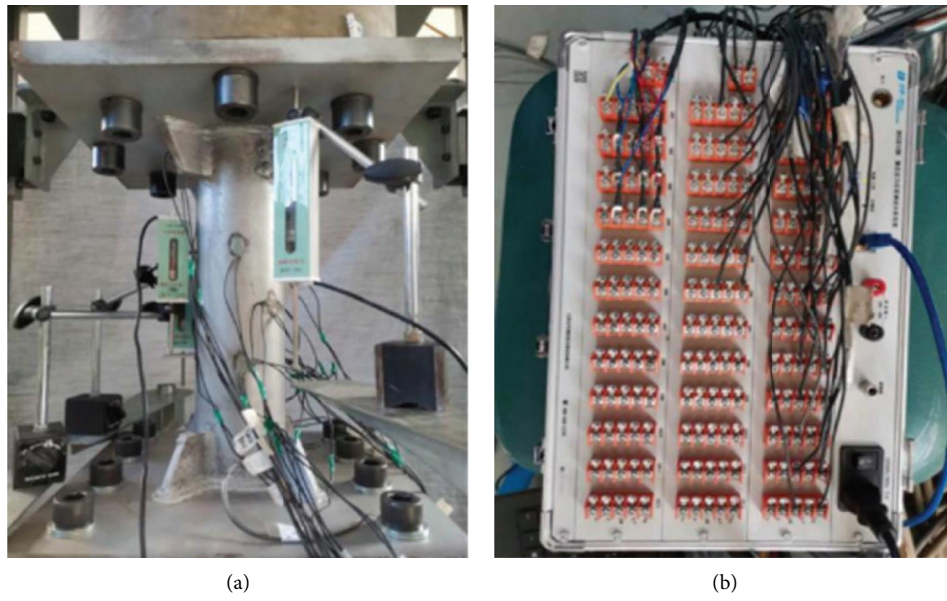


FIGURE 8: Displacement meter layout and data acquisition device: (a) displacement gauge layout drawing and (b) data acquisition unit.

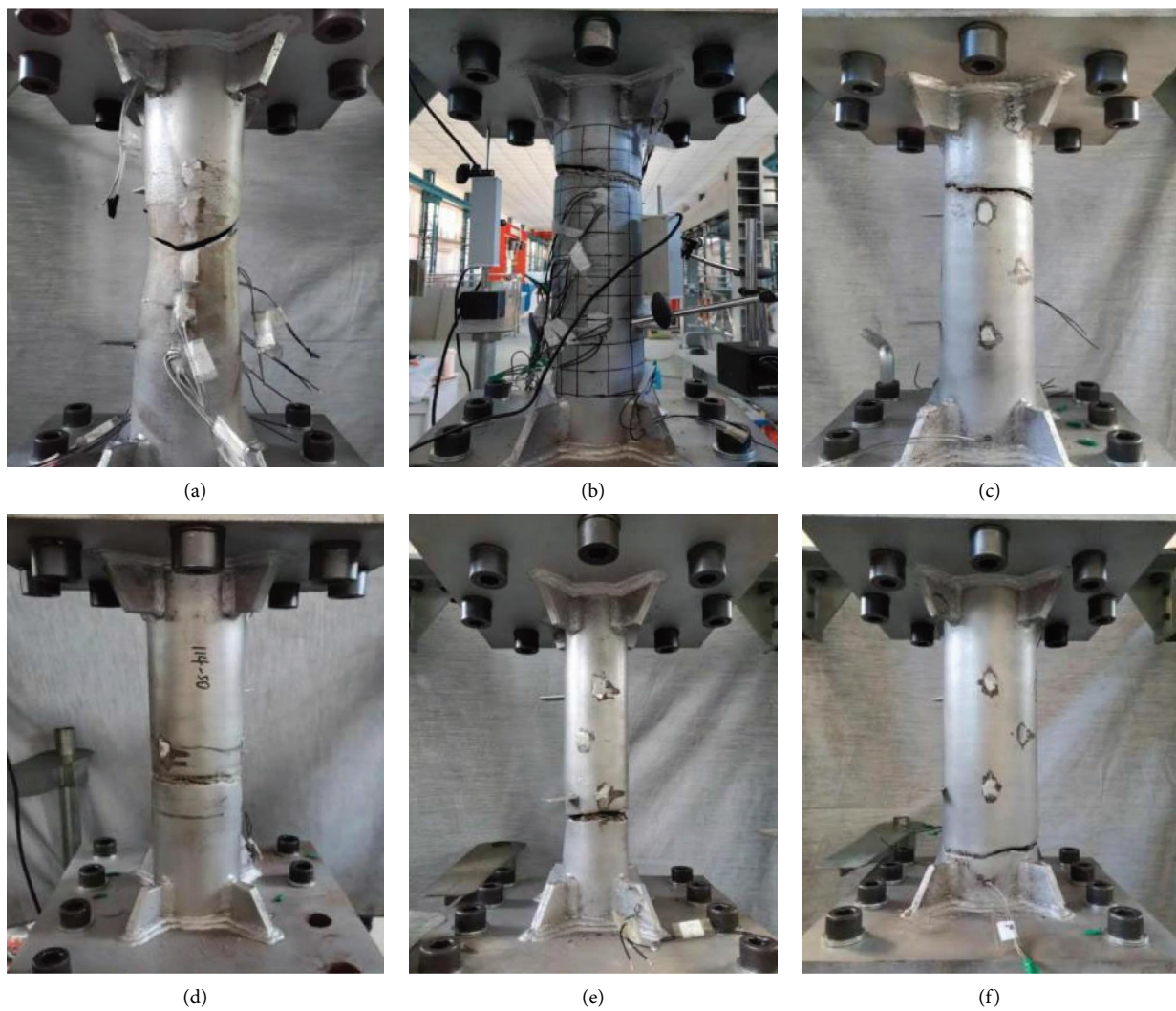


FIGURE 9: Damage of specimens: (a) 114-0, (b) 114-40, (c) 114-30, (d) 114-50, (e) 89-40, and (f) 139-40.

3.2. Analysis of Measured Curves

3.2.1. Load-Displacement Curve. Figure 10 shows the load-overall displacement curves of specimens 114-0 and 114-40. It can be seen from the figure that, due to the existence of core concrete, the CFST specimen has an increased bearing capacity compared with the pure steel pipe specimen of the same cross-sectional size, and the initial stiffness is greater. However, the overall ductility of the specimen is lower than that of the pure steel pipe specimen. This is because under the action of core concrete, the necking behavior of steel pipe is delayed, which leads to the decrease of ductility.

Figure 11 shows the comparison of load-relative displacement curves of concrete-filled steel tube specimens with different outer diameters and concrete strengths. It can be seen from the figure that the larger the outer diameter, the higher the bearing capacity of the specimen, and the greater the initial stiffness. With the change of concrete strength, the curves basically coincide. It can be seen that the concrete strength has a small influence on the axial tensile performance of the specimen and can be ignored.

3.2.2. Assumption of Flat Section. Figure 12 is the relationship curve between the transverse and longitudinal strain values (ε_x and ε_y) and the axial force (N) at different measuring points at the midspan section of the test piece. It can be seen from the figure that the longitudinal strain value is positive and the transverse strain value is negative. The strain-load curves in the same direction at different measuring points basically coincide, indicating that the deformation of the specimen conforms to the assumption of a flat section, and the deformation at each point of the specimen on the same cross section is consistent. And it can be seen from the figure that after adding concrete, under the same axial force, the lateral deformation of the specimen is much smaller than the longitudinal deformation. It can be seen that the concrete hinders the circumferential deformation of the outer steel pipe.

3.2.3. Strain Comparison of Inner and Outer Walls of Steel Pipe. Figure 13 shows the strain comparison between the inner and outer walls of the steel pipe of the typical specimen 139-40. As can be seen from the figure, the strain value on the inner wall of the steel pipe 1/3L away from the upper plate of the specimen is slightly smaller than that on the outer surface of the specimen. The reason is that the outer diameter of the steel pipe is larger than the inner diameter of the steel pipe, resulting in larger strain on the outer steel pipe.

3.2.4. Comparison of Deformation of Middle Section and 1/3L Section. Figure 14 shows the relationship between the ratio of the longitudinal strain (ε_y) of the middle section of the typical specimen 114-0 and 114-30 to the longitudinal strain

(ε_{Uy} and ε_{Dy}) at the upper and lower 1/3L sections of the coaxial load (N) curve. It can be seen from Figure 14(a) that the shapes of the two curves are basically the same, and the abscissa values of most areas are greater than 1, indicating that the deformation at the upper and lower 1/3L sections of the test piece is basically the same. The longitudinal strain is large, so the specimen is broken in the middle section. As shown in Figure 14(b), the ratio of the longitudinal strain at the middle section to the longitudinal strain at the upper 1/3L is greater than 1, and the ratio of the longitudinal strain at the lower 1/3L section is less than 1, indicating that the specimen at the upper 1/3L deforms greatly, so the specimen failure occurred near the upper 1/3L section. The rest of the test pieces will not be repeated.

3.2.5. Deformation of Stiffener. Figure 15 shows the relationship curve between longitudinal strain and load on the stiffener of some specimens. Due to the large stiffness at the position of the stiffener, the deformation is small, resulting in irregular strain data of some specimens. Therefore, only the relationship curve of the regular specimen is listed in the figure. It can be seen that the maximum longitudinal strain of the stiffener is only $400 \mu\varepsilon$, which is much smaller than the overall longitudinal strain value of the test piece, so the deformation of the stiffener is basically negligible.

3.3. Analysis of Bearing Capacity. Yao [19], Han [1], and Li et al. [8] have defined the method for calculating the axial tensile bearing capacity of concrete-filled steel tube specimens. The axial tensile load N_{u10000} of the concrete-filled steel tube specimen when the longitudinal strain reaches $10000 \mu\varepsilon$ is used as the axial tensile bearing capacity of the specimen. At the same time, according to the calculation formula (1) of the CFST member axial tensile bearing capacity in the literature [7], the bearing capacity of this test specimen is calculated, and the measured bearing capacity and the formula calculated bearing capacity are listed in Table 6 and analyzed the error between the two methods.

It can be seen from the table that the measured bearing capacity is greater than the value calculated by the formula, and the error is between 14.9%–33%. It can be seen that the calculation result of formula (1) has a high safety reserve value. And it can be seen from the table that the smaller the outer diameter, the greater the error between the measured bearing capacity and the calculated bearing capacity, and with the change of concrete strength, the bearing capacity error is basically stable at about 17%.

4. Finite Element Analysis

4.1. Choice of Constitutive Relationship. The constitutive relationship of steel is mostly defined by the five-segment secondary plastic flow model proposed by Han [1]. However, it can be seen from the related test curves in the journal

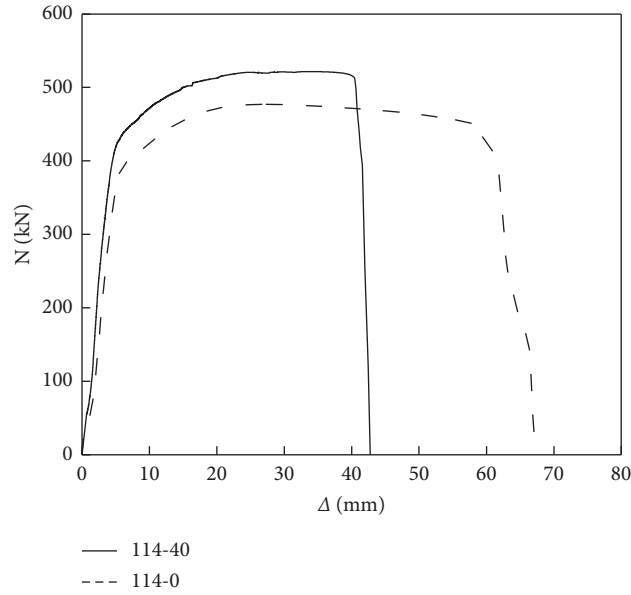


FIGURE 10: Load-overall displacement curve.

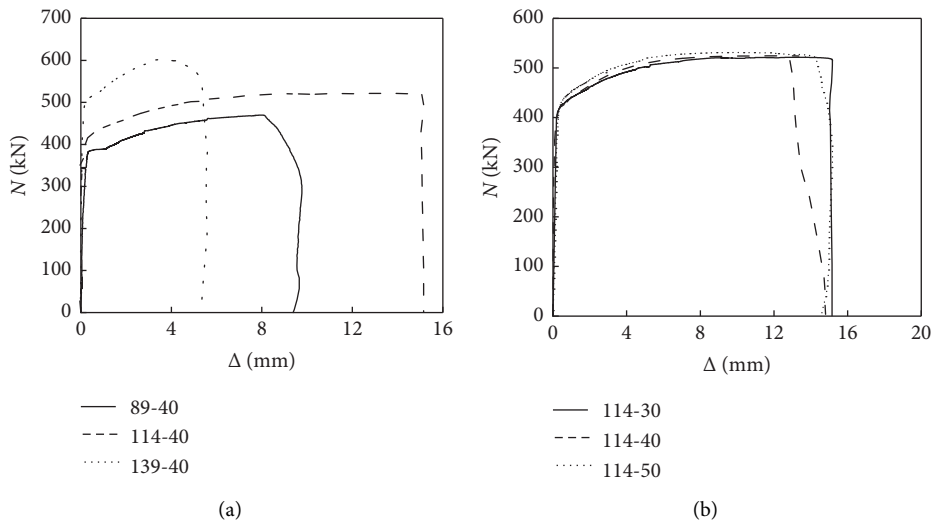


FIGURE 11: Load-relative displacement curve: (a) different outer diameter and (b) different concrete grades.

papers Ying [5] and Xu [20] as well as the load-displacement curve of the specimen 114-0 in Figure 8 of this paper, that the tensile stress-strain curve of steel pipe is not a clear yielding platform appears, and the material directly enters the strengthening stage after the elastic stage ends. Therefore, in order to be closer to the real material properties of the steel pipe, the secondary plastic flow model curve is adjusted accordingly as shown in Figure 16.

After removing the yield stage (bc) in the figure, the curve directly enters the strengthening stage (cd). After the modification, the constitutive relationship curve becomes a four-segment line (Oabde), which is more in line with the axial tensile material properties of the pipe. The expression of the four-segment constitutive relation of steel is shown in formula (4). Among them, $\epsilon_e = 0.8f_y/E_s$, $\epsilon_{e1} = 1.5\epsilon_e$, and $\epsilon_{e2} = 100\epsilon_{e1}$, and other parameters are consistent with the

calculation method in the steel secondary plastic flow model, refer to references for values.

$$\sigma = \begin{cases} E_s \epsilon, & (\epsilon \leq \epsilon_e), \\ -A\epsilon^2 + B\epsilon + C, & (\epsilon_e < \epsilon \leq \epsilon_{e1}), \\ \left(1 + 0.6 \frac{\epsilon - \epsilon_{e1}}{\epsilon_{e2} - \epsilon_{e1}}\right), & (\epsilon_{e1} < \epsilon \leq \epsilon_{e2}), \\ 1.6f_y, & (\epsilon > \epsilon_{e2}). \end{cases} \quad (4)$$

Concrete is divided into two kinds of constitutive relations of compression and tension. Compression constitutive relations are defined by the constitutive relation model

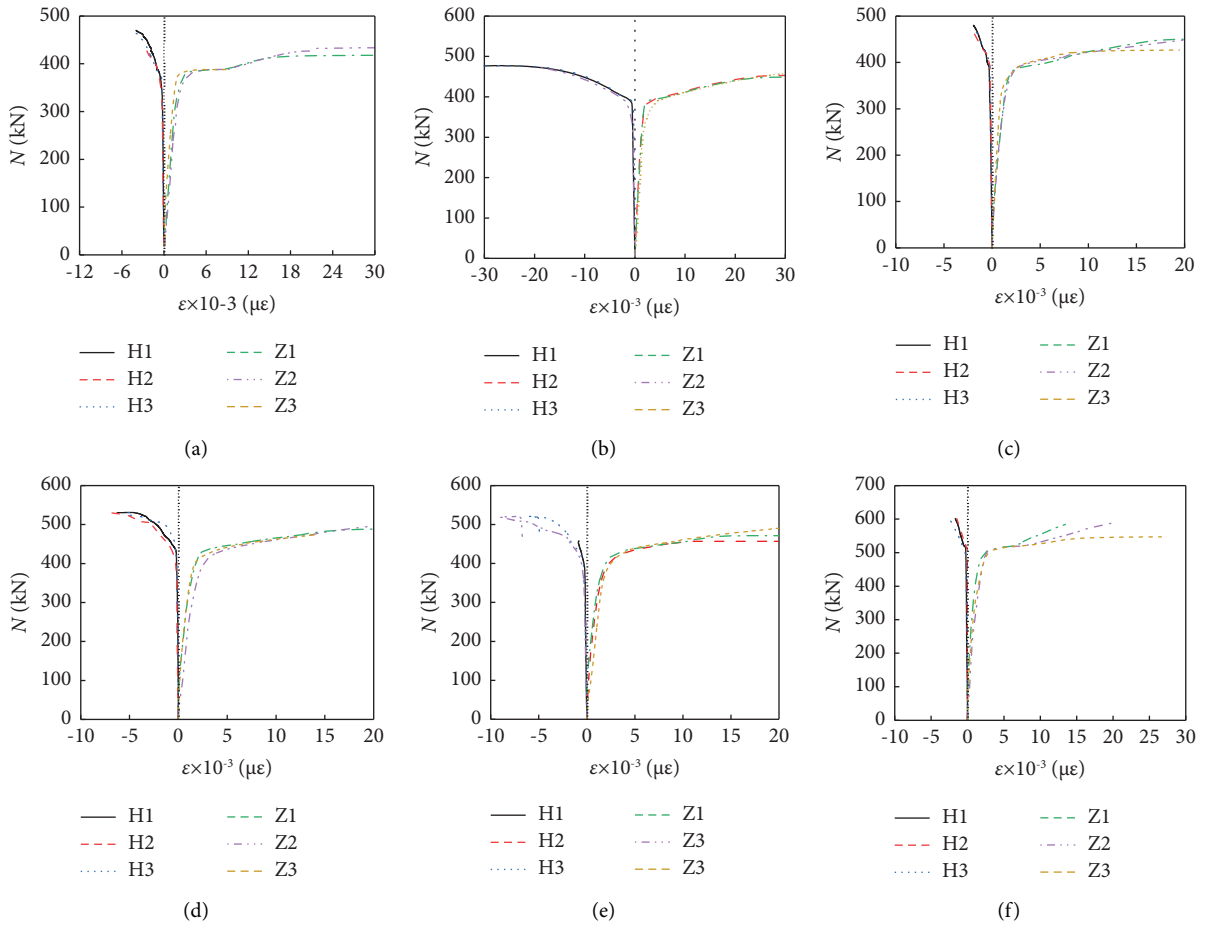


FIGURE 12: Flat section assumption: (a) 89-40, (b) 114-0, (c) 114-30, (d) 114-40, (e) 114-50, and (f) 139-40.

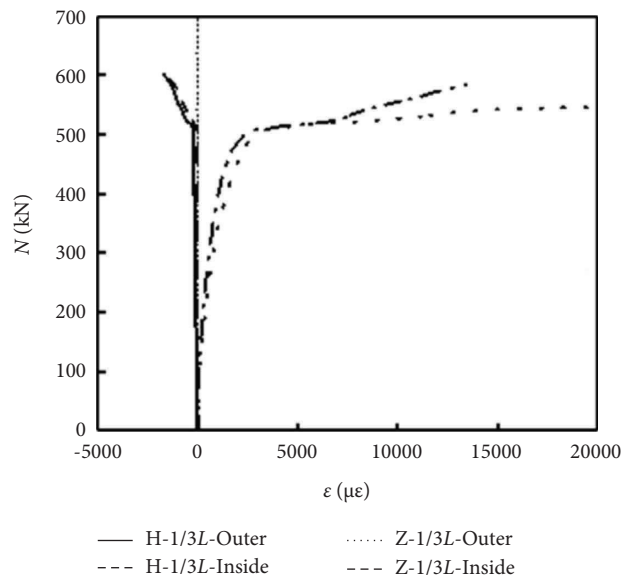


FIGURE 13: Strain comparison of inner and outer wall of steel pipe.

proposed by Han [1], and tension constitutive is defined by the fracture energy (GFI) module by Wang [21]. In this way, the influence of core concrete on the tensile properties of

CFST members is not ignored, and the model is not prone to calculation errors due to convergence problems during the calculation process.

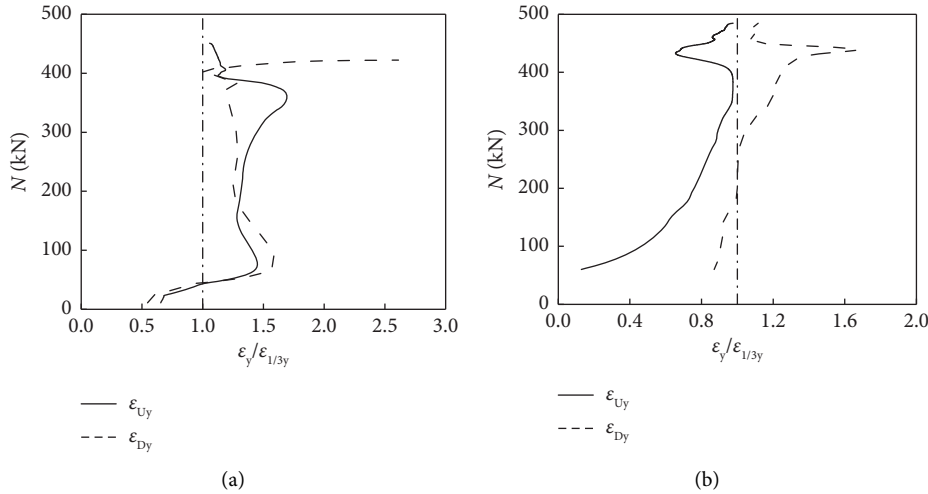


FIGURE 14: ϵ_y/ϵ_{Uy} and ϵ_y/ϵ_{Dy} with N curve: (a) 114-0 and (b) 114-30.

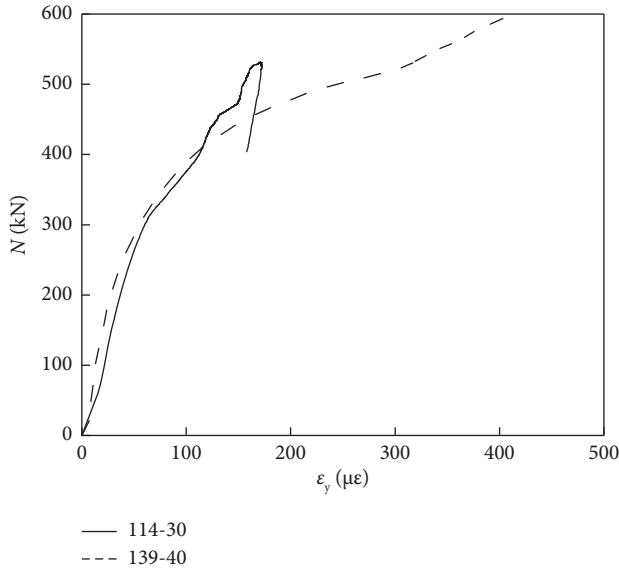


FIGURE 15: Curve of ϵ_y and N on stiffener.

TABLE 6: Bearing capacity comparison table.

Number	N_{u10000} (kN)	N_u (kN)	$ N_{u10000} - N_u /N_{u10000}$
89-40	393.45	295.78	33.0%
114-30	449.17	388.69	15.5%
114-40	455.76	388.69	17.2%
114-50	465.58	388.69	19.7%
139-40	553.35	481.29	14.9%

4.2. *Model Establishment.* In order to improve the calculation accuracy and make the calculation results closer to the test results, in this paper, the finite element software ABAQUS is used to simulate the test specimen, and all components are modeled by C3D8R units. And use sweep method to mesh each part. In order to avoid distortion of the unit grid during the calculation process, the grids of all

components are divided into hexahedral units, and the necessary parts are partitioned.

The choice of contact method refers to the related method in journal written by Han [1] where the contact between steel pipe and concrete is defined by surface-to-surface contact. The normal direction is “hard contact,” the tangential direction is defined as “penalty,” and the friction coefficient μ is 0.6. The remaining contacts are all connected by “Tie.” The reference point and the end plate are connected together by coupling.

The choice of boundary conditions is consistent with the actual boundary conditions of the experiment; that is, one end is completely fixed, and the other end is loaded with displacement. The boundary conditions are shown in Figure 17.

4.3. *Model Verification.* Using the above modeling method and constitutive relationship, simulation calculations were carried out on 6 test specimens. Figure 18 shows the comparison of the test correlation curve of each specimen with the simulated curve. It can be seen from the figure that the curves are in good agreement. The results indicated that the model calculation results can accurately reflect the actual failure of the specimen and can be used for further failure mechanisms.

4.4. *Parameter Analysis.* In order to deeply understand the influence of various parameters on the axial tensile performance of CFST components, on the basis of the verification of the finite element model, the CFST axial tensile specimen was simulated with variable parameters. A total of 7 axial tension finite element models have been established. The basic parameters of the models are shown in Table 7. The external diameter of all models in Table 7 is 120 mm, and the length of the test piece is 460 mm. In the simulation process, the end plate is set as a rigid plate, and the size is 200 mm \times 200 mm \times 25 mm. In order to simplify the calculation, the model is not provided with stiffeners.

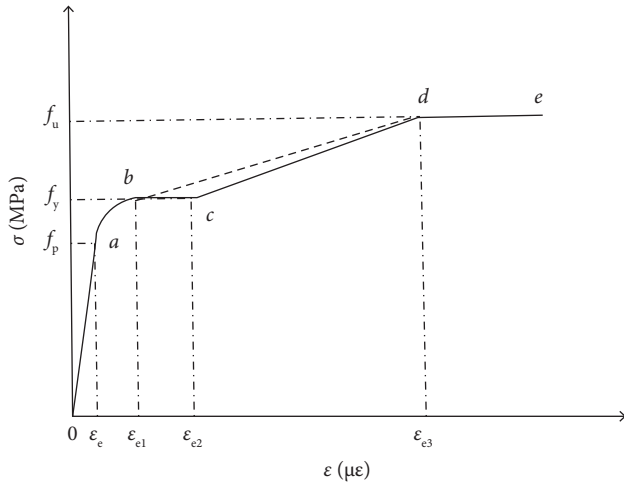


FIGURE 16: Adjustment of steel constitutive relationship.

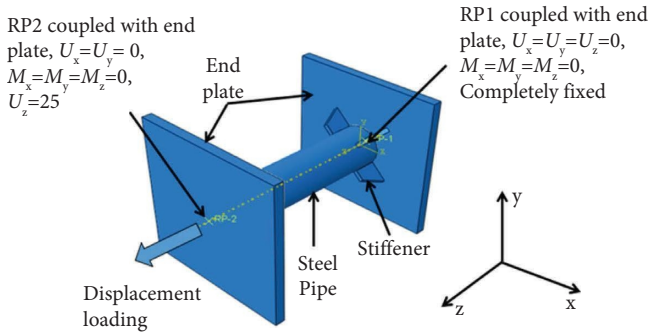


FIGURE 17: Boundary conditions.

Figure 19(a) is the N - ϵ curve of the specimens with different steel content. It can be seen that with the increase of the steel content, the load-bearing capacity of the component and the slope of the elastic phase are significantly increased, and the early stiffness of the specimen is improved. Figure 19(b) shows the comparison between the load N_{u10000} and the yield load N_{sy} of the steel pipe with the same section size when the nominal tensile strain of the specimens with different α is 10000 $\mu\epsilon$. It can be seen that when α is 0.07, the bearing capacity is increased by 24.6%, and when the steel content is 0.19, the bearing capacity is increased by 20.9%. It can be seen that the smaller the steel content, the thinner the steel pipe wall, the more obvious the restraint effect of concrete, and the better the combination effect. In the table, A, B, and C in the number are used to distinguish the f_{cu-k} value, the second Arabic numerals 1, 2, and 3 are used to distinguish the f_y value, and the last number is the wall thickness t_s of the steel pipe.

Figure 20(a) shows the N - ϵ curve of different steel strength specimens. It can be seen that the higher the steel f_y value, the greater the bearing capacity of the specimen. The curves in the early stage of the test basically coincide, indicating that changing the f_y value of the steel does not affect the early stiffness of the specimen. The f_y value increased from 234 MPa to 420 MPa, and the component N_{u10000} value

increased from 369.2 kN to 627.9 kN, an increase of 70.07%. Figure 20(b) shows the N - ϵ curves of different concrete strength specimens. It can be seen that the simulation results are the same as the test results; that is, the three curves basically overlap. It shows that concrete is not the main factor affecting the axial tensile performance of CFST members.

4.5. Simplified Calculation of Bearing Capacity. At present, the calculation formulas in domestic and foreign codes do not consider the influence of concrete and only introduce correlation coefficients based on the tensile strength of steel sections. Foreign standards reduce the tensile strength of steel sections, while domestic standards increase the coefficient of improvement by 1.1 times. Formula (1) essentially increases the improvement factor related to the steel content. In this paper, a total of 25 axial tension specimens including the test specimens are simulated and calculated. The relevant parameters of all specimens are shown in Table 8.

On the basis of a large number of finite element calculations, a formula for calculating the axial tensile bearing capacity related to the ratio of the wall thickness to the diameter of the steel pipe (t_s/D) is proposed, and t_s/D is defined as “ λ ,” and the formula is obtained by referring to formula (5) as follows:

$$N_u = (1 + B\lambda)A_s f_y \quad (5)$$

It can be seen that the bearing capacity N_u and “ λ ” are linear functions. By shifting the terms of the above formula, the formula (6) is obtained as follows:

$$N_u - A_s f_y = B \cdot A_s f_y \lambda, \quad (6)$$

where N_u is the axial tension capacity, A_s is the cross-sectional area of the steel tube, f_y is the yield strength of steel tube, B is the slope of the first order function, and λ is the ratio of steel tube wall thickness to diameter.

After fitting the bearing capacity, as shown in Figure 21, the slope and intercept values are 8.09 and 5.549, respectively. From a safety point of view, the intercept can be omitted, and the final bearing capacity calculation formula is as follows:

$$N_u = (1 + 8.09\lambda)A_s f_y \quad (7)$$

Since the steel content of the finite element specimen used for fitting is between 0.041 and 0.19, this formula is only applicable to CFST members with steel content between 0.041 and 0.19.

4.6. Verification of the Axial Tension Formula. Formula (7) is used to calculate the bearing capacity of 5 concrete-filled steel tube specimens in this test. Figures 22(a) and 22(b) show the comparison of the bearing capacity of the two. The calculation shows that the calculation result of the formula is 10000 $\mu\epsilon$. The error of the bearing capacity is between 1.3%–3.8%, and the error of the ultimate bearing capacity measured in the test is between 15.1% and 24.7%. Therefore, the

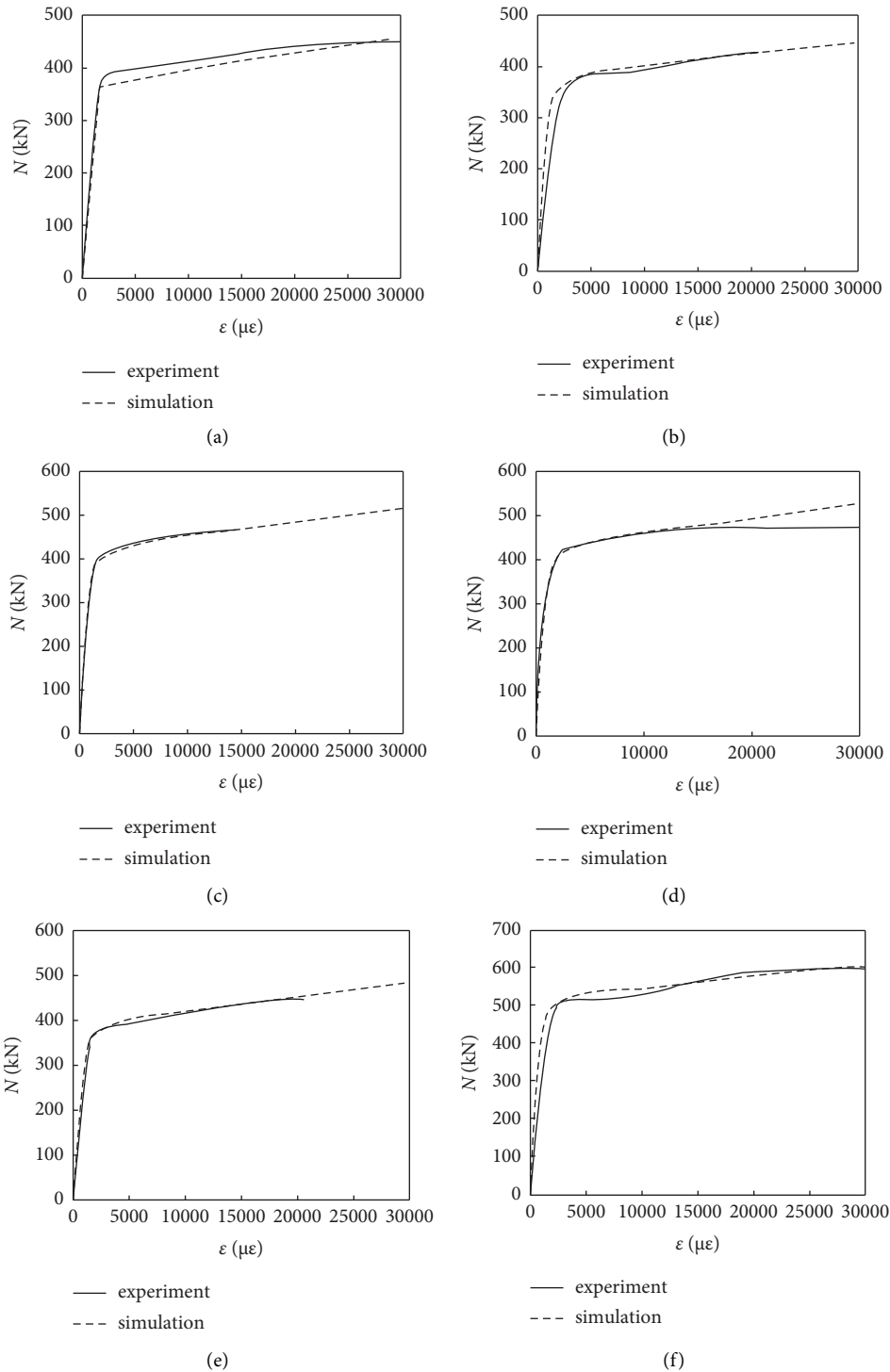


FIGURE 18: Comparison of test results and finite element calculation results: (a)114-0, (b) 89-40, (c) 114-30, (d) 114-40, (e) 114-50, and (f) 139-40.

TABLE 7: Simulation test piece parameters.

Number	Serial number	t_s (mm)	α	f_y (MPa)	$f_{cu,k}$ (MPa)
1	A1-3.5	3.5	0.13	235	30
2	B1-3.5	3.5	0.13	235	40
3	C1-3.5	3.5	0.13	235	50
4	A1-2	2	0.07	235	30
5	A1-5	5	0.19	235	30
6	A2-3.5	3.5	0.13	345	30
7	A3-3.5	3.5	0.13	420	30

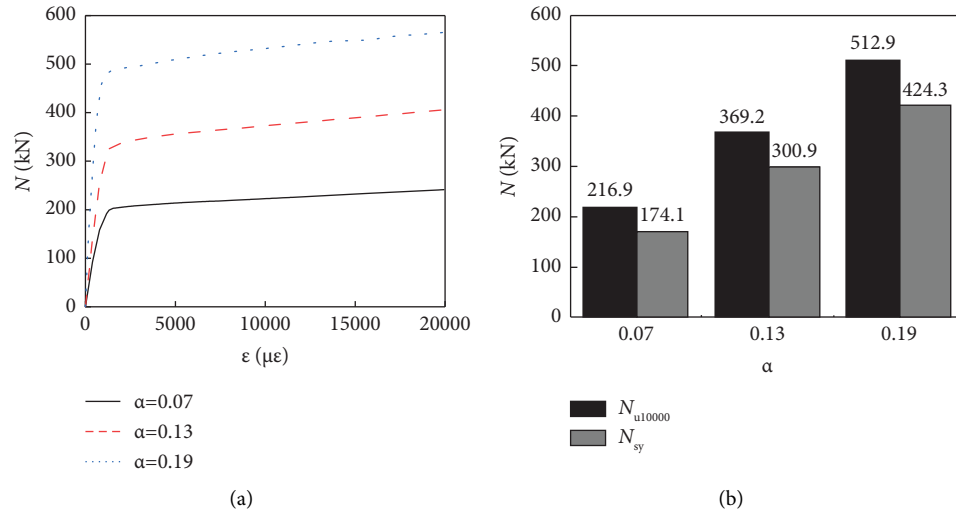


FIGURE 19: The influence of α on the axial tensile properties: (a) N - ϵ curve of specimen under different α and (b) comparison of N_{u10000} and N_{sy} under different α .

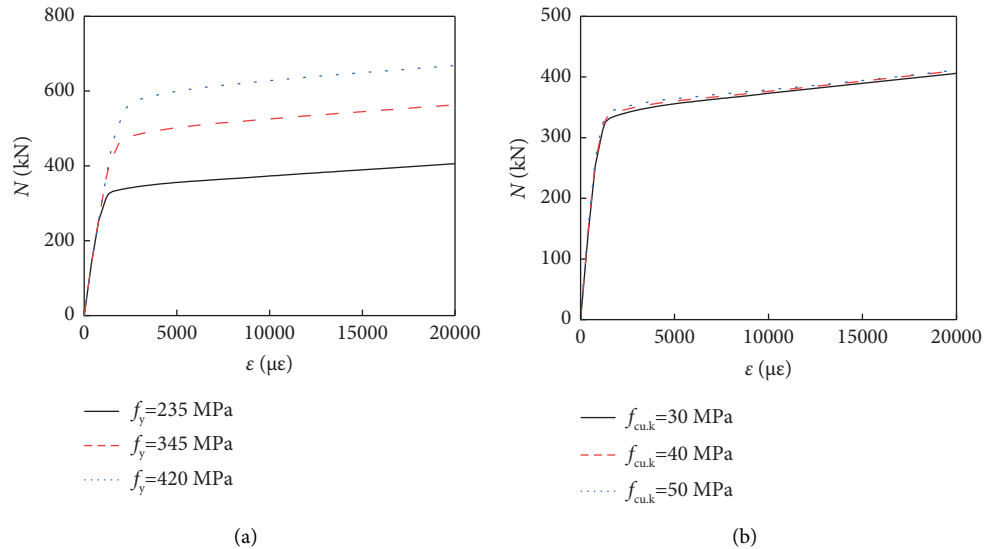


FIGURE 20: The influence of f_y and $f_{cu,k}$ on the axial tensile properties: (a) N - ϵ curve of specimen under different f_y and (b) N - ϵ curve of specimen under different $f_{cu,k}$.

TABLE 8: Simulation model summary.

Number	Number	$t_s \times D$ (mm)	α	f_y (MPa)	$f_{cu,k}$ (MPa)
1	89-40	3.5×89	0.178	306	40
2	114-40	3.5×114	0.135	306	40
3	139-40	3.5×139	0.109	306	40
4	114-30	3.5×114	0.135	306	30
5	114-50	3.5×114	0.135	306	50
6	A1-3.5	3.5×120	0.13	235	30
7	B1-3.5	3.5×120	0.13	235	40
8	C1-3.5	3.5×120	0.13	235	50
9	A1-2	2×120	0.07	235	30
10	A1-5	5×120	0.19	235	30
11	A2-3.5	3.5×120	0.13	345	30
12	A3-3.5	3.5×120	0.13	420	30
13	235-40-1	1×40	0.108	235	30
14	235-50-1	1×50	0.085	235	30
15	235-60-1	1×60	0.07	235	30
16	235-50-0.5	0.5×50	0.041	235	30
17	235-50-1.5	1.5×50	0.132	235	30
18	345-50-1	1×50	0.085	345	30
19	420-50-1	1×50	0.085	420	30
20	235-220-4	4×220	0.077	235	30
21	235-220-5	5×220	0.097	235	30
22	235-220-6	6×220	0.119	235	30
23	235-200-5	5×200	0.108	235	30
24	235-240-5	5×240	0.089	235	30

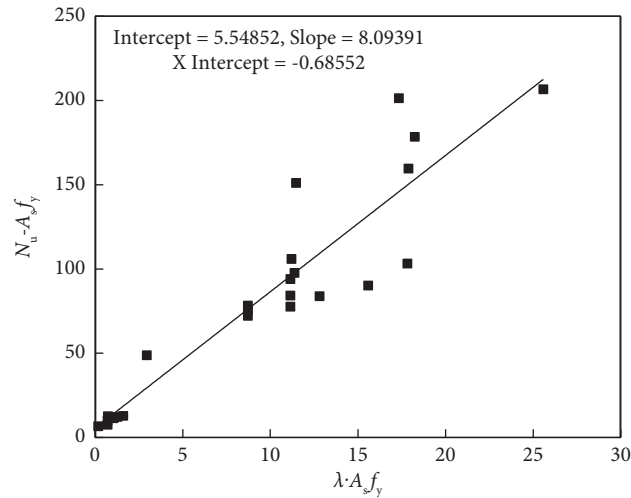


FIGURE 21: Axial pull formula fitting curve.

calculation accuracy of the formula is high, and it has a high safety reserve value.

Compare the N_{u10000} test values of 6 typical CFST axial tensile test specimens with the calculated results of the formula in documents Wang [21], Han [1], Wang [22], Hua et al. [4]. The comparison is shown in Figure 23. It can be seen that the two values are basically the

same. The smaller the outer diameter of the steel pipe, the smaller the error. And the bearing capacity value calculated by the formula is slightly smaller than the value of N_{u10000} measured in the experiment, and the error is between 9.1%–13.1%. It can be seen that the bearing capacity calculated by formula (6) is accurate and reliable.

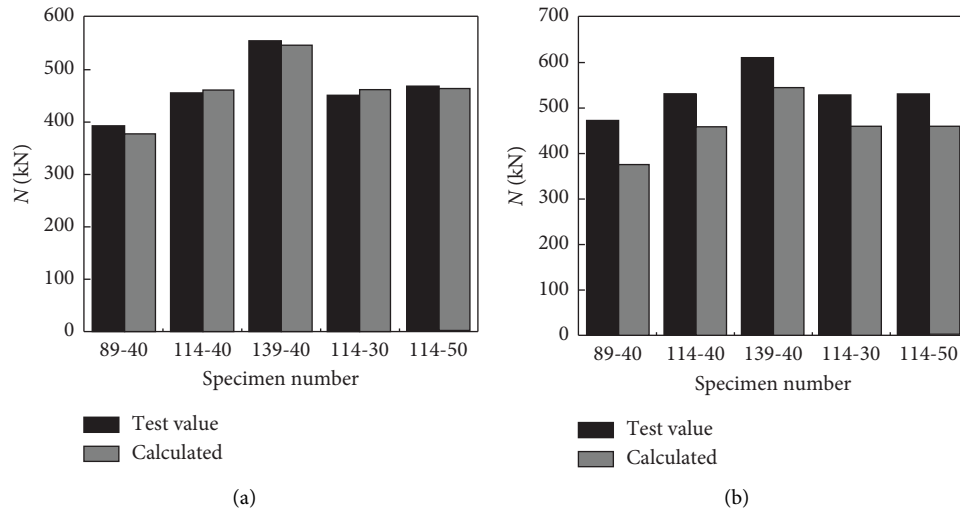


FIGURE 22: Comparison of measured bearing capacity and calculated bearing capacity: (a) $N_{u,10000}$ test value and calculated value comparison and (b) comparison of test ultimate bearing capacity and calculated value.

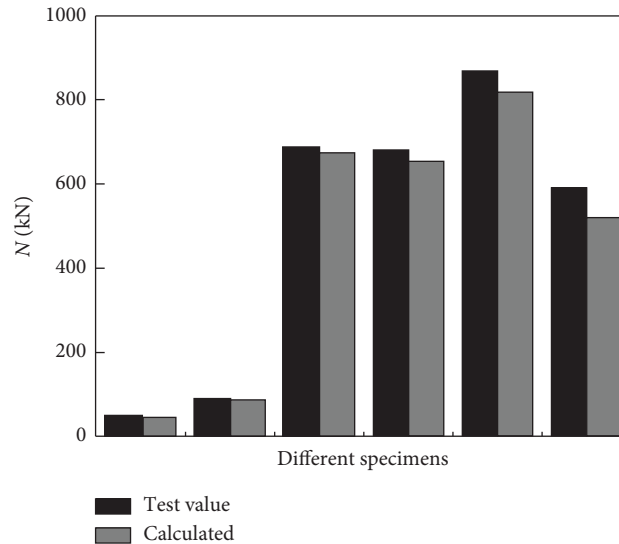


FIGURE 23: Comparison of the measured bearing capacity of the specimen in the literature and the calculated value of the formula.

5. Conclusions

- (i) The failure section of the pure steel pipe specimen appears at the midspan section position, while the failure position of the CFST specimen occurs near the $1/3L$ section and where the top of the stiffener contacts the steel pipe.
- (ii) The reason for the increase in the bearing capacity of the CFST specimen is that the core concrete limits the circumferential shrinkage of the outer steel pipe, and the increase is between 7.5% and 16.3%. However, the ductility of CFST specimens is slightly worse than that of pure steel pipe specimens.
- (iii) Compared with the tensile stress-strain curve of steel pipe and steel plate, there is no yield platform,

so the five-segment secondary plastic flow model is adjusted. The simulated calculation results of the adjusted steel constitutive relationship are in good agreement with the test results.

- (iv) Through the analysis of the test and finite element method parameters, the higher the steel content, the greater the early stiffness of the specimen, and the higher the bearing capacity, but the worse the effect of the combination of steel pipe and concrete. The increase in steel strength does not change the specimen. The initial stiffness can effectively improve the bearing capacity; concrete is not the main factor that affects the axial tensile performance of CFST specimens.
- (v) A simplified calculation formula for the axial tension bearing capacity related to t_s/D is

suggested. The error between the calculated result of the formula and the measured value of N_{u10000} is between 1.3% and 3.8%, which is 15.1%–24.7% compared with the measured ultimate bearing capacity. The safety reserve value can provide a reference for quickly calculating the bearing capacity of this type of member in actual engineering.

- (vi) When the connection between the concrete and the steel wall is failed, the friction between the concrete and the outer steel pipe will be generated when under tension, and the axial tension will be transmitted to the core concrete through the friction. When the concrete reaches the ultimate tensile stress, the concrete is pulled off (at 1/3L), the friction between the two at the pull off position disappears, the radial support effect of the core concrete on the steel pipe disappears, and the steel pipe necks here until it is damaged. However, there is still friction between the outer steel pipe and the core concrete at the unbroken position, and the concrete still plays the role of internal support.
- (vii) For various reasons, this paper only carried out the axial tension test of CFST specimens, but the eccentric tension test of CFST members was not carried out. Therefore, it is suggested to carry out the eccentric tension test and compare the test results with the theoretical results. At present, there are relatively few experimental studies on eccentrically tensioned concrete-filled steel tubular members, and the system is still not perfect. Therefore, it is necessary to carry out relevant eccentric tension experimental studies.
- (viii) In harsh environment, it will also cause corrosion of steel pipes outside CFST members, so it is necessary to study the tensile properties of corroded CFST members. At the same time, in order to study the tensile properties of strengthened CFST members, it is recommended to study the tensile properties of CFST specimens under different reinforcement methods, such as CFRP reinforcement and steel clad reinforcement.
- (ix) In order to better solve the problem of separation from the outer steel tube during concrete curing, it is suggested to use microexpansive concrete, such as adding magnesium oxide powder expansion agent, to study the influence of the bonding force between steel tube and concrete on the axial tensile properties of CFST specimens.

Data Availability

The data supporting the current study are available from the corresponding author upon request.

Conflicts of Interest

The authors declare that they have no conflicts of interest.

Acknowledgments

This work was partially supported by the General Project of the Natural Science Foundation of China (Grant no. 51678542) and the Project of Revitalizing Liaoning Talents (Grant no. XLYC1902009).

References

- [1] L. H. Han, *Concrete Filled Steel Tubular Structures - Theory and Practice*, Science Press, Beijing, China, 3rd edition, 2016.
- [2] M. Zhou, J. S. Fan, M. X. Tao, and J. G. Nie, "Experimental study on the tensile behavior of square concrete-filled steel tubes," *Journal of Constructional Steel Research*, vol. 121, pp. 202–215, 2016.
- [3] L. Y. Xu, M. X. Tao, and M. Zhou, "Analytical model and design formulae of circular CFSTs under axial tension," *Journal of Constructional Steel Research*, vol. 133, pp. 214–230, 2017.
- [4] Y. X. Hua, C. Hou, and L. H. Han, "Behaviour of CFST tensile members subjected to chloride corrosion," *Engineering Mechanics*, vol. 32, no. 1, pp. 149–152+158, 2015.
- [5] Z. Ying, *Experimental Study on Mechanical Properties of RPC-FST under Direct Tension load*, Fujian Agriculture and Forestry University, Fuzhou, China, 2016.
- [6] J. Wang, Y. Liu, X. Guo, B. Dong, and Y. Cao, "High-level expression of lipase from *Galactomyces geotrichum* mafic-0601 by codon optimization in *Pichia pastoris* and its application in hydrolysis of various oils," *3 Biotech*, vol. 9, no. 10, pp. 354–361, 2019.
- [7] L. H. Han, Z. B. Wang, W. Xu, and Z. Tao, "Behavior of concrete-encased CFST members under axial tension," *Journal of Structural Engineering*, vol. 142, no. 2, Article ID 4015149, 2016.
- [8] W. Li, L. H. Han, and T. M. Chan, "Performance of concrete-filled steel tubes subjected to eccentric tension," *Journal of Structural Engineering*, vol. 141, no. 12, Article ID 4015049, 2015.
- [9] Z. B. Wang, Q. Yu, and Z. Tao, "Behaviour of CFRP externally-reinforced circular CFST members under combined tension and bending," *Journal of Constructional Steel Research*, vol. 106, pp. 122–137, 2015.
- [10] W. Li, L. H. Han, and T. M. Chan, "Numerical investigation on the performance of concrete-filled double-skin steel tubular members under tension," *Thin-Walled Structures*, vol. 79, pp. 108–118, 2014.
- [11] J. Chen, J. Wang, and W. L. Jin, "Experimental investigation on concrete-filled steel tubes with reinforcing bars under axial and eccentric tension," *Journal of Building Structures*, vol. 38, no. 1, pp. 272–277, 2017.
- [12] Y. Ye, W. Li, X. J. Liu, and Z. X. Guo, "Behaviour of concrete-filled steel tubes with concrete imperfection under axial tension," *Magazine of Concrete Research*, vol. 73, no. 14, pp. 743–756, 2021.
- [13] L.-H. Han, S. H. He, and F. Y. Liao, "Performance and calculations of concrete filled steel tubes (CFST) under axial tension," *Journal of Constructional Steel Research*, vol. 67, no. 11, pp. 1699–1709, 2011.
- [14] J. Chen, J. Wang, and W. L. Jin, "Concrete-filled steel tubes with reinforcing bars or angles under axial tension," *Journal of Constructional Steel Research*, vol. 133, pp. 374–382, 2017b.
- [15] M. Zhou, L. Y. Xu, M. X. Tao, J. S. Fan, J. F. Hajjar, and J. G. Nie, "Experimental study on confining-strengthening, confining-stiffening, and fractal cracking of circular concrete

- filled steel tubes under axial tension,” *Engineering Structures*, vol. 133, pp. 186–199, 2017.
- [16] Q. Qiao, X. Li, W. Cao, and H. Dong, “Seismic behavior of specially shaped concrete-filled steel tube columns with multiple cavities,” *The Structural Design of Tall and Special Buildings*, vol. 27, no. 12, pp. 14855–1515, 2018.
- [17] GB/T2281, *Tensile Test of Metallic Materials Part 1: Tensile Method at Room Temperature*, Ministry of Housing and Urban-Rural Development, Beijing, China, 2011.
- [18] GB/T50081, *Standard for Test Methods of Physical and Mechanical Properties of Concrete*, Ministry of Housing and Urban-Rural Development, Beijing, China, 2019.
- [19] G. H. Yao, *Research on Behaviour of Concrete-filled Steel Tubes Subjected to Complicated Loading states*, Fuzhou University, Fuzhou, China, 2006.
- [20] X. C. Xu, *Study on Behavior of CFRP Strengthen concrete-filled Steel Tube under Eccentric tension*, Fuzhou University, Fuzhou, China, 2013.
- [21] Q. L. Wang, *CFRP - Concrete-filled Steel Tube*, Science Press, Beijing, China, 2017.
- [22] L. B. Wang, *Research on Tensile Bearing Capacity and Beams-Columns Hysteretic Behaviour of Concrete-Filled Stainless Steel Tubes*, Fuzhou University, Fuzhou, China, 2011.

Research Article

Thermal and Waterproof Properties of Foamed Concrete with Nano SiO₂ Aerogel and Organosilicon Waterproofing Agent

Baojun Cheng,^{1,2} Xiaowei Gu ,¹ Yuxin Gao,^{2,3} Pengfei Ma,^{2,3} and Shengrong Kang²

¹Northeastern University, Shenyang 110819, China

²China Construction West Building Materials Science Research Institute Co. Ltd, Chengdu 610094, China

³Chongqing University, Chongqing 400044, China

Correspondence should be addressed to Xiaowei Gu; xiaoweigu@outlook.com

Received 11 August 2021; Revised 9 March 2022; Accepted 1 April 2022; Published 10 May 2022

Academic Editor: Robert Černý

Copyright © 2022 Baojun Cheng et al. This is an open access article distributed under the Creative Commons Attribution License, which permits unrestricted use, distribution, and reproduction in any medium, provided the original work is properly cited.

This paper aimed to improve the thermal and waterproof properties of foamed concrete through the synergic work of nano SiO₂ aerogel powder (NSAP) and organosilicon waterproofing agent (OWA). Hence, several series of foamed concrete with a 0–3.0% of OWA and with 1–4% of NSAP addition were developed. The results show that OWA can decrease the dry bulk density, compressive strength, water absorption rate, and thermal conductivity. With the addition of NSAP, the water absorption rate reached a minimum value of 9.2% at 3.0% NSAP, while the thermal conductivity continued decreasing. Through the microscopic pore size distribution, XRD, and SEM, it was found that the addition of NSAP had no effect on the type of hydration product, but it can increase the average pore size and the amount of macropore and weaken the interfacial adhesion between hydration products. Comparing the heat transmission model, the presence of NSAP increased the heat transmission pathway and resistance, resulting in lower thermal conductivity.

1. Introduction

Foamed concrete is a lightweight porous material prepared by introducing premanufactured aqueous foam into the cement or mortar paste [1], with light weight, good thermal insulation and sound insulation performance, fire resistance, low cost, and recycling waste [2, 3]. However, the foamed concretes generally show a poor thermal conductivity, low mechanical strength, and high water absorption rate, which greatly restricts its application in construction industries; thus, a low-density foamed concrete with excellent properties is difficult to prepare [4, 5]. As foamed concrete or other porous materials are easily damaged by water hydrolysis, it can be blended with nanoaerogel or nanomaterials to solve the problem [6–8].

Kistler discovered aerogels 80 years ago [9] by complex synthesis in supercritical drying conditions. Depending on the silica source and the preparation process, aerogels have significant physical, thermal, optical, and acoustic properties [10]. To overcome the problems of foamed concrete, some

experiments [11, 12] were attempted to enhance the thermal transfer and moisture resistances of foamed concrete by merging with aerogel technologies. The thermal conductivity of foam concrete with hydrophobic aerogel is 0.08 W/m·K approximately, which corresponds to be 30–50% for conventional foam concrete [13]. And the waterproof capacity of foam concrete with hydrophobic aerogel was significantly improved, resulting in exhibiting 75% lower water absorption at an age of 24 hours when compared with the conventional foam concrete [13].

Nano SiO₂ aerogel is a porous and solid material with the lowest thermal conductivity and density. It is widely used in heat insulation, aerospace, environmental protection, new energy, and other fields [14]. In recent years, it has been found that adding nano SiO₂ aerogel powder (NSAP) into the foamed concrete can effectively reduce the bulk density and thermal conductivity of foamed concrete [15]. The aerogel foamed concrete (AFC) presented a lower thermal conductivity and bulk density than normal foamed concrete. However, the waterproofing properties of AFC have not

been significantly improved with the addition of NSAP, which can damage its thermal insulation performance when the AFC was contacted with water or in a humid environment. Moreover, when the AFC was used in cold or severe cold areas, the strength was hugely reduced due to the alternate freezing and thawing cycles [16], resulting in the damage of the foamed concrete structure.

From the literature, it was concluded that the addition of supplementary cementitious materials and fibers could significantly improve the mechanical properties. The waterproofing agents can improve the water resistance, and the NSAP can reduce its bulk density. However, the addition of NSAP fillers simultaneously with waterproofing agents in foamed concrete to reduce their thermal conductivity and improve their water resistance has not been engaging in the literature, which restricts its application in the construction industry. Therefore, more attention should be paid to determine the synergic work between NSAP and waterproof materials on the thermal insulation performance and water resistance of foamed concrete. In this study, the influence of NSAP and organosilicon waterproofing agents on the thermal and waterproofing properties of AFC was studied.

2. Experimental Studies

2.1. Materials. The ordinary Portland cement (PC) used in this study was P-O 42.5R conforming to the Chinese Standard for ordinary Portland cement. The fly ash (FA) used in this study was grade I FA, which conforms to the Chinese Standard for fly ash used for cement and concrete. The physical and chemical properties of PC and FA are given in Table 1. The density of PC and FA is 3080 kg/m^3 and 2340 kg/m^3 , respectively. NSAP is white and translucent produced by Suzhou Rexiang Nano Technology Co., Ltd., with an average particle size of 15 μm , a thermal conductivity of $0.015 \text{ W/(m}\cdot\text{K)}$ (25°C), and a density of 0.08 g/cm^3 . Foaming agent is HTQ-1 compound foaming agent produced by Henan Huatai New Material Technology Co., Ltd. The accelerator is a self-made composite accelerator, and hydroxypropylmethylcellulose (HPMC) is from Shandong Gomez Chemical Co., Ltd. The water reducing agent is polycarboxylic acid superplasticizer (SP) with a water reducing rate of 35% and a solid content of 50%. Organosilicon waterproofing agent (OWA) was from Wacker Chemical Co., Ltd.

2.2. Preparation of Specimens. First, the specimens with OWA at 0%, 0.1%, 0.5%, 1.0%, and 3.0% of the scale specimens were studied. Then, the specimens with OWA at 0.5% while NSAP ranging from 1.0% to 4.0% were also studied. The wet density of all AFC pastes was controlled from 280 kg/m^3 to 300 kg/m^3 . The mix designs of AFC are shown in Table 2. In order to ensure good performance of aerogel foam concrete, 10wt% fly ash is added in the mixture.

2.3. Mixing Procedure. The mixing procedures of AFC were as follows. Firstly, the PC, FA, HPMC, accelerator, OWA, and NSAP, according to the mix proportions in Table 2, were uniformly dry-mixed for 2-3 min. Then, the tap water and SP

TABLE 1: The chemical composition of cementitious materials (wt%).

Chemical composition	PC	FA
SiO ₂	21.39	50.39
Al ₂ O ₃	5.15	27.49
CaO	61.04	4.47
MgO	2.82	0.953
Na ₂ O	0.638	1.41
K ₂ O	0.615	2.03
P ₂ O ₅	0.095	0.357
Fe ₂ O ₃	3.86	8.47
TiO ₂	0.848	2.92
SO ₃	3.10	1.16
Others	0.444	0.35

were added to the premixed powders and mixed for 3 min. Finally, the preformed foam was added to the paste and mixed for 3 min. Additionally, the following specimens were cast to determine the mechanical properties: the cubic specimens $100 \times 100 \times 100 \text{ mm}^3$ for testing the compressive strength and the dry bulk density. In addition, prismatic specimen $300 \times 300 \times 30 \text{ mm}^3$ was used to test the thermal conductivity. All the specimens were cast into molds and covered with cling film to prevent water evaporation. After 72 h, the specimens were demolded and kept in a standard curing room (20°C , 100% relative humidity) for 28 days. Before tests, each specimen was dried in an oven at 60°C to a constant weight and cooled to room temperature.

2.4. Test Procedures. The 28 days compressive strength of the AFC was determined by a sensitive multifunctional testing system machine with a 200 KN capacity. The bulk density of the AFC was calculated by dividing the dry mass of the AFC to its volume ($100 \times 100 \times 100 \text{ mm}^3$) at the age of 28 days. The water absorption rate was calculated based on the difference in the mass before and after immersion in water for 24 h. The thermal conductivity (k) of AFC was measured in accordance with ASTM C518 Standard Test Method for Steady-State Thermal Transmission Properties by means of the Heat Flow Meter Apparatus on HFM 436 by NETZSCH.

The pore structure of the AFC was measured by the specimen of $100 \text{ mm} \times 100 \text{ mm} \times 100 \text{ mm}$ cut in half, and the section was the surface to be measured. DJCK-2 crack width meter manufactured by Jingmao Instrument was used to photograph the structure of the cut face. The size of the section was $11 \times 9 \text{ mm}$, and the magnification was 60 times. Finally, Namo Measurer software was used for statistical analysis of pore structure parameters.

The micromorphology of AFC was observed by scanning electron microscope (SEM). Due to the poor conductivity of the sample, the sample was sprayed with gold before testing. The phase composition of AFC was analyzed by Powder X-ray Diffraction analyzer (XRD, Shimadzu DX-6100).

3. Results and Discussion

3.1. Influence of OWA Content on Fundamental Properties. The fundamental properties of the AFC with different OWA contents are presented in Figure 1. It was observed that with

TABLE 2: The mix designs of AFC (kg/m^3).

Mix	PC	FA	Water	SP	HPMC	Accelerator	OWA (wt%)	NSAP (wt%)
AFC-0	225	25	62.5	1.5	0.075	30	0	0
AFC-1	225	25	62.5	1.5	0.075	30	0.1	0
AFC-2	225	25	62.5	1.5	0.075	30	0.5	0
AFC-3	225	25	62.5	1.5	0.075	30	1.0	0
AFC-4	225	25	62.5	1.5	0.075	30	3.0	0
AFC-5	225	25	62.5	1.5	0.075	30	0.5	1.0
AFC-6	225	25	62.5	1.5	0.075	30	0.5	2.0
AFC-7	225	25	62.5	1.5	0.075	30	0.5	3.0
AFC-8	225	25	62.5	1.5	0.075	30	0.5	4.0

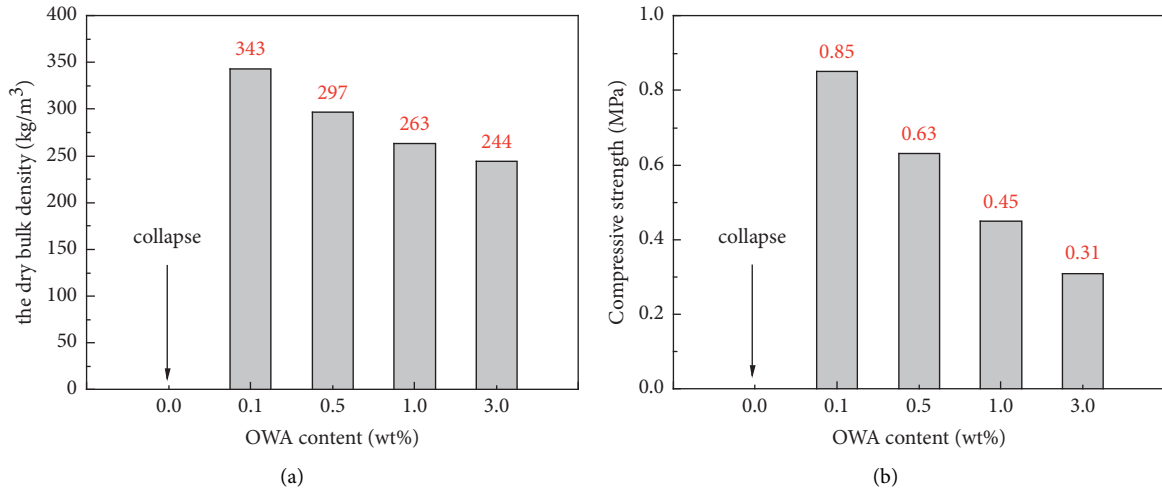


FIGURE 1: Effect of different OWA content on (a) dry bulk density and (b) compressive strength.

the increasing dosage of OWA from 0.1% to 3.0%, the dry bulk density and compressive strength were significantly decreased. This is because the hydrophobic cement particles adsorb on the gas-liquid interface of the bubble, which could prevent the bubble from further growing and merging [17] and delay the hydration reaction, resulting in reduced compressive strength of specimens [18, 19].

3.2. Influence of OWA Content on Water Absorption Rate and Thermal Conductivity. As shown in Figure 2(a), with the increase in OWA content from 0.1% to 3%, the water absorption rate of AFC was significantly decreased from 16.9% to 9.2%. As shown in Figure 2(b), the thermal conductivity of AFC was obviously reduced from 0.104 W/(m·k) to 0.073 W/(m·k). It was seen that with the content of OWA more than 0.5%, the decline tendency of water absorption rate and thermal conductivity became much less obvious. The results indicated that the optimum content of OWA is 0.5% for improving the waterproofing properties of AFC. According to the result of Hai-li [20], the aerogel is effective in enhancing the moisture resistance of foam concrete and forming hydrophobicity on the interfacial substrate of air pores.

When OWA content was kept as 0.5%, the bulk density, compressive strength, water absorption rate, and thermal conductivity of the AFC were $300 \text{ kg}/\text{m}^3$, 0.6 MPa, 12%, and

0.08 W/(m·k), respectively. The OWA content was kept constant as 0.5% in the following mix proportion.

3.3. Influence of NSAP Content on Water Absorption Rate and Thermal Conductivity. Figure 3 presents the influence of NSAP content on water absorption rate and thermal insulation of AFC. It can be seen from Figure 3(a) that with the addition of NSAP from 0% to 4.0%, the water absorption rate first slightly decreased and then significantly increased, reaching a minimum value of 9.2% at 3.0% NSAP. This is because with the increase in the content of small particle NSAP, the consistency and viscosity of foamed concrete slurry increase, resulting in a decrease in the number of connected pores. On the other hand, the microaggregate effect of NSAP reduces the number of capillary pores in the cement paste of foamed concrete [21, 22]. Once when the content of NSAP exceeded 3.0%, the reduction of C-S-H amount in hydration products led to an increase in a number of connected pores. As shown in Figure 3(b), with the increasing content of NSAP from 0% to 4.0%, the thermal conductivity was decreased from 0.074 W/(m·K) to 0.055 W/(m·K). The reasons for the decrease in thermal conductivity are as follows. Firstly, the NSAP with high void fraction decreased the heat transmission route in AFC. Secondly, the thermal conductivity of NSAP is 0.019 W/(m·K), which is lower than the thermal conductivity of air (0.024 W/(m·K)) [23]. Thirdly, concrete materials will become rougher, more loose, and

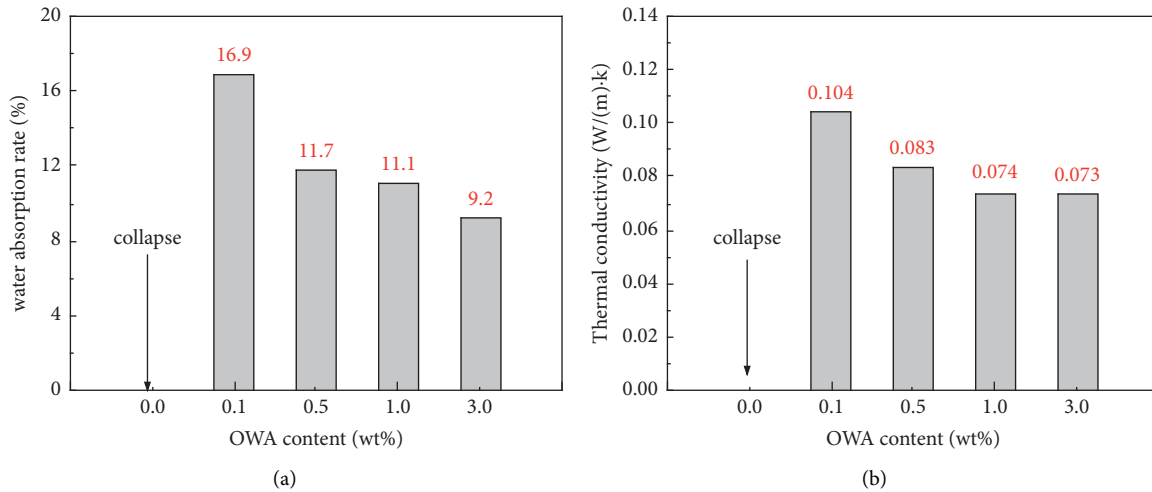


FIGURE 2: Effect of different OWA content on (a) water absorption rate and (b) thermal conductivity.

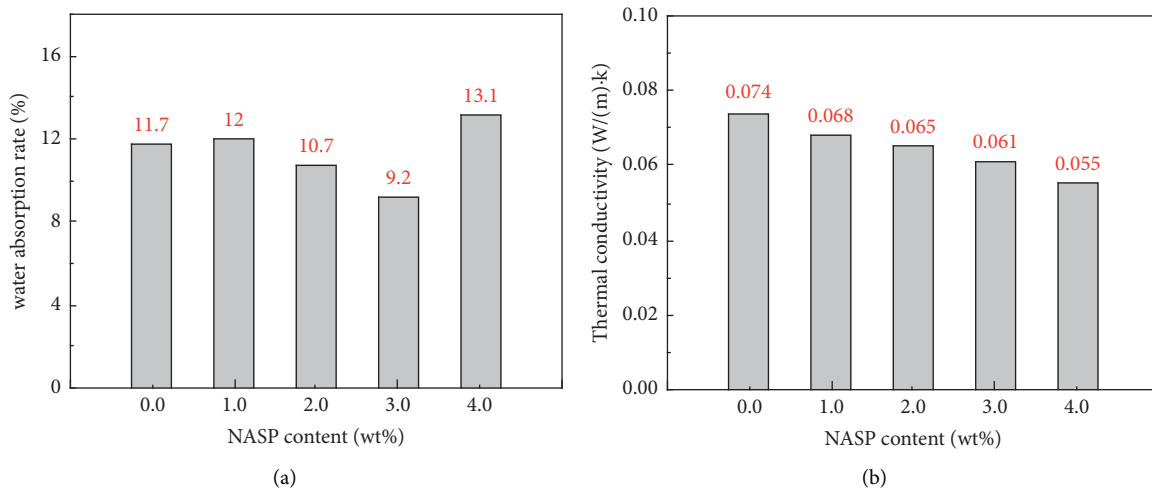


FIGURE 3: Effect of different NASP content on (a) water absorption rate and (b) thermal conductivity.

porous when NSAP particles are used [24]. Thus, the thermal conductivity was decreased.

4. Microstructure and Hydration Products Analysis

4.1. Pore Structure Analysis. The microstructure photographs and pore size distribution of AFC-2 and AFC-7 cross section are shown in Figure 4. It was seen that the AFC-2 sample has a small pore size and thick pore wall, while the AFC-7 has a larger average pore size and more macropore amount. It indicated that the addition of NSAP could significantly increase the average pore size and macropore amount of specimens due to the poor combination of NSAP and cement pastes. The results also can explain why the thermal conductivity was decreased [25].

4.2. XRD. The X-ray diffraction analysis (Figure 5) proved that the CH (PDF 84-1269) and ettringite (PDF 72-1907) are the main crystalline compounds in all the specimens with or

without NSAP. It was also seen that at the peak of 29 degree, C-S-H existed in both AFC-2 and AFC-7. These results indicated that the main hydration products of AFC are CH, C-S-H, and ettringite. Moreover, the addition of NSAP almost had no effect on the hydration products of foamed concrete.

4.3. SEM. The SEM images and EDS results of the specimens are shown in Figure 6. As shown in Figures 6(a) and 6(b), the hydration products of AFC-2 and AFC-7 were CH, C-S-H, and ettringite, which further proved the results of XRD. It is seen from Figure 6(b) that there are a large number of NSAP on the surface of AFC hydration product. The EDS results (Figure 7 and the detection position is marked with the red box in Figure 6) of AFC-2 and AFC-7 samples also proved that the particles covering the surface of the hydration product were NSAP. By comparing the SEM images of AFC-2 and AFC-7, it was obvious that the presence of NSAP on the hydration products can weaken the interfacial adhesion between hydration products [26].

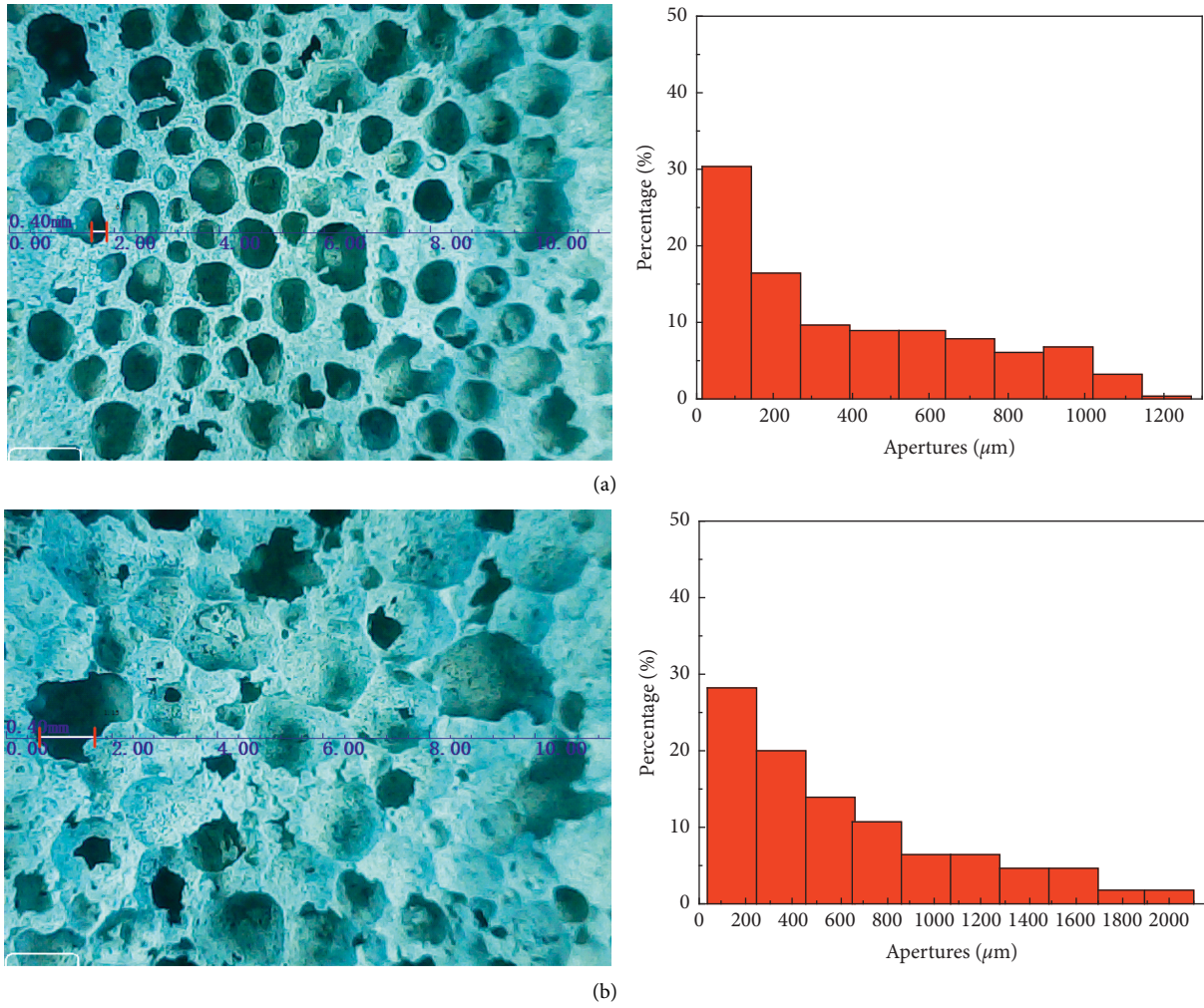


FIGURE 4: Microstructure photographs and pore size distribution of AFC sample cross section: (a) AFC-2 (without NSAP) and (b) AFC-7 (with NSAP).

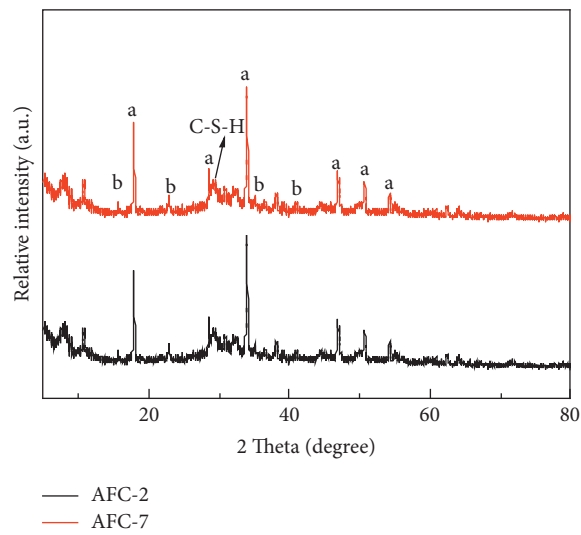


FIGURE 5: XRD analysis of the hydration products of AFC-7 sample (a for CH; b for ettringite).

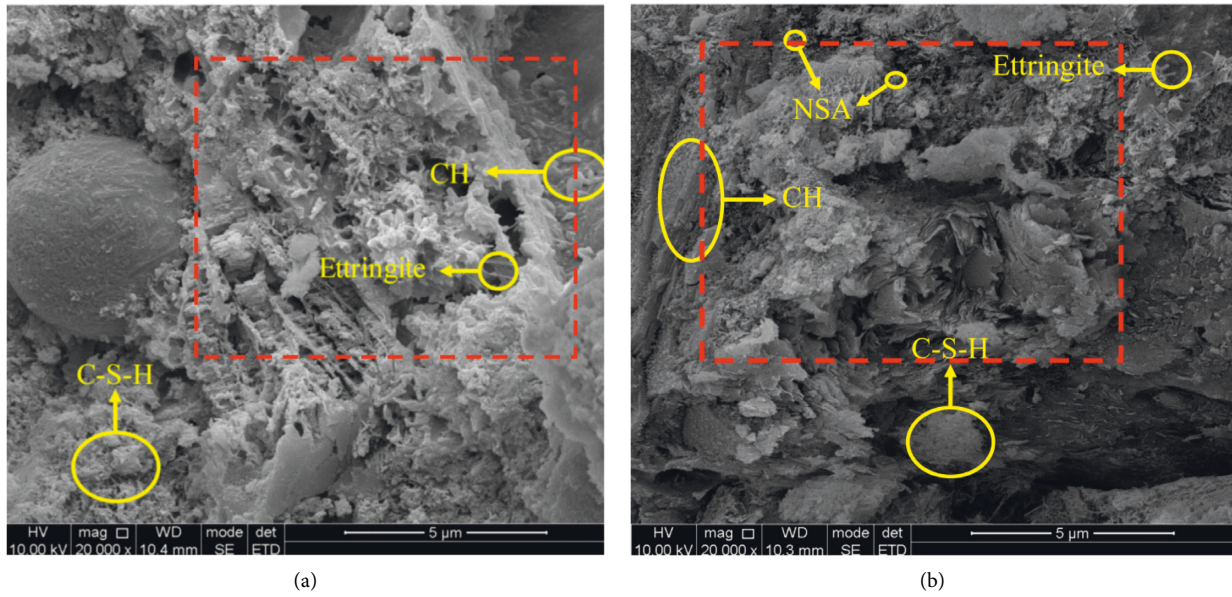


FIGURE 6: SEM images of (a) AFC-2 (without NSAP) and (b) AFC-7 (with NSAP) sample cross section.

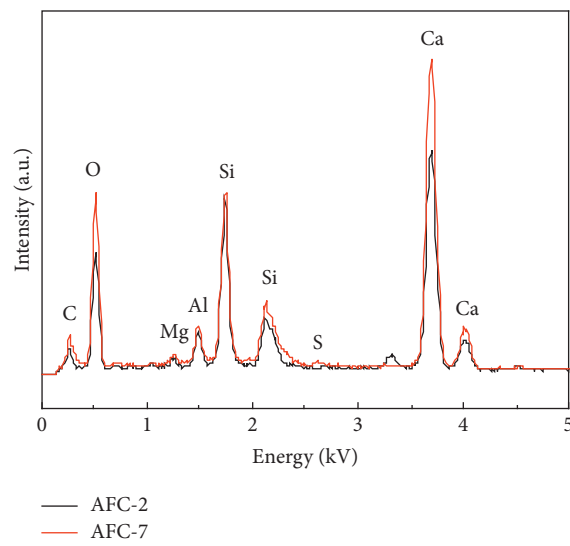


FIGURE 7: EDS result of AFC-2 and AFC-7 sample.

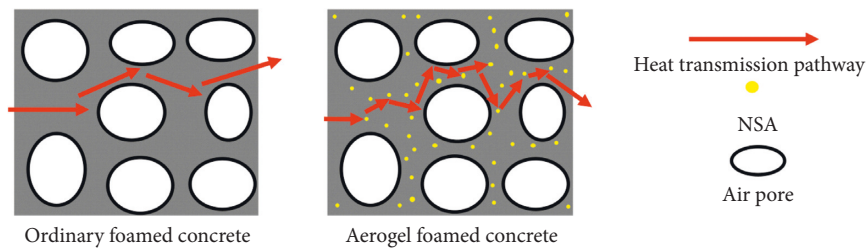


FIGURE 8: The heat transmission model.

4.4. Heat Transmission Model. The heat transmission model of foamed concrete with or without NSAP is presented in Figure 8. It was observed that due to the presence of NSAP, the heat transmission pathway was significantly increased,

resulting in more time to complete the heat transfer process [27, 28]. According to equation (1) [29], under the same total heat, material thickness, temperature difference, and heat transmission area, the longer the heat transmission time, the

lower the thermal conductivity. Furthermore, as reported in the literature, the thermal conductivity of gas is much lower than that of solid [28]. When the heat was transferred to the surface of the NSAP, the resistance transmitted through the pores of NSAP increased sharply owing to the NSAP being filled with medium gas. Therefore, the AFC has a lower thermal conductivity compared with ordinary foamed concrete.

$$\lambda = \frac{Qa}{[At(T_2 - T_1)]}, \quad (1)$$

where λ is the thermal conductivity, Q is the total heat, a is the material thickness, A is the heat transmission area, $T_2 - T_1$ is the temperature difference, and t is the heat transmission time.

5. Conclusion

- (1) As OWA content increased, the dry bulk density, compressive strength, water absorption rate, and thermal conductivity of the foamed concrete were decreased. The foam concrete with 3.0% OWA has the best waterproof and thermal insulation performance.
- (2) As NSAP content increased, the water absorption rate firstly decreased and then increased while the thermal conductivity was decreased. The AFC with 3.0% NASP not only has low thermal conductivity but also has the lowest water absorption.
- (3) The hydration product of AFC was CH, C-S-H, and ettringite. Moreover, the addition of NSAP almost had no effect on the type of hydration product. However, the average pore size and the amount of macropore were significantly increased, and the interfacial adhesion between hydration products was weakened.
- (4) In comparison to the heat transmission model, the presence of NSAP could significantly increase the heat transmission pathway and resistance, resulting in the reduction of thermal conductivity.

Data Availability

The data are generated from experiments and can be available from the corresponding author upon request.

Conflicts of Interest

The authors declare that they have no conflicts of interest.

Acknowledgments

This work was supported by National Key Research and Development Plan "Solid Waste Resource" Key Special Project of China (2019YFC1907200), Research and Development Program of CSCEC (CSCEC-2019-Z-24), and Ministry of Housing and Urban Rural Development Research and Development Project (2019-K-049 and 2020-K-173).

References

- [1] Y. H. M. Amran, N. Farzadnia, and A. A. Abang Ali, "Properties and applications of foamed concrete; a review," *Constr. Build. Mater.* vol. 101, pp. 990–1005, 2015.
- [2] E. P. Kearsley and P. J. Wainwright, "Porosity and permeability of foamed concrete," *Cement. Concrete. Res.* vol. 31, pp. 805–812, 2001.
- [3] F. Roslan, A. Ahmad, M. Hanizam, and M. A. Othuman, "Effects of various additives on drying shrinkage, compressive and flexural strength of lightweight foamed concrete (LFC)," *Adv. Mater. Res.* vol. 626, pp. 594–604, 2012.
- [4] W. She, Y. Du, and C. Miao, "Application of organic- and nanoparticle-modified foams in foamed concrete: Reinforcement and stabilization mechanisms," *Cement. Concrete. Res.* vol. 106, pp. 12–22, 2018.
- [5] M. R. Jones, K. Ozlutas, and L. Zheng, "Stability and instability of foamed concrete," *Mag. Concrete. Res.* vol. 68, pp. 1–8, 2015.
- [6] T. Gao, B. P. Jelle, and A. Gustavsen, "Aerogel-incorporated concrete: An experimental study," *Construction & Building Materials*, vol. 52, no. 2, pp. 130–136, 2014.
- [7] H. Jx, G. S. W Hn, and C. Ry, "Study on preparation and properties of intrinsic super-hydrophobic foamed magnesium oxychloride cement material," *Applied Sciences*, vol. 10, no. 8134, pp. 1–15, 2020.
- [8] S. Ng, P. B. Jelle, and L. I. C. Sandberg, "Experimental investigations of aerogel-incorporated ultra-high performance concrete," *Construction & Building Materials*, vol. 77, pp. 307–316, 2015.
- [9] S. S. Kistler, "Coherent expanded aerogels and jellies," *Nature*, vol. 127, p. 741, 1931.
- [10] C. Buratti and E. Moretti, "Glazing systems with silica aerogel for energy savings in buildings," *Appl. Energy* vol. 98, no. 5, pp. 396–403, 2012.
- [11] E. Cuce, P. M. Cuce, C. J. Wood, and S. B. Riffat, "Toward aerogel based thermal superinsulation in buildings: a comprehensive review," *Renew. Sustain. Energy Rev.* vol. 34, no. 3, pp. 273–299, 2014.
- [12] K. H. Yang, *Development of high-insulation materials using nano-aerogel and aerated concrete*, Technical report, Kyonggi University, South Korea, 2018.
- [13] H. S. Yoon, T. K. Lim, S. M. Jeong, and K. H. Yang, "Thermal transfer and moisture resistances of nano-aerogel-embedded foam concrete," *Construction and Building Materials*, vol. 236, pp. 1–7, 2020.
- [14] M. H. Jo, J. K. Hong, and H. H. Park, "Evaluation of SiO₂ aerogel thin film with ultra low dielectric constant as an intermetal dielectric," *Microelectron. Eng.* vol. 33, pp. 343–348, 1997.
- [15] A. Mccarthy and M. R. Jones, "Preliminary views on the potential of foamed concrete as a structural material," *Mag. Concrete. Res.* vol. 57, pp. 21–31, 2005.
- [16] M. A. Othuman Mydin and Y. C. Wang, "Thermal and mechanical properties of lightweight foamed concrete at elevated temperatures," *Mag. Concrete. Res.* vol. 64, pp. 213–224, 2012.
- [17] A. Hajimohammadi, T. Ngo, and P. Mendis, "Enhancing the strength of pre-made foams for foam concrete applications," *Cement. Concrete. Comp.* vol. 87, pp. 164–171, 2018.
- [18] A. Bagheri and A. Samea, "Effect of air content on rheology of foamed concrete," *Mag. Concrete. Res.* vol. 71, pp. 1–29, 2018.
- [19] S. J. Yu, B. Li, and X. L. Chen, "The steel slag fly ash foamed concrete thermal properties [J] Steel Slag Fly Ash Foamed

- Concrete Thermal Properties,” *Mater. Sci. Froum.* vol. 852, pp. 1398–1403, 2016.
- [20] C. Hai-li, “Influence on the performances of foamed concrete by silica aerogels,” *Mag. Concrete. Res.* vol. 3, pp. 183–188, 2015.
- [21] J. S. Huang, J. Y. Lin, and M. J. Jang, “Stress relaxation of foamed high-alumina cement paste,” *Cement . Concrete. Res.* vol. 35, pp. 1503–1509, 2005.
- [22] M. Zamin Jumaat, U. Johnson Alengaram, and H. Mahmud, “Shear strength of oil palm shell foamed concrete beams,” *Mater. Design.* vol. 30, pp. 2227–2236, 2009.
- [23] R. B. Montgomery, “Viscosity and thermal conductivity of air and diffusivity of water vapor in air,” *J. Atmos. Sci.* vol. 4, pp. 193–196, 1947.
- [24] Q. Zeng, T. Mao, H. D. Li, and Y. Peng, “Thermally insulating lightweight cement-based composites incorporating glass beads and nano-silica aerogels for sustainably energy-saving buildings,” *Energy and Buildings*, vol. 174, pp. 97–110, 2018.
- [25] H. Y. Sun, A. M. Gong, and Y. L. Peng, “The study of foamed concrete with polypropylene fiber and high volume fly ash,” *Appl. Mech. Mater.* vol. 92, pp. 1039–1043, 2011.
- [26] S. Wei, Y. Chen, and Y. Zhang, “Characterization and simulation of microstructure and thermal properties of foamed concrete,” *Constr. Build. Mater.* vol. 47, pp. 1278–1291, 2013.
- [27] M. R. Jones and A. Mccarthy, “Heat of hydration in foamed concrete: Effect of mix constituents and plastic density,” *Cement. Concrete. Res.* vol. 36, pp. 1032–1041, 2006.
- [28] A. Lamy-Mendes, F. S. Rui, and L. Duraes, “Advances in carbon nanostructure–silica aerogel composites: A review,” *J. Mater. Chem. A: Journal of Materials Chemistry A*, vol. 6, pp. 1340–1369, 2018.
- [29] E. P. Kearsley, A. S. Tarasov, and H. F. Mostert, “Heat evolution due to cement hydration in foamed concrete,” *Mag. Concrete. Res.* vol. 62, pp. 895–906, 2010.

Research Article

Bond Slip Behavior of Grout-Filled Concrete Members with Different Interface Materials

Eryu Zhu ¹, Teng Li ¹, Lei Liu,¹ Li Zhu,¹ and Yuanyuan Tian^{1,2}

¹Civil and Environmental Building, Department of Civil Engineering, Beijing Jiaotong University, Shangyuan Cun 3rd, Beijing 100044, China

²China Railway Fifth Survey and Design Institute Group Co., Ltd., Beijing 102600, China

Correspondence should be addressed to Eryu Zhu; eyzhu@bjtu.edu.cn

Received 18 November 2021; Accepted 21 March 2022; Published 11 April 2022

Academic Editor: Junjie Wang

Copyright © 2022 Eryu Zhu et al. This is an open access article distributed under the Creative Commons Attribution License, which permits unrestricted use, distribution, and reproduction in any medium, provided the original work is properly cited.

The present paper investigates the relationship between pressure (bond stress) and displacement at the failure load for different materials through testing and modeling. First, single-end tests were conducted on prebonded stressed and perforated concrete specimens with corrugated plastic, metal, and rubber extractive pipes. These tests reveal that corrugated plastic pipes provide good bonding performance with concrete and grout. Hence, they can be applied in the hole-forming process of posttensioned prestressed bonded structures, along with corrugated metal pipes and rubber extractive pipes. Based on the experimental observations and results, a theoretical approach for applying corrugated plastic pipes in projects such as China's high-speed rail has finally been demonstrated.

1. Introduction

In recent years, field investigations of posttensioned prestressed bonded concrete box girders in China have revealed some quality issues, such as the durability of prestressed bonded systems, which is identified as a significant problem. Applying prestressed bonding first requires forming holes using pipe materials for the most widely used post-tensioned prestressed bonded concrete structures. Therefore, hole-forming materials have become indispensable for post-tensioned prestressed bonded systems. Three main types of hole-forming materials used in posttensioning are nowadays used: corrugated metal pipes, corrugated plastic pipes, and rubber extractive pipes. Among these types, rubber extractive pipes are the most commonly used materials, followed by corrugated metal pipes and corrugated plastic pipes.

However, the engineering community is still concerned about applying corrugated plastic pipes [1]. Plastic corrugated pipes have a slightly lower bonding performance with concrete and grout than metal corrugated pipes, and they are prone to delamination, which causes overall structural body

peeling along the delamination surfaces or cracking problems due to concrete spalling. This seriously affects the durability of the prebonded stress structure and is crucial for the use of corrugated plastic pipes for pre-bonded stress concrete railway bridges.

In 1986, the Swiss company VSL [2] first proposed a hole-forming material, corrugated plastic pipes, for post-tensioned, prestressed holes and vacuum-assisted compression processes. Corrugated plastic pipes are a new type of hole-forming material based on corrugated metal pipes. They possess high-density polyethylene (HDPE), the base material [3]. Compared to corrugated metal pipes, these pipes have good corrosion resistance and antiaging properties. The friction coefficient of the pipe is about 0.14, which is a lot smaller than that of the corrugated metal pipes. The pipe's strength is enough to keep the material from getting damaged while pouring concrete. Furthermore, they are also good in permeability and sealing performance, which makes them suitable for vacuum grouting. Their high fatigue resistance leads to good performance and longer service life for the whole structure. However, as reported in existing literature [4], corrugated plastic pipes have poor ductility and

are readily bent due to their low elastic modulus and strength [5]; thus, corrugated plastic pipes are not used in high-speed railway projects.

An adequate bond between prestressed tendons and concrete can be achieved by effective bonding between prestressed tendons and grout, grout and corrugated pipes, and corrugated pipes and concrete [1]. The bonding between corrugated pipes and concrete has a significant impact on the safety performance of high-speed rail. Most of the existing studies included tests on the bond-slip of steel reinforcement, fiber-reinforced polymers (FRPs), and others such as concrete and steel [5], cement grout and steel [6, 7], FRP-reinforced concrete [6–9], different forms of steel pipes together with concrete [10, 11], and steel plates and concrete [12]. The existing experiments included pull-out tests [13] and double-lap shear tests [14]. The tests mainly considered the bond-slip properties between the bonded materials. In contrast, few of them reported the bonding properties of the inner and outer components using interface materials (such as corrugated plastic pipes, corrugated metal pipes, and rubber extractive pipes).

Corrugated plastic pipes were used as an intermediate interface material to test the bonding performance of a concrete member filled with grout. Multiple sets of single-end compression tests were designed in this study to investigate the performance of such specimens. In addition, pressure experiments were conducted on specimens with corrugated metal pipes and rubber extractive pipes as the hole-forming material to serve as comparative experiments. Considering the corrugated structure of the corrugated pipes and the large internal diameter, the overall performance of the grout-filled concrete specimens may be closer to that of concrete with steel pipes under pressure. Referring to the bond performance test of steel pipes [15], single-end compression tests were conducted on grout-filled concrete members with different interface materials. After 2–3 years of extensive experimental research supported by the China Railway Corporation, this paper reports a systematic study on the compression performance of internal grouts of structures of corrugated plastic pipes with concrete or grout structures. In addition, freeze-thaw cycle experiments with different cycles of -40 to 60°C were used to explore the effect of temperature. Finally, the effects of factors such as different contact lengths and contact areas on bond-slip performance were explored to investigate the suitability of corrugated plastic pipes in railway prestressed bonded concrete bridges. This study could significantly impact the development and application of the corrugated plastic pipe industry in China.

2. Experimental Program

2.1. Test Specimens. The experiments performed push-out tests on 27 specimens, including three corrugated metal pipe specimens, three rubber extractive pipe specimens, and 21 corrugated plastic pipe specimens with different parameters in seven groups. The details of the four groups of specimens are presented in Table 1. The length of one corrugated unit of the corrugated material was 45 mm. D represents the inner

diameter of the hole, L represents the bond length, H represents the crest height of the corrugated pipes, and T represents the thickness of the corrugated material.

The cross-sectional dimensions of the corrugated plastic pipe specimen are shown in Figure 1, where D is the inner diameter of the pipe, and L is the bond length between the interface material and concrete or grout. The dimensions of all specimens are detailed in Table 1, in which the label “P-90-135-1” defines a grout-filled concrete member with a corrugated plastic pipe as the interface material, with an inner diameter of 90 mm and a bond length of 135 mm. “1” represents the No. 1 specimen in each group. In other cases, “M” means specimens with a corrugated metal pipe as the interface material. “R” means specimens with rubber extractive pipe as the interface material. “FTC-10-1” means the No. 1 specimen in the group of 10 times of the freeze-thaw cycle.

Each test specimen was a cylinder with an outer diameter of 400 mm. A steel mold with an inner diameter of 400 mm and a height of 180 mm was selected, and a rectangular iron block was welded to the center of the mold bottom to locate the pipe. The bond lengths between the corrugated pipes and concrete were determined for each specimen before fabricating them. Specimen preparation is shown in Figure 2. The bond length between the corrugated pipes and concrete was adjusted with foam blocks of different lengths at the free end. The concrete was selected as the C50. The gap between the mold and the corrugated pipe was coated with glass glue. A nylon bag was inserted into the corrugated pipes to prevent leakage and concrete from entering the inside of the corrugated pipes, which would impact the test findings. The corrugated plastic pipes were fixed in the mold as required, and lubricating oil was applied inside the steel mold for easy demolding. The concrete was mechanically mixed for a few minutes, poured into the test mold, and vibrated with a vibrator bar to ensure that the concrete was dense at the bottom of the embedded part and the load-bearing plate of the prestressed bonded tendon and the exposed surface was smooth. When pouring concrete, a $150\text{ mm} \times 150\text{ mm} \times 150\text{ mm}$ cubic standard test block was reserved for each concrete batch to determine its mechanical properties. After the concrete was wholly vibrated, the grout was mixed, and the specimens were uniformly grouted. The test specimens and standard test blocks were maintained in a special maintenance room to ensure the development of the early strength of the concrete and prevent dry shrinkage cracks. Water was poured once in the morning and once in the afternoon for the first 14 days. Tests were performed after 28 days.

2.2. Material Properties. The material properties of the concrete were determined using compressive concrete cube tests. Concrete cubes with a nominal side length of 150 mm were produced using standard mixing and curing techniques [16, 17]. The elastic modulus of concrete was measured according to the specification “Test Methods of Cement and Concrete for Highway Engineering” [18]. The material properties of concrete are listed in Table 2.

TABLE 1: Geometric parameters of grout-filled concrete members.

Specimen	Temperature (°C)	Freeze-thaw cycles	D (mm)	L (mm)	H (mm)	T (mm)	D/45	L/45
P-90-135-1			90	135	5.0	2.5	2.0	3.0
P-90-135-2			90	135	5.0	2.5	2.0	3.0
P-90-135-3			90	135	5.0	2.5	2.0	3.0
M-90-135-1			90	135	2.5	0.3	2.0	3.0
M-90-135-2			90	135	2.5	0.3	2.0	3.0
M-90-135-3			90	135	2.5	0.3	2.0	3.0
R-90-135-1			90	135			2.0	3.0
R-90-135-2			90	135			2.0	3.0
R-90-135-3			90	135			2.0	3.0
P-90-135-FTC-10-1	-40~60	10	90	135	5.0	2.5	2.0	3.0
P-90-135-FTC-10-2	-40~60	10	90	135	5.0	2.5	2.0	3.0
P-90-135-FTC-10-3	-40~60	10	90	135	5.0	2.5	2.0	3.0
P-90-135-FTC-20-1	-40~60	20	90	135	5.0	2.5	2.0	3.0
P-90-135-FTC-20-2	-40~60	20	90	135	5.0	2.5	2.0	3.0
P-90-135-FTC-20-3	-40~60	20	90	135	5.0	2.5	2.0	3.0
P-90-90-1			90	90	5.0	2.5	2.0	2.0
P-90-90-2			90	90	5.0	2.5	2.0	2.0
P-90-90-3			90	90	5.0	2.5	2.0	2.0
P-90-180-1			90	180	5.0	2.5	2.0	4.0
P-90-180-2			90	180	5.0	2.5	2.0	4.0
P-90-180-3			90	180	5.0	2.5	2.0	4.0
P-80-120-1			80	120	5.0	2.5	1.8	2.7
P-80-120-2			80	120	5.0	2.5	1.8	2.7
P-80-120-3			80	120	5.0	2.5	1.8	2.7
P-110-165-1			110	165	5.0	2.5	2.4	3.7
P-110-165-2			110	165	5.0	2.5	2.4	3.7
P-110-165-3			110	165	5.0	2.5	2.4	3.7

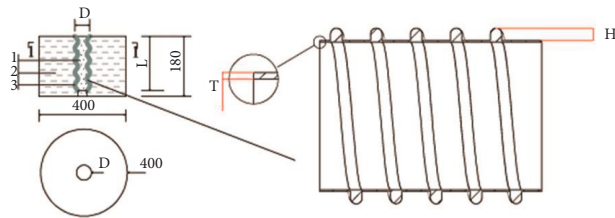


FIGURE 1: Specimen size and pipe size (mm). 1-Grout, 2-Concrete, 3-Pipe material.



FIGURE 2: Specimen preparation, (a) Pour concrete, (b) Clean inside space, (c) Un-grouted specimen, (d) Grouted specimen.

The grout met the requirements of TB/T3192 [19], and its proportion was cement: water: admixture = 1 : 0.35 : 0.09, where the cement was ordinary silicate cement with a strength grade of 52.5 MPa. The grout met the following

conditions: initial setting time higher than 4 h, final setting time less than 24 h, 30 min flow rate less than or equal to 30, and 24 h free bleeding rate of 0. According to GB/T 17671 1999 [20], the compressive strength test was conducted for

TABLE 2: Concrete properties.

	1	2	3	4	5	6	7	Mean	Standard deviation
Concrete cube strength (MPa)	61.5	62.2	63.1	59.2	58.8	60.5	59.4	60.7	1.5
Elasticity modulus (10^4 MPa)	3.9	4.1	3.6	4.1	3.7	3.9	3.7	3.9	0.2

40 mm \times 40 mm \times 160 mm specimens using a compressive strength testing machine. The grout's 28-day strength tests yielded 56.5, 59.3, and 61.4 MPa, with a mean of 59.07 MPa and a standard deviation of 2.007 MPa, meeting the requirements for strength greater than or equal to 50 MPa.

The specifications of the corrugated plastic pipes given by the factory are $\phi 90$ with an elastic modulus of 800 MPa, tensile yield bond stress of 17 MPa, a density of 900 kg/m³, and Poisson's ratio of 0.35. The specification of corrugated metal pipes is $\phi 90$ with an elastic modulus of 2.06×10^5 MPa, tensile yield bond stress of 260 MPa, a density of 7850 kg/m³, and Poisson's ratio of 0.30. The specifications of the rubber extractive pipes are $\phi 90$ with a fixed tensile strength of 6 MPa, the tensile strength of 12 MPa, elongation at break of 350%, and shore A hardness of 65.

The tensile yield bond stress and elongation at break of corrugated plastic pipes were determined according to the specification GB/T 8804.1 2003 [21], and the results are shown in Table 3.

2.3. Test Setup. In this study, all tests were conducted under a computer-controlled compression machine with a capacity of 2000 kN. Geometric and physical alignments were conducted on the machine before applying the load. During the testing, the vertical load was applied only to the grout core, and subsequently, the grout core was pushed downward. A schematic of the test is shown in Figure 3. A compression machine directly provided the displacement at the loading end of the grout. The displacement at the bottom of the grout was measured using a displacement meter, which was the free end and was fixed on the lower steel bearing. Considering that the steel bearing may cause deviations in the test results, the steel support was loaded. When the loading force was 200 kN, the deformation of the steel support was approximately 0.01 mm, which was much smaller than the test value, so the influence of the steel bearing was ignored. The test pieces were pre-loaded before the official tests with a loading of 20 kN. For safety reasons, the force was loaded step-by-step. The loading process is computer-controlled, at a speed of 100 N/s. Each 100 kN load would last for one minute. The load was continuously applied until the specimen cracked or damaged or the displacement meter reading suddenly increased.

2.4. Freeze-Thaw Cycle. Bridges with prestressed corrugated plastic pipes with bonds for hole-forming are influenced by the annual spring, summer, fall, and winter temperature cycles. As the linear expansion coefficients of corrugated plastic pipes, concrete, and grout are very different, when the temperature changes, there may be large relative deformation and temperature bond stress between corrugated plastic

TABLE 3: Corrugated plastic pipe properties.

Specimen	Tensile strength (MPa)	Elongation at break (%)
1	15.8	251.5
2	17.6	287.5
3	17.9	268.1
Mean	17.1	269.0
Standard deviation	0.9	14.7

pipes and concrete, affecting the bonding force between them. This test evaluated the impact of high and low temperature cycles on corrugated plastic pipes and concrete bonding performance by setting different temperature cycles. The range of temperature cycles set in this test ranged from -40°C to 60°C . To fully consider the range of temperature variation transferred from the bridge to the corrugated plastic pipes, a 2 h temperature holding operation was performed in the temperature box as the temperature increased or decreased. The temperature box is shown in Figure 4. The temperature inside the specimen was consistent with that outside the specimen during the experiment. As the temperature box was subjected to a limited external load, the specimens were first removed from the temperature box when the loading test was performed. Nine concrete test blocks in three groups were designed for this test. The numbers of cycles were 0, 10, and 20.

3. Results and Discussions

3.1. Axial Load-Displacement and Axial Load-Average Bond Stress Curves. Four sets of comparative tests were designed to analyze the bonding performance between corrugated plastic pipes and concrete or grout based on different test objectives. The experimental results are presented in Table 4. The ending criteria of the test were specimen failure or sudden increase in the displacement meter readings during the loading test. At this time, the displacement produced by the free end of the grout was different. At this point, most of the specimens were in the initial rise stage and reached the peak plateau stage.

The experimental results for each group are plotted in Figure 5, where for (a), the horizontal axis represents the inner grout-loaded end displacement (S), and the vertical axis represents the axial load (P). For (b), the horizontal axis represents the inner grout-loaded end displacement (S), and the vertical axis represents the average bond stress τ , defined in equation (1). P_u is the peak loading force of the specimen at the highest platform; τ_u is the peak average bond stress of the specimen at the highest platform; S_u is the displacement at the loading end just at the end of the first rising section of the bond stress curve of the specimen.

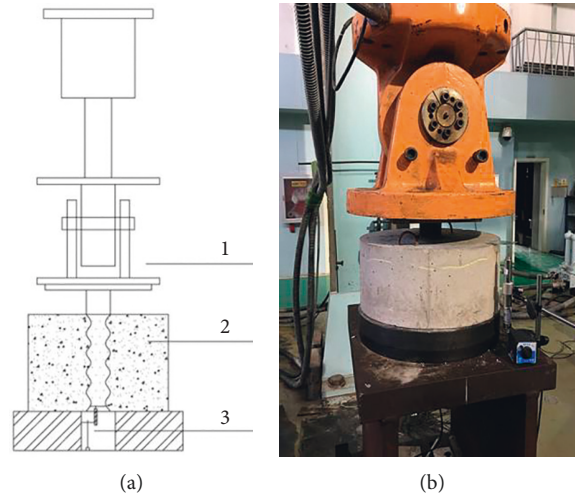


FIGURE 3: Test setup, (a) schematic diagram, (b) Real test setup. 1-Compression machine, 2-Specimen, 3-Displacement meter.



FIGURE 4: Temperature box.

The average bond stress is calculated by [22]

$$\tau = \frac{P}{\pi dl} \tag{1}$$

The initial slope is defined as the slope of the elastic stage curve between the origin (0, 0) and the turning point [23]. The slope consists of two types, one for the $P - S$ curve and the other for the $\tau - S$ curve.

TABLE 4: All specimens' compression load, bond stress, and critical displacements.

Group	Test ID	P_u (kN)	τ_u (MPa)	\bar{P} (kN)	$\bar{\tau}$ (MPa)	k_τ
1	P-90-135-1	129.0	3.4	200.7	5.3	4.0
	P-90-135-2	251.9	6.6			
	P-90-135-3	221.0	5.8			
2	M-90-135-1	301.6	7.9	317.5	8.3	10.5
	M-90-135-2	400.0	10.5			
	M-90-135-3	250.8	6.6			
3	R-90-135-1	138.9	3.6	133.6	3.6	9.3
	R-90-135-2	130.2	3.4			
	R-90-135-3	131.7	3.5			
4	P-90-135-FTC-10-1	142.0	3.7	184.1	4.8	5.2
	P-90-135-FTC-10-2	231.7	6.1			
	P-90-135-FTC-10-3	178.6	4.7			
5	P-90-135-FTC-20-1	133.6	3.5	175.6	4.6	6.3
	P-90-135-FTC-20-2	204.2	5.3			
	P-90-135-FTC-20-3	188.9	4.9			
6	P-90-90-1	111.9	4.4	134.5	5.3	5.5
	P-90-90-2	139.9	5.5			
	P-90-90-3	151.7	5.9			
7	P-90-180-1	221.4	4.4	214.3	4.2	4.0
	P-90-180-2	207.1	4.1			
8	P-80-120-1	99.5	3.3	151.4	5.0	5.9
	P-80-120-2	202.9	6.7			
	P-80-120-3	151.7	5.0			
9	P-110-165-1	294.2	5.2	294.2	5.2	5.6
	P-110-165-2	351.8	6.2			
	P-110-165-3	236.6	4.2			

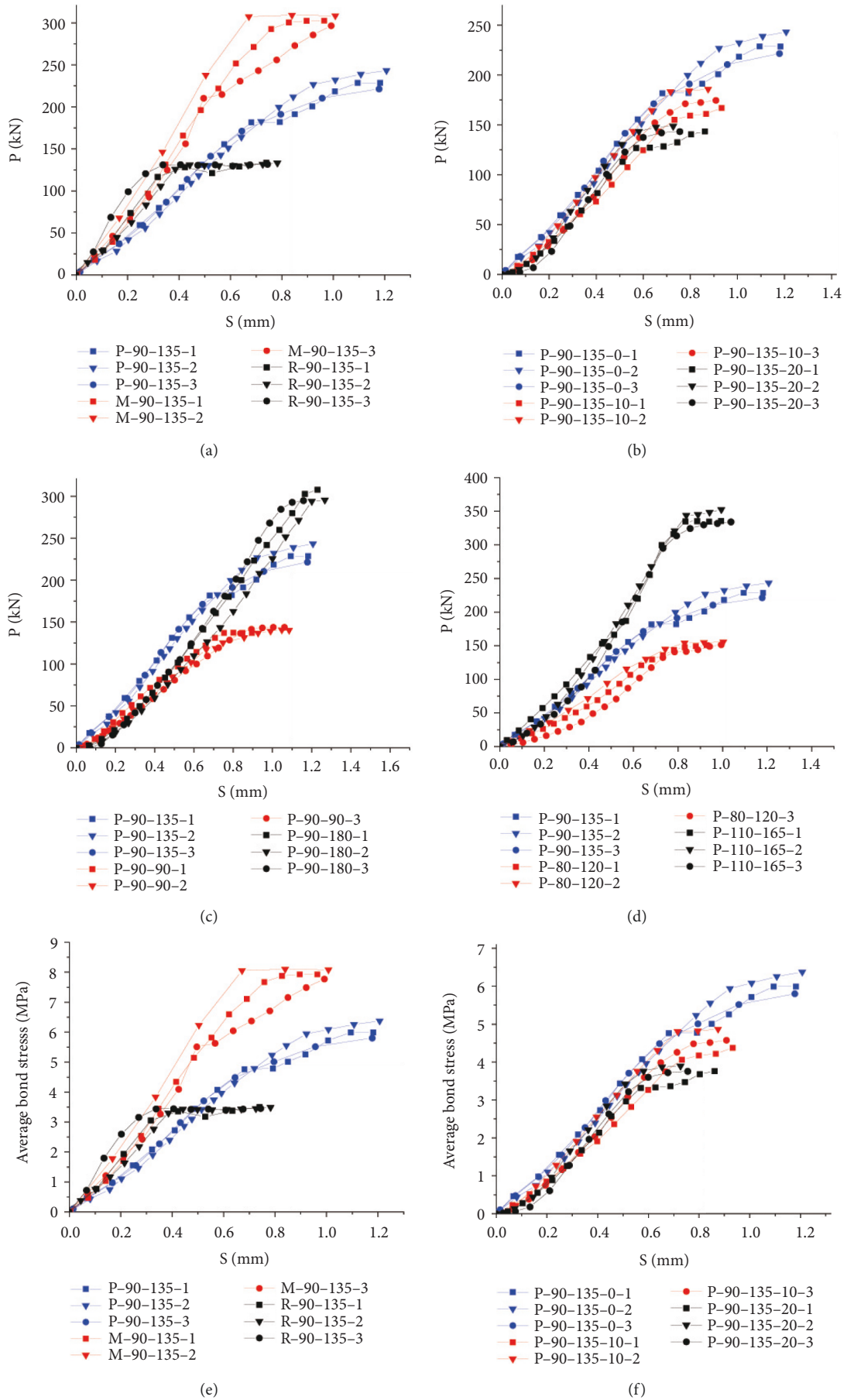


FIGURE 5: Continued.

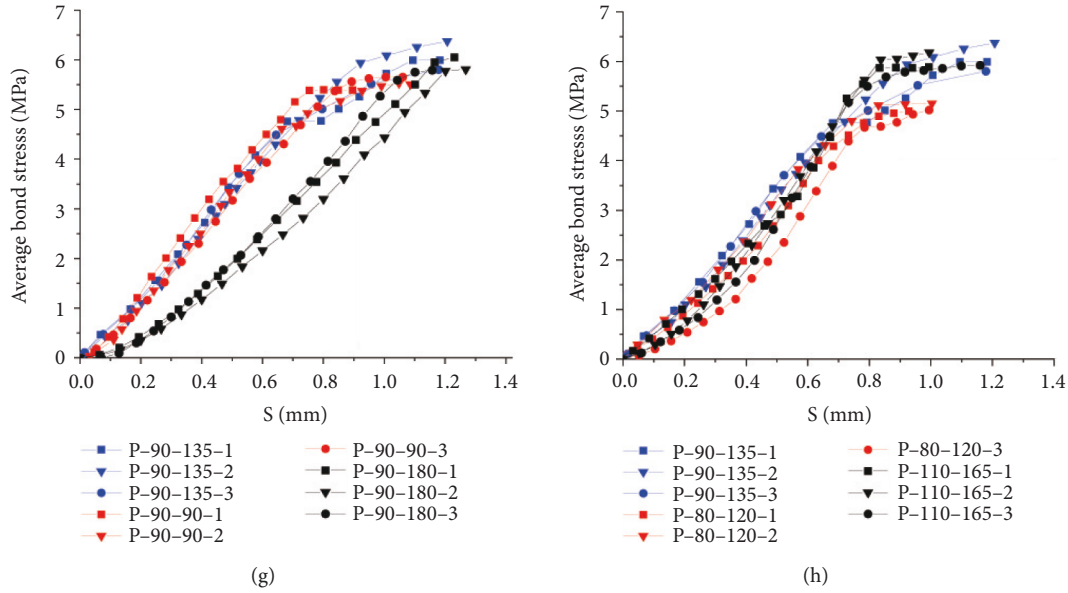


FIGURE 5: Bond-slip test results.

$$k_r = \frac{\overline{\tau_{u1}}}{s_{u1}}, \quad (2)$$

$$k_p = \frac{\overline{P_{u1}}}{s_{u1}}.$$

The following conclusions can be drawn from existing studies [24]: the higher the bond stress is, the better the overall working performance is. The smaller the slip at the loading end is, the better bonding performance is. The higher the bond stiffness is, the higher the ratio of bond strength to bond-slip before the concrete is internally cracked is, and the higher the ability of different materials is to work together. In this study, the ranking of bonding performance of different hole-forming material specimens was evaluated by comparing different groups of specimens on various metrics in the conclusion section.

Results with error bars are shown in Figure 6.

In the experimental results, the curves for all specimens reached the peak plateau because the loading was interrupted when the specimens failed. Typical curves are of two types, as shown in Figure 7. The first type of two-segment curve shown in Figure 7(a) is the most common, in which the first segment of the curve is roughly an exponential distribution, and the second segment is a straight line. As for AB1 in Figure 7(a), the axial load of the specimen remains constant after reaching the peak. This is because the contact surface is rougher at this type of curve, resulting in more interlock and adhesive forces than the initial interface friction. Therefore, only the friction remained as the bonding force when the axial load peaked, and the dynamic friction remained almost constant. As for AB2 in Figure 7(a), the axial load of the specimen increases almost linearly after the first segment. This is because the interlock forces still remain in these specimens. Thus with the increase of slip, the axial load gradually increases.

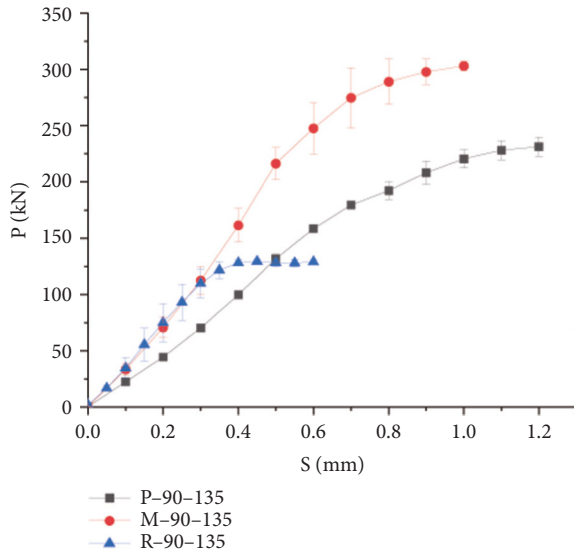
In contrast, the second type of curve shown in Figure 7(b) is fewer in number. The axial load or stress of the second type of specimen reached its peak with a negative exponential distribution. It then increased linearly for a period, after which it increased as a quadratic function to a new peak and then remained constant. This specimen's interlocking force and adhesive force are smaller than the initial interface friction [10]. Therefore, when the axial load peaks for the first time, the friction force peaks and the interlocking force or adhesive force are still present at the interface, resulting in a gradual increase in the axial load. The load or stress peaks again when the interlocking or adhesive force disappears.

3.2. Influence of Materials on Bond-Slip. Corrugated plastic, rubber extractive, and corrugated metal pipes are the three main hole-forming materials for posttensioned prestressed bridges with bonds [25]. They have the same inner diameter. Although the parameters of the three materials themselves are different, the working conditions of the three forming methods are the same. Therefore, it is possible to compare them under the same conditions.

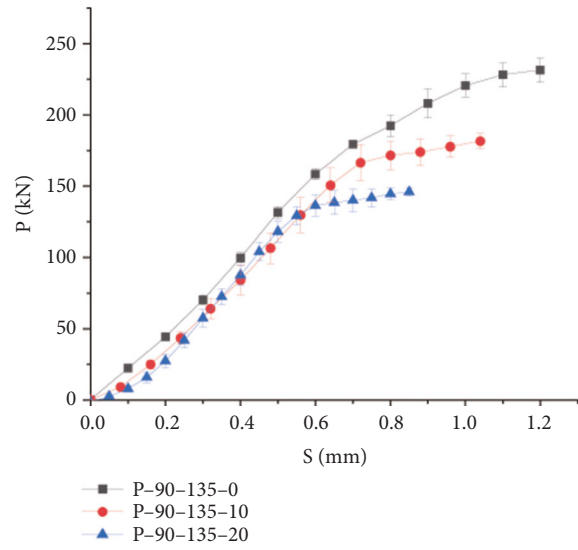
The bond-slip curves for the three sets of specimens corresponding to the three different hole-forming materials are shown in Figure 5, where (a) is the loading force-loaded end displacement curve and (b) is the average bond stress of the bond-loaded end displacement curve.

Of these, the specimens using rubber extractive pipes for hole-forming only had the first type of curve. The specimens using corrugated metal pipes for hole-forming had both types of curves. The specimens using corrugated plastic pipes for hole-forming had both types of curves.

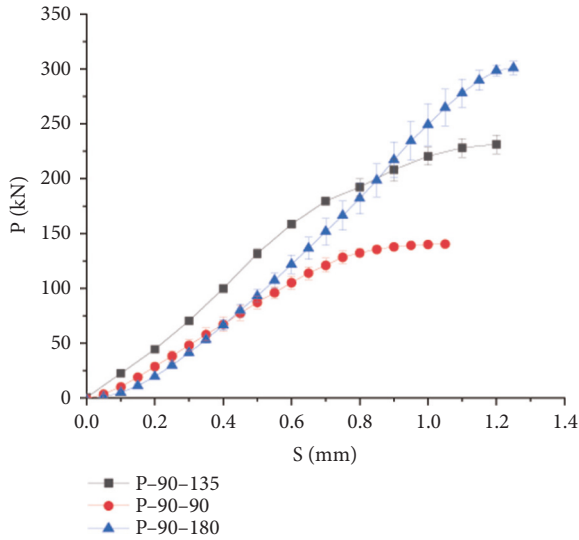
As shown in Figure 5(b), the bond-slip for all three materials can be roughly divided into two phases: the first phase is roughly a linear rise, and the second phase is a peak



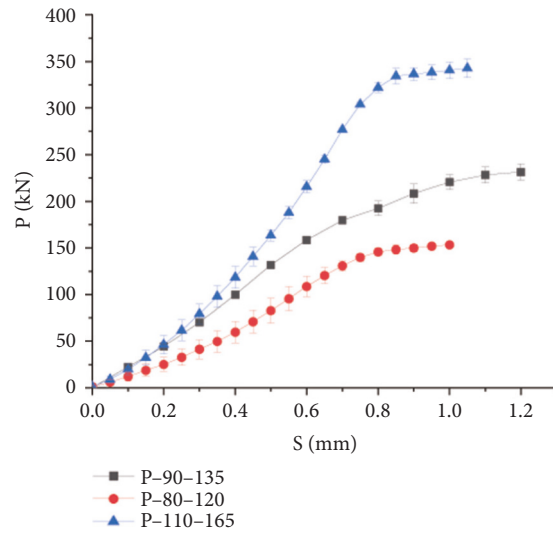
(a)



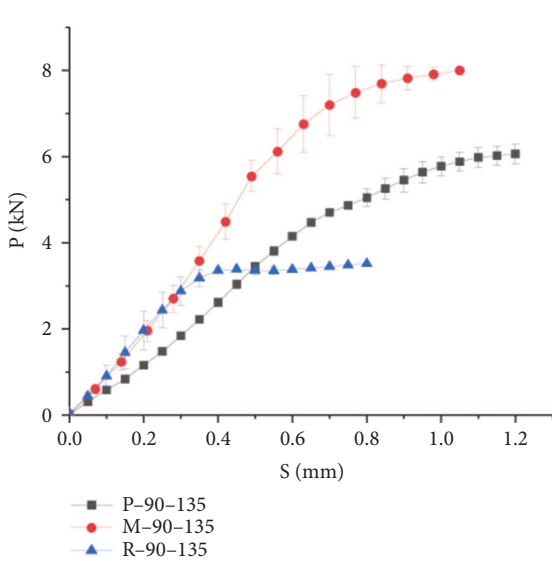
(b)



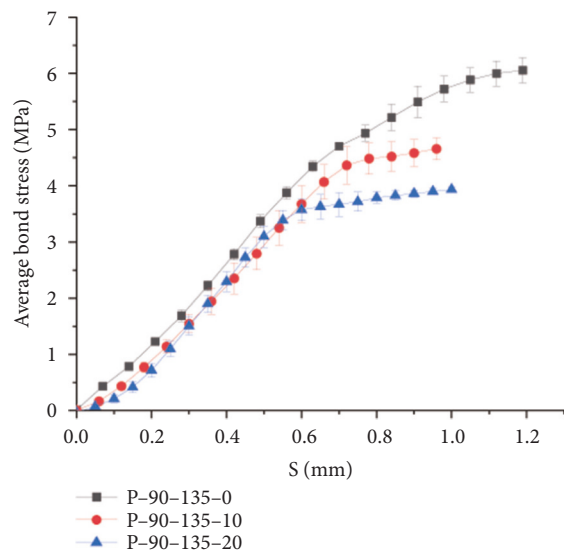
(c)



(d)



(e)



(f)

FIGURE 6: Continued.

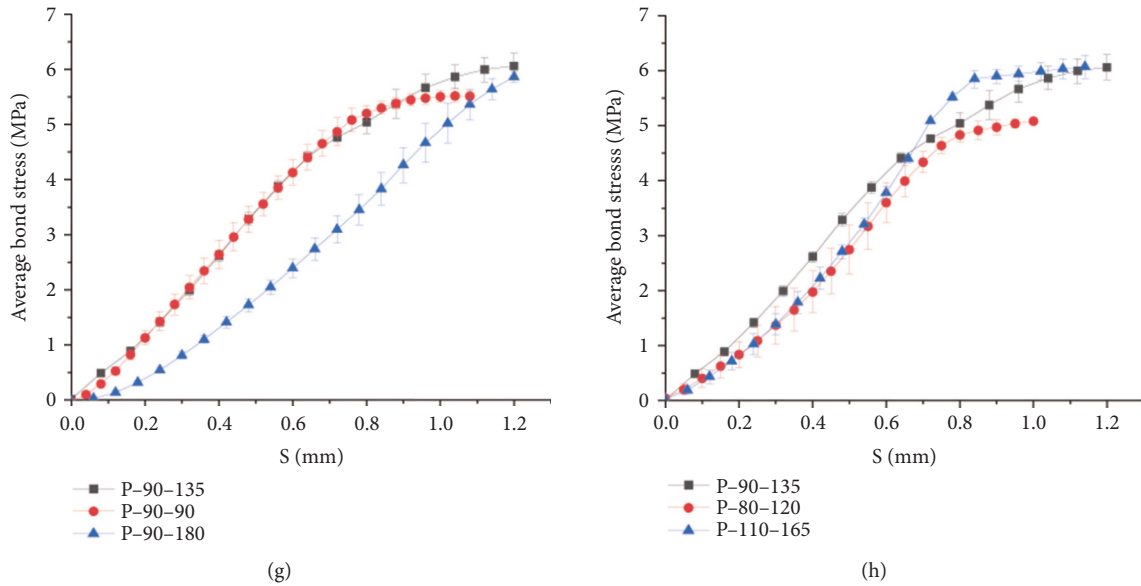


FIGURE 6: Bond-slip test results with error bars.

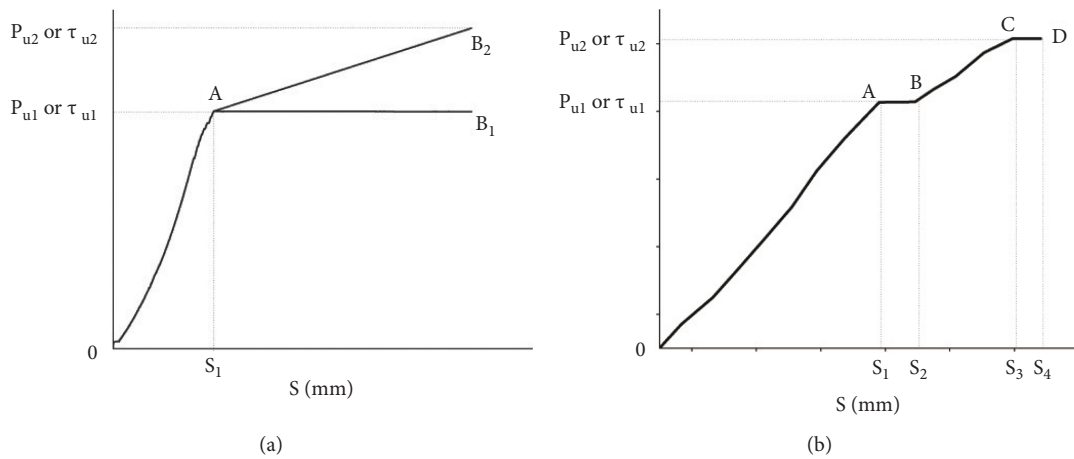


FIGURE 7: Curve types. (a) Type I curve, (b) Type II curve.

plateau phase or a linearly rising phase. Stiffness is considered the ability of different specimens to resist slip. Thus, the higher the stiffness, the higher is the force required to produce the same amount of slip. Comparing the slope of the pressure curve and that of the bond stress curve, the corrugated metal pipe specimen and the rubber extractive pipe specimen curves have similar slopes (stiffness). However, they are significantly higher than the corrugated plastic pipe specimen. This indicates that the corrugated metal pipes and the rubber extractive pipe specimens produced a stronger resistance to slip in the first stage. In contrast, the corrugated plastic pipe specimens produced a weaker resistance to slip. The bonding force consists of the chemical bonding force, mechanical bite force, and friction [27]. The antislip forces are mainly chemical bonding and mechanical bite forces in the initial slip generation.

Wang. et al. [28] has achieved improved chemical bonding by the application of two groups of accelerators, Carbonates and bicarbonates in the concrete. Through analyzing the outcome, the implications of the two accelerators, sodium carbonate (Na_2CO_3) and sodium bicarbonate (NaHCO_3), on the properties of OPC paste demonstrate that both could improve the initial and final setting time of OPC paste, but the effect of the two accelerators on compressive strength was different. The rapid development of ettringite and the creation of CaCO_3 through interactions between the two with portlandite generated the enhanced strength at 1 and 7 days. Na^+ reduces the adhesion between C-S-H gels by replacing Ca_2^+ , leading to a decrease in strength. NaHCO_3 was found to be a better accelerator than Na_2CO_3 .

Wang et al. [29] have discovered that with the increase of $\text{Ca}(\text{HCO}_3)_2$ content, the final set time and extension degree

of cement decrease. Furthermore, the initial formation of ettringite and the transformation of ettringite could be achieved by adding $\text{Ca}(\text{HCO}_3)_2$. The CaCO_3 , which is the product of the reaction of $\text{Ca}(\text{HCO}_3)_2$ and portlandite, has a better filling effect than the limestone powders. And too much $\text{Ca}(\text{HCO}_3)_2$ could cause harmful pores on concrete, which will reduce the performance of concrete.

The rubber extractive pipe has strong slip resistance. This is mainly because the concrete and the internal grout are in direct contact when the rubber extractive pipe is pulled out after the hole is formed. Thus, the contact surface between them is rougher, which produces a higher mechanical bite force. Compared to corrugated plastic pipes, mostly made of HDPE or polypropylene, the corrugated metal pipe specimens made of soft steel strip [26] have a higher chemical bonding force with the concrete and grout, explaining their superior slip resistance. In addition, from Figure 5, it can be seen that the slopes of almost all curves first increased and then decreased. The initial increase occurred because the mechanical bite between the materials increased as the loading force increased, and the friction also increased. Thus, the slope continued to increase. When the amount of slip reached a certain level, the chemical bonding force disappeared, the slip resistance decreased, and the slope of the curve decreased accordingly. When the curve reaches the turning point, the overall sliding between multiple materials is produced, and the chemical bonding force and mechanical bite force disappear entirely. The bonding force is mainly provided by the dynamic friction force, which remains constant during the relative sliding of the members.

Comparing the critical displacement S_{u^*} in the initial linear phase, the rubber extractive pipe specimens have a critical displacement of approximately 0.33 mm, followed by corrugated metal pipe and corrugated plastic pipe specimens with critical displacements of around 0.64 mm and 0.75 mm. As a result, chemical bonding and mechanical bite force dissipate at a much smaller slip. However, the corrugated metal pipe between the grout and concrete is entirely in contact with both, creating a higher total chemical bonding and mechanical bite force. The corresponding displacement is high. However, the corrugated plastic pipe specimens produced the most significant displacement. One of its reasons is that the corrugated plastic pipe has a higher contact area with the concrete and grout. Furthermore, the corrugated plastic pipe is softer than the corrugated metal pipes, thus allowing more deformation during relative slip.

Comparing the peak platform bond stress τ_u , we found that the rubber extractive pipe specimens had the most negligible forces when reaching the peak platform, followed by corrugated plastic and corrugated metal pipes. The contact area between the corrugated pipes at the interface and the concrete and grout is greater than that of the rubber extractive pipe specimens with direct contact between the concrete and grout, resulting in a higher chemical bonding force. The corrugated metal pipe is a soft steel strip with a more rigid texture. Its chemical bonding and mechanical bite forces are more significant than the corrugated plastic pipe. The plastic bellows exhibit shear failure during the middle and late loading periods (Figure 8). The bonding

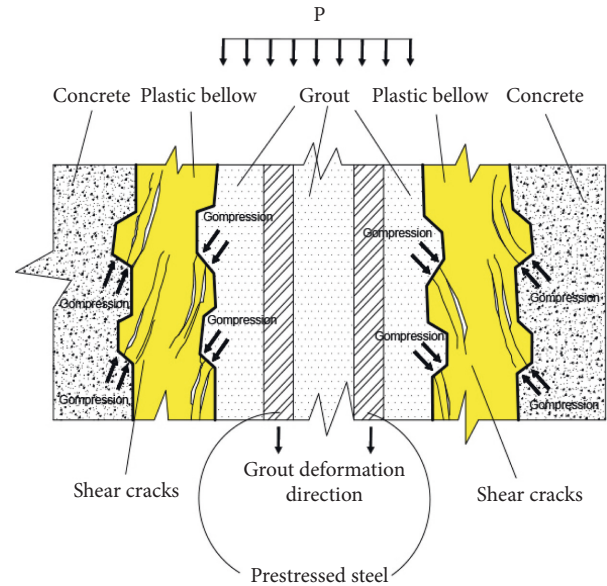


FIGURE 8: Inside pipe break.

stress of the plastic bellows specimen is higher than that of the rubber extractive pipe specimen because of the increased mechanical biting force between the broken bellows and concrete.

In summary, rubber extractive pipes have a comparable slope (slide resistance stiffness) to the corrugated metal pipe. Both are higher than those of the corrugated plastic pipes. Corrugated metal pipes have the highest peak bond stress, followed by corrugated plastic pipes and rubber extractive pipes; rubber extractive pipes have the smallest critical displacement, followed by corrugated metal pipes. The most significant value is for corrugated plastic pipes.

3.3. Influence of Freeze-Thaw Cycles on Bond-Slip. The corrugated plastic pipe concrete specimens did not show cracks after 10 and 20 freeze-thaw cycles in the temperature box without an external load. The corrugated plastic pipe did not detach or delaminate from the surrounding concrete or grout. This indicates that under a temperature cycle of -40°C to 60°C without load, the corrugated plastic pipes and concrete did not fail owing to the difference in deformation along the direction of the corrugated pipes owing to the difference in their linear expansion coefficients.

After checking the concrete specimens for cracks after freeze-thaw cycles, the corrugated plastic pipe concrete specimens were subjected to axial one-end compression. The test data were read, and the test results were processed.

From Figures 5, 9, 10 and Table 4, it can be seen that the average peak compressive loading force (bond stress) decreased by 8.54% after 10 freeze-thaw cycles and by 13.28% after 20 freeze-thaw cycles. In contrast, the average peak compressive loading force (bond stress) decreased by 5.19% after 20 freeze-thaw cycles compared to 10 freeze-thaw cycles. The data shows that the number of freeze-thaw cycles affects the bond performance, with a higher impact in the initial cycles and a decrease in impact strength in

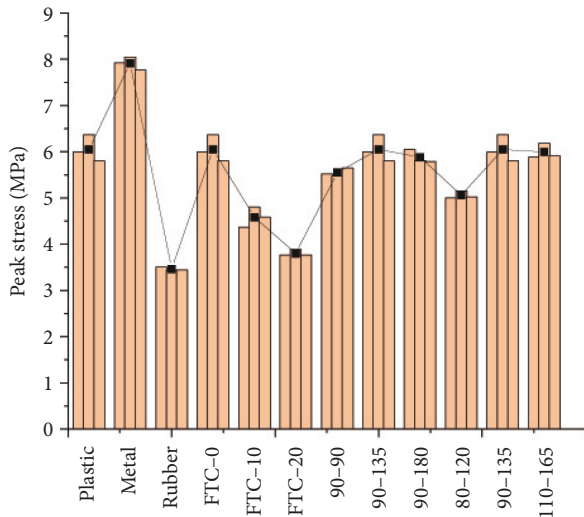


FIGURE 9: Peak stress comparison.

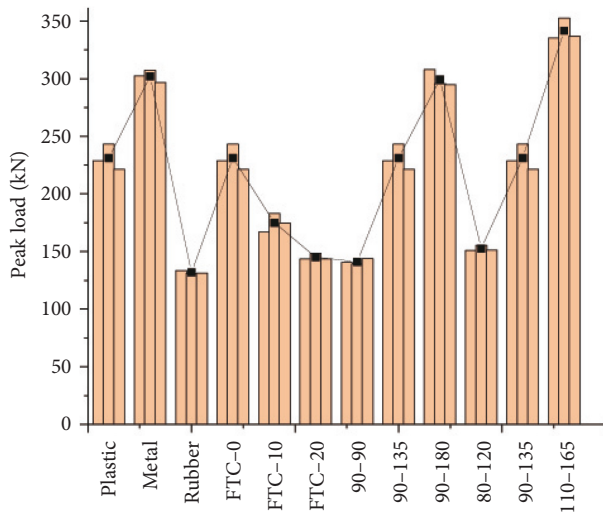


FIGURE 10: Peak load comparison.

later cycles. According to the existing literature [30], the length of the contact area is related to the transfer of stress across the interface. Eventually, the peak compressive loading force (bond stress) decreases as the number of freeze-thaw cycles increases. These increases cause a decrease in the effective stress transfer zone, which reduces the frictional force.

In contrast, according to the existing literature [27], freeze-thaw cycles cause deterioration of the concrete strength, which also leads to a decrease in the interfacial shear force. In other words, in actual projects, as the service life of prestressed bonded concrete railway bridges increases, the bond stress between corrugated plastic pipes and concrete or grout decreases, with significant changes in the first few years. However, the decreasing tendency decelerates as the service life increases. We also found that the initial stiffness continues to increase with an increase in the number of freeze-thaw cycles.

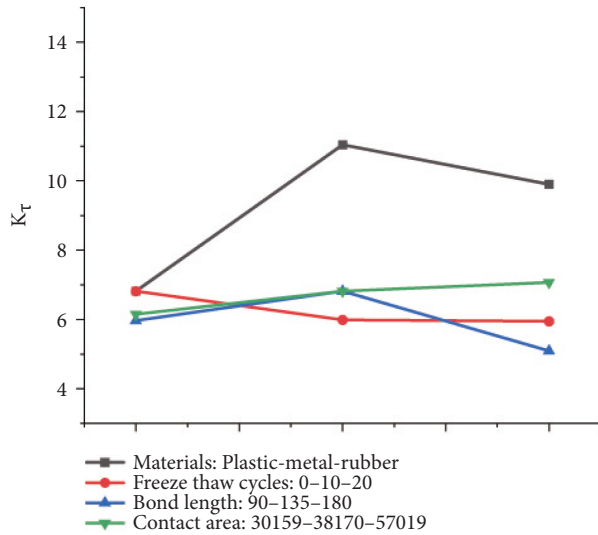
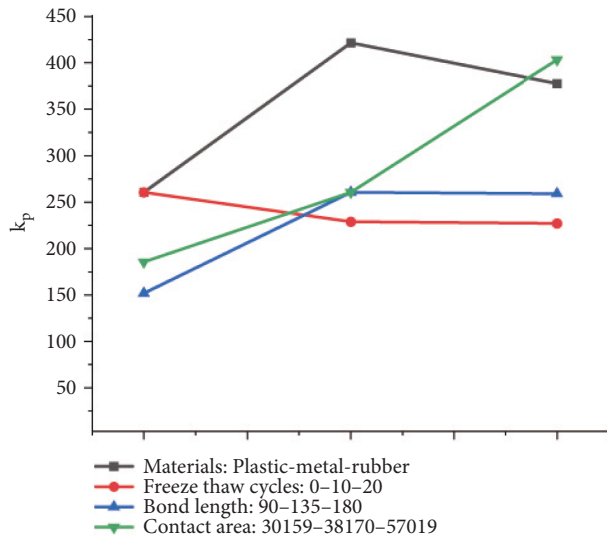
By observing the loading force and curve stiffness of bond stress (Figures 11 and 12), we found that the stiffness was the highest for 0 freeze-thaw cycles when the loading end displacement was less than approximately 0.3 mm, followed by 10 freeze-thaw cycles, and finally for specimens with 20 freeze-thaw cycles. Again, this was due to the reduction in chemical bonding forces caused by the freeze-thaw cycles. However, when the loading end displacement was higher than 0.3 mm, the slope increased the most with 20 freeze-thaw cycles, followed by specimens with 10 freeze-thaw cycles, and finally specimens with 0 freeze-thaw cycles.

Comparing the critical displacement S_u (Figure 13), we found that 10 freeze-thaw cycles had almost no effect on the results, with the displacement changing from 0.75 mm to 0.74 mm. However, the average critical displacement of the specimens after 20 freeze-thaw cycles was 0.59 mm. This indicates that the chemical bonding force decreases after 20 freeze-thaw cycles and that the displacement is smaller when the chemical bonding force disappears. This also shows a progressively significant effect after 20 freeze-thaw cycles.

3.4. Influence of Bond Length on Bond-Slip. In this study, the influence of the bond length on the bonding performance of corrugated plastic pipes with concrete or grout was considered. Under the same concrete strength, grout strength, inner diameter, and various parameters of corrugated plastic pipes, three types of specimens with bond lengths $l_a = d$, $l_a = 1.5d$ and $l_a = 2d$ were used, where d is the inner diameter of the corrugated plastic pipes ($d = 90$ mm). The bonding lengths were 90, 135, and 180 mm, respectively.

From Figure 5(a) and 10, it can be seen that as the bond length increases, the peak loading force of the specimen gradually increases. The increase in specimens with a bond length of 135 mm relative to specimens with a bond length of 90 mm was more significant than the increase in specimens with a bond length of 180 mm related to specimens with a bond length of 135 mm. The increase in loading force was due to the increase in bond length and the higher contact area between the internal and external materials; hence, there was a higher chemical bonding force, mechanical bite force, and friction between the materials. According to existing studies [31–34], when the bond length is less than a specific value, the peak loading force increases rapidly with increasing bond length; when the bond length is higher than a specific value, the increase in the peak loading force is no longer significant.

In addition, the intensity of the peak bond stress (Figure 9) of the specimen decreased with the increasing bond length. First, as the bond length increases, the contact area increases. According to formula (1), the bond stress is inversely proportional to the contact area; thus, the higher the bond length, the lower the bond stress of the peak bond. It can also be seen that the peak bond stresses for specimens with 90 mm and 135 mm bond lengths were close and significantly higher than the peak bond stress for specimens with a bond length of 180 mm. According to the conclusion above, the increase in peak loading force from the 135–180 mm bond length range was no longer significant. As

FIGURE 11: Stiffness (k_r) comparison.FIGURE 12: Stiffness (k_p) comparison.

the contact area considerably increased, the bond stress decreased considerably. Moreover, it can be seen that the initial stiffness decreased as the bond length increased.

Comparing the curve stiffness, we found that as the bond length increased, the force stiffness (Figure 12) first increased and then remained almost constant, whereas the stiffness of the bond stress curve (Figure 11) increased and then decreased. First, when the bond length changed from 90 to 135 mm, the contact area increased almost linearly for the force stiffness. The chemical bonding force and mechanical bite force also increase; thus, the stiffness increases. However, the stiffness remained unchanged when the bond length changed from 135 to 180 mm. This is possible because when the bond area increased linearly, the increase in chemical bonding force and mechanical bite force was comparable to the increase in force. However, observing the stiffness of the bond stress, we found that when the bond

length changed from 90 to 135 mm, the contact area increased, and the chemical bonding force and mechanical bite force also increased considerably. Although the area also increased, the increase in the force was higher; thus, the stiffness increased. When the bond length changed from 135 to 180 mm, the area increased almost linearly and was inversely proportional to the bond stress. The increase in chemical bonding and mechanical bite forces was relatively small; thus, the stiffness decreased.

Comparing the critical displacement (Figure 13), we found that it gradually increased with increasing contact length, from 0.75 mm to 0.84 mm to 1.14 mm. This is mainly because a larger contact area produces a higher chemical bonding force and mechanical bite force. As a result, the chemical bonding and mechanical bite forces disappeared only after the internal grout displacement reached a sufficient level.

3.5. Influence of Contact Area on Bond-Slip. Formula (1) shows that under the same loading force P , bond stress τ , and inner diameter of the corrugated pipe d , the bond lengths of the corrugated pipe and concrete or grout l are inversely proportional. If the corrugated plastic pipe is assumed to be a hollow, smooth cylinder, then $\pi \cdot d \cdot l$ is the surface area of the hollow cylinder. In other words, the bond stress of the bond τ and the surface area of the hollow cylinder are inversely proportional. It can be seen that the contact areas between the corrugated plastic pipes and concrete or grout have a certain impact on the bond stress of bonds between corrugated plastic pipes and concrete or grout.

This test analyzes the effect of different contact areas of corrugated plastic pipes on the bond stresses, with all other conditions being the same. According to Figures 5, 10, and Table 4, the larger the bond area is, the greater the peak loading force is because of the larger contact area, and the greater the chemical bonding force, mechanical bite force, and friction force are. The friction force increases significantly. The peak bond stress (Figure 9) of specimens 80-120 was the smallest, followed by specimens 110-165 and 90-135. It is seen that the peak bond stress does not increase or decrease in one direction with increasing contact area. This may be because when the area is small, the various components of the bond force increase more as the area increases, increasing the bond stress. When the area exceeds a specific range, the increase in the components of the bond force is no longer significant, and the bond stress decreases.

In addition, the initial stiffness of both curves (Figures 11 and 12) increased as the bond area increased because each component of the bonding force increased. The critical displacement (Figure 13) also increased as the contact area increased. A larger contact area resulted in a higher chemical bonding force and a higher mechanical bite force. When these two forces disappear, the internal slip is relatively higher.

4. Theoretical Modeling

Only the initial rise phase of the bond stress-slip curve was studied because the post-ascend stage is complicated and cannot be predicted by a uniform function.

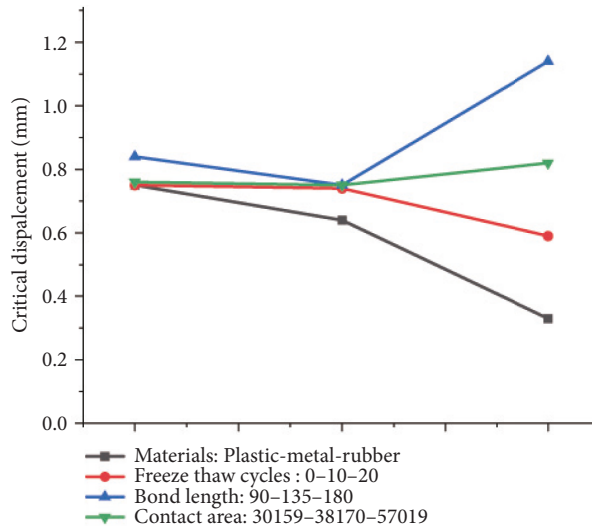


FIGURE 13: Critical displacement comparison.

TABLE 5: α values of different specimens.

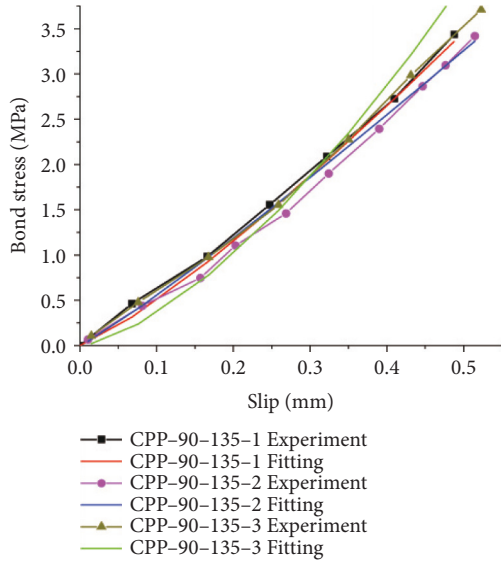
Group	Test ID	τ_s	S_s	α
1	P-90-135-1	6.0	0.7	1.2
	P-90-135-2	6.4	0.9	1.1
	P-90-135-3	5.8	0.6	1.5
2	M-90-135-1	7.9	0.8	1.2
	M-90-135-2	8.1	0.7	1.2
	M-90-135-3	7.8	0.5	1.6
3	R-90-135-1	3.5	0.3	1.5
	R-90-135-2	3.4	0.4	1.3
	R-90-135-3	3.4	0.3	1.0
4	P-90-135-FTC-10-1	4.4	0.7	1.0
	P-90-135-FTC-10-2	4.8	0.7	1.1
	P-90-135-FTC-10-3	4.6	0.8	1.1
5	P-90-135-FTC-20-1	3.8	0.6	1.2
	P-90-135-FTC-20-2	3.9	0.6	1.0
	P-90-135-FTC-20-3	3.8	0.6	1.5
6	P-90-90-1	5.5	0.7	1.2
	P-90-90-2	5.5	0.9	1.0
	P-90-90-3	5.7	0.9	1.1
7	P-90-180-1	6.1	1.2	1.4
	P-90-180-2	5.8	1.2	1.5
	P-90-180-3	5.8	1.0	1.5
8	P-80-120-1	5.0	0.7	1.5
	P-80-120-2	5.2	0.8	1.0
	P-80-120-3	5.0	0.8	1.6
9	P-110-165-1	5.9	0.8	1.3
	P-110-165-2	6.2	0.8	1.4
	P-110-165-3	5.9	0.8	1.6

As the material properties of GFRP bars are similar to those of grout-filled pipes, the bond stress-slip relationship of GFRP bars in concrete was investigated to understand the bond behavior of the grout-filled concrete specimens. The BPE model proposed by Eligehausen et al. [35] is a classical model. This model was applied to the bond between steel bars and concrete and then successfully used to study the bond behavior between FRP bars and concrete by Rossetti et al.

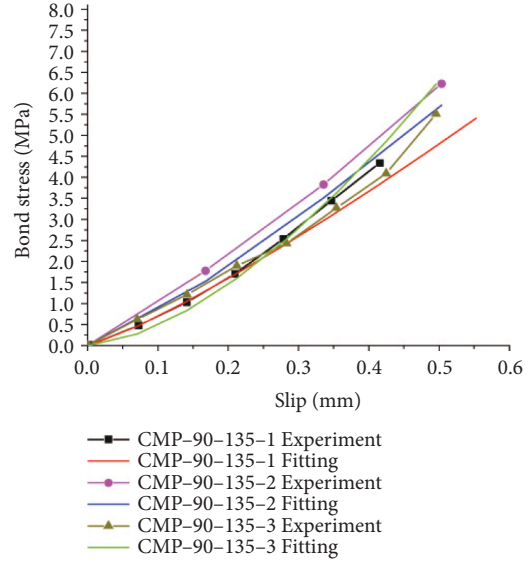
[36]. The bond stress-slip curve in this model is divided into different parts based on some representative parameters, such as the ultimate bond stress (τ_s), ultimate slip (S_s), and α .

Using curve-fitting on the experimental results of different specimens, the parameter α in this model was determined, as shown in Table 5.

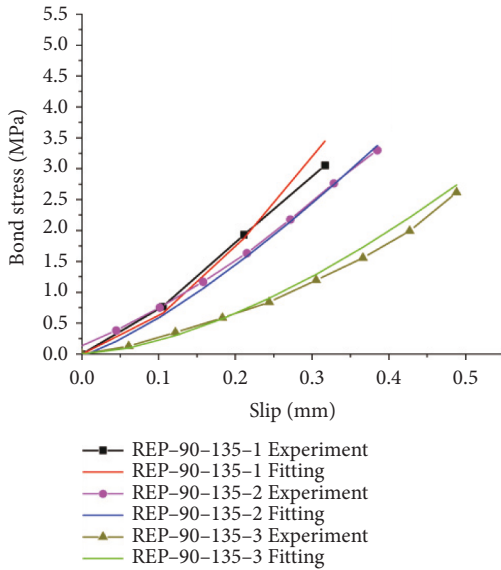
Therefore, the bond stress-slip relationship in the curvilinear ascending branch is proposed as follows:



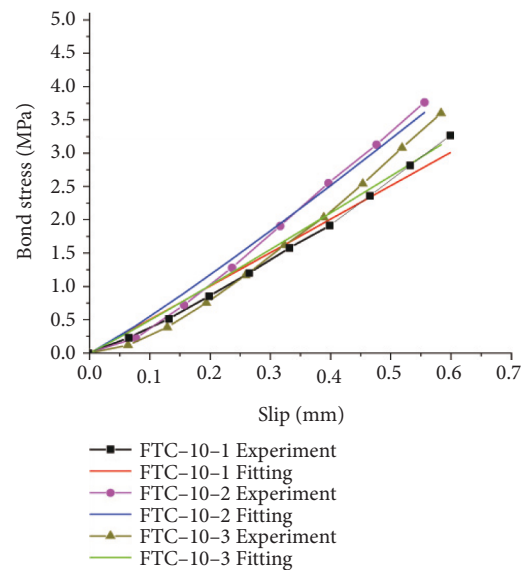
(a)



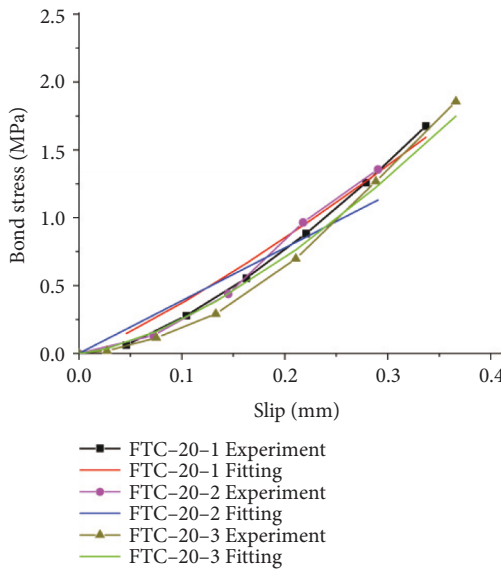
(b)



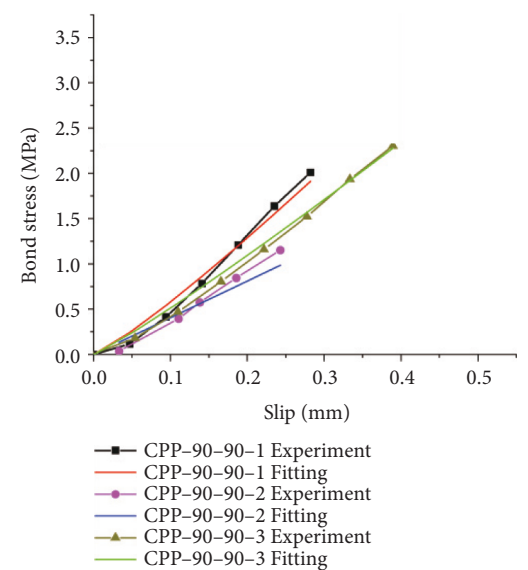
(c)



(d)



(e)



(f)

FIGURE 14: Continued.

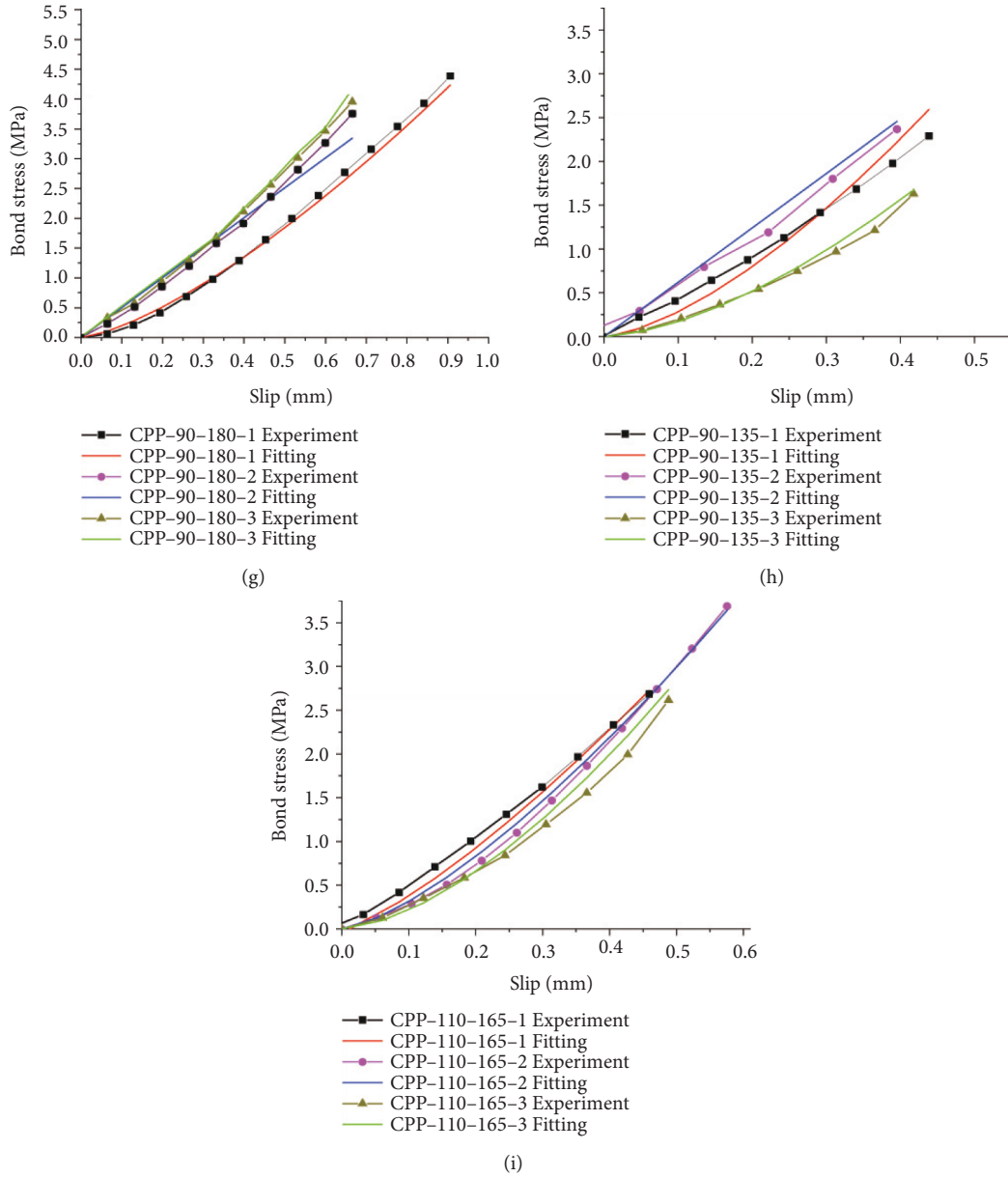


FIGURE 14: Comparison of theoretical results and fitting curves. (a) Cpp-90-135, (b) CMP-90-135, (c) REP-90-135, (d) CPP-FTC-10-135, (e) CPP-FTC-20-90-135, (f) CPP-90-90, (g) CPP-90-180, (h) CPP-80-112, (i) CPP-110-165.

$$\tau = \tau_s \left(\frac{S}{S_s} \right)^\alpha, \quad (3)$$

where S is the slip at the loaded end and τ is the average bond stress. The experimental results of the ultimate bond stress (τ_s) and ultimate slip (S_s) were used in this calculation. A comparison between the fitting data and experimental results is presented in Figure 14. A good agreement was observed in the ascending branch for all the specimens.

5. Conclusions

In this study, the relationship between force (bond stress) and displacement at the loading end was investigated using single-end compressive tests on grout-filled concrete

components with multiple interface materials. The stronger the bond stress is, the greater the overall performance will be. Before the cracking of concrete structure, the stronger the bond stiffness is, the higher the bond strength to bond-slip ratio is, and the greater the ability of the diverse range of materials is to function together.

In support of the above, after experimental study, two types of curves were obtained: the axial load or stress of the first type of specimen reached peaks with a negative exponential distribution and then remained constant or increased linearly. The axial load or stress of the second type of specimens reached peaks with a negative exponential distribution, then increased linearly for a period, then increased to a new peak as a quadratic function, and finally remained constant. The specimens with rubber extractive pipes for

hole-forming included only the first type of curve. The specimens with corrugated metal and plastic pipes for hole-forming included both types of curves.

During specimen failure by loading, the corrugated metal pipe specimens were subjected to the highest pressure (and bond stress), followed by the corrugated plastic pipe specimens and the rubber extractive pipe specimens. The stiffness of the force curve (bond stress curve) was the highest for the corrugated metal pipe specimens, followed by the rubber extractive pipe and corrugated plastic pipe specimens. The critical displacement was the highest for the corrugated plastic pipe specimens, followed by the corrugated metal pipe and rubber extractive pipe specimens.

An increase in the number of freeze-thaw cycles reduced the load-bearing capacity of the specimen, bond stress curve, stiffness of the force curve, and stiffness of the bond stress curve. The reduction in these values for 20 freeze-thaw cycles relative to 10 freeze-thaw cycles was lower than that for 10 freeze-thaw cycles relative to 0 freeze-thaw cycles. For critical displacement, the reduction in value for 20 freeze-thaw cycles relative to 10 freeze-thaw cycles was higher than that for 10 freeze-thaw cycles relative to 0 freeze-thaw cycles.

The load-bearing capacity and bond stress increased significantly with an increase in the bond length. The stiffness of the force curve first increased and then remained almost constant, whereas the stiffness of the bond stress curve first increased and then decreased; the critical displacement increased gradually.

With an increase in bonding area, the load-bearing capacity and bond stress increased significantly. The stiffness of the force and displacement curves increased gradually, and the critical displacement increased gradually, but the increase was not significant.

The theoretical results are in good agreement with the experimental curves in light of peak loading force and peak bond stress, stiffness of loading force curve and bond stress curve, and bonding performance on critical displacement. From the perspective of peak loading force and peak bond stress, the bonding performance of the three hole-forming materials was ranked as follows: corrugated metal pipes > corrugated plastic pipes > rubber extractive pipes. From the perspective of the stiffness of the loading force curve and that of the bond stress curve, the bonding performance of the three types of hole-forming materials was as follows: corrugated metal pipes > rubber extractive pipes > corrugated plastic pipes. The bonding performance of the three materials was ranked based on critical displacement as follows: rubber extractive pipes > corrugated metal pipes > corrugated plastic pipes.

Data Availability

The data used to support the research are included within this manuscript.

Disclosure

Eryu Zhu and Teng Li should be regarded as co-first authors.

Conflicts of Interest

The authors declare that they have no known competing financial interests or personal relationships that could have influenced the work reported in this paper.

Authors' Contributions

Eryu Zhu and Teng Li contributed equally to this work.

Acknowledgments

The authors wish to express their gratitude to the Fundamental Research Funds for the Central Universities (Grant no. 2021JBM427).

References

- [1] Y. Yu, *Experimental study on mechanical behavior of prestressed concrete beams with plastic sheath*, Ph.D. thesis, Southeast University, China, 2003.
- [2] M. Zhou, Y. Huang, and B. Ge, "Some problems and suggestions in the application of corrugated plastic pipes for prestress concrete with bonds for hole-forming," *Jiangsu Transportation Research*, vol. 4, pp. 25–27, 2005.
- [3] Z. Wang, "Application of corrugated plastic pipes in prestressed concrete bridges with bonds," *Plastics Industry*, vol. 44, no. 8, pp. 146–149, 2016.
- [4] C. Gu, S. Chen, and S. Zhang, "Application of geo-radar in the grout plumpness detection of prestressed corrugated plastic pipes with bonds in box girder structures of prestressed concrete continuous rigid bridges with bonds," *Engineering Technology*, vol. 4, pp. 00267–00269, 2016.
- [5] Y. Nie and B. Yu, "Hidden trouble and countermeasure of plastic bellows for prestressed concrete engineering," *Construction Technology*, vol. 5, pp. 29–32, 2009.
- [6] X. Liu, Y. Liu, T. Wu, and H. Wei, "Bond-slip properties between lightweight aggregate concrete and rebar," *Construction and Building Materials*, vol. 255, Article ID 119355, 2020.
- [7] X. Hu, G. Peng, D. Niu, X. Wu, and L. Zhang, "Bond behavior between deformed steel bars and cementitious grout," *Construction and Building Materials*, vol. 262, Article ID 120810, 2020.
- [8] J. Khalaf and Z. Huang, "Analysis of the bond behaviour between prestressed strands and concrete in fire," *Construction and Building Materials*, vol. 128, pp. 12–23, 2016.
- [9] S. Liu, H. Yuan, and J. Wu, "Full-range mechanical behavior study of FRP-to-concrete interface for pull-pull bonded joints," *Composites Part B: Engineering*, vol. 164, pp. 333–344, 2019.
- [10] H. Yuan, J. G. Teng, R. Seracino, Z. S. Wu, and J. Yao, "Full-range behavior of FRP-to-concrete bonded joints," *Engineering Structures*, vol. 26, no. 5, pp. 553–565, 2004.
- [11] Y. Chen, R. Feng, Y. Shao, and X. Zhang, "Bond-slip behaviour of concrete-filled stainless steel circular hollow section tubes," *Journal of Constructional Steel Research*, vol. 130, pp. 248–263, 2017.
- [12] H. Dong, X. Chen, W. Cao, and Y. Zhao, "Bond-slip behavior of large high-strength concrete-filled circular steel tubes with different constructions," *Journal of Constructional Steel Research*, vol. 167, Article ID 105951, 2020.

- [13] J. Song, W. Wang, S. Su, X. Ding, Q. Luo, and C. Quan, "Experimental study on the bond-slip performance between concrete and a corrugated steel plate with studs," *Engineering Structures*, vol. 224, Article ID 111195, 2020.
- [14] F. Tariq and P. Bhargava, "Bond-slip models for super ductile TMT bars with normal strength concrete exposed to elevated temperatures," *Journal of Building Engineering*, vol. 32, Article ID 101585, 2020.
- [15] L. Augusthus Nelson, M. Al-Allaf, and L. Weekes, "Analytical modelling of bond-slip failure between epoxy bonded FRP and concrete substrate," *Composite Structures*, vol. 251, Article ID 112596, 2020.
- [16] Y. Cheng, *Experimental Study and Theoretical Analysis of the Interfacial Bond Performance of concrete-filled Square Steel Tube*, Ph.D. thesis, Xi'an University of Architecture and Technology, China, 2007.
- [17] JGJ 52-2006, *Quality of Normal Concrete with Sand and Stone and Test Method Standard*, Chinese Standard, Beijing, China, 2006.
- [18] GB 50204-2002, *Code for Construction Acceptance of Concrete Structure Engineering*, Chinese Standard, Beijing, China, 2002.
- [19] TGE30-2005, *Test Methods of Cement and Concrete for Highway Engineering*, Chinese Standard, Beijing, China, (in Chinese), 2005.
- [20] TB/T 3192-2008, *Technical Specification of Cable Grouts on Post-Prestressed Concrete Railway Girder*, Chinese Standard, Beijing, China, (in Chinese), 2008.
- [21] GB/T 17671-1999, *Method of Testing Cements-Determination of Strength*, Chinese Standard, (in Chinese), 1999.
- [22] GB/T. 8804.1-2003, *Thermoplastic Pipes-Determination of Tensile Properties-Part 1: General Test Method*, 2003, Chinese Standard, (in Chinese), 2003.
- [23] O. Gooranorimi, W. Suaris, and A. Nanni, "A model for the bond-slip of a GFRP bar in concrete," *Engineering Structures*, vol. 146, pp. 34–42, 2017.
- [24] K. He, Y. Chen, and S. Han, "Experimental investigation of square stainless steel tubular stub columns after elevated temperatures," *Journal of Constructional Steel Research*, vol. 159, pp. 397–414, 2019.
- [25] Q. Hao, Y. Wang, and J. Hou, "Experimental study on bond behavior of GFRP ribbed rebars," *Engineering Mechanics*, vol. 25, no. 10, pp. 158–165, 2008.
- [26] JB T 6169-2006, *Metal Bellows*, Chinese Standard, Chennai, India, 2006.
- [27] Z.-H. Wang, L. Li, Y.-X. Zhang, and W.-T. Wang, "Bond-slip model considering freeze-thaw damage effect of concrete and its application," *Engineering Structures*, vol. 201, Article ID 109831, 2019.
- [28] Y. Wang, F. He, J. Wang, and Q. Hu, "Comparison of effects of sodium bicarbonate and sodium carbonate on the hydration and properties of portland cement paste," *Materials*, vol. 12, no. 7, p. 1033, 2019.
- [29] Y. Wang, F. He, J. Wang, C. Wang, and Z. Xiong, "Effects of calcium bicarbonate on the properties of ordinary Portland cement paste," *Construction and Building Materials*, vol. 225, pp. 591–600, 2019.
- [30] Y. Pan and G. Xian, "Effects of freeze-thaw cycles on the behavior of the bond between CFRP plates and concrete substrates," *Journal of Composites for Construction*, vol. 22, no. 3, Article ID 04018011, 2018.
- [31] A. Hosseini and D. Mostofinejad, "Effective bond length of frp-to-concrete adhesively-bonded joints: experimental evaluation of existing models," *International Journal of Adhesion and Adhesives*, vol. 48, pp. 150–158, 2014.
- [32] J. Chen and J. Teng, "Anchorage strength models for FRP and steel plates bonded to concrete," *Journal of Structural Engineering*, vol. 127, no. 7, 2001.
- [33] R. Seracino, M. R. Raizal Saifulnaz, and D. J. Oehlers, "Generic debonding resistance of eb and nsm plate-to-concrete joints," *Journal of Composites for Construction*, vol. 11, no. 1, pp. 62–70, 2007.
- [34] Fédération Internationale du Béton (FIB), "Bulletin d'information no. 14," *Externally bonded FRP reinforcement for RC structures*, 2001.
- [35] R. Eligehausen, E. Popov, and V. Bertero, "Local bond stress-slip relationships of deformed bars under generalized excitations: experimental results and analytical model," in *Proceedings of the Earthquake Engineering Research Center*, University of California, Berkeley, CA, USA, 1983.
- [36] V. A. Rossetti, D. Galeota, and M. M. Giammatteo, "Local bond stress-slip relationships of glass fibre reinforced plastic bars embedded in concrete," *Materials and Structures*, vol. 28, no. 6, pp. 340–344, 1995.

Research Article

Experimental Analysis of Recycled Aggregate Concrete Beams and Correction Formulas for the Crack Resistance Calculation

Xuyong Chen,^{1,2} Zhixin Zhang,¹ Zhifeng Xu ,^{1,2} Qiaoyun Wu ,^{1,2} Jianping Fan,³ and Xuri Zhao⁴

¹School of Civil Engineering and Architecture, Wuhan Institute of Technology, Wuhan 430073, Hubei, China

²Hubei Provincial Engineering Research Center for Green Civil Engineering Materials and Structures, Wuhan 430073, Hubei, China

³School of Civil and Hydraulic Engineering, Huazhong University of Science and Technology, Wuhan, Wuhan 430073, Hubei, China

⁴China Construction Commercial Concrete Co. Ltd, Wuhan 430073, Hubei, China

Correspondence should be addressed to Zhifeng Xu; 20120102@wit.edu.cn

Received 11 January 2022; Accepted 12 March 2022; Published 29 March 2022

Academic Editor: Dora Foti

Copyright © 2022 Xuyong Chen et al. This is an open access article distributed under the Creative Commons Attribution License, which permits unrestricted use, distribution, and reproduction in any medium, provided the original work is properly cited.

This paper studies the similarities and the differences between natural aggregate concrete (NAC) beams and recycled aggregate concrete (RAC) beams in terms of concrete material properties, bearing capacity, and crack resistance and further proposes correction formulas for cracking moment calculation of RAC beams that consider different recycled aggregate substitution ratios. First, the basic mechanical properties (e.g., cube compressive strength, axial compressive strength, and elastic modulus) of RAC blocks were tested; second, comparative bending tests of RAC beams and natural aggregate concrete beams were conducted, in order to obtain the cracking moments, yield bending moments, ultimate bending moments, mid-span deflections and crack development forms; finally, numerical simulations were performed to investigate the cracking performances of RAC beams. Through analyzing the experimental results, it is found that the crack development pattern of RAC beams resembles that of natural aggregate concrete beams, while the cracking performance of RAC beams significantly deviates from that of NAC beams. Finally, the correction formulas for the cracking moment calculation of RAC beams are proposed based on the numerical simulation results and verified by data from other researchers, which can be regarded as a correction for the cracking moment calculation formulas in the current code for RAC beams with respect to varied recycled concrete aggregate substitution ratios.

1. Introduction

With the developments of urbanization and advancements of infrastructure constructions, concrete, as the most common engineering material in constructions, is now experiencing a soar in its consumption. At the same time, exploitations of tremendous nonrenewable resources and generations of a large amount of construction wastes are consequently unavoidable, which is, however, against the global concept of environmental protections and sustainable developments [1]. Therefore, many scholars have recently focused on recycled aggregate concrete (RAC) and its components [2–4]. Nevertheless, before actual engineering

applications, it is necessary to comprehensively evaluate the strength, stiffness, stability, and other indicators of RAC members, in order to make the designs and the manufacturing to be consistent. As the most crucial mechanical property, the bearing capacity of RAC beams has been extensively studied [5, 6]. Many studies show that the bending strength of RAC beams is similar to that of natural aggregate concrete (NAC) beams, in which the substitution ratio of recycled concrete aggregates (NCA) has little effect on the bending strength [7–9]. Yet, some researchers believe that when the substitution ratio of NCA is less than 50%, the bending strength of RAC beams is almost the same as that of NAC beams; while when the substitution ratio reaches 100%,

the bending strength of RAC beams can decrease significantly [10]. As for the bending stiffness, the mainstream viewpoint states that the influence of recycled aggregate substitution ratio on mid-span deflection is much higher than that of reinforcement ratio [7, 8, 11, 12], which is still true for the case when natural fine aggregate (NFC) is replaced by recycled fine aggregate [13, 14]. On the other hand, to promote the applications of components made of RAC, the serviceability limit states should also be taken into account, in which the crack resistance is of paramount importance. The cracking behavior of concrete beams is basically determined by the maximum tensile strain. Some researchers demonstrate that, with the increase of substitution ratio of NCA, the maximum tensile strain of RAC beams goes higher than that of NAC beams, resulting in poor tensile properties and increasing ductility [15]. When the substitution ratio of NCA hits 100%, the cracking moment of RAC beams decreases to a value about 25% lower than that of NAC beams, causing a loss of stiffness, premature cracking, and early withdrawal from the working stage [16, 17]. In addition, the crack width and crack spacing should also be considered, which is affected by the bond-slipping behavior between concrete and reinforcement [9, 18]. Although the fact that the decrease of stiffness after cracking leads to the decrease of its bond strength is doubtless, there are few quantitative studies on the influence of recycled aggregate substitution ratio on the crack development.

From the above discussion, it can be concluded that existing researches on the mechanical properties of RAC members lack of quantitative analysis, which is insufficient for practical engineering. To this end, taking the bending performance of RAC beams as the research subject, this paper studies the influence of replacement ratio and longitudinal reinforcement ratio on the bending performance of RAC beams, whose conclusions provide practical structural designs with useful guidance. In order to analyze the short-term bending behaviors, four-point bending tests were carried out on full-scale RAC beams. The cracking moment, yield moment, ultimate moment, and mid-span deflection are measured and analyzed, in which the cracking moment is analyzed in detail. The experimental results were analyzed by two stages: the first stage aims to understand the influence of NCA and longitudinal tensile reinforcement ratio on the mechanical properties of RAC beams, and four kinds of test beams with varied recycled aggregate substitution ratios and three different reinforcement ratios were designed manufactured and tested, whose test results were compared and analyzed; in the second stage, the practicability of the cracking moment formulas in the current code for RAC beams is analyzed, which compared the relative error between the test values and the corresponding values computed by the code. The results show that RAC beams and NAC beams share similar crack development patterns, while their cracking performances deviate from each other significantly. Thus, the current code cannot accurately describe the cracking behaviors of recycled aggregate concrete beams, which requires corrections. Hence, correction formulas for the cracking moment calculation with respect to RAC beams

are proposed and verified based on a series of numerical analyses and experimental data from different researchers.

This paper is organized as follows: Section 2 describes the test method and the test content; in Section 3, the test results are presented and analyzed in detail, and the similarities and differences between RAC beams and NAC beams are obtained; the correction formulas for the cracking moment calculation of RAC beams are proposed and verified in Section 4.

2. Experimental Tests of RAC Beams

This section presents the details of the experimental tests of RAC beams in terms of material properties, specimen configurations, and experimental schemes.

2.1. Material Properties. The cement used in this test was Huaxin brand pm42.5 ordinary Portland cement, and the reducing ratio of water reducing agent was 15%. The natural aggregate (NA) used in the test was nature crushed stone, and the aggregate was the continuous gradation meeting the standard JGJ 52–2006 [19]. RCA consists of three kinds of coarse aggregates with different particle sizes, which were mixed into a continuous gradation of 5–25 mm that satisfying the classification standard of class II aggregates in GB/T 25177–2010 [20]. The fine aggregates used in the test were all natural fine aggregates, and the fineness modulus is medium coarse. The physical properties of various aggregates are shown in Table 1.

For C30 concrete defined by JGJ55-2011 [21], the water-cement ratio is 0.49, and the substitution ratios of NCA are 0% (reference group), 50%, 70%, and 100%, respectively. The corresponding four kinds of numbers were, respectively, NAC, RAC-50, RAC-70, and RAC-100. It can be seen from Table 1 that the water absorption of NCA is dramatically higher than that of natural aggregates, which is caused by the adhesion of mortar on the surface of NCA [22]. This characteristic leads to greater free water absorption of NCA in the mixing process of concrete, while the decrease of W/C value contributes to the decrease of the cohesion of RAC. To solve this problem, additional water was added. The mix proportion parameters are shown in Table 2 and additional water consumption is shown in Table 3. The reinforcements in the beam body meet the relevant provisions of GB/T 50010–2010 [23]. The stirrups and erecting reinforcements were HPB335 with a diameter of 8 mm, and the tensile reinforcements were HRB400. According to the requirements for reinforcement ratio, 14 mm, 16 mm, and 18 mm are used, respectively. In order to obtain the mechanical parameters (shown in Table 4), the tensile test of stressed reinforcement is carried out using the tensile test method of reinforcement according to GB/T 28900–2012 [24].

2.2. Specimen Configurations. A total of 7 beams were designed and manufactured in this study, with a cross-sectional size of 150 mm × 300 mm and a length of 1800 mm. The variables considered are substitution ratio of NCA and reinforcement ratio of longitudinal stressed reinforcements,

TABLE 1: Physical properties of aggregates.

Aggregate type	Particle size range (mm)	Apparent density (kg/m ³)	Water absorption (%)	Water absorption and mud content (%)	Crushing index	Fineness modulus
NFA	≤5	2559	2.2	1.2	-	2.8
NA	5–20	2673	0.6	0.9	11	—
RCA	5–20	2534	4.6	0.2	17	—

TABLE 2: Concrete consumption per unit volume.

Label	Substitution ratio of RCA (%)	W/C	Material consumption (kg/m ³)				
			Cement	Sand	NA	RCA	Water reducing agent
NAC	0	0.49	367.4	686.5	1167.2	0	
RAC-50	50				583.6	553.3	
RAC-70	70				350.2	774.6	4.04
RAC-100	100				0	1106.6	

TABLE 3: Additional water consumption per unit volume.

Category of coarse aggregate	Label	Water absorption (%)	Substitution ratio (%)	Additional water consumption (kg)
NA	NAC	0.6	0	0
	RAC-50		50	23.34
RCA	RAC-70	4.6	70	32.68
	RAC-100		100	46.69

TABLE 4: Mechanical properties of stressed reinforcement.

Diameter of reinforcement (mm)	Yield strength (MPa)	Ultimate strength (MPa)	Elastic modulus (GPa)
14	455	627	205
16	466	635	203
18	432	607	200

which is divided into the following two groups: Group 1 has 5 beams with varied substitution ratio of NCA, the stressed reinforcements were 2C14, the substitution ratios of NCA are, respectively, 0%, 30%, 50%, 70%, and 100%, and the numbers were NAC-0.77, RAC-30-0.77, RAC-50-0.77, RAC-70-0.77, and RAC-100-0.77 respectively; Group 2 has 3 beams with varied reinforcement ratios. The substitution ratios of NCA were all 100%, the load-bearing steel bars were 2 HRB400 14, 2 HRB400 16, and 2 HRB400 18; the reinforcement ratios were 0.77%, 1.01%, and 1.28%; and the numbers were, namely, RAC-100-0.77, RAC-100-1.01, and RAC-100-1.28. In order to reduce the influence of stirrups on the mechanical analysis of the pure bending section, neither stirrup nor erection bar was arranged at the pure bending section at the middle of the span. The specific design parameters of the test beam are shown in Table 5, and the details of reinforcements are shown in Figure 1. The test beam was poured and maintained in the Structure and Disassembly Laboratory of Wuhan University of Technology, and the test beams of two sizes (100 mm × 100 mm × 100 mm and 100 mm × 100 mm × 300 mm respectively) were reserved for 28 days under the same conditions (shown in Figure 2).

2.3. Experimental Schemes. The loading mode of the test beams was four-point bending. The main instruments were the reaction frame and the 500 kN electro-hydraulic

servo brake, and then, the load was evenly distributed through the distribution beam. The bending beam was simply supported by a roller and a pin support both placing at 150 mm away from each end of the beam, respectively. The distribution beam was also supported on the test beam by a roller and a pin support that were both placed at 650 mm away from each end of the beam, respectively (shown in Figure 3). The loading procedure was strictly in accordance with GB/T 50152–2012 [25]. In order to facilitate the observation and analysis of the crack development pattern, a small square of 100 mm × 100 mm was marked in front and at the back of the beam. Before the formal loading, the preloading was carried out 2 times in order to check whether the dial gauge, strain gauge, and mechanical sensor can work normally. In the formal loading stage, when the loading force value was close to 80% of the cracking load, yield load, and ultimate load, the load value of each level should not exceed 5% of their corresponding calculated values, and the stable load time should be controlled at least 10 minutes to observe the development trend of mechanical properties.

The deflections at the middle of the span and the strain of the tensile reinforcement in the beam were measured by dial indicator and DH3818 y, respectively. The six strain gauges were symmetrically arranged on the tensile steel bars on both sides of the pure bending section at the middle of the span, and the dial indicator was arranged at the bottom of the middle of the span, as shown in Figure 3.

TABLE 5: Design parameters of test beams.

Specimen number	Cross section (mm×mm)	Length (mm)	Tensile reinforcement	Erecting reinforcement	Stirrup	Reinforcement ratio (%)	Thickness of protective layer (mm)
NAC-0.77			2 HRB400 14			0.77	
RAC-30-0.77			2 HRB400 14			0.77	
RAC-50-0.77			2 HRB400 14			0.77	
RAC-70-0.77			2 HRB400 14			0.77	
RAC-100-0.77	150×300	1800	2 HRB400 14	HPB300 8	HPB300@100	0.77	20
RAC-100-1.01			2 HRB400 16			1.01	
RAC-100-1.28			2 HRB400 18			1.28	

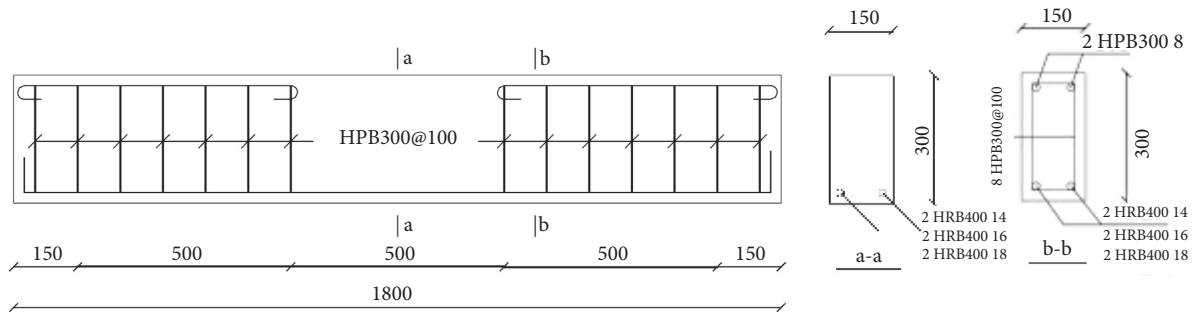


FIGURE 1: Reinforcement details of test beams (mm).



FIGURE 2: Experimental specimens. (a) Curing test block under the same condition. (b) Casting and forming.

3. Test Results and Discussions

In this section, the test results are presented and investigated, and the similarities and differences between RAC beams and NAC beams are studied.

3.1. Material Properties of RAC. In order to obtain the material properties of RAC, blocks of RAC with varied recycled aggregate substitution ratios were manufactured and tested according to GB/T 50080–2016 and GB/T 50081–2019 [26, 27]. The slump index was used to characterize its workability. The data show that, when additional water is considered, even with an increased substitution ratio

of NCA, the slump will not decrease significantly, whose slump can still meet the standard of flowing concrete. On the mechanical properties of the indicators, the cube compressive strength, axial compressive strength, and elastic modulus are mainly measured. The test results are shown in Table 6, from which it can be seen that the three mechanical properties decrease with the increase of substitution ratio of NCA. The main reason for this phenomenon is that there are two different interface transition zones (ITZ): one is the interface between new and old cement mortar, and the other is the interface between new cement mortar and recycled aggregate. This ITZ weakens bonds between aggregate and cement, reducing the strength of concrete and increasing its deformation performance [28].

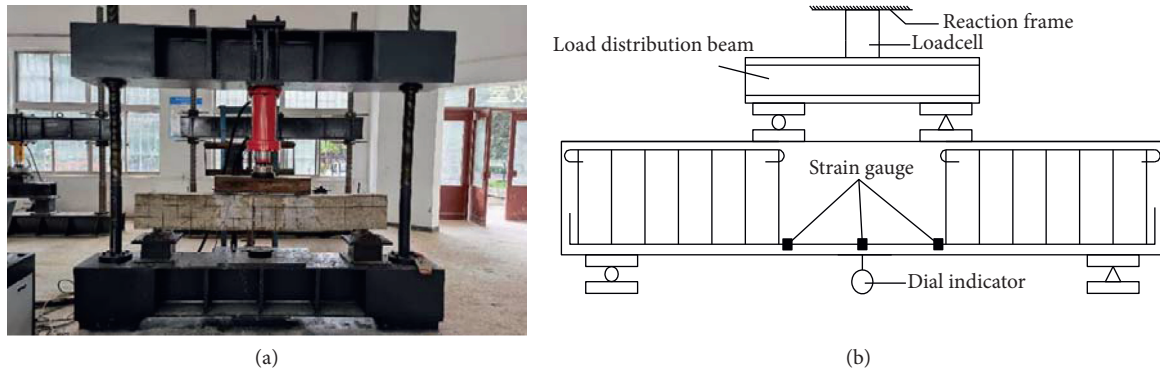


FIGURE 3: Loading mode and layout of measuring instruments. (a) Test device and loading mode. (b) Layout of strain gauge and displacement gauge.

TABLE 6: Physical and mechanical properties of concrete.

Substitution ratio of RCA (%)	Slump (mm)	f_{cu} (MPa)	f_c (MPa)	E_c (GPa)
0	144	35.4	28.7	41.3
50	138	34.7	28.5	38.7
70	140	32.1	27.6	32.2
100	141	30.3	27.3	30.8

3.2. Analysis of Bearing Capacity of RAC Beams. The test results show that the test beams with different replacement ratios of recycled aggregate and different reinforcement ratios can meet the ductility design, which means the stressed reinforcement yields before the beam failure. Simultaneously, due to the existence of the pure bending section at the mid-span, the bending cracks first appeared at the bottom of both ends of the pure bending section. As the load increases, the number and length of cracks increase gradually. When there were inclined cracks in the shear-bending section, the number of cracks at the middle of the span tended to be stable. When the load reached the yielding load, the width of the mid-span crack became wider, the crack length developed longer, and the mid-span deflection started to increase rapidly. Finally, the concrete at the mid-span was crushed, and the test beam was damaged (shown in Figure 4).

The load-mid-span deflection curves of each test beam are shown in Figure 5, from which it can be seen that the stress development trend of the RAC beam and NAC beam is similar. This indicates that the structural engineering application of RAC is feasible. The development stage of the beams is divided into the elastic stage, the working stage with cracks, and the failure stage. It can be seen from the figure that the substitution ratio of NCA has little effect on the ultimate load of the RAC beams compared to the significant effect due to the reinforcement ratio. This phenomenon is the same as that of NAC beams. In addition, similar to the NAC beam, it can be seen from Figure 5 that, with the increase of reinforcement ratio, the mid-span deflection of steel bars at the yielding stage increases gradually, but the deflection increments decrease.

By recording the cracking moment (M_{cr}^t), yielding moment (M_y), and ultimate moment (M_u), the bending performances of RAC beams with different recycled



FIGURE 4: Failure state of the test beam.

aggregate replacement ratios and different reinforcement ratios were compared, whose results are shown in Table 7. The bending moment values in the table are all obtained through the conversion of test load values. It can be seen from Table 7 that with the increase of the substitution ratio of NCA, the cracking moment decreases significantly, indicating that RAC has lower tensile strengths that lead to premature cracking of RAC beams. At this junction, it should be pointed out that the maximum reduction of the cracking moment can reach 31.9%. On the other hand, the change of recycled aggregate substitution ratio has little effect on the yield moment and ultimate moment, which is due to the ductility design (with appropriate reinforcement ratio) of concrete beams. In contrast, the reinforcement ratio has a great influence on the yield moment and ultimate moment, whose influence on the cracking moment is negligible though.

Figure 6 shows the load-strain curves of the loading steel, which demonstrates that all the steel bars reach the yield point before the failure of the beam, and therefore, RAC beams meet the ductile failure characteristics. The use of tensile reinforcements also increases the yield limit and the

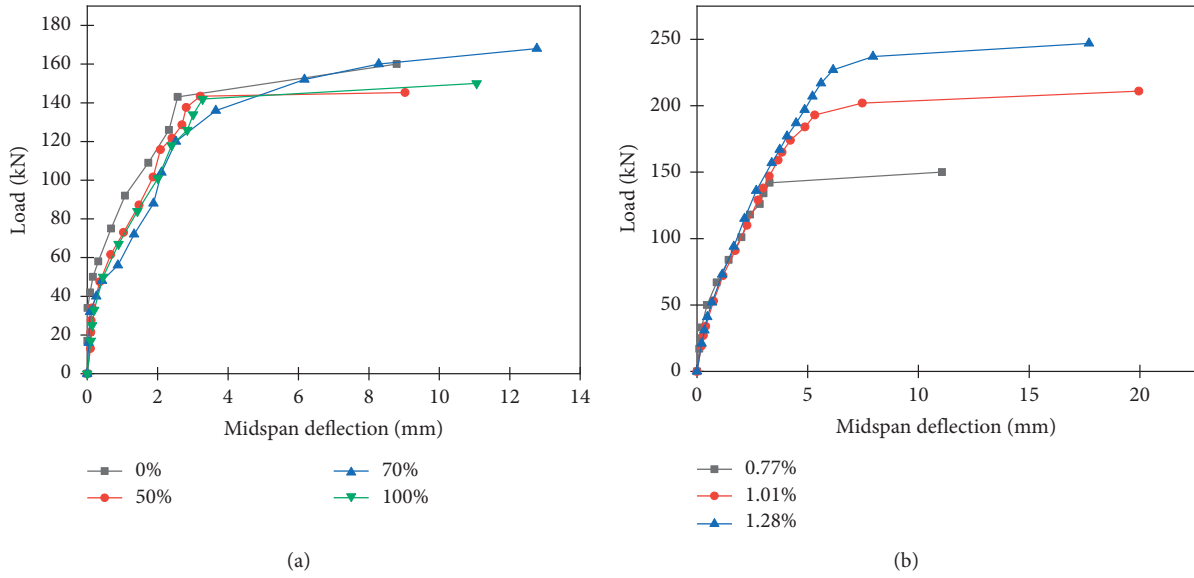


FIGURE 5: Load-mid-span deflection curves. (a) Substitution ratio of RCA. (b) Reinforcement ratio of tensile reinforcement.

TABLE 7: Mechanical properties of test beams.

Test beam number	M_{cr}^t (kN · m)	M_y (kN · m)	M_u (kN · m)	M_{cr}^t/M_u (%)
NC-0.77	10.5	35.75	40	26.25
RAC50-0.77	7.53	35.25	39.25	19.59
RAC70-0.77	6.59	36	40	17.88
RAC100-0.77	7.2	35.5	38.5	18.83
RAC100-1.01	7.25	46	51.5	14.56
RAC100-1.28	7.13	56.75	60.5	11.79

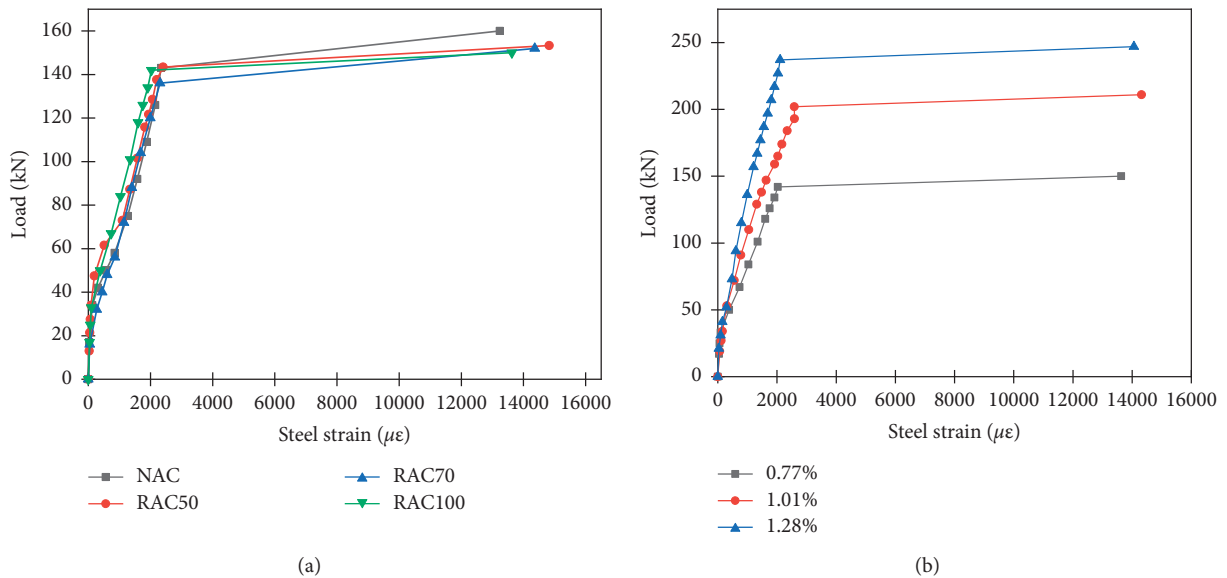


FIGURE 6: Load VS steel strain curves. (a) Substitution ratio of RCA. (b) Reinforcement ratio of tensile reinforcements.

ultimate strength of beams, which weakens the role of concrete in the experimental failure of simply supported beams. Therefore, the change of substitution ratio of NCA has no effect on the yield limit or the ultimate strength, and

there is no obvious difference among the ultimate state between the RAC beam and NAC beam. This conclusion is inconsistent with the research results of Knaack and other scholars [7–9].

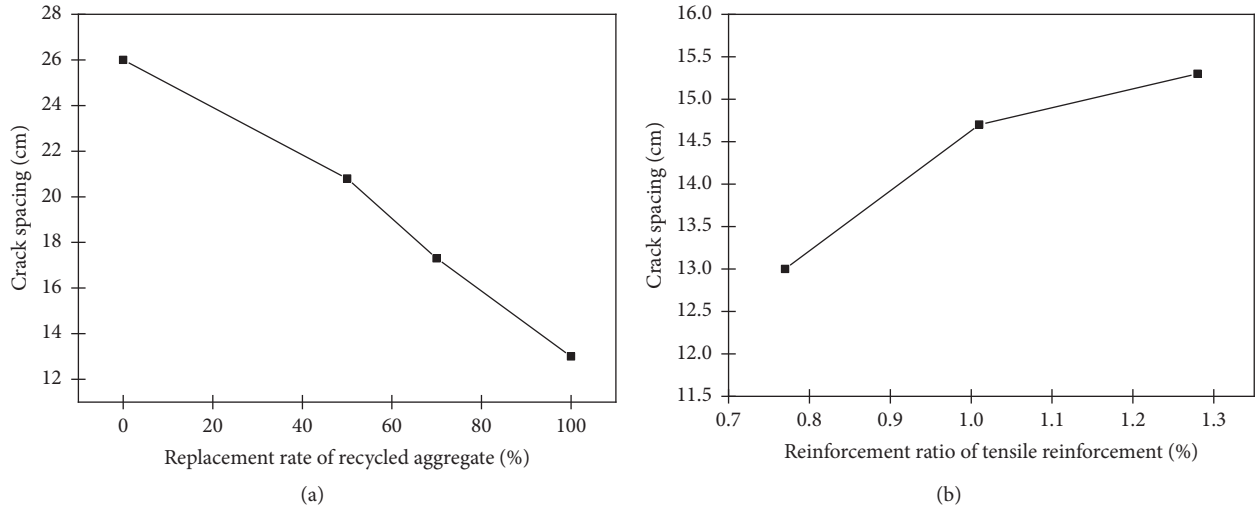


FIGURE 7: Crack development diagram of test beams. (a) NAC-0.77. (b) RAC-50-0.77. (c) RAC-70-0.77. (d) RAC-100-0.77. (e) RAC-100-1.01. (f) RAC-100-1.28.

3.3. Crack Resistance of RAC Beams. Crack resistance is an important index for the serviceability limit state of concrete members. In order to analyze the crack resistance of RAC beams, the ratio of cracking moment to ultimate moment was calculated (M_{cr}^t / M_u) (as shown in Table 7). It is obvious that RAC beams will crack earlier than natural concrete beams under the same reinforcement ratio. In the experiment, the NAC beam cracked when the applied bending moment reached about 25% of the ultimate bending moment, while for the RAC beam, it will crack when the applied bending moment is only 17% to 19% of the ultimate bending moment.

Figure 7 is the crack development diagram of each test beam, from which it can be seen that the test beams with different substitution ratios all have similar crack development patterns. The crack of all test beams started from the pure bending section near the load application point, whose length was less than 50 mm. As the load increases, the length and the number of cracks increase gradually, while the change of crack width was inconspicuous. When the load increases to a certain threshold, oblique shear cracks appear on both sides of the beam, while there is nearly no crack in the supporting area. When the longitudinal reinforcement yields, the mid-span deflection suddenly increased, and the vertical cracks became wider than 1.7 mm, showing the failure of the beam.

It can be seen from Figure 8 that, under the same reinforcement ratio, as the substitution ratio of NCA increases, the crack number in the mid-span increases gradually, and the crack spacing decreases gradually. This is because, although the bond effect between RAC and reinforcement decreases and the crack spacing increases, the reduction of elastic modulus and tensile strength of RAC trigger the beams easier to crack, which reduces the crack spacing. However, even if the substitution ratio of NCA remains unchanged and the reinforcement ratio increases, the crack spacing also increases, which is in line with the development law of NAC.

4. Correction Formulas for the Cracking Moment Calculation of RAC Beams

The correction formulas for the cracking moment calculation of RAC beams are proposed and verified in this section, which can account for different RCA substitution ratios.

4.1. Theoretical Analysis of Cracking Moment Calculation of RAC Beams. According to the above discussion, the crack resistance of RAC beams is mainly affected by the ultimate tensile strain of RAC. Some studies stated that the tensile peak strain of RAC is greater than that of ordinary concrete [29]. Wu et al. demonstrated that the ultimate strain of RAC is similar to that of NAC [30]. And he further assumed that, when the substitution ratio of recycled aggregate is 100%, the ultimate tensile strain of the RAC beam is 1.5 times the peak strain, which is 2 times of that NAC. Hence, the stress-strain diagram of normal section of RAC beam when cracking can be obtained is shown in Figure 9.

The balance equation of horizontal force is established as follows (shown in Figure 9):

$$\frac{1}{2}bx \frac{x}{h-x} \frac{3}{2}f_t^R = \frac{2}{3}b(h-x)f_t^R. \quad (1)$$

The height of the compression zone is calculated as $x = 0.485h$. And the maximum compressive stress is $1.413 f_t^R$.

The cracking moment of the RAC beam is calculated as follows:

$$M_{cr}^R = 1.338W_0f_t^R, \quad (2)$$

where W_0 is the moment of resistance of the section, and for rectangular section, $W_0 = bh^2/6$, and f_t^R is the tensile strength of RAC.

From equation (2), it can be seen that the basic value of plastic influence coefficient of resistance moment (γ_m^R) of RAC beam is 1.338, which is less than the standard value of

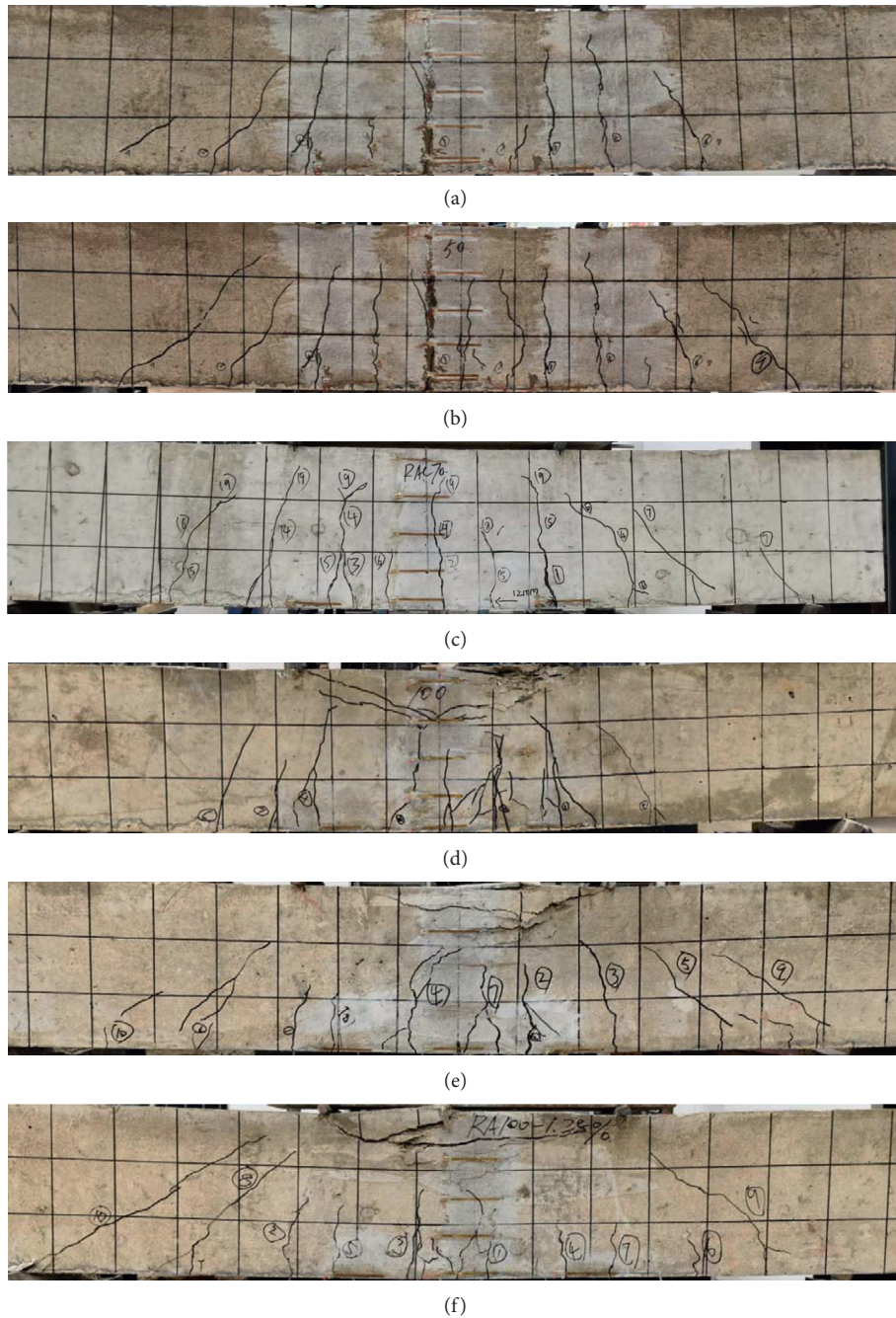


FIGURE 8: Variations of crack spacing of RAC beams. (a) Substitution ratio of RCA. (b) Reinforcement ratio of tensile reinforcements.

NAC 1.55 [23]. In other words, when the tensile peak strain increases and the ultimate tensile strain remains unchanged, the crack resistance of RAC beams will inevitably decrease. Since the cracking strain of RAC in this paper is assumed and the influence of reinforcement is not considered, it is necessary to further verify the calculation formulas of the cracking moment.

4.2. Correction Formulas for the Cracking Moment Calculation Based on Numerical Simulations. In order to obtain the cracking moment of RAC beams with respect to different

substitution ratios of recycled aggregate, a three-dimensional finite element model was established and analyzed by ABAQUS software based on the existing test data.

4.2.1. Geometry, Material Modeling, and Meshing of the Finite Element Simulations. As shown in Figure 10, the corresponding finite element model of the test beams is presented. Figure 10(a) shows the concrete beam geometry, the load location, and the support arrangement. Figure 10(b) shows the geometry of the steel skeleton model. The reinforcement ratio of all the models was 0.77% without

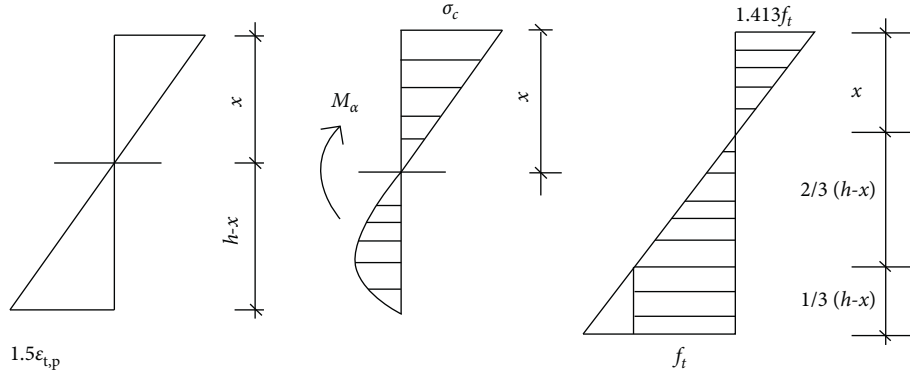


FIGURE 9: Stress-strain relationship of RAC beams.

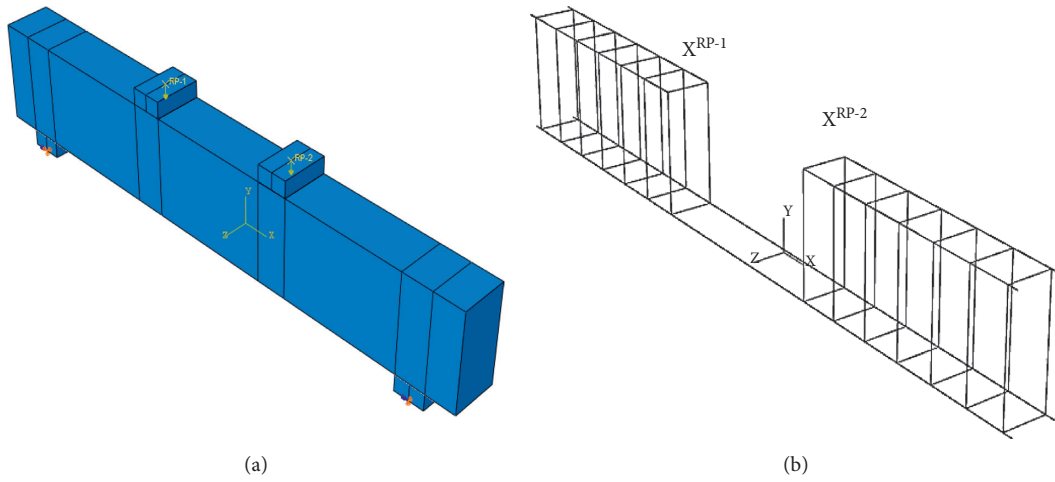


FIGURE 10: Finite element model of the simply supported RAC beam. (a) Beam model. (b) Steel skeleton model.

considering the change of reinforcement ratio in the numerical analysis. The concrete damage plastic model (CDP) was used to define the constitutive characteristics of the beam. The constitutive curve of RAC proposed by Ding has a good fit with that of NAC, which can avoid the attenuation of elastic modulus of concrete in the elastic stage [31]. Therefore, such a constitutive curve is adopted in the simulation, which is described by equation (3) [31].

$$y = \begin{cases} \frac{A_{n(r)}x + (B_{n(r)} - 1)x^2}{1 + (A_{n(r)} - 2)x + B_{n(r)}x^2} & x \leq 1 \\ \frac{x}{\alpha_{n(r)}(x - 1)^2 + x} & x > 1 \end{cases}, \quad (3)$$

where $A_{n(r)}$ is the ratio of elastic modulus to peak secant modulus of RAC; $B_{n(r)}$ is the parameter of ascending section; $\alpha_{n(r)}$ is the parameter of descending section; $y = \sigma/f_c$ (σ is the stress, f_c is the test value of axial compressive strength); $x = \varepsilon/\varepsilon_c$ (ε is the strain, ε_c is the peak strain). When RAC is under uniaxial compression ($n=1$), equation (3) can be rewritten as follows:

$$\begin{aligned} A_{1(r)} &= \frac{(1 - 0.3r)(1 + 0.2r)}{1 - 0.1r} \times 9.1 f_{cu}^{-4/9}, \\ B_{1(r)} &= \frac{5(A_{1(r)} - 1)^2}{3}, \\ \alpha_{1(r)} &= 2.5 \times 10^{-5} f_{cu}^3. \end{aligned} \quad (4)$$

When the RAC is in a uniaxial tension state and ($n=2$), then equation (3) become

$$\begin{aligned} A_{2(r)} &= 1.306 \frac{(1 - 0.3r)(1 + 0.1r)}{1 - 0.1r}, \\ B_{2(r)} &= \frac{5(A_{2(r)} - 1)^2}{3}, \\ \alpha_{2(r)} &= 1 + 3f_{cu}^2 + 10^{-4}, \end{aligned} \quad (5)$$

where r is the substitution ratio of RCA, and f_{cu} is the test value of concrete cube compressive strength.

In order to obtain the damage parameter of the damage constitutive formula in the CDP model, this paper adopts the calculation formula derived from Sidoroff's energy equivalence principle, whose specific formula is as follows [32]:

$$\delta = E_0 (1 - d)^2 \varepsilon. \quad (6)$$

The following calculation formula of damage factor is obtained after conversion:

$$d = 1 - \sqrt{\frac{\delta}{E_0 \varepsilon}}, \quad (7)$$

where E_0 is the initial elastic modulus; d is the damage factor. In order to obtain the basic parameters of the damage constitutive model and match the basic mechanical data of the test beam, the basic mechanical property tests corresponding to the test beam are carried out. The specific data are shown in Table 8.

In the model, a three-dimensional solid element with 8 nodes and 6 facets using reduced integral (C3D8R) was used to define the main concrete element. The reinforcement skeleton element consists of longitudinal reinforcement, vertical reinforcement, and stirrup, which was simulated by a three-dimensional two-node truss element (T3D2). The T3D2 element only has three degrees of freedom and can only undertake axial tension or pressure, which was suitable to simulate the components with large stiffness. The cushion block unit was simulated by the C3D8R element. In order to increase the accuracy, the mesh size of the main beam was set to 10 mm, while the length of the reinforcement skeleton was 25 mm.

4.2.2. Boundary Conditions and Loading Configurations. The boundary conditions refer to the constraint of the simply supported beam in the actual situation, and cushion blocks were placed at 150 mm (lower edge) and 650 mm from both ends of the beam. Three axial constraints and rotation constraints around Y axis and Z axis were set on the cushion block in the opposite direction of X axis. Axial constraints in Y and Z directions and rotation constraints around Y axis and Z axis were set on the cushion block in the positive direction of X axis. In order to simulate the actual loading system, the loading mode of monotonic concentrated force was used. The load of the two loading points was 100 kN (200 kN in total). The bond-slip behavior between steel and concrete was simulated by the built-in region constraint of the finite element node, which can simulate the ideal slip state between steel and concrete.

4.2.3. Analysis of the Numerical Simulation Results. It can be seen from Figure 6 that, when the concrete in the tensile zone of the lower part of the beam cracks, the tensile stress is borne by the reinforcement, which will cause the strain mutation of the reinforcement. Therefore, the inflection point of the bending moment steel strain curve obtained by ABAQUS postprocessing can be used as the sign for the cracking bending moment (M_{cr}^c). In order to compare the simulation value of the cracking bending moment with the corresponding result calculated from the current code value, the cracking moment formula (8) in GB/T 50010-2010 is

used for calculation [23]. The numerical simulation results and results calculated by the code are shown in Table 9.

$$M_{cr} = \gamma f_{tk} W_0, \quad (8)$$

$$\gamma = \gamma_m \left(0.7 + \frac{120}{h} \right), \quad (9)$$

where M_{cr} is the cracking moment; f_{tk} is the axial tensile strength; W_0 is the elastic moment of resistance after conversion of cross section; γ is the plastic influence coefficient of section resistance moment; γ_m is the basic value of the plastic influence coefficient of the resistance moment of the section, which is 1.55 for rectangular sections.

It can be seen from Table 9 that, with the increase of substitution ratio of recycled aggregate, the relative error between the code calculation value and the test value increases obviously. That is, the calculation formula of cracking moment for NAC beam is no longer applicable to RAC beam. The ratio of the cracking moment test value (M_{cr}^c) to the code calculation value (M_{cr}) is taken as y value (see Table 9), and the substitution ratio of recycled aggregate is taken as r for curving fitting (Figure 11). Consequently, the correction formula (10) of the basic value of the plastic influence coefficient of the corresponding section moment of resistance can be obtained by curve fitting, whose correlation coefficient $R^2 = 0.992$.

$$y = 0.772 + 0.215 \times e^{-x/0.643}. \quad (10)$$

The modified basic value of plastic influence coefficient of section moment of resistance and the calculated value of cracking moment are as follows:

$$\gamma_m^R = y \times \gamma_m, \quad (11)$$

$$\gamma^R = \gamma_m^R \left(0.7 + \frac{120}{h} \right),$$

$$M_{cr}^R = \gamma^R f_{tk} W_0, \quad (12)$$

where γ_m^R , γ^R , and M_{cr}^R are the basic value of the plastic influence coefficient of section moment of resistance, the plastic influence coefficient of section moment of resistance, and the value of cracking moment, respectively.

4.3. Verification of Correction Formulas for the Cracking Moment Calculation. In order to verify the proposed modified formula (12) for cracking moment of RAC beams proposed, this section analyzes the test data obtained from other researchers and further compares the test results with the calculation results of (12). The results are shown in Table 10, from which it can be seen that the calculation results obtained by the modified formulas are in good agreement with the experimental data obtained by various researchers. The average relative error is 3.83%, the standard deviation of relative error is 2.12%, and the maximum absolute relative error is 7.66%, which further proves the correctness and the accuracy of (12).

TABLE 8: Basic test parameters.

Aggregate type	Specimen number	f_{cu}/MPa	f_c/MPa	E_c/GPa
NC	NAC	37.1	29.7	41.6
		36	28.6	41.4
		33.2	27.1	41.2
	RAC-30	37.5	30.5	35.4
		35.8	29	33.7
		35.5	27.7	32.1
RAC	RAC-50	34.9	29.1	30.8
		34.7	28.6	30.1
		34.5	28.3	31
	RAC-70	32.9	28.2	30.9
		32.2	27.5	30.4
		31.2	27.3	30.2
RAC-100	30.9	29.4	28.5	
	30.3	27.5	27	
		29.6	26.3	26.3

TABLE 9: Numerical simulation results of cracking moment.

Aggregate type	Beam number	M_{cr}^c (kN·m)	M_{cr} (kN·m)	Relative error	M_{cr}^c / M_{cr}
NC	NC-1	10.781	11.348	0.053	0.950
	NC-2	10.493	10.93	0.042	0.960
	NC-3	11.541	11.722	0.016	0.985
	RAC-50-1	8.732	10.211	0.169	0.855
	RAC-50-2	8.44	9.905	0.174	0.852
	RAC-50-3	8.154	9.470	0.161	0.861
RAC	RAC-70-1	8.344	9.840	0.179	0.848
	RAC-70-2	7.577	9.001	0.188	0.842
	RAC-70-3	7.186	8.581	0.194	0.837
	RAC-100-1	7.578	9.348	0.234	0.811
	RAC-100-2	6.675	8.361	0.253	0.798
	RAC-100-3	6.846	8.594	0.255	0.797

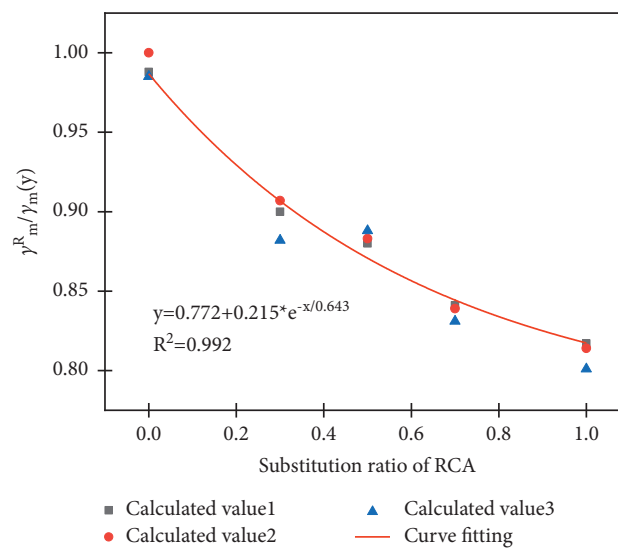


FIGURE 11: Fitting curve.

TABLE 10: Verification of the proposed formulas.

Researchers	Maximum relative error (%)	r (%)	M_{cr}^R (kN·m)	M_{cr}^t (kN·m)	M_{cr}^t / M_{cr}^R
This study	20	50	7.42	7.53	1.03
		70	6.68	6.59	0.99
		100	7.04	7.2	1.02
		30	8.35	8.99	1.08
Wang [33]	25	50	8.34	8.38	1.00
		70	7.76	7.45	0.96
		100	7.65	7.38	0.95
		30	8.35	8.6	1.03
Lan [34]	20	50	8	7.5	0.94
		100	7.21	7.5	1.04
		30	8.35	8.99	1.08
Du [35]	24	50	21.85	20.3	0.93
		70	20.86	21.75	1.04
Mean value					0.997

5. Conclusions

This paper first studies the similarities and the differences between NAC beams and RAC beams with respect to concrete material properties, bearing capacity, and crack resistance via experimental observations and tests. Based on the experimental test results, correction formulas for the cracking moment calculation of RAC beams are proposed and verified through numerical simulations and optimal fitting of test data from other researchers. Moreover, the following conclusions are drawn:

- (1) Under the same reinforcement ratio, the cracking moment of RAC beams decreases as the substitution ratio of RCA increases, while the substitution ratio of RCA has an only subtle influence on the yield moment or the ultimate moment of RAC beams due to the ductile design
- (2) The reinforcement ratio has the same effect on the yield performance and the ultimate bearing capacity of both RAC beams and NAC beams
- (3) The premature cracking effect increases with an increasing substitution ratio of RCA
- (4) Although the cracking behavior of RAC beams is similar to that of natural aggregate concrete beams, the decrease of bond effect between recycled aggregate concrete and reinforcement will lead to an increase of crack width, while the decreases of elastic modulus and tensile strength of recycled aggregate concrete both lead to early cracking, the decrease of crack spacing, increasing reinforcement strain, and the increase of midspan deflection
- (5) It is found that the cracking moment of RAC beams gradually decreases as the substitution ratio increases, in which the cracking moment of RAC beams can be more than 25% lower than that of NAC beams if RCA completely replaces the natural aggregates, indicating the current code is not applicable to RAC beams on cracking moment calculation

- (6) The corrected formulas of the cracking moment calculation have sufficient accuracy, whose average relative error is merely 3.83%.

Data Availability

The data used to support the findings of this study are included within the article.

Conflicts of Interest

The authors declare that they have no conflicts of interest regarding the publication of this article.

Acknowledgments

The authors wish to acknowledge the financial support provided by the National Natural Science Foundation of China (No. 52178301), the Key Research and Development Program of Hubei Science and Technology Department (No. 2020BAB071), and the Science Research Foundation of Wuhan Institute of Technology (K2021030).

References

- [1] A. Kanellopoulos, P. Savva, M. F. Petrou, I. Ioannou, and S. Pantazopoulou, "Assessing the quality of concrete - reinforcement interface in Self Compacting Concrete," *Construction and Building Materials*, vol. 240, Article ID 117933, 2020.
- [2] D. Foti and D. Cavallo, "Mechanical behavior of concretes made with non-conventional organic origin calcareous aggregates," *Construction and Building Materials*, vol. 179, pp. 100–106, 2018.
- [3] D. Foti and M. Lerna, "New mortar mixes with chemically depolymerized waste PET aggregates," *Advances in Materials Science and Engineering*, vol. 2020, Article ID 8424936, 9 pages, 2020.
- [4] D. Foti, M. Lerna, M. Sabbà, and V. Vacca, "Mechanical characteristics and water absorption properties of blast-furnace slag concretes with fly ashes or microsilica additions," *Applied Sciences*, vol. 9, no. 7, p. 1279, 2019.

- [5] B. Lei, H. Wu, Y. S. Yan, and C. H. Rao, "Research on the calculation method for bending rigidity of recycled concrete beams," *Advanced Materials Research*, vol. 919–921, pp. 1396–1399, 2014.
- [6] Y. Gui-xin, W. Jin, and Y. Qiang, "Study on deflection of recycled concrete beams," *Engineering Mechanics*, vol. 28, no. 2, pp. 147–151, 2011.
- [7] A. M. Knaack and Y. C. Kurama, "Behavior of reinforced concrete beams with recycled concrete coarse aggregates," *Journal of Structural Engineering*, vol. 141, no. 3, Article ID B4014009, 2015.
- [8] M. Arezoumandi, A. Smith, J. S. Volz, and K. H. Khayat, "An experimental study on flexural strength of reinforced concrete beams with 100% recycled concrete aggregate," *Engineering Structures*, vol. 88, pp. 154–162, 2015.
- [9] S. Seara-Paz, B. González-Fontebo, F. Martínez-Abella, and J. Eiras-López, "Flexural performance of reinforced concrete beams made with recycled concrete coarse aggregate," *Engineering Structures*, vol. 156, pp. 32–45, 2018.
- [10] R. Dhir, M. Limbachiya, T. Leelawat, and B. Bs, "Suitability OF recycled concrete aggregate for use IN BS 5328 designated mixes," *Proceedings of the Institution of Civil Engineers-Structures and buildings*, vol. 134, no. 3, pp. 257–274, 1999.
- [11] I. S. Ignjatović, S. B. Marinković, Z. M. Mišković, and A. R. Savić, "Flexural behavior of reinforced recycled aggregate concrete beams under short-term loading," *Materials and Structures*, vol. 46, no. 6, pp. 1045–1059, 2013.
- [12] F. Yu, C. B. Yin, and M. Jiang, "Study on the recycled concrete beam's stiffness," *Applied Mechanics and Materials*, vol. 193–194, pp. 1361–1364, 2012.
- [13] L. Evangelista and J. De Brito, "Flexural behaviour of reinforced concrete beams made with fine recycled concrete aggregates," *KSCE Journal of civil engineering*, vol. 21, no. 1, pp. 353–363, 2017.
- [14] W.-C. Choi, H.-D. Yun, and S.-W. Kim, "Flexural performance of reinforced recycled aggregate concrete beams," *Magazine of Concrete Research*, vol. 64, no. 9, pp. 837–848, 2012.
- [15] J. S. Ryu, "An experimental study on the effect of recycled aggregate on concrete properties," *Magazine of Concrete Research*, vol. 54, no. 1, pp. 7–12, 2002.
- [16] Q. Yu, M. Shi, Y. Cheng, M. Wang, and H.-z. Chen, "Fe₃O₄@Au/polyaniline multifunctional nanocomposites: their preparation and optical, electrical and magnetic properties," *Nanotechnology*, vol. 19, no. 26, Article ID 265702, 2008.
- [17] G. Kaklauskas, V. Gribniak, D. Bacinskas, and P. Vainiunas, "Shrinkage influence on tension stiffening in concrete members," *Engineering Structures*, vol. 31, no. 6, pp. 1305–1312, 2009.
- [18] Z. Deng, Y. Wang, H. Yang, and J. Qian, "Research on crack behavior of recycled concrete beams under short-term loading," *KSCE Journal of Civil Engineering*, vol. 22, no. 5, pp. 1763–1770, 2018.
- [19] Jgj-52, *Standard for Technical Requirements and Test Method of Sand and Crushed Stone (Or Gravel) for Ordinary concrete*, China Architecture & Building Press, Beijing, China, 2006.
- [20] Gb/T-25177, *Recycled Coarse Aggregate for concrete*, China Standards Press, Beijing, China, 2010.
- [21] Jgj-55, *Recycled Coarse Aggregate for concrete*, China Construction Industry Press, Beijing, China, 2011.
- [22] M. Joseph, L. Boehme, Z. Sierens, and L. Vandewalle, "Water absorption variability of recycled concrete aggregates," *Magazine of Concrete Research*, vol. 67, no. 11, pp. 592–597, 2015.
- [23] Gb/T-50010, *Code for Design of concrete Structures*, China Construction Industry Press, Beijing, China, 2010.
- [24] GB/T-28900, *Test Methods of Steel for Reinforcement of concrete*, China Standards Press, Beijing, China, 2012.
- [25] GB/T-50152, *Standard for Test Method of concrete Structures*, China Construction Industry Press, Beijing, China, 2012.
- [26] Gb/T-50080, *Standard for Test Methods of Performance on Ordinary Fresh concrete*, China Construction Industry Press, Beijing, China, 2016.
- [27] Gb/T-50081, *Standard for Test Methods of concrete Physical and Mechanical Properties*, China Construction Industry Press, Beijing, China, 2019.
- [28] S. Seara-Paz, V. Corinaldesi, B. González-Fontebo, and F. Martínez-Abella, "Influence of recycled coarse aggregates characteristics on mechanical properties of structural concrete," *European Journal of Environmental and Civil Engineering*, vol. 20, no. sup1, pp. s123–s139, 2016.
- [29] J.-z. Xiao and J.-b. Li, "Study on relationships between strength indexes of recycled concrete," *Journal of Building Materials*, vol. 2, 2005.
- [30] J. Wu, D.-f. Ding, and W. Zhang, "Experimental study on shear behavior of recycled aggregate concrete beams," *Journal of Hohai University (Natural Sciences)*, vol. 1, 2010.
- [31] F.-x. Ding, C.-j. Fang, Y.-z. Gong, Z.-w. Yu, and L.-n. Hu, "Unified calculation method of uniaxial mechanical performance index of recycled concrete," *Journal of Architecture and Civil Engineering*, vol. 4, 2014.
- [32] L. Tian and J. Hou, "Reasonable plastic damaged factor of concrete damaged plastic model of ABAQUS," *Journal of Hubei University (Natural Science)*, vol. 37, no. 4, pp. 340–345, 2015.
- [33] J. Wang and C. Zhang, "Experimental study on flexural behavior of recycled concrete beams," *Journal of Lanzhou University of Technology*, vol. 42, no. 2, pp. 130–134, 2016.
- [34] Y. Lan, *Experimental study on flexural behavior of recycled concrete beams*, Journal of Tongji University, Shang Hai, China, 2004.
- [35] Z. H. Du, T. Hao, and L. X. Liu, "Experimental study on flexural property of reinforced concrete beams with recycled aggregate of construction waste," *Key Engineering Materials*, vol. 517, pp. 601–605, 2012.

Research Article

Analysis of Stress-Strain Relationship of Earthen Soil Based on Molecular Dynamics

Jianwei Yue,^{1,2} Xuanjia Huang,¹ Peng Li ,^{1,2} and Tingting Yue²

¹School of Civil Engineering and Architecture, Henan University, Kaifeng, Henan 475004, China

²Key Laboratory for Restoration and Safety Evaluation of Immovable Cultural Relics in Kaifeng, Henan University, Kaifeng, Henan 475004, China

Correspondence should be addressed to Peng Li; chipren@163.com

Received 23 July 2021; Accepted 24 February 2022; Published 25 March 2022

Academic Editor: Qian Chen

Copyright © 2022 Jianwei Yue et al. This is an open access article distributed under the Creative Commons Attribution License, which permits unrestricted use, distribution, and reproduction in any medium, provided the original work is properly cited.

The calibration of material mechanical parameters and deformation and failure mechanism of earthen soil have always been difficult problems in the field of cultural relics protection. How to establish a relationship between physical and mechanical properties of soil at macro and micro scales is the focus of the research. The nanostructure model of earthen soil composed of many atoms was established by molecular dynamics (MD) method. The stress-strain relationship of different moisture content was obtained by uniaxial compression simulation. Based on the electron micrograph image (magnification $\times 500$) and the image reconstruction method, a micromodel composed of particles and pores was constructed. Furthermore, using the displacement loading method, we obtained the stress-strain relationship of the earthen soil with different moisture contents. Our results showed that the displacement of the left and right boundaries of the circular pore model is 1.26 times more than that of the polygonal pore model, and the displacement of the polygonal pore model is 1.28 times more than that of the circular pore model. The stress-strain curve simulated by the polygonal pore model is consistent with the experimental results. The results of the numerical analysis are in good agreement with those of the macro test, which indicates that the research ideas and the methods used for earthen soil exploration in this work are feasible. Our present findings provide reference for deterioration research and safety evaluation of cultural relic buildings such as earthen sites.

1. Introduction

Soil sites are significantly affected by the environment, and soil sites are unique and nonrepeatable [1]. A large number of samples cannot be taken on the existing soil sites, which makes the research progress of soil mechanical properties of undisturbed sites slow. MD is a new micromechanical method developed in recent years. Its purpose is to obtain the required macroscopic physical and mechanical quantities of the object through long-time operation of a few particles [2]. With the help of theoretical calculation method and molecular dynamics simulation, the research information from multiple angles (microstructure, dynamics, etc.) and multiple levels (from microatomic level to macrostatistical level) is obtained [3] (Figure 1), so as to save the test cost and increase the test efficiency.

Theoretical and experimental research has been performed on the macromechanical properties of earthen soil. For example, Song et al. [4] conducted a macroscopic assessment on the soil mechanical characteristics of sites in Northwest Henan Province, China. In addition, Yue et al. [5] established a theoretical model of slope failure cusp catastrophe based on elastic sliding mass. However, fewer studies have been done on the microscale physical and mechanical properties, and the deterioration mechanism of earthen soil has not been elucidated. With the rapid development of computer technology, numerical simulation of complex mechanical behavior can effectively eliminate the influence of human and environmental factors in physical tests, better simulate the damage and failure process of microstructures, and fulfill the purpose of studying the characteristics of earthen soil foundation. The establishment of the

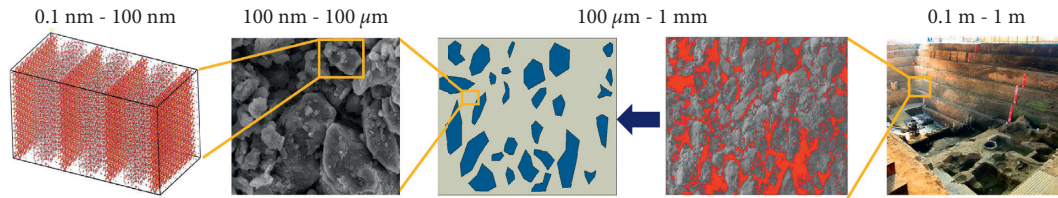


FIGURE 1: Multiscale structural characteristics of site soil materials.

constitutive relationship and numerical model of the materials of the earthen soil is not only the first step to meeting engineering application requirements but an important factor affecting numerical simulation results.

Many scholars have carried out a lot of research work around the physical and mechanical properties and structural characteristics of soil [6, 7]. The research trend shows the characteristics of multiscale integration, multimethod combination, and multidisciplinary intersection. The research shows that the microbehavior plays an extremely important role in the mechanical properties of soil. The research method of “combination of macro and micro” has become the mainstream of soil mechanical properties research at present and even in the future [8, 9]. Shen et al. first introduced the damage theory for research of soil sample constitutive models and established the elastic-plastic damage model [10] and nonlinear damage mechanics model [11]. Furthermore, Kuang et al. [12] carried out molecular dynamics (MD) simulation on the water molecular structure between crystal layers of montmorillonite minerals with different water content, and revealed the basic mechanism of high-pressure mechanical properties of clay from multiscale level. Yang et al. [13] used molecular dynamics simulation to study the hydration properties and adsorption properties of clay minerals, and clarified the structure and dynamic properties of clay in hydration. Liu et al. [14] applied molecular dynamics to study the influence relationship between the connection characteristics of soil particles (structural units) and the deformation and failure characteristics of soil, and found that the macromechanical properties of soil are controlled by the microstructure of soil. The structural fracture surface of soil passes through the connection surface between particles and particle aggregates, not through the particles themselves, that is, the weakest part of the connection between particles is destroyed first. In addition, Tang et al. [15] evaluated the microstructure and mechanical changes of expansive soil under multiscale cyclic loading and established a unified expression of stress-strain characteristics reflecting soil macrostructure and microstructure and considering microdamage. Chen [16] analyzed the elastoplastic constitutive model of soil samples based on numerical and physical simulation; the author also elaborated the relationship between physical and numerical simulation of soil samples. Zhao et al. [17] used molecular dynamics method to establish a variety of molecular models in Materials Studio software to analyze the influence of interlayer cation types on water molecules adsorbed by montmorillonite.

The aforementioned research results have promoted the development of research on mechanical properties of macrosoil and microsoil samples to a certain extent.

However, in view of the complexity and variability of soil samples [18], the intraparticle earthen soil cement has been simplified to a certain extent in the established models; the influence of the environment on cement has also been neglected. Obviously, deeper knowledge is needed on the microscale stress variation law of the soil sample and its components [19]. In previous studies, we found that the stress and strain results of earthen soil samples were different when diverse water samples were used. As can be seen in Figure 2, the compressive strength of the soil samples made with pure water is higher than that of the soil samples prepared with pit water from the site. The decrease in their moisture content made these differences even more obvious.

First, earthen sites are unique. On-site sampling would disturb the site body and is hence limited by the requirements of cultural relic protection. Thus, the number of soil samples taken from such site cannot be large, resulting in low test repeatability and slow progress of research on the mechanical properties of undisturbed earthen soil. Second, cements exist widely in natural geotechnical materials, and intergranular cementitious materials have an important impact on the mechanical properties of geotechnical materials. However, the cost of micromechanical model tests is high, hindering appropriate observations of the microevolution law of cementation failure. Therefore, based on the idea of Molecular dynamics (MD) simulation method, in this paper, with the help of material studio 7.0 simulation software, we established the nanostructure model of Zhouqiao earthen soil and applied lamps software to analyze the mechanical properties of Zhouqiao earthen soil; based on the SEM image of earthen soil and a small number of mechanical test results, a micromodel composed of particles, cements, and pores was established. Furthermore, we assessed the method for the determination of the microscale mechanical properties of the intraparticle earthen soil cement.

2. Construction and Simulation of Molecular Dynamics Model

2.1. Modeling Basis. By comparing the electron microscope images of soil samples under different magnification, the differences of microstructure of soil samples under different orders of magnitude are studied. For heterogeneous geotechnical materials, when the material is transformed into an image, different substances in the material can be reflected in the image through the change of gray or color, and the image reproduces the structural characteristics of the material well. Using digital image technology, the gray image of SEM is

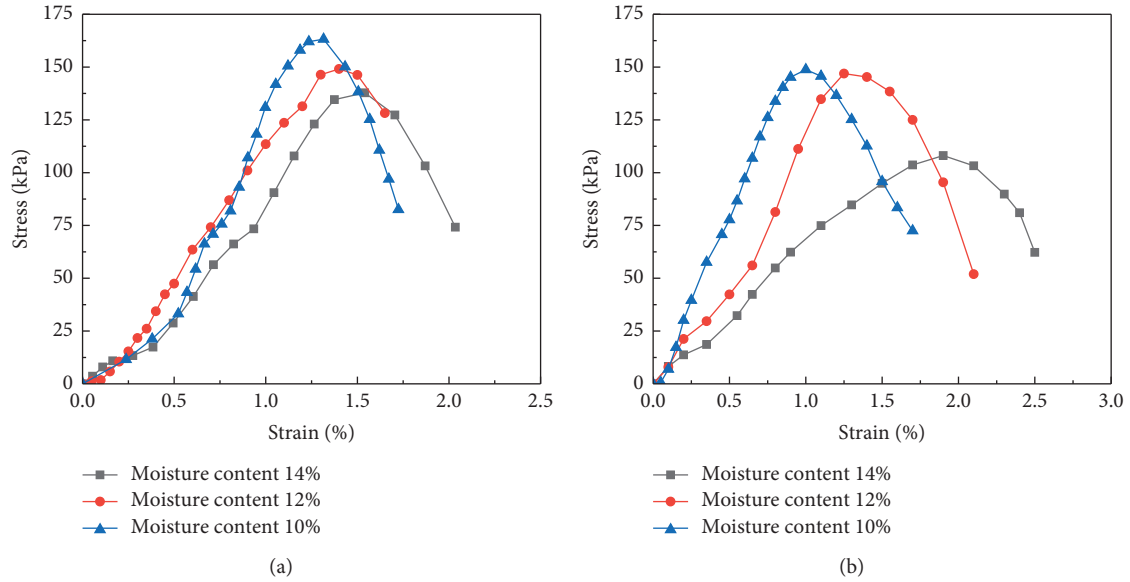


FIGURE 2: Stress-strain results of site soil samples: (a) sample made with pure water and (b) samples prepared with pit water from the site.

regarded as a three-dimensional coordinate system in MATLAB software. The length and width of the image are X and Y coordinate axes respectively, the gray value of the image is regarded as Z axis, and the gray value is regarded as $Z = f(x, y)$. After three-dimensional simplification of the gray image, the integral value of a three-dimensional irregular body with two-dimensional image size as the bottom and threshold as the high is calculated. The microstructure distribution image of soil sample in Figure 3 is transformed into a three-dimensional real microstructure diagram (Figure 4). Figure 4 shows the three-dimensional structural characteristics of soil samples. It can be obtained from Figures 4(a) to 4(e). With the increase of the magnification of the SEM image, the yellow and green parts gradually decrease, and the threshold tends to a certain range, which is reflected in the gradual simplification of the soil sample information contained in the picture, and the soil sample can only be determined as heterogeneous material in the macro state. When a certain observation scale is reached, the soil sample can be assumed to be soil sample and pore. The nano model of soil sample is constructed using Materials Studio software, and the mechanical properties of soil sample under different moisture content are studied by Monte Carlo method and molecular dynamics method. The research results provide data support for the subsequent microscale model.

Zhang et al. [20] studied the pore type, scale, and shape of clay and proposed that the pores contained in clay mineral structure can be divided into three types: intergranular pores formed by mineral particle compaction and deposition. Clay intergranular pores formed during diagenetic transformation of minerals. The gap (layer spacing) caused by the distance between crystal layers in clay crystal and the relationship between various pores is shown in Figure 5. Li et al. [21] found that most montmorillonite clay minerals are in flake structure and stacked into montmorillonite basic

particles. The thickness of the wafer layer is 1 nm, and the length and width are tens to hundreds of nanometers. When the crystal layer contains water, it can expand to produce interlayer nanopores with different thicknesses of about 0.2 to 2 nm. The research results of the aforementioned scholars provide a basis for the establishment of molecular models at the nanoscale.

2.2. Modeling. Based on the research of Bish et al. [22], the main component of silty clay is clay based mineral montmorillonite, and the geometric configuration of crystal is shown in Figure 6. In this work, the initial model of soil sample is based on montmorillonite, and the random water molecule modeling of Monte Carlo method is carried out using Material Studio software and setting the water molecule density as 1 g/cm^3 in the amorphous cell module at room temperature 298 K. The montmorillonite molecular model and random water molecule model are superimposed using the build layers function. Based on the density of soil samples with different moisture content, the molecular models of 10%, 12%, 14%, and 16% moisture content are established respectively. The atomic number and density of the model are shown in Table 1. Finally, discover setup is used to establish the force field and discover minimization is used to minimize its energy. In order to avoid the influence of periodic boundary in the process of uniaxial compression, the initial model of soil sample with water content is amplified by supercell, so that the size of molecular model reaches the visualized soil sample in microscale [23]. The simulation area size of the final initial model of soil sample is $A = 104 \text{ \AA}$, $B = 89 \text{ \AA}$, $C = 118 \text{ \AA}$, $\alpha = 90^\circ$, $\beta = 90^\circ$, and $\gamma = 90^\circ$, as shown in Figure 7. In Figure 6, the yellow ball, red ball, purple ball, and white ball represent silicon atom, oxygen atom, aluminum atom, and hydrogen atom, respectively. In Figure 7, the purple part is the crystal layer and the yellow

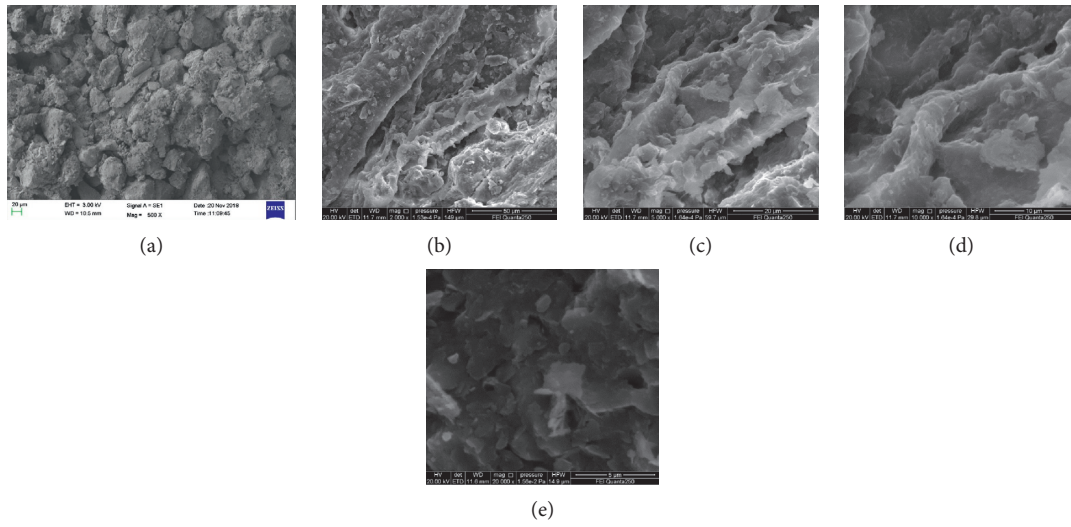


FIGURE 3: Distribution of the soil particle structure at the macroscale and microscale at different magnifications: (a) 500 times magnification, (b) 1000 times magnification, (c) 3000 times magnification, (d) 5000 times magnification, (e) and 10,000 times magnification.

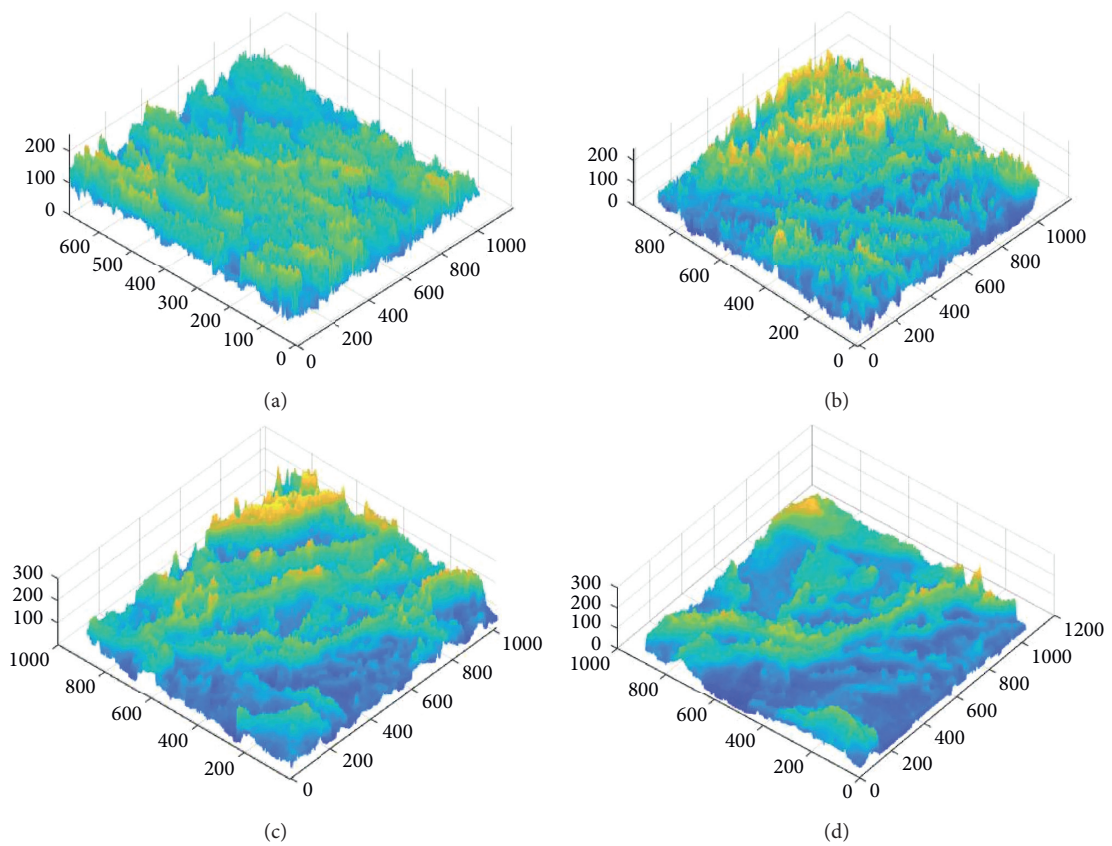


FIGURE 4: Continued.

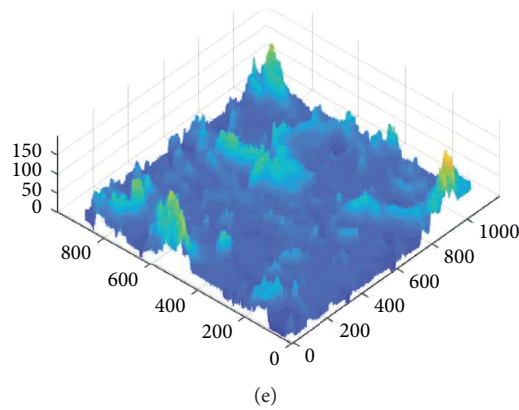


FIGURE 4: Three-dimensional structural characteristics of soil sample: (a) 500 times magnification, (b) 1000 times magnification, (c) 3000 times magnification, (d) 5000 times magnification, (e) and 10,000 times magnification.

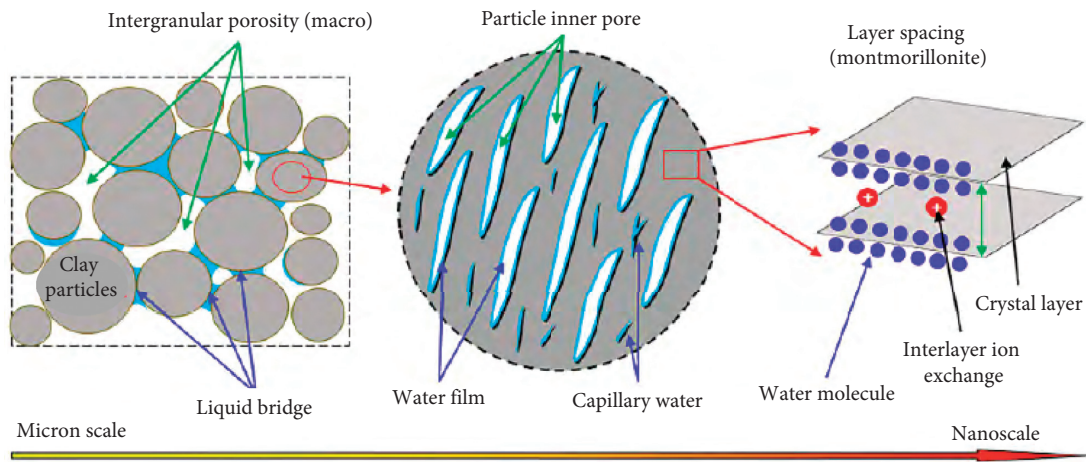


FIGURE 5: Characteristics of gas water distribution of clay minerals [21].

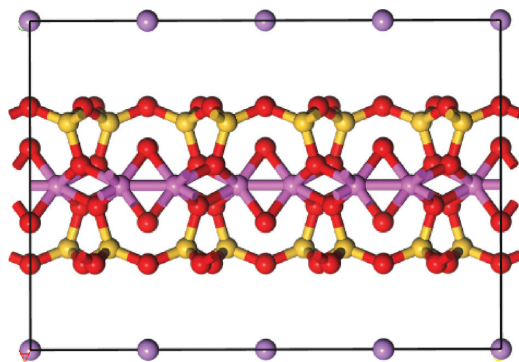


FIGURE 6: Unit cell of montmorillonite.

TABLE 1: Atomic number and density of molecular model.

Model name	Quantity of Si	Quantity of O	Quantity of Al	Quantity of Li	Quantity of H ₂ O	Density (g/cm ³)
10% moisture content model					16,000	1.47
12% moisture content model	6400	20,800	4800	2800	17,500	1.50
14% moisture content model					19,000	1.53
16% moisture content model					20,500	1.58

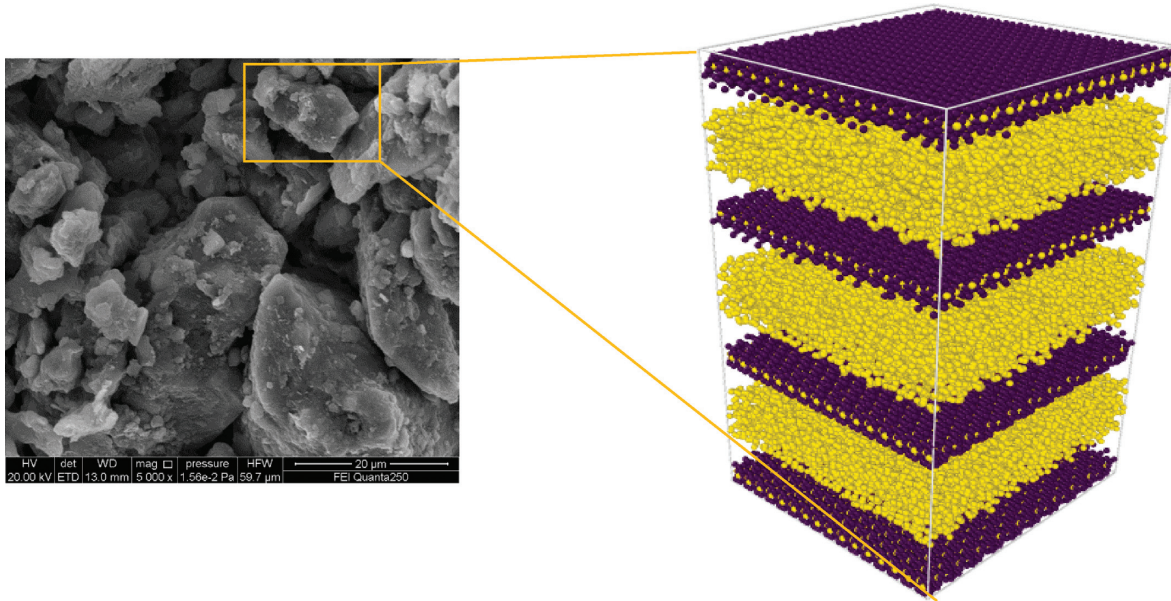


FIGURE 7: Initial model construction intention of soil sample.

part is the water layer. Through uniaxial compression simulation of the model, the stress-strain relationship of the molecular model is obtained, as shown in Figure 8.

3. Construction of the Microscale Simulation Model

The uniaxial compression test can simulate the most unfavorable situation of material failure under the three-dimensional unconstrained condition of the structure, and the deterioration of earthen sites is mostly concentrated on the outer surface of the soil and the quasi-brittle material (concrete damage plasticity) [24, 25]. A HITACHI S-2700 scanning electron microscope was used in this experiment, which is composed of a vacuum electron beam emission, and image generation systems (Figure 9). In this paper, the analysis is based on the numerical model building method already proposed by our group, and the specific model building process is as follows [1].

3.1. Modeling Basis. Similarly to the analysis of the physical and mechanical properties of ordinary buildings, we also need to consider the microperspective in the exploration of the relationship between microstructure and macro-mechanical properties. Figure 3 shows the images of soil particles under the electron microscope, within the field of view magnified by 500 times. It is clear to see the details of the particles, including the irregular cracks on the surface and the shape and size of the particles. At this scale, the particles with a diameter within 5 and 25 μm can be observed, and the corresponding pore distribution and disorderly arrangement of viscous particles is visible by the accumulated materials between particles. At further increased magnification from 1000 to 3000 times, the shape of the particles is clear, but the number of particles is low; at a magnification from 5000 to 10,000 times, the size and shape

of the particles in the microstructure begin to distort, and lose their microscale guiding significance. Therefore, the microscopic modeling of earthen soil is to be based on the electron micrograph images of earthen soil at $\times 500$ magnification.

To avoid the influence of the randomness of the SEM images on the research results, when the SEM images were taken, on the basis of meeting the screening test level, the area of 1 mm \times 1 mm was shot from the left to the right and from the bottom to the top. According to the pixel size area of the photo taken by $\times 500$ magnification lens, the number of electron microscope pictures to be taken is obtained by

$$\frac{1 \times 1}{0.644 \times 0.431} \approx 4 \text{ photos.} \quad (1)$$

The determination and selection of a threshold is essential to image binarization. Owing to the different properties of objects and the diversity of gray changes in various images, it is difficult for traditional binarization methods to achieve ideal processing results. To make the processed image consistent with the structure of the real soil sample, the Image-Pro Plus 6.0 software (IPP, Media Cybernetics, Inc., Silver Spring, MD, USA) was used to process the SEM photos at $500\times$ magnification [14]. To reduce the error caused by the randomness of the calculation results under a single threshold, the area ratio of the black and white colors was determined by adjusting the level of the cutting plane represented by the threshold value, based on the porosity. The best threshold [26] that can truly reflect the microstructure of soil was found.

3.2. Modeling. ABAQUS software was used to construct a rigid plate with a length of 0.644 mm and a two-dimensional geometric model of 0.644 mm \times 0.431 mm. With the pressure equipment in the rigid plate simulation test, and the

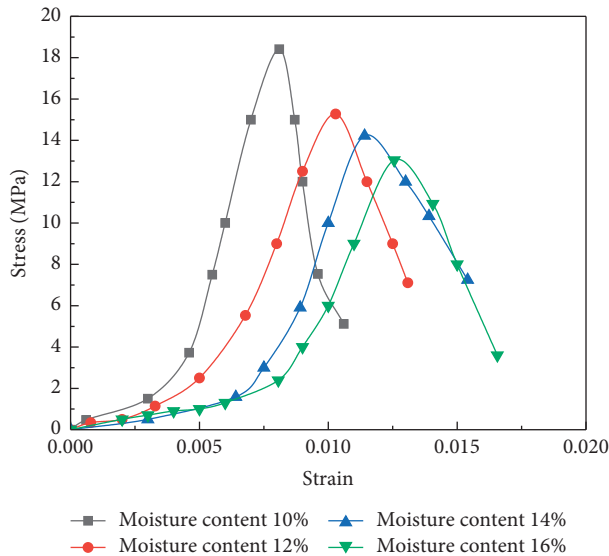


FIGURE 8: Stress-strain curves of molecular dynamics model.

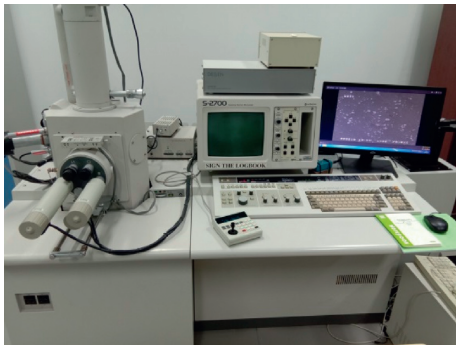


FIGURE 9: HITACHI S-2700 scanning electron microscope.

two-dimensional solid element was selected to provide the section attribute. The plane thickness of the rigid plate was set at 0.020 mm to simulate the uniaxial compression test.

The numerical model was composed of soil particles, pores, and cements. The soil particles were regarded as elastic rigid bodies [27]. The properties of the intraparticle cementation materials were determined by the constitutive model of concrete damage plasticity (CDP). The material parameters of each phase in the numerical simulation model were calibrated according to the specific working conditions (Table 2).

In Table 2, Ψ is the expansion angle; ϵ is the flow potential offset; f_{b0}/f_{c0} is the ratio of biaxial ultimate compressive strength to uniaxial ultimate compressive strength; K is the ratio of the second stress invariant on the tensile meridian plane to that on the compressive meridian plane; and μ is the viscosity coefficient.

In this study, vertical displacements of 0.006, 0.009, and 0.012 mm were applied to the top of the upper platen by the displacement loading method [28]. The friction coefficient was selected to be $\mu = 0.492$ [24]. After the finite-element model was established, the X direction, Y direction, and the rotation angle of the lower boundary of the model were set as

fixed-end constraints. CPE4R was used as the model cell type. The initial value of increment step size was set to 0.001, and the minimum value was $1E-012$. Figure 10 is the electron microscope image of Zhouqiao earthen soil, Figure 11 is the uniaxial compression test model results of soil samples with polygonal pores, and Figure 12 is the uniaxial compression simulation model results of soil samples with circular pores.

4. Simulation Verification and Analysis of the Results of the Uniaxial Compression Test

Figure 13 shows the macro test and simulation results. By comparing the results of the theoretical model and the uniaxial compression numerical model, it is found that the curve obtained by the simulation calculation of the polygonal pore model is slightly higher than the test stress-strain curve. The main reason is that the simulated strength is higher than that of the test because there are microcracks in the real soil sample, and there are no initial cracks in the model. The calculation result is reasonable.

By adding a difference interval of 10 kPa to the indoor test stress-strain curve, it can be found from Figure 13 that the curve simulated by the circular pore model deviates greatly from the indoor test stress-strain curve. The circular pore model has smooth boundary and less constraints between soil samples. With the increase of compressive load, the displacement change is more continuous, which is one of the reasons for the larger peak strain and smaller peak stress. Although there is a deviation between the results of circular pore model and indoor test results, the change law in the early stage of curve development is basically consistent because the elastic modulus of soil sample is consistent. And with the increase of soil moisture content, the coincidence degree of the result curve is also further increasing. When the moisture content is 10%, the peak strain difference is about 0.5%, and the peak stress difference is about 40 kPa; When the moisture content is 16%, the peak strain difference is about 0.2%, and the peak stress difference is about 15 kPa.

Owing to the limited space and the similarity of the work, in this paper, we have analyzed only the results of polygonal pore model 1 and circular pore model 5. Figure 14 represents the simulation results of model 1. Figure 15 represents the simulation results of model 5, the legend “+” in the axial stress diagram is the tensile stress, “-” is the compressive stress, the legend “+” in the displacement diagram is the positive direction of the coordinate axis and “-” is the negative direction of the coordinate axis. As can be seen from Figures 14(a) and 15(a), regular changes occurred in the soil displacement; the overall displacement was altered in a descending order. The bottom displacement was the smallest, whereas the upper displacement was larger. As the bottom boundary of the model was a fixed support constraint, the axial load displacement at the bottom had to be zero. In the process of uniaxial compression, the internal displacement distribution of the test block was not balanced, and the nonuniformity of the displacement increased with the increase of the load. Under the continuous action of the compression displacement, the local displacement would

TABLE 2: Unified hardening model parameters.

Ψ (°)	ϵ	f_{b0}/f_{c0}	K	μ
30	0.1	1.16	0.6667	0.0005

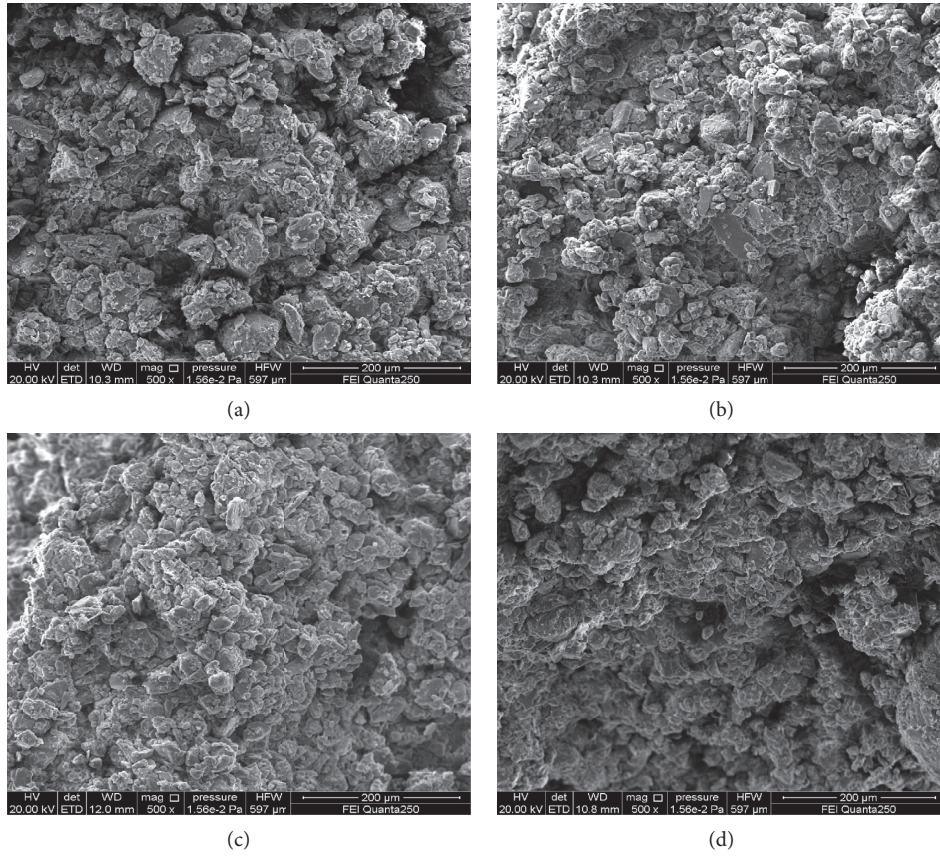


FIGURE 10: SEM image of Zhouqiao earthen soil: (a) SEM image 1, (b) SEM image 2, (c) SEM image 3, and (d) SEM image 4.

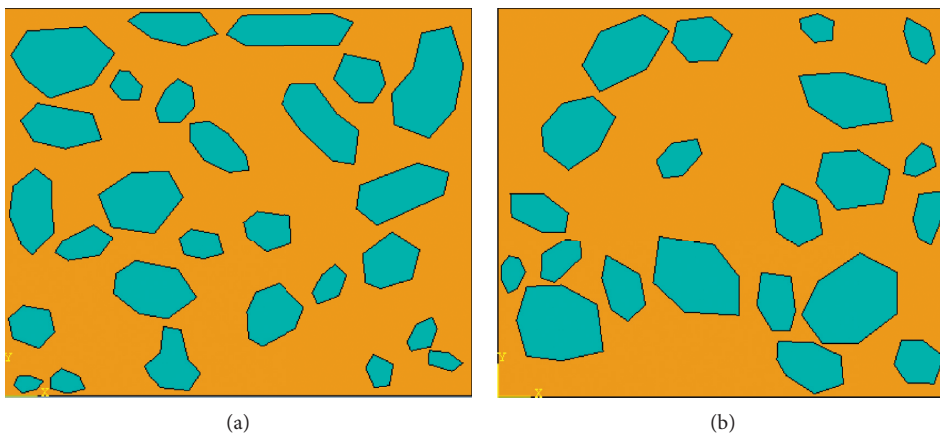


FIGURE 11: Continued.

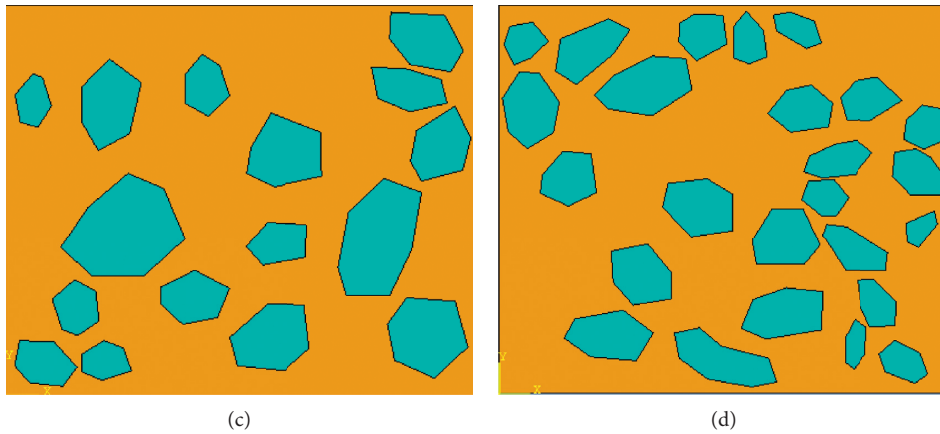


FIGURE 11: Simulation model of the uniaxial compression test with polygonal pores: (a) simulation model 1, (b) simulation model 2, (c) simulation model 3, and (d) simulation model 4.

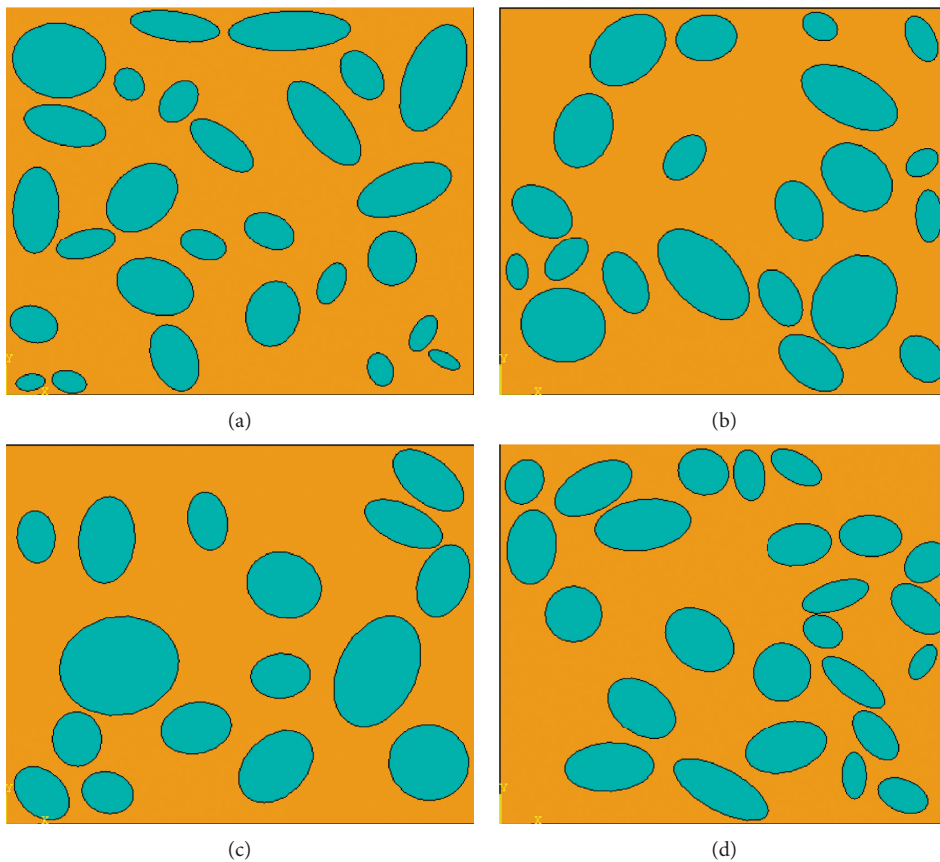


FIGURE 12: Simulation model of the uniaxial compression test with circular pores: (a) simulation model 5, (b) simulation model 6, (c) simulation model 7, and (d) simulation model 8.

change suddenly. The pore boundary of the circular pore model is smooth, the constraints between soil samples are less, and the displacement change is relatively continuous. Compared with the rubbing between soil samples and irregular particles in the polygonal pore model, the displacement change is affected by the irregular boundary, and the change is uneven. The vertical compression displacement

of the circular pore model reaches $11.44e-03$ mm, The displacement of polygonal pore model under vertical compression is $14.606e-02$ mm, which is 1.28 times more than that of circular pore model. Through the analysis of Figures 14(b) and 15(b), it is found that the displacement of the left and right boundaries of the polygonal pore model is $3.392e-02$ mm, while the displacement of the left and right

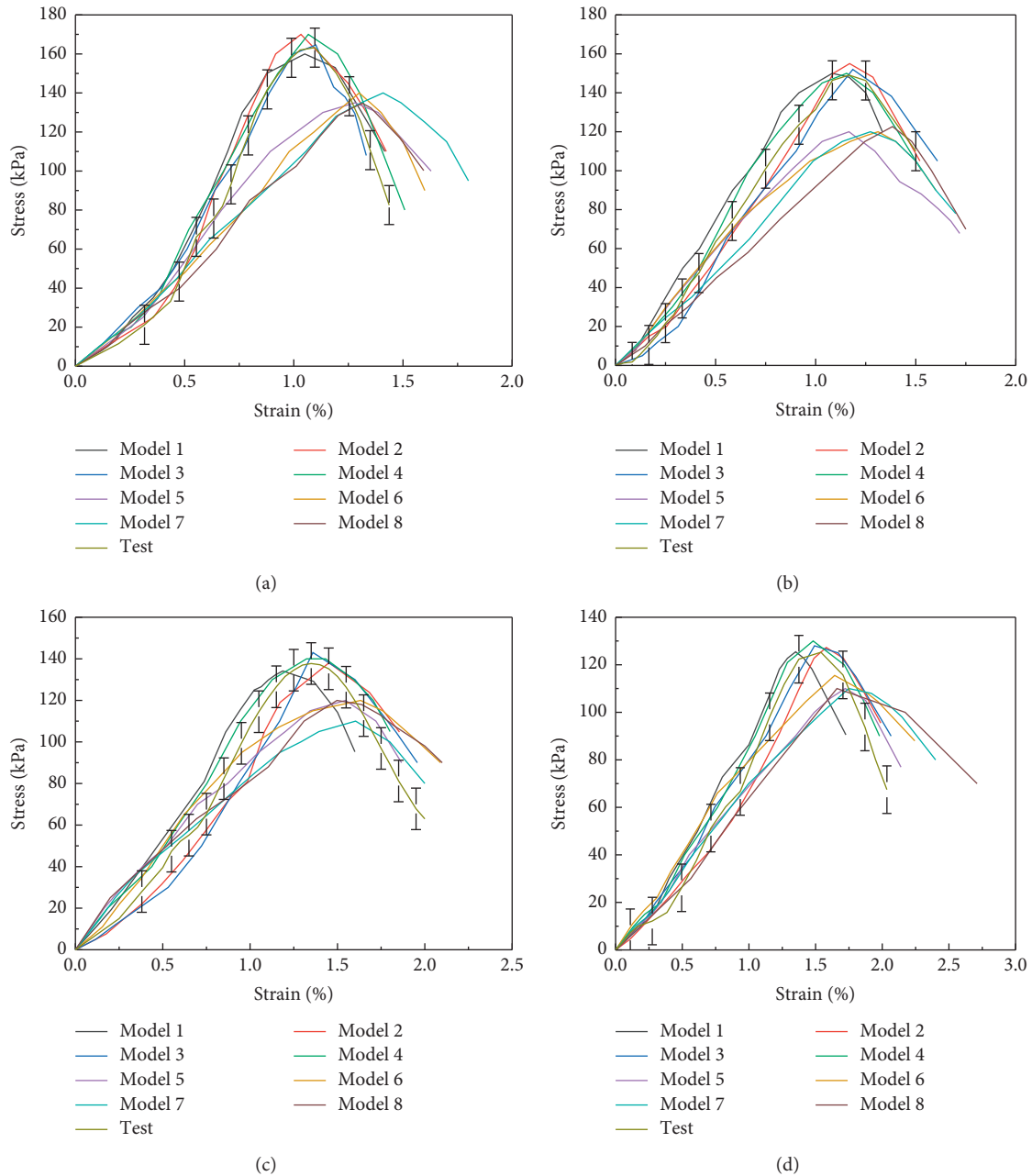


FIGURE 13: Stress-strain curves of macroscopic test and simulation: (a) moisture content 10%, (b) moisture content 12%, (c) moisture content 14%, and (d) moisture content 16%.

boundaries of the circular pore model is $4.266e-02$ mm, which is 1.26 times more than that of the left and right boundaries of the polygonal pore model. With the increase of compressive load, the polygonal pore model is prone to stress concentration around the pores due to the irregular pore boundary. The maximum stress of the model is $3.027e-02$ kPa, while the maximum stress of the circular pore model is $1.867e-02$ kPa. Finally, the macroscopic response in Figure 13 is that the stress-strain curves of the circular pore model are smaller than those of the polygonal pore model.

Based on the results of the analysis of Figures 14(d) and 15(d), it can be concluded that the damage of the specimen begins to initiate and started at both ends of the bottom of the specimen. At this time, the internal cohesion of the soil facilitated the recovery from the deformation of the specimen recover, and there is, with no cracks on its surface of the specimen. With the increase of the compression load, a small number of microcracks appeared in the soil matrix, resulting in irrecoverable deformation. With the further expansion and aggregation of damage microcracks, the microcracks do not develop in a single way, but propagate microcrack

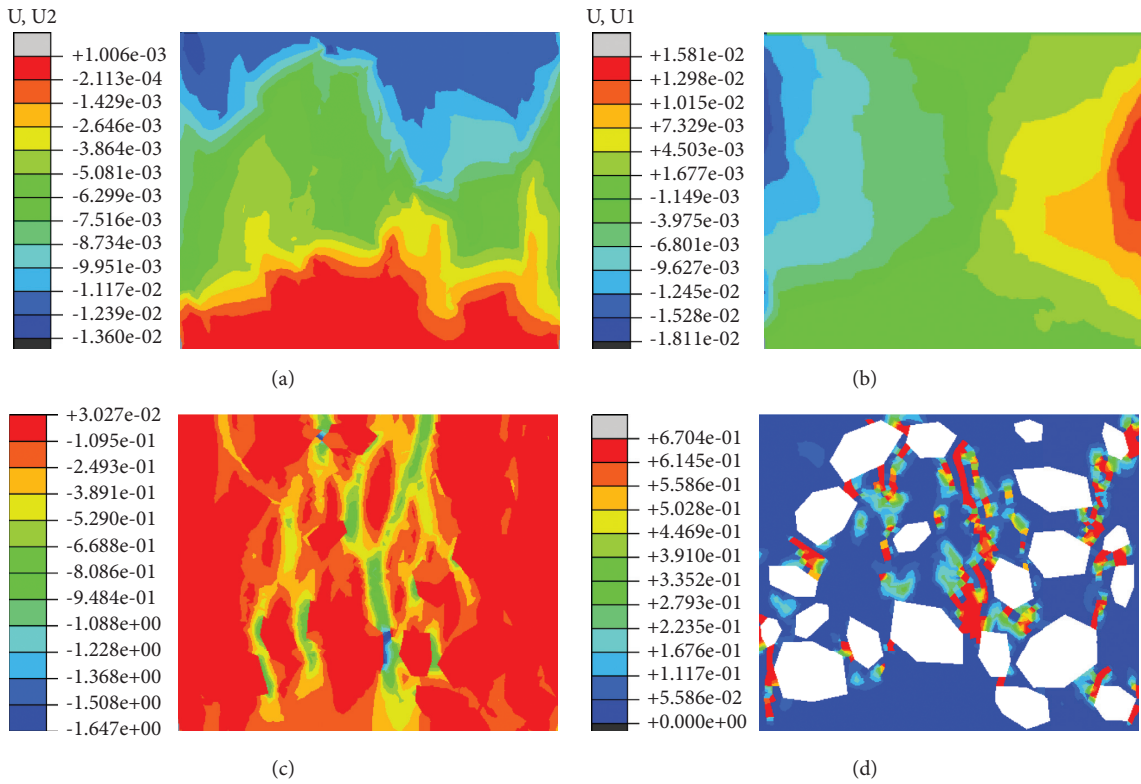


FIGURE 14: Model 1 simulation results: (a) displacement diagram in U2 direction, (b) displacement diagram in U1 direction, (c) axial stress diagram, and (d) damage diagram.

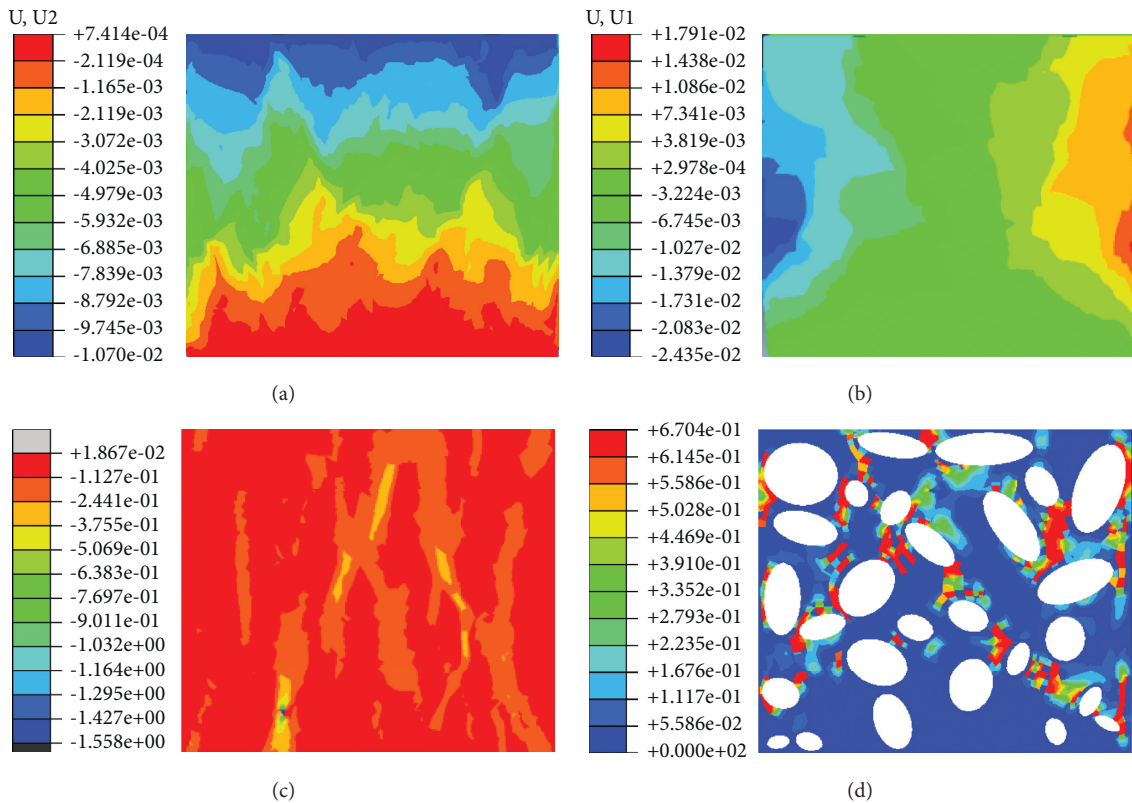


FIGURE 15: Model 5 simulation results: (a) displacement diagram in U2 direction, (b) displacement diagram in U1 direction, (c) axial stress diagram, and (d) damage diagram.

damages, they were simultaneously propagated along the whole section of the soil particle edge at the same time. Moreover, the damaged part of the circular pore model mostly appears between the pores, while the damaged part of the polygonal pore model not only exists between the pores but also extends to the interior of the soil sample.

5. Conclusion

The nanostructure model of site soil composed of many atoms was established by molecular dynamics method. The stress-strain relationship of different moisture content was obtained by uniaxial compression simulation. Based on the 500-fold magnified electron micrograph image and the image reconstruction method, we constructed a micromodel composed of particles, cements, and pores. The stress-strain relationship of different moisture contents of earthen soil was obtained by the displacement loading method, and the results were compared with those of the macro test. The mechanical microproperties of the cemented particles were analyzed. The aim of this study was to establish an effective method for the assessment of the safety and surface deterioration of earthen sites, which would provide a basis for follow-up research on the deterioration of earthen sites. Considering the obtained results, we can conclude that our work has met the needs and purposes of the scientific project, and a foundation has been laid for next step analysis of the deterioration effect of the environment on earthen sites and their safety evaluation. The following main conclusions have been drawn:

- (1) Based on molecular dynamics simulation method, a nano structure model of Zhouqiao earthen soil composed of Si, O, Al, H, and Li atoms is established, in which water and soil are distributed in layers. By analyzing the mechanical properties of Zhouqiao earthen soil, the stress-strain relationship of site granular materials with different moisture content at nanoscale is obtained.
- (2) According to the cementation characteristics of the earthen soil, it was divided into a three-phase structure composed of soil particles and pores. The shape, size, and distribution of particles were determined by SEM image reconstruction, and a micro-finite-element model reflecting real soil properties was established.
- (3) Through uniaxial compression tests of the micro-finite-element model, we found that the displacement of the left and right boundaries of the circular pore model is 1.26 times more than that of the polygonal pore model, and the displacement of the polygonal pore model in vertical compression is 1.28 times more than that of the circular pore model. The simulated curve of the polygonal pore model is consistent with the test stress-strain curve, which can better reflect the change of the microstructure of the soil sample under load. There is a deviation between the results of the circular pore model and the indoor test results, but comparing the simulation results of

different water content, it is found that the coincidence degree of the result curve is further increasing with the increase of the water content of the soil sample.

- (4) By comparison, we found that the results of the numerical analysis were in good agreement with the results of the macrotest stress-strain curves, which indicates that the research ideas and methods in this work are feasible. We have also established a new method for difficult indoor sampling.

Data Availability

All data generated or analyzed in this study are included in this article.

Conflicts of Interest

The authors declare no conflicts of interest.

Acknowledgments

This work was supported by the National Natural Science Foundation of China (grant no. 51978634), Henan University's First-Class Discipline Cultivation Project (Science and Technology) (grant no. 2019 YLZDCG05), and Henan Province Science and Technology Development Plan Project (grant no. 212300410012).

References

- [1] J. Yue, X. Huang, L. Zhao, and Z. Wang, "Study on the factors affecting cracking of earthen soil under dry shrinkage and freeze-thaw conditions," *Scientific Reports*, vol. 12, no. 1, p. 1816, 2022.
- [2] Z. Zhao and Z. Sun, "Ring shear mechanical properties and numerical simulation of sand," *Chinese Journal of Underground Space and Engineering*, vol. 13, no. S1, pp. 70–74, 2017.
- [3] L. Liu, L. Zhao, Y. Chen, and J. Gao, "Research progress of molecular simulation of diffusion in zeolites," *Chemical Industry and Engineering Progress*, vol. 30, no. 7, pp. 1406–1415, 2011.
- [4] D. Song, J. W. Yue, J. B. Yuan et al., "Study of soil mechanical characteristics of ruins in northwest Henan Province," *Journal of Experimental Mechanics*, vol. 34, no. 1, pp. 121–130, 2019.
- [5] J. W. Yue, G. H. Yang, S. Y. Wang, Y. F. Wang, and Y. F. Zhang, "Cusp catastrophe model for slope failure based on elastic slip mass," *Journal of Henan University*, vol. 49, no. 3, pp. 354–361, 2019.
- [6] C.-S. Tang, Y.-J. Cui, B. Shi, A.-M. Tang, and N. An, "Effect of wetting-drying cycles on soil desiccation cracking behaviour," *Web of Conferences*, vol. 9, Article ID 12003, 2016.
- [7] C. Wang, Z. Y. Zhang, Y. Liu, and S. M. Fan, "Geometric and fractal analysis of dynamic cracking patterns subjected to wetting-drying cycles," *Soil and Tillage Research*, vol. 170, pp. 1–13, 2017.
- [8] J. Yue, X. Huang, L. Zhao, Q. Kong, Y. Chen, and Z. Wang, "Finite element method study on stress-strain relationship of site soil," *Mechanics in Engineering*, vol. 43, no. 6, pp. 921–932, 2021.
- [9] M. Huang, Y. Yao, Z. Yin, and E. Liu, "An overview on elementary mechanical behaviors, constitutive modeling and

- failure criterion of soils,” *China Civil Engineering Journal*, vol. 49, no. 7, pp. 9–35, 2016.
- [10] Z. J. Shen, “Elastic-plastic damage model of structural clay,” *Chinese Journal of Geotechnical Engineering*, vol. 33, no. 4, pp. 637–642, 1993.
- [11] Z. J. Shen, “Nonlinear damage mechanical model of structural clay,” *Hydro-Science and Engineering*, vol. 57, no. 3, pp. 247–255, 1993.
- [12] L. F. Kuang, G. Q. Zhou, X. Y. Shang, and X. D. ZHAO, “Molecular dynamic simulation of interlayer water structure in sodium montmorillonite,” *Journal of China Coal Society*, vol. 38, no. 3, pp. 418–423, 2013.
- [13] W. Yang, R. Chen, and X. Kang, “Application of molecular dynamics simulation method in micro-properties of clay minerals,” *Chinese Journal of Geotechnical Engineering*, vol. 41, no. S1, pp. 181–184, 2019.
- [14] Y. Liu, X. Yang, L. Luo, Z. Li, S. Liang, and H. Fang, “Experimental research on relationship between triaxial shear properties and microstructure of saturated soft soil,” *China Journal of Highway and Transport*, vol. 32, no. 7, pp. 15–22, 2019.
- [15] L. Tang, S. Cong, X. Ling, W. Xing, and Z. Nie, “A unified formulation of stress-strain relations considering micro-damage for expansive soils exposed to freeze-thaw cycles,” *Cold Regions Science and Technology*, vol. 153, pp. 164–171, 2018.
- [16] Y. M. Chen, P. C. Ma, and Y. Tang, “Constitutive models and hypergravity physical simulation of soils,” *Chinese Journal of Theoretical and Applied Mechanics*, vol. 52, no. 4, pp. 901–915, 2020.
- [17] H. Zhao, S. Jiang, Y. Ge, and C. Liu, “Molecular dynamics simulation of water molecules adsorption by different cations based montmorillonite,” *SCIENTIA SINICA Technologica*, vol. 49, no. 6, pp. 703–715, 2019.
- [18] T. Hu, D. Liu, and J. Chang, “Experimental study on strain rate effect of strength characteristics of unsaturated silty clay,” *Case Studies in Construction Materials*, vol. 12, Article ID e00332, 2020.
- [19] S. Zike, B. F. Sørensen, and L. P. Mikkelsen, “Experimental determination of the micro-scale strength and stress-strain relation of an epoxy resin,” *Materials & Design*, vol. 98, pp. 47–60, 2016.
- [20] J. Zhang, J.-H. Chen, and C. Edwards, “Lab NMR study on adsorption/condensation of hydrocarbon in smectite clay,” *The Day*, vol. 4, no. 4, pp. 315–339, 2012.
- [21] J. Li, Z. Chen, X. Li et al., “A quantitative research of water distribution characteristics inside shale and clay nanopores,” *SCIENTIA SINICA Technologica*, vol. 48, no. 11, pp. 1219–1233, 2018.
- [22] D. L. Bish, “Rietveld refinement of non-hydrogen atomic positions in kaolinite,” *Clays and Clay Minerals*, vol. 37, no. 4, pp. 289–296, 1989.
- [23] D. Hou, Y. U. Jiao, J. Zhang et al., “Insights on hydrolysis weakening of calcium silicate hydrate: a ReaxFF molecular dynamics study,” *Journal of Hydraulic Engineering*, vol. 52, no. 1, pp. 34–41, 2021.
- [24] H. F. Xu, H. J. Wu, S. P. Guo, and T. P. Liao, “Study on the parameters of pile soil contact surface element,” *Exploration Engineering (rock and Soil Drilling and Tunneling)*, vol. 29, no. 5, pp. 10–12, 2002.
- [25] Y. Zhang, C. Y. Liu, Y. Y. Wang, and H. Yin, “Mesoscale modeling based numerical study on size effect of concrete compressive strength,” *Journal of Building Structures*, vol. 38, no. S1, pp. 493–501, 2017.
- [26] H. P. Feng, D. L. Ma, Q. Y. Liu, and C. L. YE, “Method for calculating three dimensional apparent porosity of soils based on SEM images,” *Chinese Journal of Geotechnical Engineering*, vol. 41, no. 3, pp. 574–580, 2019.
- [27] M. J. Jiang, C. H. Li, W. Liu, A. Zhang, and X. W. Zhang, “Extension and compression tests mechanical behaviors of bonded granules with different bond widths,” *Chinese Journal of Geotechnical Engineering*, vol. 40, no. S2, pp. 12–16, 2018.
- [28] M. Li and H. N. Li, “Investigation into dynamic properties of damaged plasticity model for concrete in ABAQUS,” *Journal of Disaster Prevention and Mitigation Engineering*, vol. 31, no. 3, pp. 299–303, 2011.

Research Article

Hysteresis Behavior and Design of the New Autoclaved Lightweight Concrete (ALC) External Panel Connector with the Steel Frame

Kewei Ding ¹, Chikun Zhang ^{1,2}, Shulin He ¹ and Yunlin Liu ¹

¹College of Civil Engineering, Anhui Jianzhu University, Hefei, Anhui 230601, China

²Architecture and Civil Engineering, City University of Hong Kong, Kowloon Tong 999077, Hong Kong

Correspondence should be addressed to Kewei Ding; dingkw@ahjzu.edu.cn

Received 18 November 2021; Revised 22 January 2022; Accepted 25 January 2022; Published 22 February 2022

Academic Editor: Rotana Hay

Copyright © 2022 Kewei Ding et al. This is an open access article distributed under the Creative Commons Attribution License, which permits unrestricted use, distribution, and reproduction in any medium, provided the original work is properly cited.

This paper proposes a new flexible connector for the autoclaved lightweight concrete (ALC) panel with the steel beam. It is a universal upper and lower crossing connector, with load-bearing and limitation holes; then, the seismic capacity of this connector is investigated in the simulations and full-scale tests. Firstly, the finite element simulations of the new connector and traditional connector (L-hooked bolt) were made by ABAQUS, which proved the reliability of the new connector by comparing them in low-cyclic loading. Secondly, in order to analyze the phenomenon and data of the two connectors which are in the same test conditions of simulation, the full-scale tests of the steel frame were conducted. The damage of the ALC panel at different connectors and at different test load displacements is described in detail. The contribution of the connectors to the steel frame and the ALC panel is investigated in depth during the elastic, elastoplastic, and plastic stages of the steel frames. The test result is similar to the simulation result roughly, in which the new connector has better seismic capability. In minor earthquakes, the ALC panel frame with the new connector has better synergistic capacity of panels, while in large earthquakes, it can provide certain stiffness to the structure. Compared with the L-hooked bolt, the maximum bearing capacity of the structure with the new connector increases by 5.2%, and the yield displacement delays by 27.5%, which results in the increase of ductility by 9.8%. In terms of energy consumption capacity, the equivalent damping factor of the new connector increases by 10.2% and 35.3% at the yield and ultimate state, respectively. The FEM simulation results can represent the actual test results well. To summarize, the new ALC panel connector in this paper has excellent seismic capacity and good synergistic, which can provide a reference for the development and application of new types of the ALC connector.

1. Introduction

Along with rising housing demand as a result of growing urbanization, prefabricated building is thought to be a cost-effective and environment-friendly way to address this problem [1–3]. Steel structure is currently one of the main choices for the development of prefabricated buildings, and the enclosure system is a critical component of the prefabricated structure, and its capabilities have a direct impact on the building's overall capacity [4]. In prefabricated steel structures, autoclaved lightweight concrete (ALC) has been proposed for application in building enclosure systems. ALC allows for a reasonable reduction in enclosure weight due to

the prefabricated system's light self-weight, as well as an increase in assembly and transportation efficiency [5]. ALC panel is a new type of panel that merges lightweight panel technology and concrete block technology, which is formed by high temperature, high pressure, and steam curing using a specific technique [6]. In nonstructural applications, although the recycled aggregate concrete (RAC) has better compressive strength [7], the ALC meets specifications and has higher productivity [8]. In comparison to typical solid clay bricks and hollow clay bricks, ALC panels have a low gravity and resistance of fire and seepage, which provide superior construction physical capacity. Although double-skin façade (DSF) and AAC block panels can have these

advantages better, they are not as easy to construct as ALC panels [9–11]. Currently, research on ALC panels is mostly focused on the improvement of the stiffness, seismic resistance, and energy consumption of the whole building structure [12]. In terms of simulation, Qu et al. [13] conducted structural testing and numerical modeling on four ALC panels, and the test panel was simulated using finite element software. By using numerical modeling, Matteis and Landolfo [14] researched the seismic reaction and assessed the hysteretic capacity and energy dissipation capacity of a steel frame structure wrapped in the light wall panel. In terms of test, Yang et al. [15] investigated the hysteresis capacity of the hinged steel frames with embedded ALC panels and found that the hysteresis capacity of the panels connected by the tube connector is better than the U-connector, although both of them have good synergistic capacity. Wang et al. [16] studied repeated low-cycle loading tests on ALC panels and block-filled CFST frame structures in order to determine the effect of U-shaped steel clips, L-hooked bolts, swinging connectors, and angle steel on the seismic capacity of panels. For determining the displacement ductility of ALC panels, Zhang et al. [17] conducted four-point loading experiments on six ALC external panels and three roof panels. Gou et al. [18] expounded the construction process, installation and operation points, material and equipment input, the quality control, and other aspects of the ALC panel, according to engineering examples on-site. Among the prefabricated ALC panel building structures, cladding and embedding are the most common connectors between prefabricated external wall panels and the main structure [19]. Not only should the structure be securely connected when the panel and frame cladding connector are used but the deformation of the two components should also be coordinated under a variety of impacts [20]. If the connector is damaged during an earthquake, the panel would collapse which means it would cause secondary accidents [21]. There are few studies on the connector of cladding panels in China, and the most commonly used connector is the L-hooked bolt on-site. Although the L-hooked bolt has a high bearing capacity when the structure is in obvious displacement, it would crack especially in mortar joints just under slight seismic load, which would make the whole structure of heat insulation and thermal insulation drop drastically [22, 23].

Based on these achievements, a NALC connector, which requires secondary special cement pouring, was invented and used in its own research of NALC panel by Nanjing Xujian Company [24]. This type of connector could increase the time of wet work and reduce the efficiency of assembly work because it needs to be poured twice on-site. In order to improve the external ALC panel connector, Cao et al. [25] developed an embedded ALC connector that consists of embedded components, stiffening plate, and steel angle. Although the embedded connector partially solves for the L-hooked bolt connector problem, its construction is complicated and expensive. ALC panels require high-temperature and high-pressure manufacturing, which can deflect or deform the preburied parts so that they could not set up on-site. In addition, transportation may also cause

damage to the embedded ALC panels [26, 27]. Bai proposed a flexible ALC panel connector, while the connector is much complicated because it is divided into different shapes of above and below [28].

To solve these problems, a new connector was proposed based on previous works, named crossing ALC panel connector. Instead of being hooked by a traditional L-hooked bolt, the ALC panel is supported from the bottom by a new connector. Additionally, the limitation hole is designed to resisting seismic loads which can achieve a flexible connector of panels, steel beams, and columns. The limitation hole can also increase the part of freedom during installation. This connector has the following advantages: beyond wet work, simple design, quick assembling, and great seismic capacity. To ensure the connector's reliability, the simulations and low-cyclic reversed load tests were taken by using ABAQUS and full-scale steel of low-cyclic reversed load, respectively. According to the investigation, the new crossing connector offers a comprehensive range of functions, which could replace the traditional L-hooked bolt for steel constructions.

The remainder of this paper is organized as follows: in Section 2, the design details of the new connector, the conditions for building the finite element model, and the simulation results are presented. Section 3 introduces the test details including the assembling process, material properties' test, test device, and loading system. Section 4 provides the test results including the detailed phenomenon and the hysteresis curves of each specimen. As for Section 5, the seismic capacity of the new connector and traditional L-hooked bolt is analyzed in depth. Finally, Section 6 summarizes and concludes the content of the full work.

2. Design and Simulation

2.1. Connector Design. When the building structure undergoes a significant lateral shift, the damage of the ALC panel can be decreased proportionally to its sway caused by the connector. As a result, a new connector was designed to interconnect the ALC panel and steel frame, named the crossing ALC panel connector. The new integral structural system can be coordinated well in response to resisting or dissipating external forces by connector deformation (internal displacement of bolts) and maintain the stability and integrity of the whole wall system. It can ensure that the whole wall does not crack under high-frequency low-level earthquakes (small interstory displacement deformation). It can also provide certain stiffness to the structure in the large earthquake. This can also increase the part of freedom during assembling and can avoid some problems that cannot be set up due to inconsistent accuracy and transportation collisions. This connector with good aseismic behavior can easily achieve the antiseismic design principles, named "strong joint-weak member." [29]

The new crossing ALC panel connector is a cross-shaped connector composed of load-bearing and restriction holes. It consists of the following components: I-beam, ALC panel, cross-shaped connector, bolt, and nut. To facilitate installation, a slotted hole is opened in the upper part of the

connector to serve the lower load-bearing node for the upper exterior wall panel, bearing the vertical, outward horizontal, and inward horizontal loads of the upper exterior wall panel; a long circular hole is opened in the lower part of the connector in the horizontal direction (limitation hole), with a hole diameter slightly larger than the diameter of the bolt; the type of upper bolt hole is long circle. Both upper and lower connectors can bear the weight and limit the slip, but the lower node completely limits the slip in the horizontal direction. It is possible for the panel and the central structure to generate followership. The ALC panel connector is shown in Figure 1.

2.2. Finite Element Analysis Models. ABAQUS finite element analysis software was used to analyze the capacity of the new connector by comparing with the traditional L-hooked bolt [30]. The length of the L-hooked bolt was 200 mm, and the specification was M12. Q235 and Q345 grade hot-rolled H-beams were selected. The steel beam length was 3800 mm, and its size was HM 244 mm × 175 mm × 7 mm × 11 mm. Steel column height was 3888 mm; its size was HW 200 mm × 200 mm × 8 mm × 12 mm. The dimensions of the ALC panel were 3000 mm × 600 mm × 200 mm. Two models are exhibited in Figure 2 consisting of five ALC panels with five sets of traditional L-hooked bolt and new panel connector, respectively.

The ALC, connector, and steel beam used C3D8R hexahedral linear reduction integral solid elements, and the reinforcement used T3D2 linear truss elements [31, 32]. The grids at the connectors and hole of the ALC panel were refined, while the rest of the grids were sparse. The ALC panel was made of ALC and reinforcement which used the plastic damage model. The connector used Q345B, and the steel beam and column used Q235B [33]. A3.5B05 standard was chosen for the ALC panel. An elastoplastic constitutive model of ALC panel was used according to previous studies [34, 35], shown in Figure 3.

All welding processes were replaced by the “Tie” constraint (between beams and columns, between connectors and beams, etc.). By considering the relationship between reinforcement and concrete, the embed command (built-in command) was used to embed the reinforcement directly into ALC panels [36]. Because ALC is only about 1/8–1/10 of the strength of ordinary concrete, it is easy to crush and make the friction effect smaller. Therefore, the principle that the maximum static friction coefficient and sliding friction coefficient are approximately equal is adopted. To simulate real contact, the method of defining friction coefficients by tangential characteristics is used. The contact surfaces between the connectors, bolt, and panel were set to hard contact. The friction coefficient μ_1 between the connector and ALC panel is taken as 0.2, and the friction coefficient μ_2 between the panel and panel of ALC is taken as 0.3 [37].

The coupling point was constrained and loaded in accordance with the boundary conditions of some research studies, which included displacement constraints in the x - and z -directions ($u_y = u_z = 0$) and rotation constraints in the x - and z -directions ($x = y = z = 0$) on the top of the column, as well as rotation constraints in the x - and

z -directions ($x = y = z = 0$) on the bottom of the column. In addition to the displacement restriction at the bottom of the column ($u_x = u_y = u_z = 0$), it was a rotation constraint in the x - and z -directions ($x = y = z = 0$). The pretightening force for the 10 connector bolts was determined by 1 kN bolt pretension force. A vertical axial compressive force was imposed at the opposite side of the contact surface between the steel column and beam. This force was cyclic load which was applied at the coupling point, shown in Figure 4. The load was controlled by the displacement angle, where the maximum displacement was 130 mm. Three turns were loaded at each stage before 30 mm, and two turns were loaded at each stage afterwards (since 40 mm stage) [38].

2.3. Result of the Finite Element Simulation. According to the simulation results, it can be seen that the two connectors have a similar trend under displacement loading (± 135 mm maximum), both experiencing elastic and yielding stages. From force-displacement hysteric curves (Figure 5(a)), the hysteresis loop of the new connector (FEM2) covered the hysteresis loop of the L-hooked bolt (FEM1), indicating that the energy dissipation capacity of new connectors was better. Meanwhile, the new connector (169.95 kN) has the better load capacity than the L-hooked bolt (189.33 kN) according to the skeleton curves (Figure 5(b)) which increases by 11.4% averagely. To further confirm the function of the new connector, full-sized tests are necessary.

3. Details of Test Research

3.1. Test Design. Full-sized steel frames were used for the low-cyclic reversed load test. According to the standard of residential building height, column span, beam, and column section size, the final design is a single span flat steel frame which is 3888 mm storey height and 3800 mm storey width, which was the same as the size and material of finite element analysis models in Section 2. The wall was made of 5 external ALC panels, and the seams of the panels were made of ALC panels' special patchwork binder. All specimens are prefabricated at the factory according to dimensional requirements. In this test, there are two sets of specimens to connect the panel and the main frame, respectively, and specimens are shown in Figure 6.

After all the specimens were produced and maintained, they were delivered and assembled on the test site. The setup process and overview of test specimens are shown in Figures 7 and 8.

3.2. Test Facility and Setup. The test utilizes an American MTS servo loading system with a 500 mm actuator displacement stroke. A quasi-static loading strategy was used in this test: a horizontal low-cycle reciprocating load was given to the column's top panel, and the column's top panel was coupled to the hydraulic servo actuator. Figure 9 illustrates the test facility.

As shown in Figure 10, the test loading device includes an electrohydraulic servo loading system, hydraulic jack, hydraulic actuator, connecting rod, anchor bolt, and

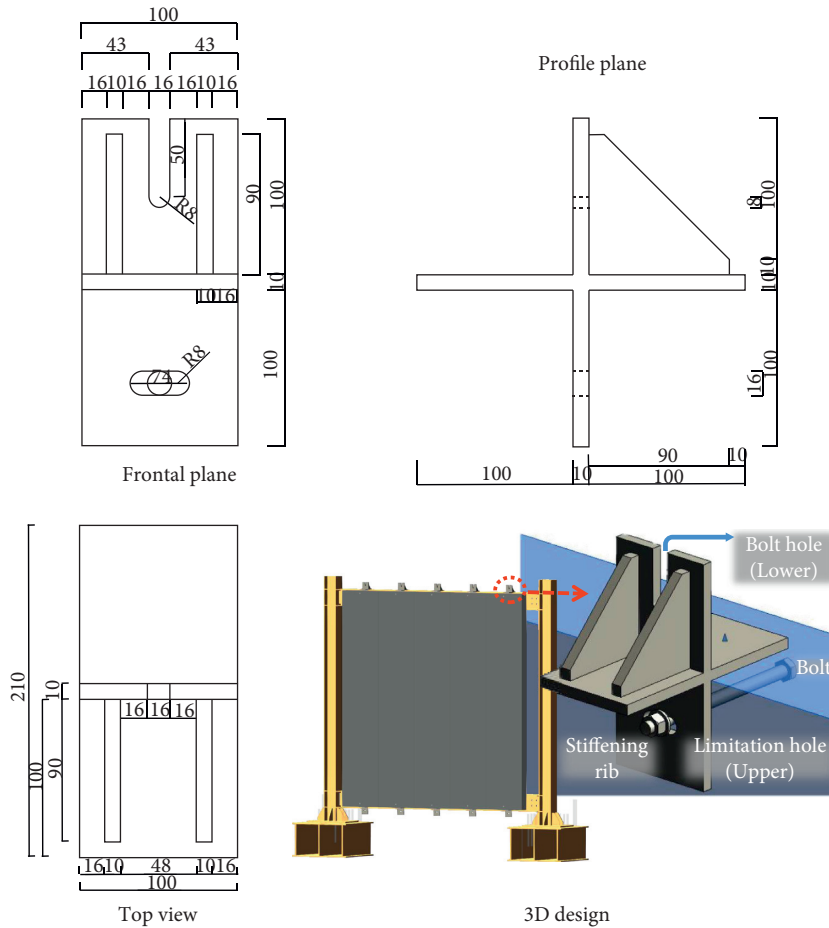


FIGURE 1: Geometric dimension of the new connector.

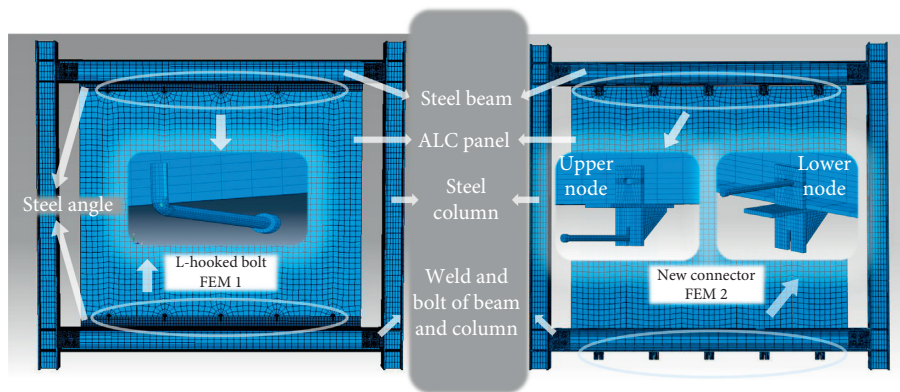


FIGURE 2: Finite element analysis models.

reaction frame. The electrohydraulic servo loading system is attached to the actuator for the loading test.

3.3. Material Properties. Six ALC cube test blocks measured $100\text{ mm} \times 100\text{ mm} \times 100\text{ mm}$ and three ALC rectangular test blocks measured $100\text{ mm} \times 100\text{ mm} \times 300\text{ mm}$ [39] were poured under the same conditions as stated in Figure 11. Steel coupons were cut from steel tubes and sheets and tested for tensile strength, modulus of elasticity, and breaking

elongation by using the universal testing machine, as shown in Figure 12. The result of steel material tests is summarized in Table 1, and the mechanical ALC panel is shown in Table 2, which shows few differences of material properties of the test and simulation.

3.4. Loading System of the Test. The loading protocol for the tests is FEMA 461 [40], in which the displacement-controlled method was employed for 0.5 mm/s low rate loading.

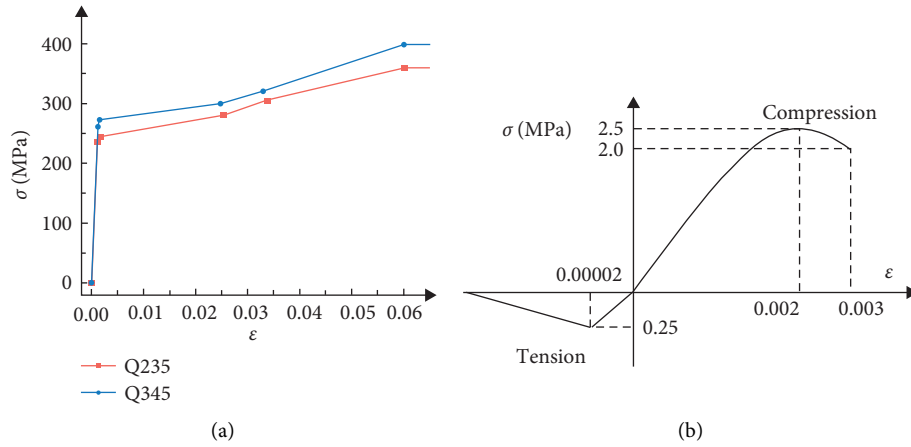


FIGURE 3: Stress-strain curves of the materials. (a) Constitutive curve of steel. (b) Constitutive curve of the ALC panel.

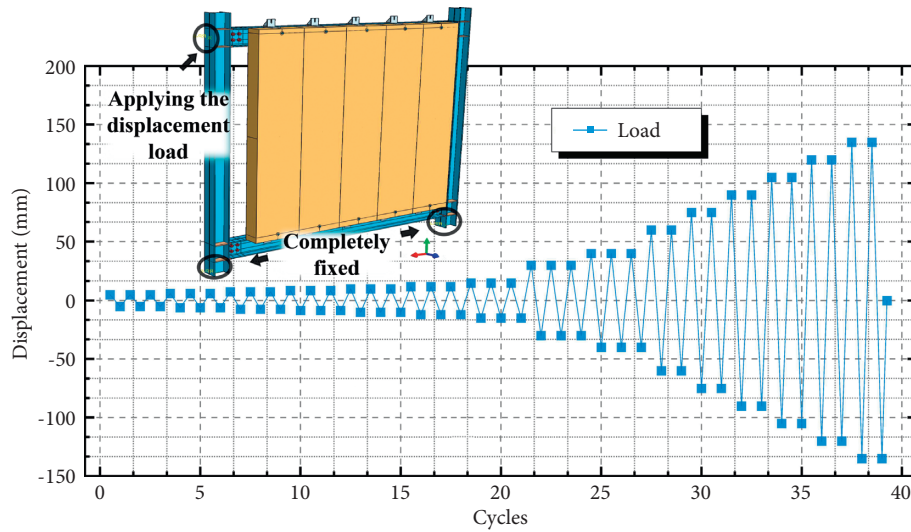


FIGURE 4: Boundary and loading system.

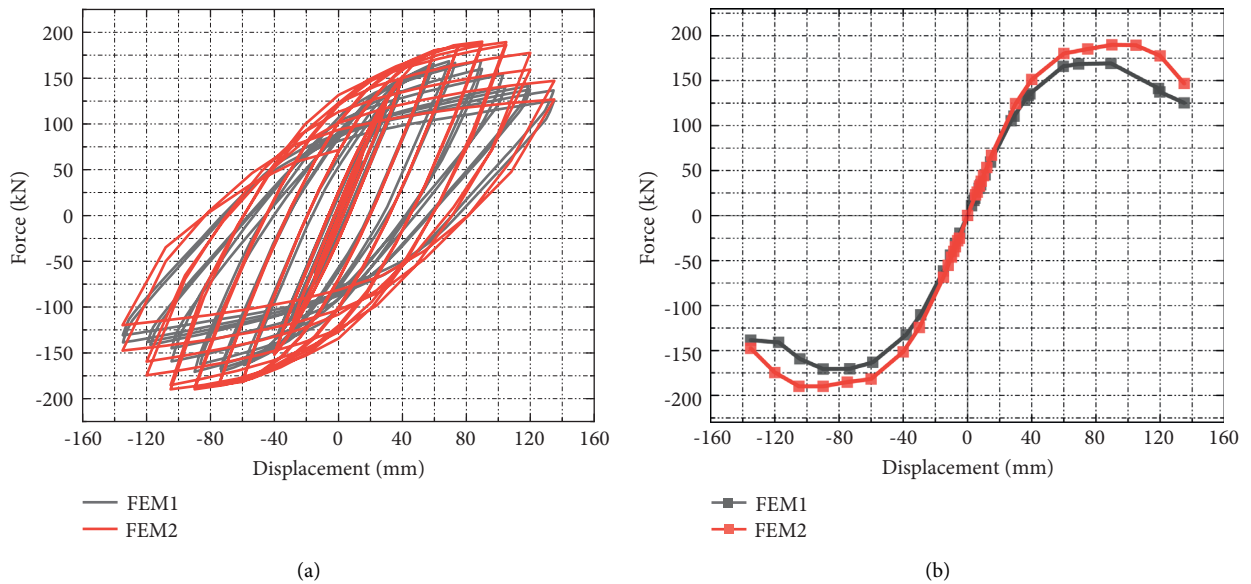


FIGURE 5: Simulated comparison. (a) Load (force)-displacement hysteric curves. (b) Skeleton curves.



FIGURE 6: Test specimens. (a) L-hooked bolt (FW1). (b) Crossing ALC panel connector (FW2).

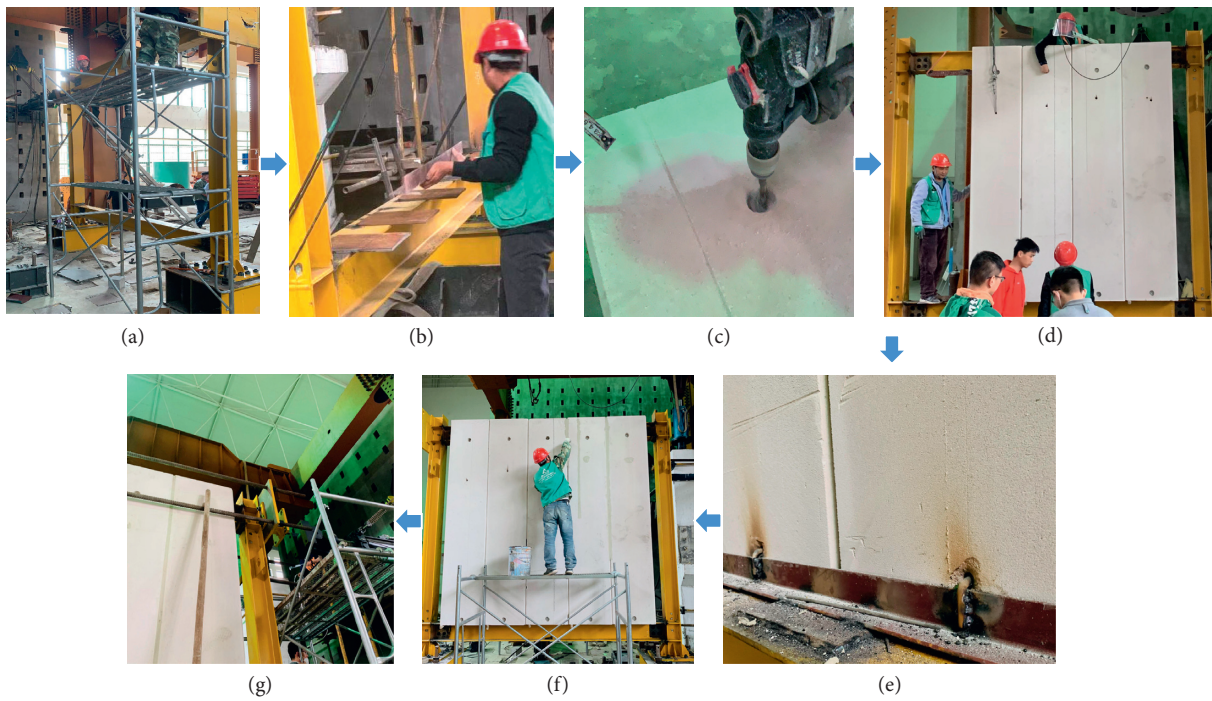


FIGURE 7: Assembling process. (a) Construction of the steel frame. (b) Welding steel angle on the beam. (c) Hole drilling on the ALC panel. (d) Panels were assembled orderly. (e) Bolts were connected to the connectors. (f) Filling special patchwork binder. (g) MTS device was connected to the column.

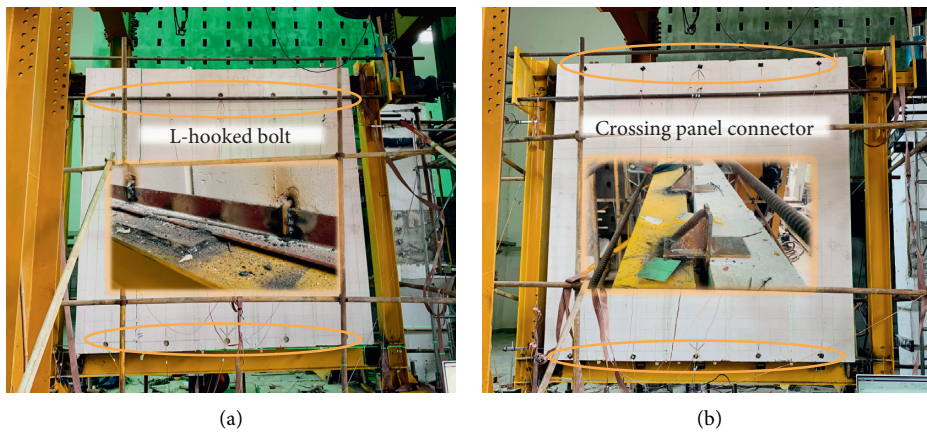


FIGURE 8: Overview of the test specimens. (a) FW1. (b) FW2.

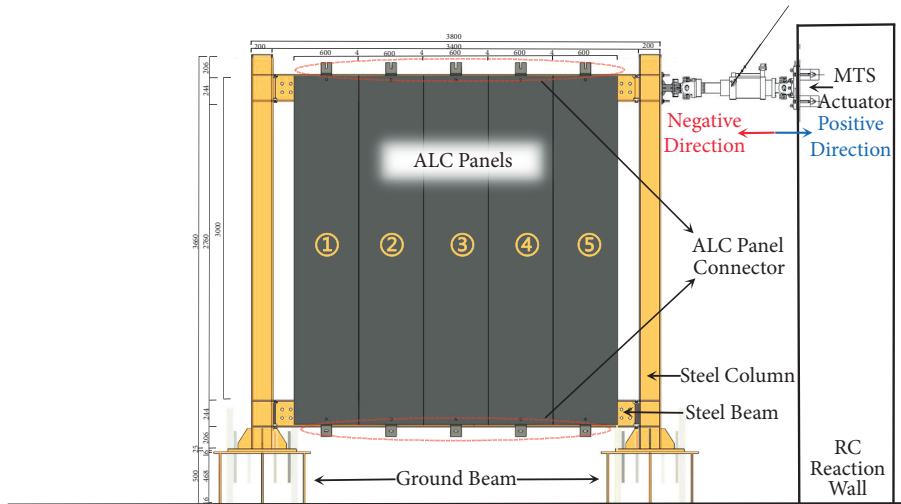


FIGURE 9: Schematic of test working conditions.

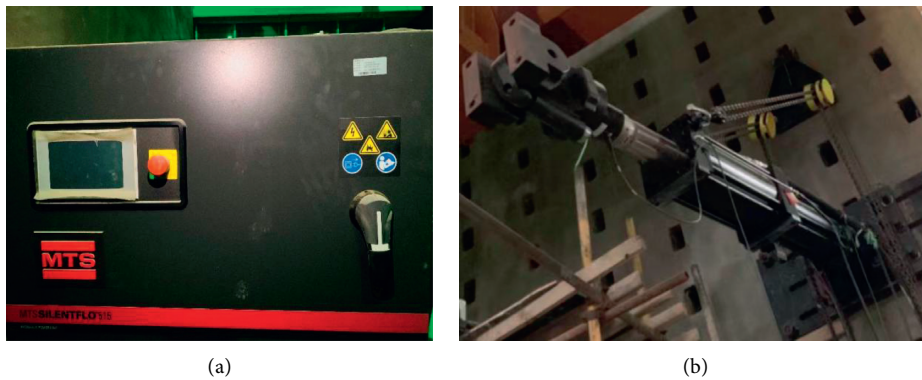


FIGURE 10: Photograph of the test devices. (a) MTS servo loading system. (b) The actuator of MTS with the column.



FIGURE 11: Test ALC blocks and steel coupons.

The push-down is positive, whereas the pull-up is negative. Before 60 mm, displacement was applied three times for each displacement. After 60 mm, displacement was applied twice for each. This test was preloaded with 2 mm and loaded for three rotations to confirm that both the steel frame loading version and the booster’s splice gap were properly adjusted [38]. The displacement load is identical to the size and material of the finite element analysis models described in Section 2, as shown in Figure 13.

4. Test Results

4.1. Specimen FW1. Specimen FW1 was a traditional L-hooked bolt used to rigidly connect the external ALC panel to the steel frame. When the displacement load reached the 6 mm stage, cracks in the joint mortar at the bottom of the No. 1 and No. 2 panel joints emerged. In the 10–12 mm stage, little chunks of ALC panels fell off continuously. When load achieved the 15 mm stage, there was



FIGURE 12: Universal testing machine.

TABLE 1: Material properties of steel.

Specimen		Sectional dimension (mm)	Thickness (mm)	Yield stress (MPa)	Ultimate stress (MPa)	Elongation stress (%)
Beam (HM)	Flange	244 × 175 × 7 × 11	11	263.4	401.6	25.2
	Web		7	275.3	411.3	22.3
Column (HW)	Flange	200 × 200 × 8 × 12	12	289.5	435.4	24.7
	Web		8	278.2	409.8	20.8
Connector	Q345	—	10	376.6	510.1	19.6

TABLE 2: Material properties of the ALC panel.

Specimen	Dimension (mm)	Measured compressive strength (MPa)	Elastic modulus (GPa)
Sac1	100 × 100 × 100	3.89	
Sac2	100 × 100 × 100	2.97	
Sac3	100 × 100 × 100	3.26	
Sac4	100 × 100 × 100	3.78	
Sac5	100 × 100 × 100	3.96	
Sac6	100 × 100 × 100	3.49	
Average		3.56	
Sae1	100 × 100 × 300		1640
Sae2	100 × 100 × 300		1880
Sae3	100 × 100 × 300		1790
Average			1770

visible dislocation between the panels which had fallen off the patchwork joints, as illustrated in Figure 14(a). Angle steel welds on the upper portion of the No. 2 panel failed when the displacement was in the 60 mm stage, as shown in Figure 14(b), and the L-hooked bolt hole started cracking. Therefore, when the displacement reached the 75 mm stage, the L-hooked bolt hole under the No. 3 panel developed a large crack. Besides, under No. 4 and No. 5 panels, the corners of each panel came away from the L-hooked bolt holes, revealing extensive fissures at bolt holes. Meanwhile, the holes of bolts began to expand, and the bolt swings with the steel angle as the displacement is applied as shown in Figures 14(c) and 14(d). When the displacement reached

90 mm, the welds of the left upper beam-column joints were fractured by loud sound, as shown in Figure 14(e). When it reached the 120 mm stage, the large areas of damage in the corners fell off, until it reached 135 mm, where several welds fractured as shown in Figure 14(f).

4.2. Specimen FW2. Specimen FW2 is the new connector (crossing ALC panel connector). When the displacement reached the 30 mm stage, the friction sound between the enclosure reinforcement and the end panel became audible. The frame and panel are unchanged, and only the bolts at the upper panel connector have dropped into their bolt holes,

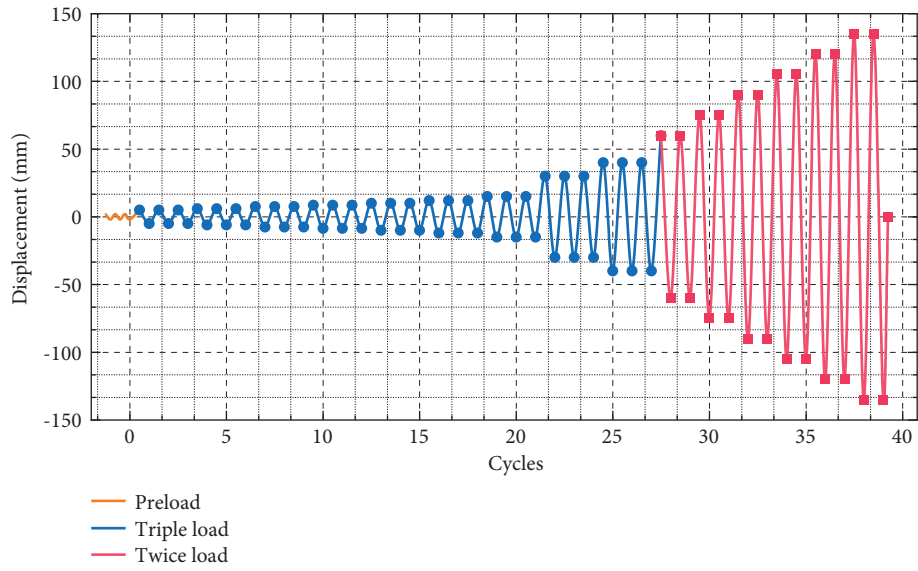


FIGURE 13: Loading system of the test.



FIGURE 14: Test results of FW1. (a) Obvious dislocation between panels. (b) Angle steel weld fractured. (c) Extended cracks at bolt holes. (d) The broken phenomenon of the panel angle. (e) Weld fractured. (f) Large areas of damage in each panel corner.

indicating that the junction follower performance is quite good, as illustrated in Figure 15(a). When arrived 40 mm, small pieces of debris came off, and the corner of the panel behind panel No. 5 was broken. When loading to 60 mm, the splicing mortar between No. 1 and No. 2 panels was broken, cracks appeared in the lower left panel corner of No. 1 panel, cracks appeared in the corner of No. 2 panel, and the relative movement between No. 1 and No. 2 panels could be seen. When loading to 75 mm, cracks appeared at the upper bolt holes of No. 2 and No. 3 panels, and the lower node of the second panel was loose, and obvious panel dislocation could be seen, as illustrated in Figure 15(b). When it arrived at 90 mm, the mortar of the joints collapsed in panels, and the corner of the back of the No. 1 panel was broken off, as shown in Figure 15(c). When loaded to 105 mm, the back corner of panel No. 3 was broken off, and the weld at the upper left beam-column node was chipped, as demonstrated in Figure 15(d). When loaded to the 120 mm stage, all the mortar of the joints of each panel was broken off, the weld at the upper left beam-column node was chipped, and the upper corner of panel No. 5 was broken off, as presented in Figure 15(e). When loaded to 135 mm, the back of panel No. 4 was diagonally cracked.

4.3. Load (Force)-Displacement Hysteretic Behavior. Figure 16 illustrates the cyclic response curves (hysteretic curves) obtained from the traditional L-hooked bolt and crossing panel connector (FW1 and FW2), respectively. As the displacement of the column end increases, the overall stiffness and strength of FW1 at the same amount of loading degrade, and the same process occurs in FW2, though to a lesser extent. This is primarily due to that the frame gradually transitions from the elastic to the elastic-plastic and plastic stages, as well as mortar splitting between ALC panels or blocks, cracking or crushing on the ALC panels' plastic deformation, and welding fracture at the beam-to-column and wall-to-frame connectors, all of which result in the destroying of the composite frame.

Two different types of ALC panel-connected frames have inverse S-shaped hysteresis curves. The area of FW2 is larger than that of FW1, which means the new connector has the better energy dissipation than the traditional L-hooked bolt. It further illustrates the excellent capacity of the new connector for steel frames. At the same late-stage displacement level, the new connector group (FW2) has a better bearing capacity than the L-hooked bolt group (FW1). Furthermore, specimen FW1 is shown to be more brittle than FW2 in terms of test phenomena and hysteretic behavior. This is because of the weld between the L-hooked bolt group (FW1) fractures at the 60–75 mm stage, resulting in a loss of stiffness and load-carrying ability after 75 mm, despite the fact that its load-carrying capacity is previously greater than that of the other groups. In comparison, FW2 absorbs energy during the early stage (before 30 mm) and provides the frame with increasing load capacity during the later stage due to the restricted displacement of the slip on the limitation hole.

5. Experimental Results' Analysis and Discussion

5.1. Skeleton Curves. Figure 17 shows the skeleton curves of the test connector specimens. The horizontal load-displacement skeleton curves for the tested specimens are produced by linking the maximum load point at each displacement level to the load-displacement hysteretic curves. Three stages of elasticity, elastomer-plasticity, and damage are observed on two specimens. The skeleton curves are approximately S-shaped, and the deterioration in stiffness is more apparent. The characteristic parameters of the skeleton curves are presented in Table 3, which indicates that the average of maximum force load-bearing capabilities in the positive and negative loading directions is 163.54 kN and 171.97 kN for FW1 and FW2, respectively. The maximum force load-bearing capacities of FW2 increase slightly by 5.2%, compared to FW1. However, it is much obvious in the positive loading direction (9.8% increasing). The calculation diagram of the yield point and the ultimate point is shown in Figure 18 in which they are determined by the Park method [41]. The yield load factor is 0.75, and these points can be determined according to the sequence of numbers shown in Figure 18 [34]. As for average of yield force bearing capability, FW2 (161.12 kN) is larger than FW1 (141.47 kN) by 13.9%. The average yield point delays hugely, 54.88 mm for FW1 to 69.98 mm for FW2 (27.5% delay).

At the early period (5 mm–40 mm stage), the tendency of the two skeleton curves is almost identical, with FW1 being larger than FW2, indicating that both specimens are in the elastic stage. However, because the bolt of FW2 connectors slipped into the limitation holes under loading, their load capacity and stiffness would be lower than the L-hooked bolt (FW1), indicating that the new connector (FW2) has great energy dissipation. The fact that the partial stiffness of the new connector (FW2) is only obtained during the intermediate stage of the test (40 mm–75 mm stage) indicated that the displacement of the new connector bolt at the limitation hole has reached its limitation. It is because the rigid connector of FW1 enters the yield stage first, and the rise in load-carrying capacity of FW1 becomes flat as FW2 exceeds the displacement loading. At this point, the new connector (FW2) begins to obtain more stiffness to the frame, hence increasing the frame's load capacity. Each specimen is in the yield stage during the 75 mm–90 mm stage. The curve of FW1 swings abruptly and then rapidly decreases which is significantly less than FW2. It is because the weld between the L-hooked bolt (FW1) and angle steel is broken at the 75 mm stage so that the FW1 connector type becomes much flexible, and the stiffness of frame contribution decreases rapidly. The bearing capacity of the L-hooked bolt reaches its maximum and enters the damage phase immediately, and the maximum value is obviously less than the scenario with FW2. Then, at the 105 mm–135 mm stage, the overall frame's load capacity decreases with the gradual increase of the load, so both skeleton curves of test groups decrease, in which FW1 declines more obviously.



FIGURE 15: Test results of FW2. (a) Upper connector slipped within the bolt hole. (b) Cracks appeared at the upper bolt holes. (c) Corner of the panel back was broken off. (d) Weld of the beam-column node was chipped. (e) Corner and all mortar of joints were broken.

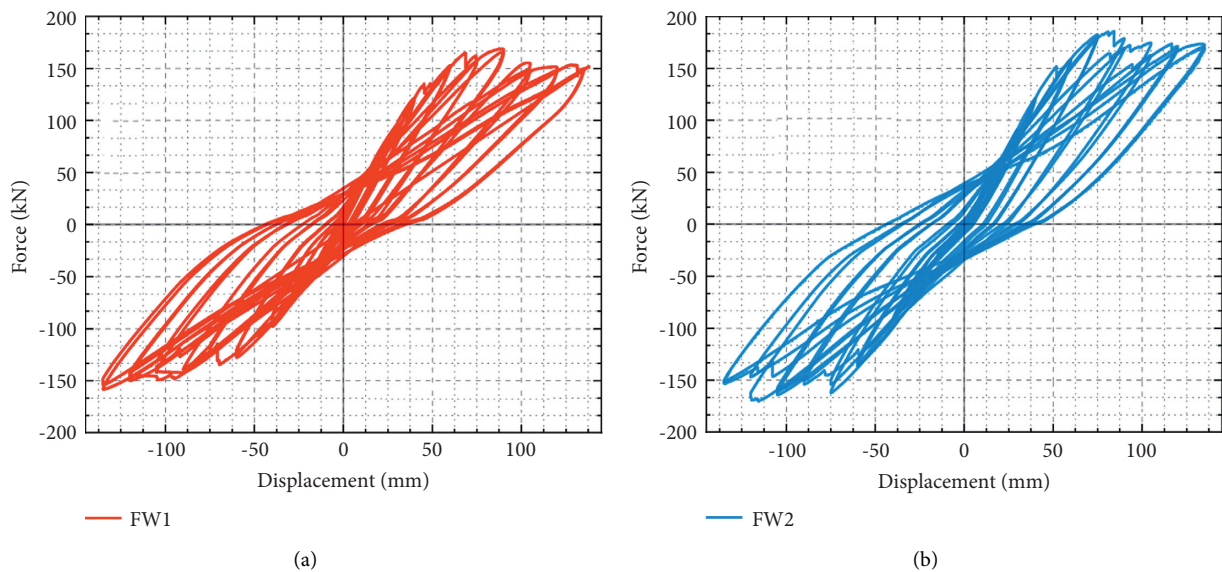


FIGURE 16: Load (force)-displacement hysteric curves of specimens. (a) Specimen FW1. (b) Specimen FW2.

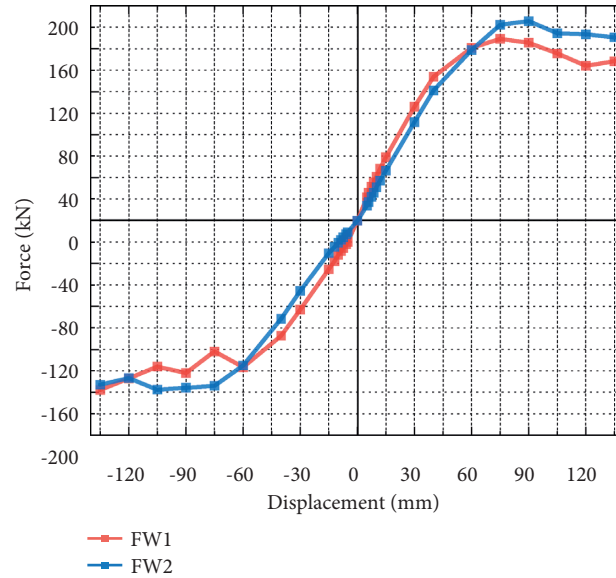


FIGURE 17: Skeleton curves of specimens FW1 and FW2.

TABLE 3: Skeleton curves of specimens.

Specimen	Direction	Yielding point		Peak point		Ultimate point	
		P_y (kN)	Δ_y (mm)	P_m (kN)	Δ_m (mm)	P_u (kN)	Δ_u (mm)
FW1	Push (+)	155.12	55.8	169.20	75.0	169.20	
	Pull (-)	127.82	54.0	157.89	135.0	121.85	
	Average	141.47	54.9	163.55	105.0	145.53	75.0
FW2	Push (+)	174.58	69.9	185.78	90.0	174.45	
	Pull (-)	147.74	70.1	158.15	105.0	157.64	
	Average	161.16	70.0	171.97	97.5	166.05	105.0

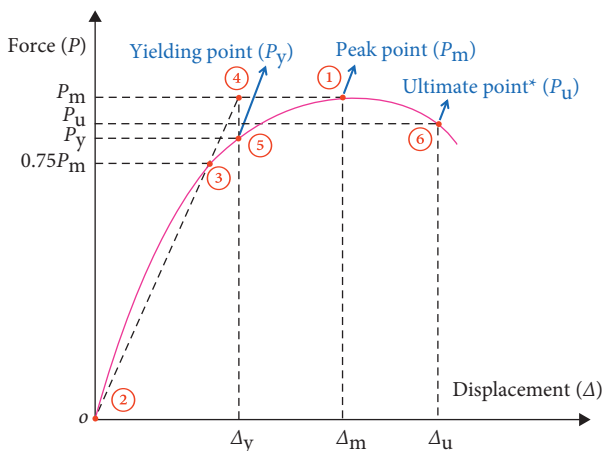


FIGURE 18: Schematic diagram of the method to determine characteristic points.

5.2. Ductility Coefficient. The high ductile structure has a high capacity for plastic deformation, which may prevent the emergence of brittle collapse and provide more time for people to try to hide or escape in the event of an earthquake or other accidents [42]. As a result, ductility is absolutely essential in seismic design. In this paper, Park's method is used to find the yield point in the skeleton curve. The

ductility coefficient ($\mu = \Delta u / \Delta y$) of the test wall specimens in the positive and negative loading directions is shown in Table 4. The ductility is defined as the ratio of the ultimate displacement (Δu is the corresponding displacement when the lateral load value decreases to 85% of the load-bearing capacity or when the structural member is broken) to the yielding load displacement (Δy is the displacement when the structure first yields) on the ascending branch.

In Table 3, the 75 mm point is taken as the ultimate point of FW1 because the weld (between the L-hooked bolt and the angle steel) was fractured during the loading to ± 75 mm stage. As for FW2, 105 mm is taken as the ultimate point because the new connector was fractured at the beam-column weld of the new connector during the ± 105 mm stage. Each ductility coefficient of specimens in the positive and negative loading directions is calculated. It can be seen from the average values of specimens that the ductility coefficient of FW2 is larger than that of FW1 by 8.9%. It shows that the new connector has better ductility contribution to the structure.

5.3. Stiffness Degradation. The stiffness degradation factor of specimens versus displacement is described in Figure 19 to illustrate the stiffness deterioration. The stiffness degradation coefficient (K_i) is as follows [43]:

TABLE 4: Ductility coefficient of specimens.

Specimen	Push (+)	Pull (-)	Average
FW1	1.345	1.389	1.367
FW2	1.502	1.500	1.501

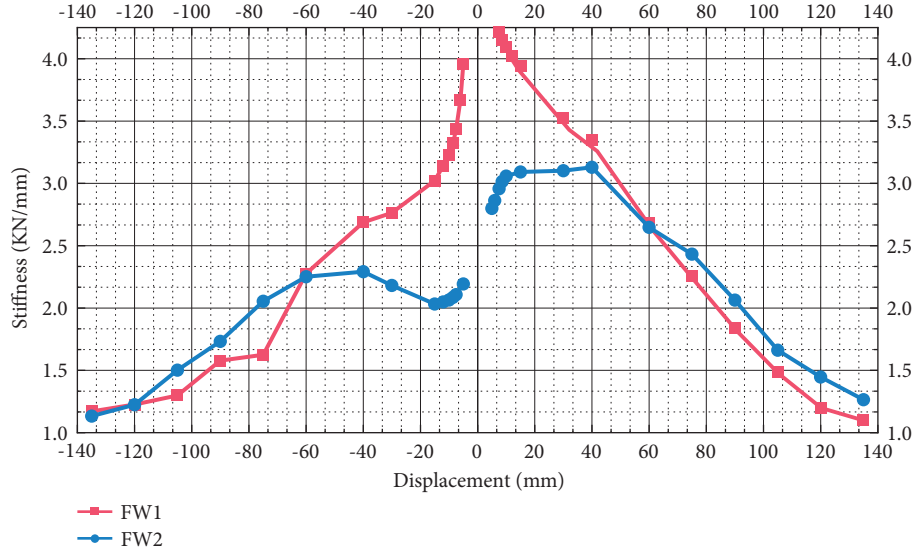


FIGURE 19: Comparing stiffness degradation of specimens FW1 and FW2.

$$K_j = \frac{\sum_{i=1}^n P_j^i}{\sum_{i=1}^n u_j^i}, \quad (1)$$

where P_j^i and u_j^i indicate the maximum load and displacement, respectively, during the i th loading cycle when the displacement equals j . The number of loading cycles in each loading cycle is defined by n .

As expected, stiffness of FW1 reduces significantly as lateral displacement increases. From the initial stiffness, it can be seen that FW1 (4.16 kN/mm average) is much larger than FW2 (2.50 kN/mm average) because the new joint is typically a flexible joint as its bolt swung in the limitation hole of the connector (which was consuming energy) during the early period. Therefore, the initial stiffness of FW2 is smaller, compared to the rigid joint of the traditional L-hooked bolt of FW1. In the 40 mm stage, the stiffness deterioration of FW2 appears to increase temporarily as the bolt of the new connector approached its limitation hole. Then, during 60–90 mm, the stiffness deterioration of FW1 falls significantly, while FW2 remains reasonably stable and exceeds FW1 at 60 mm, as illustrated in Figure 16. The averages of the two stiffness degradations following the elastic stage (75 mm) are 2.15 and 2.38, respectively, in which FW2 improves 10.6% compared to the traditional L-hooked bolt (FW1).

5.4. Energy Dissipation. The energy dissipation capacity of the structure in this test is measured by the area of force to displacement enclosed. The capacity of structural energy dissipation is directly proportional to the area of the

hysteresis loop. The more the energy is dissipated by a structure, the safer and less is affected. The equivalent damping factor (ξ_e) was defined by the following equation [44]:

$$\xi_e = \frac{1}{2\pi} \cdot \frac{S_{ABC} + S_{CDA}}{S_{OBE} + S_{ODF}}, \quad (2)$$

where $S_{ABC} + S_{CDA}$ is the area enclosed by the hysteresis curve and $S_{OBE} + S_{ODF}$ is the sum of the areas of the two triangles, as shown in Figure 20.

The equivalent damping factor (ξ_e) versus the displacement relationship of specimens is shown in Figure 21. The trend of the FW1 curves is that ξ_e reduces rapidly during the 0–10 mm and then increases rapidly (after 10 mm). This indicates that the ALC panel is compressed by the L-hooked bolt, and the hole becomes larger. As for FW2, it raises quickly in the 0–40 mm stage because the bolts of the new connectors are dissipating energy by sliding in the limitation holes. Then, it declines slowly after 40 mm and raises after 60 mm rapidly because when the bolt reaches its limitation hole, the panels start to be compressed. At the displacement less than 60 mm, ξ_e of FW2 is larger than that of FW1. Subsequently, FW1 is slightly larger than FW2 because of the broken weld joints and the part of damage of the ALC panel. Then, it is overtaken by them after 80 mm because of the partial destruction of the ALC panel of FW2. However, FW2 is overtaken by FW1 at the 130 mm stage because almost every weld of FW1 is broken, making the connector completely flexible, while the new connector is working stably. The equivalent damping factor (ξ_e) of the new connector (FW2) is obviously larger than the L-hooked bolt one (FW1)

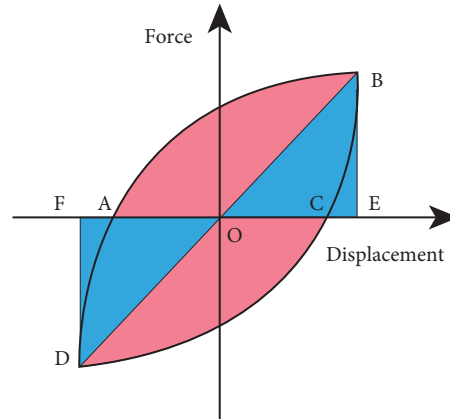


FIGURE 20: The dissipation capacity area.

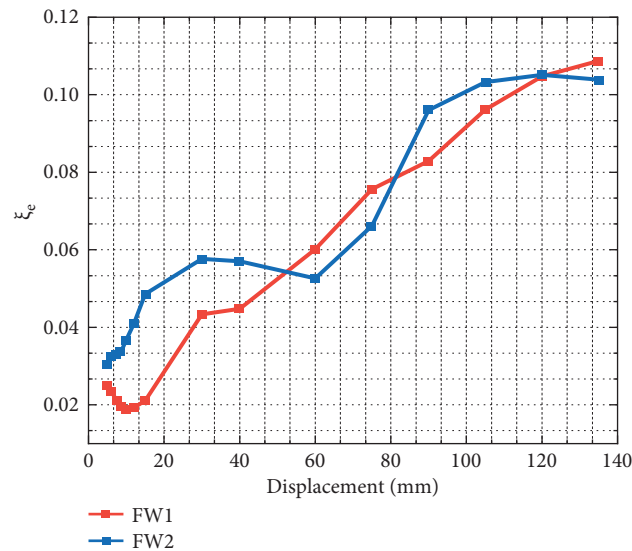


FIGURE 21: The equivalent damping factor (ξ_e) of specimens.

at the ultimate limit stage. At the yield state, the equivalent damping factor of FW2 increases by 10.2%, compared to FW1. As for the ultimate state, FW2 increases by 35.3%. The energy dissipation parameters of specimens at the yield and ultimate state are shown in Table 5. Generally, the frame with new connectors with the ALC panel has good dissipated energy capacity.

TABLE 5: Energy dissipation parameters of specimens at the yield and ultimate state.

Specimen	Yielding point		Ultimate point	
	Δ_y (mm)	$\xi_{e,y}$	Δ_u (mm)	$\xi_{e,u}$
FW1	54.88	0.05619	75	0.07564
FW2	69.98	0.06171	105	0.10232

5.5. *Verification of Finite Element Results.* The simulation results of ABAQUS are validated by comparing them to the test data, as shown in Figures 22–24. Specifically, the hysteresis curve and skeleton curve results indicate that the positive directions are nearly similar, the ABAQUS simulation trend is generally similar with the trend of the test, and the initial stiffness of the simulation results is slightly greater than that of the test results. Additionally, the test hysteresis

curve’s “pinch” effect is more significant than the simulation results. It is because the slipping of the ground beam occur during large displacement loading in test. The FEM simplifies the complex boundary conditions in the experiment (slippage of the ground beam, small gaps between specimens, etc.) [36]. Moreover, the steel mesh slippage on the ALC panel was not considered. However, all of the above differences are within a reasonable range [45]. As a result,

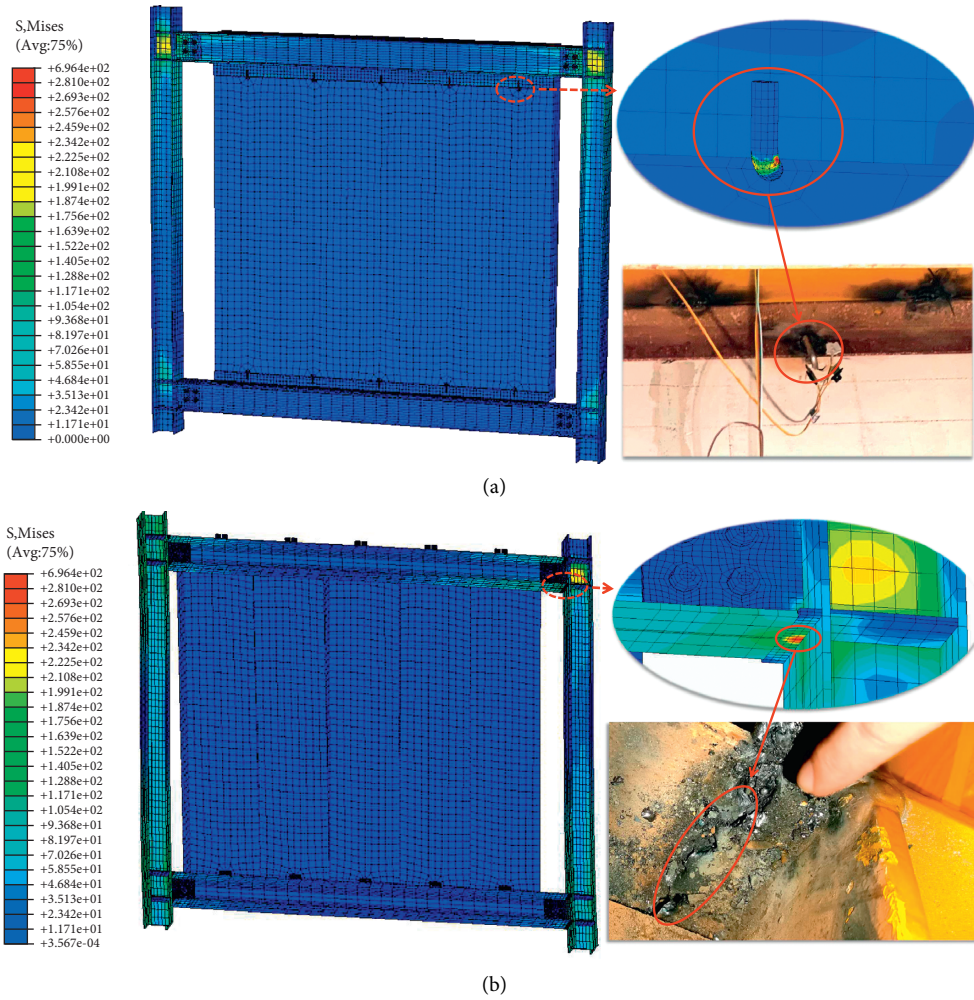


FIGURE 22: Comparing test observations and finite element simulation. (a) L-hooked bolt. (b) New crossing ALC panel.

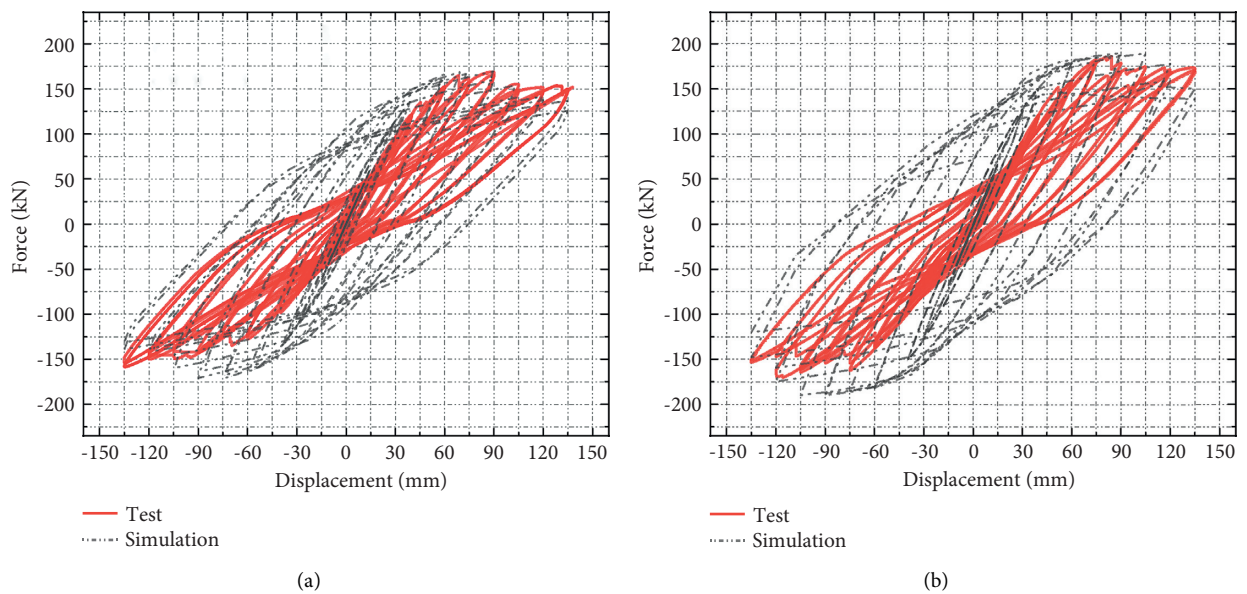


FIGURE 23: Comparing force-displacement hysteric of specimens in the test and simulation. (a) L-hooked bolt. (b) New crossing ALC panel.

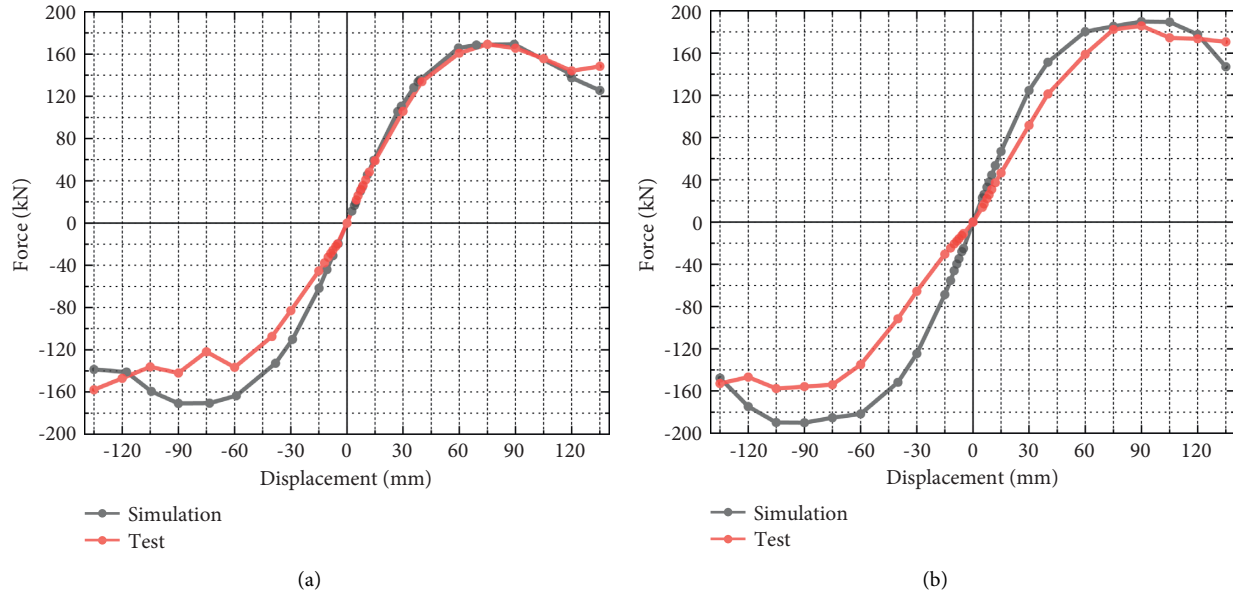


FIGURE 24: Comparing skeleton curves of specimens in the test and simulation. (a) L-hooked bolt. (b) New crossing ALC panel.

the finite element model and analysis method could accurately reflect the structure's seismic capacity of the new ALC panel connector and L-hooked bolt.

6. Conclusion

In this paper, a new flexible ALC panel connector is invented for solving construction problems. The FEMs were established, and the full-scale tests in low-cyclic loading were carried out. It has better seismic and synergistic capacities of panels, especially in the small earthquakes (cracks occur late). In the large earthquake, it can also provide certain stiffness to the structure. The new crossing connector has a wide range of applications, which can replace traditional connectors for steel buildings. The results are shown as follows:

- (1) The new connector has better seismic capability. Its synergistic capacity is better as the occurrence of cracks in the wall of the ALC panel of the new connector is much later than the L-hooked bolt. By comparing the L-hooked bolt, the maximum bearing capability of the structure of the new connector increases by 5%, the yield bearing capability increases by 13.9%, and the yield displacement delays by 27.5%, resulting in the ductility increasing by 9.8%.
- (2) The new connector worked stably in the full-scale low-cyclic loading test, while the weld of the traditional L-hooked bolt was fractured at the 75 mm stage. After the new connector reaches its limitation of the limitation hole, the maximum load capacity of the frame increases by 5.2% compared with the L-hooked bolt. The damage pattern is the same for both specimens. The joint of panels is the first to be damaged, followed by the hole and corner of the ALC panel.

- (3) Although the L-hooked bolt has relatively larger initial stiffness, its stiffness degradation rate is larger than the new connector and decreases by 10.6% in the elastic stage, benefitting from the design of the limitation hole of the new flexible connector, which makes the structure's energy consumption capacity rise significantly. The equivalent damping factor of the new connector increases by 10.2% and 35.3% at the yield and ultimate state each.
- (4) The result of the finite element simulation is similar with the test roughly, and the crossing connector has better seismic capability. The test hysteresis curve's "pinch" effect is more significant than the simulation results, which is in reasonable range. This finite element model by ABAQUS can simulate the new connector and L-hooked bolt in structures accurately, and the results of FEMs have reference value.

Data Availability

The data of the test and simulation used to support the findings of this study are included within the article.

Conflicts of Interest

The authors declare that they have no conflicts of interest.

Authors' Contributions

Kewei Ding conceptualized the study, provided resources, and edited and reviewed the article. Chikun Zhang provided the methodology, performed simulation, test, and analysis, wrote the original draft, and edited and reviewed the article. Shulin He performed simulation and test and edited the article. Yunlin Liu conceptualized the study and provided resources.

Acknowledgments

This research was financially supported by the National Natural Science Foundation of China (11472005), the University Synergy Innovation Program of Anhui Province (GXXT-2019-005), and the University-Industry Collaborative Education Program of the Ministry of Education (202002129042).

References

- [1] Y. C. Kurama, S. Sritharan, and R. B. Fleischman, "Seismic-resistant precast concrete structures: state of the art," *Journal of Structural Engineering*, vol. 144, no. 4, Article ID 03118001, 2018.
- [2] M. I. Khan, M. A. Al-Osta, S. Ahmad, and M. K. Rahman, "Seismic behavior of beam-column joints strengthened with ultra-high performance fiber reinforced concrete," *Composite Structures*, vol. 200, pp. 103–119, 2018.
- [3] B. Cheng, K. Lu, J. Li, H. Chen, X. Luo, and M. Shafique, "Comprehensive assessment of embodied environmental impacts of buildings using normalized environmental impact factors," *Journal of Cleaner Production*, vol. 334, Article ID 130083, 2022.
- [4] B. Li, "The present situation and development of prefabricated building in China," *China Science and Technology Information*, vol. 7, pp. 114–115, 2014.
- [5] D. Zhang, G. Kuai, H. Xu, L. Luo, and H. Leng, "Application research of autoclaved sand aerated concrete wall panel in fabricated steel structure system," *Steel Structure*, vol. 31, no. 1, pp. 89–93, 2016.
- [6] W. Li, X. Yang, Y. Wang, R. Shang, Y. Gui, and Z. Hou, "Application of composite insulation wall panel in a prefabricated steel structure building," *Industrial Building*, vol. 50, no. 3, pp. 147–150+123, 2020.
- [7] J. J. Wang, J. H. Xie, J. H. He, M. Sun, J. Yang, and L. Li, "Combined use of silica fume and steel fibre to improve fracture properties of recycled aggregate concrete exposed to elevated temperature," *Journal of Material Cycles and Waste Management*, vol. 204, pp. 384–398, 2020.
- [8] J. Wang and B. Li, "Cyclic testing of square CFST frames with ALC panel or block walls," *Journal of Constructional Steel Research*, vol. 130, pp. 264–279, 2017.
- [9] A. Raj, D. Sathyan, and K. M. Mini, "Physical and functional characteristics of foam concrete: a review," *Construction and Building Materials*, vol. 221, pp. 787–799, 2019.
- [10] R. Hay and C. P. Ostertag, "Life cycle assessment (LCA) of double-skin façade (DSF) system with fiber-reinforced concrete for sustainable and energy-efficient buildings in the tropics," *Building And Environment*, vol. 142, pp. 327–341, 2018.
- [11] A. Artino, G. Evola, G. Margani, and E. M. Marino, "Seismic and energy retrofit of apartment buildings through autoclaved aerated concrete (AAC) blocks infill walls," *Sustainability*, vol. 11, no. 14, p. 3939, 2019.
- [12] M. Kalpana and S. Mohith, "Study on autoclaved aerated concrete: review," *Materials Today Proceedings*, vol. 22, pp. 894–896, 2020.
- [13] X. Qu, Z. Chen, and G. Sun, "Experimental and numerical analysis study on the structural performance of autoclaved aerated concrete (AAC) wall slab," *Journal of Building Materials*, vol. 15, no. 2, pp. 268–273, 2012.
- [14] G. D. Matteis and R. Landolfo, "Diaphragm action of sandwich panels in pin-jointed steel structures: a seismic study," *Journal of Earthquake Engineering*, vol. 4, no. 3, pp. 251–275, 2000.
- [15] Y. Yang, D. Zhang, P. Chen, and F. Gao, "Hysteretic capacity test of articulated steel frame with embedded ALCPanel," *Journal of Civil Engineering and Management*, vol. 38, no. 5, pp. 118–124, 2021.
- [16] B. Wang, J. Wang, H. Wan, H. Hou, and J. Wang, "Research on capacity and connector structure of filling wall of high-rise steel structure building under cyclic loading," *Construction steel structure progress*, vol. 17, no. 6, pp. 44–50, 2015.
- [17] G. Zhang, W. Xiao, B. Chen, Q. Miao, and H. Wu, "Research on hysteretic capacity of autoclaved aerated concrete external wall," *Industrial Building*, vol. 46, no. 11, pp. 86–92, 2016.
- [18] L. Gou, F. Guo, Y. Yang, Z. Wang, and G. Zhu, "Installation technology of autoclaved lightweight Aerated concrete (ALC) wall panel in prefabricated steel frame structure," *Tianjin Technology*, vol. 45, no. 11, pp. 56–59, 2018.
- [19] T. S. Kim, H. Kuwamura, and T. J. Cho, "A parametric study on ultimate strength of single shear bolted connections with curling," *Thin-Walled Structures*, vol. 46, no. 1, pp. 38–53, 2008.
- [20] K. Ding and W. Chen, "Experimental study and restoring force modeling on seismic capacity of prefabricated concrete beam-column joints," *Journal of Shenyang Jianzhu University (Natural Science)*, vol. 37, no. 1, pp. 51–60, 2021.
- [21] J. Wu, J. Lu, Z. Xu, and Z. Zheng, "Upper load-bearing joint design method of the precast concrete wall panels," *Building Structure*, vol. 44, no. 13, pp. 47–51, 2014.
- [22] F. Jin, A. Guo, and Z. Wang, "Application of autoclaved lightweight aerated concrete slab in internal partition and retaining wall," *Construction Technology*, vol. 30, no. 8, pp. 24–25, 2001.
- [23] S. Dai, "Structural capacity and supporting Technology of steel frame-concrete tube housing," Doctoral dissertation, *Wuhan University of Technology*, Wuhan, China, 2004.
- [24] L. Li and R. Chong, "20 years of work review of Nanjingxu Construction, a world-class ALC enterprise with craftsman spirit," in *Proceedings of the 35th Annual Meeting of China Aerated Concrete Association*, pp. 60–70, Weifang, Shandong, China, December 2015.
- [25] S. Cao, G. Shu, K. Lin, S. Fan, and H. Gao, "Analysis and design method of a new type of prefabricated steel structure external wall panel joint," *Building Structure*, vol. 47, no. 10, pp. 46–52, 2017.
- [26] X. Wang, X. Liu, L. Ma, and X. Zhou, "Experimental study on seismic capacity of assembled ALC external wall panel," *Steel Structure*, vol. 32, no. 4, pp. 22–26+63, 2017.
- [27] Y. Meng, "Research on lateral force resistance of steel frame with multi-layer inner cladding wall panel," Doctoral dissertation, *Harbin Institute of Technology*, Harbin, China, 2012.
- [28] L. Bai, "Development and mechanical properties study of the connector between ALC wall panels and steel frame," Doctoral dissertation, *Shenyang Jianzhu University*, Shenyang, China, 2015.
- [29] Y. Lin, K. Liu, T. Xiao, and C. Zhou, "Shear bearing capacity of framework joints of steel-reinforced concrete-filled circular steel tube," *Advances in Materials Science and Engineering*, vol. 2020, Article ID 7324865, 15 pages, 2020.
- [30] Z. Chen, "Study on deformation behavior of steel frame external ALC wallboard under earthquake action," Doctoral dissertation, *Chongqing University*, Chongqing, China, 2017.
- [31] L. Huang, W. Lv, and Z. Yi, "Finite element analysis of a new composite wall-slab," *Journal of Central South University of Forestry & Technology*, vol. 3, pp. 54–58, 2002.

- [32] Y. Zhou, T. Chen, Y. J. Pei, X. Hu, W. Yi, and L. Deng, "Static load test on progressive collapse resistance of fully assembled precast concrete frame structure," *Engineering Structures*, vol. 200, Article ID 109719, 2019.
- [33] J. Wang, Q. Li, and G. Wei, "Seismic performance analysis of steel beam to CFST column connection with ductility and energy dissipation components," *Journal of Vibroengineering*, vol. 22, no. 1, pp. 131–144, 2020.
- [34] E. Tuncer, B. Binici, and E. Canbay, "Behavior and design of FRP bonded autoclaved aerated concrete beams," *Construction and Building Materials*, vol. 282, Article ID 122712, 2021.
- [35] C. Liu, J. Hou, Y. Hao, H. Hao, and X. Meng, "Effect of high strain rate and confinement on the compressive properties of autoclaved aerated concrete," *International Journal of Impact Engineering*, vol. 156, Article ID 103943, 2021.
- [36] K. Ding, D. Zong, Y. Liu, and S. He, "Experimental and finite element analysis of external ALC panel steel frames with new semi-rigid connector," *Applied Sciences*, vol. 11, no. 22, Article ID 10990, 2021.
- [37] D. Zhao, L. Chen, and W. Wang, "Hysteretic behavior analysis of Steel frame structure with ALC walls," *Journal of Zhejiang University of Technology*, vol. 38, no. 4, pp. 448–452, 2010.
- [38] K. Ding, Y. Ye, and W. Ma, "Seismic performance of precast concrete beam-column joint based on the bolt connection," *Engineering Structures*, vol. 232, Article ID 111884, 2021.
- [39] H. Lu, H. Zhang, K. Ma, Q. Wu, and L. Jiang, "Experimental study and numerical study on shear bearing capacity of shear key joints of reinforced concrete open-web sandwich plates," *Advances in Materials Science and Engineering*, vol. 2021, Article ID 6197472, 22 pages, 2021.
- [40] D. Wang, H. Zhao, and X. Lv, "Loading protocols for quasi-static test of structural components for buildings," *Sichuan Building Science*, vol. 40, no. 3, pp. 62–67, 2014.
- [41] R. Park and T. Paulay, *Reinforced Concrete Structures*, Wiley, New York, NY, USA, 1975.
- [42] J. Xu, J. Wang, H. S. Mohamed et al., "Post-earthquake fire resistance of bolted end-plate connection joint with end-plate and web stiffeners," *Journal of Constructional Steel Research*, vol. 185, Article ID 106835, 2021.
- [43] K. Ding and Y. Zhang, "Experimental study on seismic performance of fabricated bolted joint under low-cycle reciprocating loads," *Results in Engineering*, vol. 9, Article ID 100208, 2021.
- [44] Y. Ma and J. Jia, "The influence of different parameter on the seismic behavior of SRUHSC frame," *Advances in Materials Science and Engineering*, vol. 2017, Article ID 3495150, 2017.
- [45] W. Ma, K. Xu, and B. Cheng, "Experimental study on the seismic behavior of a new single-faced superposed shear wall with the concealed column," *Structures*, vol. 33, pp. 4446–4460, 2021.

Research Article

An Empirical Model for Geopolymer Reactions Involving Fly Ash and GGBS

Beulah M ¹, MR Sudhir ¹, Shenan Chen ², Sasha Rai,³ and Deekshith Jain ⁴

¹Department of Civil Engineering, School of Engineering & Technology, CHRIST (Deemed to be University), Bangalore, Karnataka, India

²Civil and Environmental Engineering, University of North Carolina, Charlotte, NC 28223, USA

³Department of Civil Engineering, School of Engineering, KS School of Engineering & Management, Bangalore, Karnataka, India

⁴Department of Construction Technology and Management, Bule Hora University, Blue Hora, Ethiopia

Correspondence should be addressed to Deekshith Jain; deekshith.jain@bhu.edu.et

Received 8 October 2021; Revised 6 December 2021; Accepted 27 December 2021; Published 15 January 2022

Academic Editor: Rotana Hay

Copyright © 2022 Beulah M et al. This is an open access article distributed under the Creative Commons Attribution License, which permits unrestricted use, distribution, and reproduction in any medium, provided the original work is properly cited.

Numerous works are reported in literature regarding the enhancement of compressive strength of fly ash-GGBS geopolymer combinations with addition of alkali activators of varying concentrations. However, a limited study has been chronicled, revealing the specific role of alkali or alkaline earth contributed by the fly ash-GGBS combinations on the compressive strength development. It is well known that the strength of a geopolymer is dependent on gel formation from Al/Si ratio, Ca/Si ratio, and Ca/(Si + Al) ratio but their exact role when cured for various extended periods is unknown as yet. In the present study, alkali concentration in a fly ash-GGBS geopolymer combination was varied from 6 M to 12 M with increments of two mol in six different fly ash-GGBS combinations with a minimum of 20 percent and a maximum of 70 percent GGBS. The correlation coefficients between compressive strength and Al/Si, Ca/Si, and Ca/(Si + Al) ratios exhibited values higher than 0.95 taken individually. Multiple linear regression analysis with compressive strength (as dependent parameter) and individual values of Al/Si, Ca/Si, and Ca/(Si + Al) ratios (as independent parameters) was effectuated. It was observed that, depending on the composition, the compressive strength circumstantiated a changeover from Ca/Si to Ca/(Si + Al) ratio in the intermediate composition range. Such a detailed analysis is considered supportive of developing a suitable composition which will provide the optimum compressive strength of the combination.

1. Introduction

In alkali-activated geopolymer systems with calcium-containing solid alumina silicate sources, such as ground granulated blast-furnace slag (GGBS) and calcium fly ash (FA), rapid formation of C-A-S-H gels [1–3] (along with calcium in class C FA) resulting in quick setting [4, 5] has been reported. The C-A-S-H gel showed similar features like C-S-H gel presented in conventional OPC (ordinary Portland cement) concrete. Addition of soluble silicates is generally done into the alkaline activating solution for obtaining a rapid sol/gel transition with improved properties. Calcium has been attributed to the early age setting, which increases with time [6–8]. In the Na₂O-CaO-SiO₂-Al₂O₃-H₂O system, the coprecipitation of geopolymer gel due

to Si-Al-H and C-A-S-H has been found to have an exchange reaction where Na is replaced by Ca [9–11].

Regarding the role of Ca on the metakaolin based geopolymers, Chen et al. [10] suggested that the addition of Ca in metakaolin resulted in faster geopolymer gel formation leading to faster setting time and that there is evidence of C-A-S-H formation. These conclusions were supported by NMR (nuclear magnetic resonance) studies. Pulgalia and Mondal [11] indicated that in calcia-based systems, the phase characterization becomes difficult because of the coexistence of C-A-S-H, (C(N, K)-A-S-H), and (N, K)-A-S-H in the reaction products of fly ash-metakaolin geopolymers containing soluble form of calcium. They further suggested that conventional FTIR analysis provided vibrations from initial

unreacted slag and calcium silicate hydrate and an overlapping pattern which is similar to OPC sample patterns. They resorted to conventional selective acid dissolution technique but also suggested that they could not differentiate between N-A-S-H and C-S-H gels.

1.1. Geopolymer Paste Modelling in Literature. Previous attempts using numerical modelling to investigate the geochemical reactions in the polymerization of fly ash-GGBS geopolymer combinations included that by Dao et al. (2019) [12], which estimated the compressive strength of geopolymers using numerical methods (neural networks and genetic algorithms) to find an optimum mix design. Dao et al. (2019) [12] also showed that their models have strong potential for predicting the 28-day compressive strength and suggested that the modelling would help in reducing the time and cost of laboratory tests in the optimal design of geopolymer. Yadollahi et al. (2015) [13] estimated the compressive strength of geopolymer concrete using artificial neural networks (ANN) method and found that parameters including silica modulus, Na₂O content, water/solid ratios, and curing time can affect the compressive and tensile strengths of geopolymer concrete. Naseri et al. (2017) [14] estimated the results of compressive strength of concrete using SVM (Support Vector Machine). Nano-CuO was added at different content levels in self-compacting concrete and CuO effects were determined. Khotbehsara et al. (2018) [15] estimated the compressive strength of concrete with SnO₂, ZrO₂, and CaCO₃ nanoparticles. Both SVM (Support Vector Machine) and ANFIS (adaptive neurofuzzy interface system) were used to analyze the results. Badarloo et al. (2018) [16] estimated the relationship between compressive and tensile strengths of concrete using MATLAB software and probabilistic methods, and the error estimated with the experimental data was found to be nil. Awoyera et al. (2020) [17] included mechanistic properties including slump flow and funnel flow in a machine learning model for self-compacting geopolymer concrete. However, the model had not been tested in full commercial production of geopolymer concrete.

For more mechanistic-based modelling, Zhang et al. (2018) [18] produced theoretical models of geopolymer gels and found them to be close to those produced experimentally using computer simulation through MD (Molecular Dynamics) models with Si/Al molar ratios of 2 and 3. The simulation was carried out at temperatures ranging from 650 to 1800 K and the effect of Si/Al ratio and temperature on the polymerization process and the properties of computationally synthesized geopolymer gels were investigated. Cui et al. (2020) [19] compared the flexural behaviors of OPC and geopolymer concretes using Abaqus modelling. Using data obtained from testing and the literature, empirical equations were derived to describe the nonlinear correlation between the compressive strength and elastic modulus of fly ash based geopolymer concrete (CFGPC). They observed that the suggested formula had a reasonably high R² value of 0.7663, and when the variations in density were added to the regression analysis, R²

increased to 0.8652. Ling (2019) [20] observed the role of SiO₂/Na₂O mole ratio in alkaline solution, alkaline solution concentration in mass percent, and liquid-to-fly ash mass ratio (L/F). Ling observed using artificial neural network (ANN) that the curing temperature and time had significant influences on the setting time, compressive strength, and heat of geopolymerization which are critical properties for a concrete binder. It was concluded that the optimum mix design parameters result in favourable fly ash geopolymer properties (i.e., compressive strength, setting time, and heat generation). By using both Levenberg-Marquardt and Bayesian regularization algorithms, Siva Krishna and Ranga Rao (2019) [21] were able to use ANN models to predict the mechanical properties such as compressive, split tensile, and flexural strength values of concrete and observed that the Levenberg-Marquardt algorithm gave more accurate results than the Bayesian model. Finally, Mehdizadeh et al. (2018) [22] used a statistical experimental design based on response surface methodology (RSM) on an alkali-activated phosphorus slag to predict and optimize the compressive strength of different ages (3, 7, and 28 days). In their study, the binder samples were prepared with different molar ratios of SiO₂/Na₂O (S/N), Na₂O/Al₂O₃ (Na/Al), and H₂O/Al₂O₃ (H/Al) as alkali activators and the results showed that S/N molar ratio had a significant effect on 7 and 28 days of compressive strength. On the other hand, H/Al molar ratio was found to have the most significant effect on compressive strength when compared to other parameters. They concluded that RSM models were statistically adequate and could be used to predict the compressive strength.

1.2. Significance of Research. As per literature, Al/Si ratio, Ca/Si ratio, and Ca/(Si + Al) ratio in combinations may have a critical role to play in the development of compressive strength of the geopolymer system containing calcium and alkaline activators that are responsible for initiating polymeric reactions. Depending on the CaO/SiO₂ ratio, Al₂O₃/SiO₂ ratio, and CaO/(Al₂O₃ + SiO₂) ratio, the composition and properties of the gel may change and may affect the overall compressive strength of the product. In this paper, an attempt of using an empirical approach to establish the correlations is reported.

In the current study, the focus is also on the material transition; geopolymers have displayed compressive strengths comparable to the compressive strengths of Portland cements and with additional benefits of high temperature resistance and stability under acid attack. The setting of geopolymers, however, is closely associated with the transition from fluid to solid which can be accelerated with the addition of calcium. Calcium was found to decrease the Al/Si ratio for geopolymer formation, in particular the Al-substituted calcium silicate hydrate (C-A-S-H) formation and also the calcium silicate hydrate (C-S-H) formation. When compared to noncalcium mixes which are controlled by Al/Si ratios in normal geopolymer gel, calcium mixes experienced faster dissolution with higher compressive strengths.

It has been suggested that, with calcium addition, the gel substantially accelerated the setting behavior and the formation of (C-S-H) and (C-A-S-H) gels has caused the enhanced dissolution of the source material precursors.

In the current study, NMR tests showed that comparable amount of geopolymer gel existed at setting for both calcium and noncalcium mixes, which suggested that the geopolymer gel was partially responsible for the setting process. Since faster geopolymer gel formation was caused by faster dissolution, which yielded more Al and lowered the Al/Si for geopolymer gel formation (as confirmed by quantitative analysis using both ^{29}Si and ^{27}Al NMR spectroscopy), the lower Al/Si ratio can be considered to be sufficient to cause the significantly different setting behaviors. Furthermore, calcium consumes Si in the solution, which has been proven from indirect experiment and simulation.

In synthetic (C-S-H), a low Ca/Si ratio leads to high dissolved silica concentrations and low calcium concentrations, while at high Ca/Si ratio and in presence of high pH of 12.5 high calcium and low silica are typically measured. In (C-S-H) with a $\text{Ca/Si} \geq 1$, the aluminum uptake in (C-S-H) depends on the total amount of aluminium present in the sample and a close relation between aqueous aluminium concentrations and the molar Al/Si ratio in C-A-S-H is observed up to an Al/Si of approximately 0.1 (10, 12).

It should be noted, however, that the experimental samples prepared are based on synthetic materials that are not as complicated as commercial samples and do not represent the actual conditions of commercial products, and therefore it is logical to conclude that the above-mentioned observations may occur concurrently as the reaction proceeds with prolonged curing period. Furthermore, any change in the strength of the samples is an indirect measurement of the different phase formations and is an approximate representation of the dynamic situation, controlled by Si-Al-Ca-Na complex association in different stages of reaction, in actual commercial productions. Thus, the dynamic situations prevailing in geopolymer reactions with time cannot be compared with reported static experimental conditions in actuality. However, application and help of both correlation coefficients and multiple linear regression analysis together are definite indicators of the validity of the assumptions and scientific observations made in real-life situations.

The scientific communities have relied on the help of statistical correlations between two observations to establish the direct proof of the dependence/independence of the

observations; and, in time-dependent events, multiple linear regression analyses have been the means to establish the correlation between different temporal events. For the current study, a similar approach is used.

1.3. Theory. If a number of samples (A to G, Table 1) are related to the dependent variable (Y) and independent variables A, B, and C (as shown in the table), then the relationship can be expressed as

$$Y = [K1 (A)^{N1}]_x [K2 (B)^{N2}]_x [K3 (C)^{N3}], \quad (1)$$

where Y1 to Y6 are dependent variables (for different sets of experimental data points) related to the independent experimental variable parameters A (A1 to A6), B (B1 to B6), and C (C1 to C6).

Here, K1, K2, and K3 are proportionality constants in the correlation relationship between different Y and X values:

$$Y \propto (A)^{N1} \text{ or } Y = K1 (A)^{N1}, \quad (2)$$

$$Y \propto (B)^{N2} \text{ or } Y = K2 (B)^{N2}, \quad (3)$$

$$Y \propto (C)^{N3} \text{ or } Y = K3 (C)^{N3}. \quad (4)$$

These may be generalized as

$$Y = [K1 (A)^{N1}]_x [K2 (B)^{N2}]_x [K3 (C)^{N3}]. \quad (5)$$

In equation (2), if $N1 = 1$, then the equation exhibits a perfect linear relationship. In actual experiments, it is conventional to plot $\ln(Y)$ versus $\ln(A)$ values and to observe if the data points follow a linear relationship indicating high correlation between the variables. Similar regression plots between $\ln(Y)$ (Y1 to Y6) and $\ln(B)$ (B1 to B6) and $\ln(C)$ (C1 to C6) can be made to examine the correlations. A very high correlation coefficient (nearly one) is indicative of an excellent relationship between the dependent and independent variables.

From equations (2)–(5), the following modified expressions can be determined:

$$\begin{aligned} \ln(Y) &= \ln(K1) + N1 \ln(A), \\ \ln(Y) &= \ln(K2) + N2 \ln(B), \\ \ln(Y) &= \ln(K3) + N3 \ln(C). \end{aligned} \quad (6)$$

And

$$\ln Y = \{\ln(K1) + N1 \ln(A)\} + \{\ln(K2) + N2 \ln(B)\} + \{\ln(K3) + N3 \ln(C)\}. \quad (7)$$

Or

$$\ln Y = [\ln((K1) + \ln(K2) + \ln(K3))] + N1 \ln(A) + N2 \ln(B) + N3 \ln(C). \quad (8)$$

Or

$$[\ln Y - [\ln(K1) + \ln(K2) + \ln(K3)]] = N1 \ln(A) + N2 \ln(B) + N3 \ln(C)]. \quad (9)$$

The values of $\ln(K1)$, $\ln(K2)$, and $\ln(K3)$ can be ascertained from the intercepts on the Y-axis from individual $\ln(Y)$ versus $\ln(A)$ values, $\ln(Y)$ versus $\ln(B)$ values, and $\ln(Y)$ versus $\ln(C)$ plots.

Equation (9) is modified into multiple linear regression analyses and consists of solving algebraic equations with three unknown parameters. Furthermore, the Y values are modified as $[\ln(Y) - [\ln(K1) + \ln(K2) + \ln(K3)]]$ values. The numerical values of different modified Ys ($Y1, Y2, Y3$, etc.) are equated to the different A, B, and C values in the multiple linear regression analysis.

If there are a number of experimental data points (A, B, C, D, E, F, and G), then the individual graphs can be made with $\ln(Y)$ ($Y = Y1, \dots, Y6$) versus $\ln(A)$ ($A = A1, \dots, A6$) to determine the correlation coefficient values between Y and A. Similar plots can also be made with $\ln(Y)$ versus $\ln(B)$ and $\ln(Y)$ versus $\ln(C)$. Only correlation coefficients close to one should be included in the relationship equations.

The multiple linear regression analysis, with different combinations (ABC, ABD, ABE, ABF, ABG, BCD, BCE, BC, etc.) and the $N1, N2$, and $N3$ values obtained after solving the different equations, illustrates the influence of these individual parameters $N1, N2$, and $N3$ on the Y values. For example, if certain $N1$ or $N2$ or $N3$ values are negative, then they have no effect on Y. Further, a comparison of the numerical values of $N1, N2$, and $N3$ will highlight the relative influences from each variable on the Y values.

In the present experimental work, the compressive strength values were taken as dependent parameters (Y), while the molar ratios of Al/Si, Ca/Si, and Ca/(Si + Al) were taken as independent parameters (namely, A1, A2, and A3).

It is assumed that the power term associated with each reacting species (Al/Si, Ca/Si, and Ca/(Si + Al)) is related to the gel formation and thereby the strength of the samples (indicated in numerical values of power $N1, N2$, and $N3$). Also, a numerical value close to 1 is considered as optimum correlation. In actual practice, correlation coefficient calculations among each of the above-mentioned individual combinations with compressive strength should provide values higher than 0.95.

Determination of the Moles of Al/Si, Ca/Si, and Ca/(Si + Al) from the Chemical Compositions. It is pertinent to recognize that silica (SiO_2), alumina (Al_2O_3), and calcia (CaO) mainly participated in the formation of Al-Si gel, Ca-Si gel, and Ca-Si-Al gel, all of which contributed to the compressive strength of the final product.

2. Materials (Details of the Materials)

The chemical compositions of fly ash and GGBS slag are given in Table 2.

The XRD pattern and SEM images of the samples are given below (Figures 1–4).

2.1. Alkaline Solution. The alkaline activator was a combination of sodium hydroxide and sodium silicate solutions, where sodium hydroxide solution (of 98% purity) was used as alkaline activator along with sodium silicate ($\text{SiO}_2 = 31.0\%$, $\text{Na}_2\text{O} = 11.6\%$, and water = 57.4%). These sodium hydroxide solutions of required molarity (6 M = 240 gm and 12 M = 480 gm) were separately prepared. Sodium hydroxide solution of the required molarity and the sodium silicate in liquid state were then mixed and stored at room temperature before use.

2.2. Sample Preparation for Experimental Study. Fly ash and GGBS, with 10% variation by weight in dry condition, were pan-mixed. The mixture varied from 80% fly ash and 20% GGBS (F80G20) to 30% fly ash and 70% GGBS (F30G70) in six different compositions (A to F). The mixtures were activated by adding alkaline activator solutions (6 M and 12 M sodium hydroxide separately) and sodium silicate solution and thoroughly mixed.

The external source materials (fly ash and GGBS) were mixed in proportions as described above. Depending on the mix proportion, the alkali activator solution quantities were varied. The minimum addition of solution was for the higher fly ash-based compositions, while the maximum was for the higher GGBS-based compositions. The fresh mixtures of six different compositions (with 6 M sodium hydroxide molarity) and six other different compositions (with 12 M sodium hydroxide molarity) were cast in 50 mm × 50 mm × 50 mm steel moulds. On completion of 7 days and 28 days of curing, the cubes were tested for compressive strength as per standard testing methods, under exposure to ambient conditions (temperature 25°C to 27°C and humidity 65% to 70%). The resultant empirical model has been based on the experimental results of approximately 500 test samples.

3. Results

Considering the molar quantities of each of the chemicals present in the individual compounds, Table 3 summarizes the details of Al/Si, Ca/Si, and Ca/(Si + Al) mole in each individual batch compositions along with the compressive strengths.

The correlation coefficient between experimental compressive strength (Y) and the individual values of \ln , Al/Si ratio, \ln , Ca/Si ratio, and \ln , Ca/(Si + Al) ratio for 6 M and 12 M samples are given in Figures 5–7.

TABLE 1: Dependent and independent variables.

Sample names	Y (dependent variable)		A (independent variable)		B (independent variable)		C (independent variable)	
A		Y1		A1		B1		C1
B		Y2		A2		B2		C2
C		Y3		A3		B3		C3
D		Y4		A4		B4		C4
E		Y6		A5		B5		C5
F		Y6		A6		B6		C6

TABLE 2: Chemical analysis of fly ash and GGBS (in weight %).

Material	SiO ₂	Al ₂ O ₃	CaO	MgO	MnO ₂	TiO ₂	Iron oxide	LOI
Fly ash	60.8	26.34	1.17	1.31	—	—	4.21	1.8
GGBS	34.79	20.07	32.78	7.23	—	—	0.87	0.1

3.1. *Intercept (K Value) Determination.* Table 4 highlights the regression equations of the different experimental samples.

3.2. *Multiple Linear Regression Analysis.* It is observed that the correlation coefficient values for the different compositions are all nearly one and therefore multiple linear regression analysis was performed with all the different combinations with three different variables N1, N2, and N3. Figures 8–13 display the plots of N1, N2, and N3 with different combinations for 28 days of curing.

Table 5 brings out the trend of silica, alumina, and calcia moles and the ratios of Al/Si, Ca/Si, and Ca/(Si + Al) in the four combinations considered.

4. Analysis and Discussion

4.1. *Analysis of N1 Values Both with Increasing Molarity of Alkaline Solution and with Increasing Compositions from A to F.* Figures 8 and 9 corroborate N1 (related to Al/Si composition) variations with both increasing molarity and increasing compositions for 28 days of curing. However, with regard to the composition dependence, it is noticed (Figure 9) that the compositions 2(B + C + D) and 3(C + D + E) are critical as there is a fall in N1 values (representing fall in strength). The average chemical compositions were SiO₂ (0.7–0.8 mol), Al₂O₃ (0.23 mol), and CaO (0.27–0.33 mol). It may therefore be reasonable to conclude that a change in mechanism of strength development of the cubes occurred around this composition. This is found to be true for both 7 days' and 28 days' curing periods.

4.2. *Analysis of N2 Values Both with Increasing Molarity of Alkaline Solution and with Increasing Compositions from A to F.* Values of N2 (related to strength development by Ca/Si ratios) exhibited a general negative trend with regard to both the increasing molarity and the increasing compositions. The negative values indicated that they played no role in the strength development process. Here also it is noted that the middle compositions have shown negative values with regard to both the increasing molarity and the increasing combinations of compositions (compositions 2 and 3).

4.3. *Analysis of N3 Values Both with Increasing Molarity of Alkaline Solution and with Increasing Compositions from A to F.* Figure 12 shows the distribution of N3 values of Ca/(Al + Si) ratio with respect to the strength under increasing molarity of alkaline solution. It is shown that the middle compositions (comp. B and C) demonstrate positive trend with regard to strength for both 7 days' and 28 days' curing. These compositions, in fact, exhibited negative N2 values. It is deduced that the loss in strength in these compositions due to negative N2 values is compensated by positive N3 values. Also, compositions 1 and 4 show negative values indicating that N3 values in these compositions have played no role in strength development. Figure 13 shows the effect of composition on strength at different molarities. It is again observed that the middle compositions showed positive N3 values, while compositions 1 and 4 showed negative values in both low molarity and high molarity and also with increasing curing period. The composition where such strength changeovers in the mechanism have occurred was not unique and was dependent on many other factors such as activity of the reacting source materials which vary depending on their place of origin.

It may be noted that combinations 2 and 3 exhibited wide variations in relationship between compressive strength and N1, N2, and N3 values in the different samples. This could be interpreted as indirect evidence of the formation of transient Ca-Si based combinations and/or Ca-Al based combinations or some other unknown transient phase formations as reported by Pulgalia and Mondal [11] influencing compressive strength. While combinations 1 and 4 exhibited variations in mean and standard deviations of different experimental parameters (within acceptable 3%–5% variations), combinations 2 and 3 represented variations beyond 5%. However, the nature of the qualitative relationships as represented by variations in compositions with variations in compressive strength has suggested that the analytical results can be satisfactorily explained with the help of statistical tools like correlation coefficients and multiple linear regression analysis.

5. Summary

The study conducted several experiments to determine the alkali concentration in a fly ash-GGBS geopolymer combination with varied molar concentrations of 6 mol to 12 mol with increments of two mol in six different fly ash-GGBS combinations with a minimum of 20 percent and a maximum of 70 percent GGBS. Multiple linear regression analysis with compressive strength (as dependent

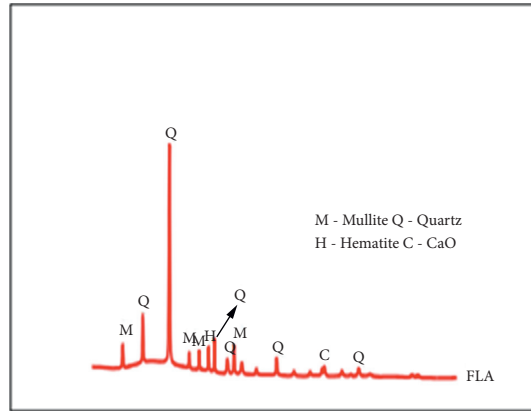


FIGURE 1: XRD pattern of fly ash.

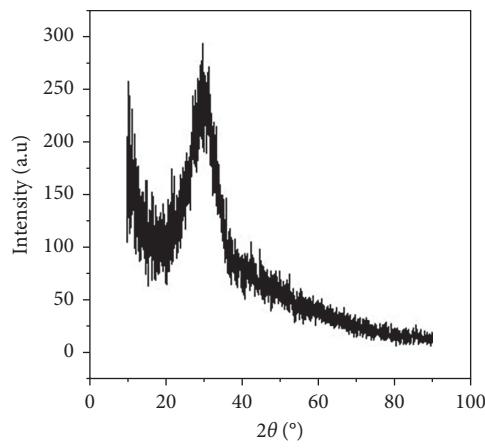


FIGURE 2: XRD pattern of GGBS.

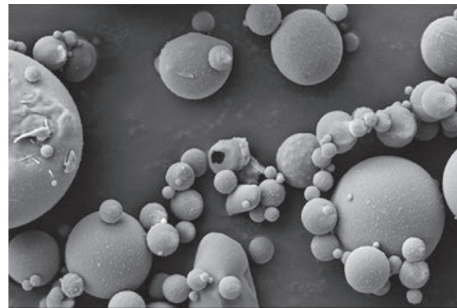


FIGURE 3: SEM image of fly ash.

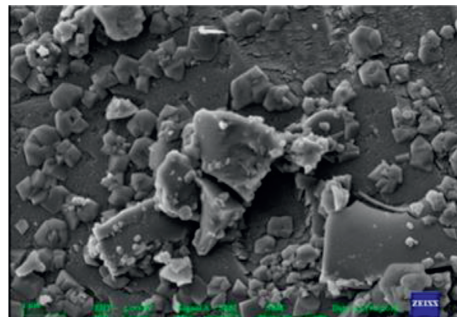


FIGURE 4: SEM image of GGBS.

TABLE 3: The details of Al/Si, Ca/Si, and Ca/(Si + Al) moles in each individual batch compositions and their compressive strengths.

Composition fly ash-GGBS (F-G)	Ln	Ln	Ln	Ln comp.	Ln comp.	Ln comp.	Ln comp.	Ln comp.	Ln comp.	Ln comp.	Ln comp.	Ln comp.	Ln comp.
	(Al/ Si)	(Ca/ Si)	(Ca/ Si + Al)	strength 7 days/(6 M) REVISED	strength 28 days/(6 M) REVISED	strength 7 days/(8 M) REVISED	strength 28 days/(8 M) REVISED	strength 7 days/ (10 M) REVISED	strength 28 days/ (10 M) REVISED	strength 7 days/ (12 M) REVISED	strength 28 days/(8 M) REVISED	strength 7 days/(10 M) REVISED	strength 28 days/(10 M) REVISED
80F/20G (A)	-1.30/	-1.63	-1.87	-27.66	-24.97	-28.14	-23.31	-27.8	-22.46	-23.23	-19.6	-23.31	-27.8
70F/30G (B)	-1.27/	-1.37	-1.62	-27.59	-24.88	-28.07	-23.11	-27.74	-22.31	-23.09	-19.32	-23.11	-27.74
60F/40G (C)	-1.24/	-1.08	-1.35	-27.1	-24.56	-27.57	-22.86	-27.26	-21.95	-22.91	-19.25	-22.86	-27.26
50F/50G (D)	-1.23/	-0.87	-1.14	-26.76	-24.15	-27.28	-22.62	-27.03	-21.89	-22.78	-19.21	-22.62	-27.03
40F/60G (E)	-1.20/	-0.65	-0.94	-26.58	-24.05	-27.05	-22.52	-26.74	-21.79	-22.50	-19.13	-22.52	-26.74
30F/70G (F)	-1.17/	-0.49	-0.77	-26.4	-23.96	-26.84	-22.37	-26.53	-21.58	-22.27	-18.87	-22.37	-26.53

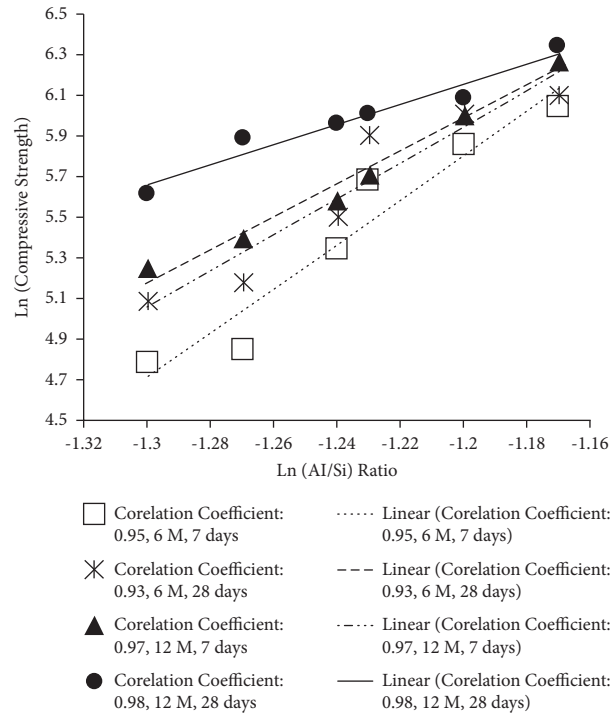


FIGURE 5: Correlation coefficient between experimental compressive strength and Ln, Al/Si ratio for 6 M and 12 M samples.

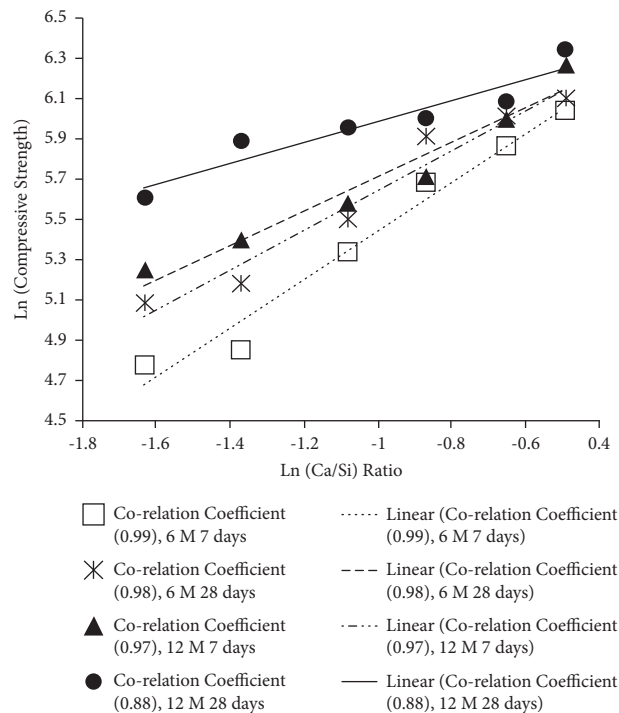


FIGURE 6: Correlation coefficient between experimental compressive strength and Ln, Ca/Si ratio for 6 M and 12 M samples.

parameter) and individual values of Al/Si, Ca/Si, and Ca/(Si + Al) ratios (as independent parameters) was performed. The study demonstrated that the strength of a geopolymer was dependent on gel formation from Al/Si ratio, Ca/Si ratio, and Ca/(Si + Al) ratio and brought out the role played in the setting process during curing.

6. Prospects, Challenges, Future Work, and Limitations

The industrial wastes are being produced in large quantities globally with no effective disposal solutions. In this context, the study has attempted to explain the role of fly ash and

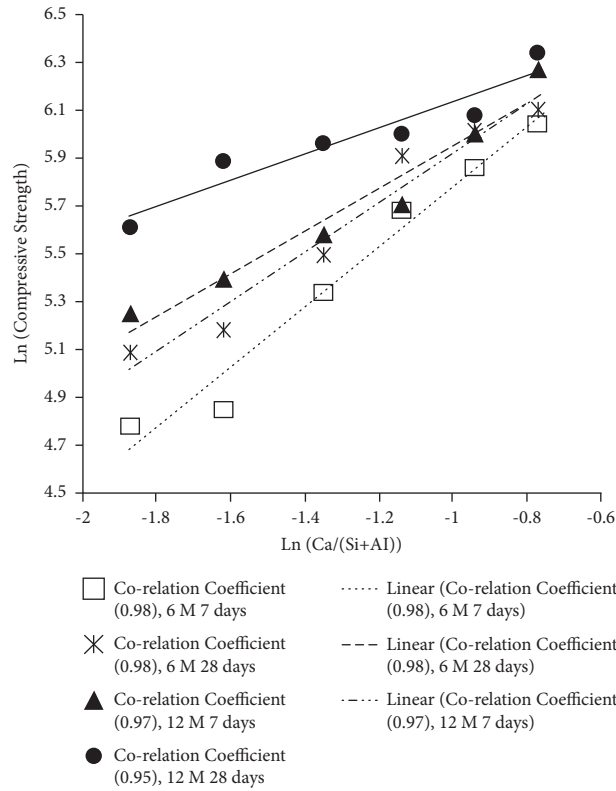


FIGURE 7: Correlation coefficient between experimental compressive strength and Ln, Ca/(Si + Al) ratio for 6 M and 12 M samples.

TABLE 4: Determination of K values from the linear regression equations.

Description of 6 mol samples	Linear regression equation	Numerical value of K to be subtracted from experimental compressive strength values
Al/Si, corr. coeff. = 0.95 (6 M, 7 days' strength)	$y = 18.84 + 10.86x$	
Ca/Si, corr. coeff. = 0.99 (6 M, 7 days' strength)	$y = 6.58 + 1.10x$	$18.84 + 6.58 + 7.02 = 32.44$
Ca/(Si + Al), corr. coeff. = 0.98 (6 M, 7 days' strength)	$y = 7.02 + 1.25x$	
Al/Si, corr. coeff. = 0.93 (6 M, 28 days' strength)	$y = 16.54 + 8.83x$	
Ca/Si, corr. coeff. = 0.98 (6 M, 28 days' strength)	$y = 6.57 + 0.90x$	$16.54 + 6.57 + 6.95 = 30.06$
Ca/(Si + Al), corr. coeff. = 0.98 (6 M, 28 days' strength)	$y = 6.95 + 1.03x$	
8 mol samples		
Al/Si, corr. coeff. = 0.97 (8 M, 7 days' strength)	$y = 19.18 + 11.11x$	
Ca/Si, corr. coeff. = 0.97 (8 M, 7 days' strength)	$y = 6.70 + 1.22x$	$19.18 + 6.70 + 7.09 = 32.97$
Ca/(Si + Al), corr. coeff. = 0.97 (8 M, 7 days' strength)	$y = 7.09 + 1.26x$	
Al/Si, corr. coeff. = 0.98 (8 M, 28 days' strength)	$y = 15.10 + 7.57x$	
Ca/Si, corr. coeff. = 0.88 (8 M, 28 days' strength)	$y = 6.59 + 0.83x$	$15.10 + 6.59 + 6.86 = 28.55$
Ca/(Si + Al), corr. coeff. = 0.95 (8 M, 28 days' strength)	$y = 6.86 + 0.86x$	
10 mol samples		

TABLE 4: Continued.

Description of 6 mol samples	Linear regression equation	Numerical value of K to be subtracted from experimental compressive strength values
Al/Si, corr. coeff. = 0.96 (8 M, 7 days' strength)	$y = 18.88 + 10.81x$	
Ca/Si, corr. coeff. = 0.97 (8 M, 7 days' strength)	$y = 6.73 + 1.17x$	$18.88 + 6.73 + 7.11 = 32.72$
Ca/(Si + Al), corr. coeff. = 0.95 (8 M, 7 days' strength)	$y = 7.11 + 1.22x$	
Al/Si, corr. coeff. = 0.96 (8 M, 28 days' strength)	$y = 14.39 + 6.91x$	
Ca/Si, corr. coeff. = 0.92 (8 M, 28 days' strength)	$y = 6.61 + 0.748x$	$14.39 + 6.61 + 6.85 = 27.85$
Ca/(Si + Al), corr. coeff. = 0.95 (8 M, 28 days' strength)	$y = 6.85 + 0.78x$	
12 mol samples		
Al/Si, corr. coeff. = 0.97 (12 M, 7 days' strength)	$y = 15.24 + 7.73x$	
Ca/Si, corr. coeff. = 0.97 (12 M, 7 days' strength)	$y = 6.46 + 0.74x$	$15.24 + 6.46 + 6.79 = 28.49$
Ca/(Si + Al), corr. coeff. = 0.97 (12 M, 7 days' strength)	$y = 6.79 + 0.86x$	
Al/Si, corr. coeff. = 0.98 (12 M, 28 days' strength)	$y = 12.10 + 4.95x$	
Ca/Si, corr. coeff. = 0.88 (12 M, 28 days' strength)	$y = 6.44 + 0.44x$	$12.10 + 6.44 + 6.67 = 25.21$
Ca/(Si + Al), corr. coeff. = 0.95 (12 M, 28 days' strength)	$y = 6.67 + 0.55x$	

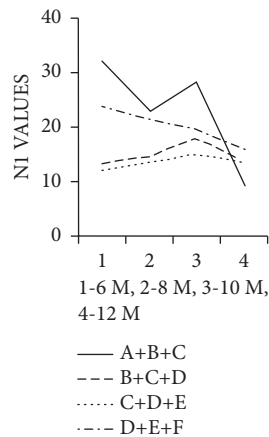


FIGURE 8: N1 values with increasing molarity (28 days' curing) combinations from A to F.

GGBS on compressive strength development by an empirical model. The major challenge for the researchers will be to find ways to increase the usage of these industrial wastes in proportion to their large production. The second challenge will be to accurately establish the individual/collective contributions of the waste constituents in the manufacture of construction materials without comprising on the

strength parameters. The scope of research work undertaken was limited to 6 M and 12 M. The study can be extended to cover 4 M, 8 M, and 14 M to validate the results of this study over a wider spectrum of research. Also, similar studies can be carried out on other industrial wastes such as metakaolin, silica fumes, slug, rice husk, and various mine wastes with different molarities.

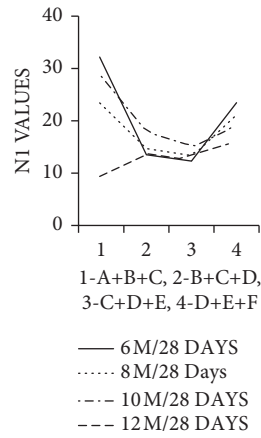


FIGURE 9: N1 values with increasing composition (28 days' curing) combinations from A to F.

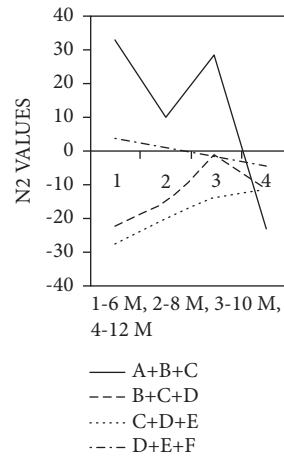


FIGURE 10: N2 values with increasing molarity of alkaline solution (28 days' curing).

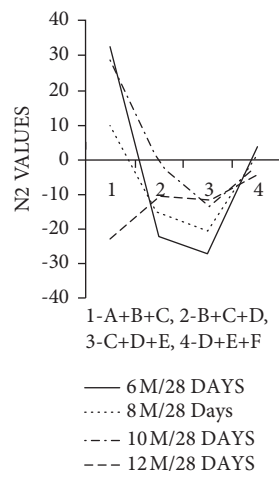


FIGURE 11: N2 values with increasing composition combinations from A to F (28 days' curing).

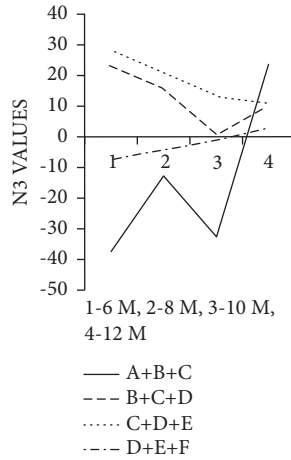


FIGURE 12: N3 values with increasing molarity alkaline solution (28 days' curing) combinations.

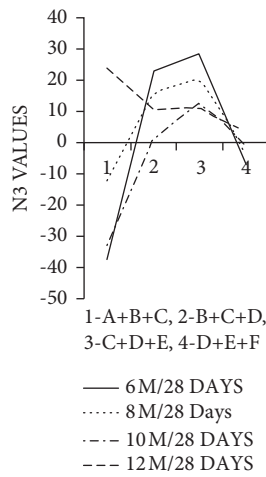


FIGURE 13: N3 values with increasing composition from A to F (28 days' curing).

TABLE 5: Trend of silica, alumina, and calcia moles and the ratios of Al/Si, Ca/Si, and Ca/(Si + Al).

Combinations	SiO2 mol	Al2O3 mol	CaO mol	Al/Si	Ca/Si	Ca/(Si + Al)
A + B + C (1)	0.87	0.24	0.22	0.28	0.25	0.20
B + C + D (2)	0.83	0.23	0.27	0.28	0.33	0.25
C + D + E (3)	0.78	0.23	0.33	0.29	0.42	0.32
D + E + F (4)	0.74	0.22	0.38	0.30	0.51	0.40

7. Conclusions

The proposed empirical model of the geopolymer reactions has drawn out the following conclusions:

(1) Depending on overall silica, alumina, and calcia ratios in the mix compositions, the compressive

strength changed and this aspect was found to be dependent on overall Al/Si, Ca/Si, and Ca/(Si + Al) ratios.

(2) The mix compositions (B and C) showed positive trend with regard to the compressive strength, for both 7 days' and 28 days' curing.

- (3) An interdependence between Ca/Si ratio and Ca/(Si + Al) ratios is found to exist. A fall in the strength due to Ca/Si ratio catalyzes the role of Ca/(Si + Al) to become more effective towards strength development of tested bricks.
- (4) The method proposed in the study, involving the combination of correlation coefficient and linear regression analysis, is considered useful to empirically capture the complex nature of geopolymerization.

Data Availability

The data used to support the findings of this study are included within the article, and further data or information required is available from the corresponding author upon request.

Conflicts of Interest

The authors declare that they have no conflicts of interest.

References

- [1] C. Shi and J. Qian, "High performance cementing materials from industrial slags - a review," *Resources, Conservation and Recycling*, vol. 29, no. 3, pp. 195–207, 2000.
- [2] C. Li, H. Sun, and L. Li, "A review: The comparison between alkali-activated slag (Si+Ca) and metakaolin (Si+Al) cements," *Cement and Concrete Research*, vol. 40, no. 9, pp. 1341–1349, 2010.
- [3] C. L. Nicholson, B. J. Murray, R. A. Fletcher, D. Brew, K. J. D. Mackenzie, and M. Schmücker, *Novel Geopolymer Materials Containing Borate Structural Units*, Vol. 31–33, World Congress Geopolymer, (Saint-Quentin), 2005.
- [4] J. Tailby and K. J. D. MacKenzie, "Structure and mechanical properties of aluminosilicate geopolymer composites with Portland cement and its constituent minerals," *Cement and Concrete Research*, vol. 40, no. 5, pp. 787–794, 2010.
- [5] V. Benavent, P. Steins, I. Sobrados, J. Sanz, D. Lambertin, and F. Frizon, "Impact of aluminium on the structure of geopolymers from the early stages to consolidated material," *Cement and Concrete Research*, vol. 90, pp. 27–35, 2016.
- [6] S. Alonso and A. Palomo, "Alkaline activation of metakaolin and calcium hydroxide mixtures: influence of temperature, activator concentration and solids ratio," *Materials Letters*, vol. 47, pp. 55–62, 2001.
- [7] P. Suraneni, S. Puligilla, E. H. Kim, X. Chen, L. J. Struble, and P. Mondal, "Monitoring setting of geopolymers," *Adv Civil Eng Mater*, vol. 3, pp. 177–192, 2014.
- [8] W. K. W. Lee and J. S. J. van Deventer, "The effect of ionic contaminants on the early-age properties of alkali-activated fly ash-based cements," *Cement and Concrete Research*, vol. 32, pp. 577–584, 2002.
- [9] C. K. Yip and J. S. J. van Deventer, "Microanalysis of calcium silicate hydrate gel formed within a geo-polymeric binder," *Journal of Materials Science*, vol. 38, no. 18, pp. 3851–3860, 2003.
- [10] X. Chen, A. Sutrisno, and L. Struble, "Effects of calcium on setting of metakaolin based geopolymer," *Journal of the American Ceramic Society*, vol. 101, pp. 957–968, 2018.
- [11] S. Pulgalia and P. Mondal, "Co-existence of aluminosilicate and calcium silicate gel characterized through selective dissolution and FTIR spectral subtraction," *Cement and Concrete Research*, vol. 70, pp. 39–49, 2015.
- [12] D. V. Dao, S. H. Trinh, H. B. Ly, and B. T. Pham, "Prediction of compressive strength of geopolymer concrete using entirely steel slag aggregates: novel hybrid artificial intelligence approaches," *Applied Sciences*, vol. 9, no. 6, p. 1113, 2019.
- [13] M. M. Yadollahi, A. Benli, and R. Demirboğa, "Prediction of compressive strength of geopolymer composites using an artificial neural network," *Materials Research Innovations*, vol. 19, no. 6, pp. 453–458, 2015.
- [14] F. Naseri, F. Jafari, E. Mohseni, W. Tang, A. Feizbakhsh, and M. Khatibinia, "Experimental observations and SVM-based prediction of properties of polypropylene fibres reinforced self-compacting composites incorporating nano-CuO," *Construction and Building Materials*, vol. 143, pp. 589–598, 2017.
- [15] M. M. Khotbehsara, B. M. Miyandehi, F. Naseri, T. Ozbakkaloglu, F. Jafari, and E. Mohseni, "Effect of SnO₂, ZrO₂, and CaCO₃ nano particles on water transport and durability properties of self-compacting mortar containing fly ash: experimental observations and ANFIS predictions," *Construction and Building Materials*, vol. 158, pp. 823–834, 2018.
- [16] B. Badarloo, A. Kari, and F. Jafari, "Experimental and numerical study to determine the relationship between tensile strength and compressive strength of concrete," *Civil Engineering Journal*, vol. 4, no. 11, pp. 2787–2800, 2018.
- [17] P. O. Awoyera, M. S. Kirgiz, A. Q. Vilorio, and D. Ovallos-Gazabon, "Estimating strength properties of geopolymer self-compacting concrete using machine learning techniques," *Journal of Materials Research and Technology*, vol. 9, no. 4, pp. 9016–9028, 2020.
- [18] M. Zhang, N. A. Deskins, G. Zhang, and R. T. Cygan, "Modeling the polymerization process for geopolymer synthesis through reactive molecular dynamics simulations," *Physical Chemistry C*, vol. 122, no. 12, pp. 6760–6773, 2018.
- [19] Y. F. Cui, K. K. Gao, and P. Zhang, "Experimental and statistical study on mechanical characteristics of geopolymer concrete," *Materials*, vol. 13, no. 7, p. 1651, 2020.
- [20] Y. F. Ling, *Proportion and Performance Evaluation of Fly Ash-Based Geopolymer and its Application in Engineered Composites*, PhD Dissertation, Iowa State University, Iowa, USA, 2019.
- [21] A. Siva Krishna and V. Ranga Rao, "Strength prediction of geopolymer concrete using ANN," *International Journal of Recent Technology and Engineering (IJRTE)*, vol. 7, no. 6C2, pp. 661–667, 2019.
- [22] H. Mehdizadeh, E. N. Kani, M. Hamideh, and E. N. Kani, "Modelling the influence of chemical composition on compressive strength behavior of alkali-activated phosphorus slag cement using statistical design," *Canadian Journal of Civil Engineering*, vol. 45, no. 12, pp. 1073–1083, 2018.

Research Article

Seismic Behavior of Elliptical Concrete-Filled Steel Tubular Columns under Combined Axial Compression and Cyclic Lateral Loading

YouWu Xu ¹, Jian Yao ¹, Feng Hu ², Ying Zhou ¹, and Shuai Jiang ¹

¹College of Civil Engineering and Architecture, Quzhou University, Quzhou 324000, China

²Ningbo Urban Planning and Design Institute, Ningbo 315000, China

Correspondence should be addressed to YouWu Xu; xuyouwu@zju.edu.cn

Received 11 August 2021; Revised 9 December 2021; Accepted 10 December 2021; Published 31 December 2021

Academic Editor: Rotana Hay

Copyright © 2021 YouWu Xu et al. This is an open access article distributed under the Creative Commons Attribution License, which permits unrestricted use, distribution, and reproduction in any medium, provided the original work is properly cited.

Elliptical concrete-filled steel tubular (CFST) column is a new form of CFST columns, consisting of an outer elliptical tube filled with concrete. Although the study on mechanical performance of the elliptical CFST members is receiving more and more attention, they have been limited to static behavior. Against this background, an experimental study on elliptical CFST columns was carried out under combined axial compression and cyclic lateral loading. The failure modes, hysteretic curves, skeleton curves, load carrying capacity, deformability, stiffness degradation, and energy dissipation ability was obtained and discussed. The test results indicated that the elliptical CFST columns possess excellent seismic performance and ductility. Valuable experimental data were provided for the formulation of the theoretical hysteresis model of the elliptical CFST columns.

1. Introduction

Concrete-filled steel tubular (CFST) columns have been widely used in modern construction due to their high strength, high ductility, and ease of construction [1]. In the past few decades, a lot of research on the performance and design of CFST members under various loading condition [2] have been published. As a new section form of CFST, elliptical CFST (Figure 1) has attracted the attention of many scholars from home and abroad. In recent years, research has been carried out on the mechanical behavior and design method of elliptical CFST.

Experimental study on elliptical CFST stub columns with different thickness and concrete strength subjected to axial loading have been conducted by Yang et al. [3], Zhao and Packer [4], Jamaluddin et al. [5], Chan et al. [6], and Cai et al. [7]. They proved the merits of elliptical CFST stub columns, but all the specimens they tested have the same aspect ratio ($a/b = 2.0$). With the development of manufacturing technology, the elliptical steel tube with various aspect ratios is available in construction practice. Thus, elliptical CFST stub

columns with an aspect ratio from 1.0 to 2.5 were tested by Zha et al. [8], Uenaka [9], Yi and Young [10], Liu et al. [11], and Xu et al. [12]. All the test results confirmed that the confinement effect decreases significantly with the increasing aspect ratio. Simultaneously, the eccentrically compressed columns were also investigated by Sheehan et al. [13], Zha et al. [14], Ren et al. [15], Qiu [16], and Yang et al. [17]. On the other side, systematic finite element analysis [18–22] was performed to simulate elliptical CFST columns subjected to concentric and eccentric axial compression. However, these studies mainly focused on static behavior, and research on their seismic behavior is very limited, which may hamper the application of elliptical CFST members in the seismic region. To the best of the authors' knowledge, the pseudostatic tests on 5 specimens with an aspect ratio of 2.0 conducted by Ma [23] proved the influence of concrete cube strength and axial compression ratio on the seismic behavior of elliptical CFST columns. Fang et al. [24] further considered the thickness of the elliptical steel tube, axial compression ratio, and the loading direction of horizontal loading; nevertheless, the aspect ratio of the specimens was

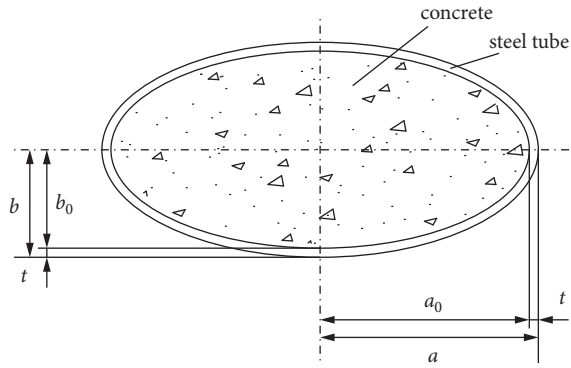


FIGURE 1: Cross-section of elliptical CFST.

also limited to 2.0. Consequently, the studies on the seismic behavior of elliptical CFST columns with an aspect ratio of a wider range is urgently needed.

In this study, 13 elliptical CFST columns tested under combined axial compression and cyclic lateral loading, the failure mode, carrying capacity, deformation capacity, hysteretic curve, and energy dissipation capacity of the specimens are discussed in detail. The experiment results may provide the reference to the analysis and application of elliptical CFST columns in the seismic area.

2. Experimental Program

2.1. Test Specimens. A total of 13 specimens were tested under combined constant axial compression and cyclic lateral loading through either the long or short axis. The key parameters were aspect ratio a/b , concrete cube strength f_{cu} , axial compression ratio n , and slenderness ratio λ_{sc} , which is expressed as column height h . As shown in Figure 2, each specimen consists of an elliptical CFST column, a top end-plate with a thickness of 20 mm, a series of stiffeners with a thickness of 10 mm welded to the top end-plate and the column, and a 30 mm thick bottom end-plate. The height of welding is $h_f = 6$ mm. According to the insite condition, rolling support on the vertical jack was not so smooth for sliding. So, the stiffeners were not used at the column base to achieve an equivalent calculation length to the cantilever component.

Table 1 provides the details of the 13 specimens, in which a is the length of semimajor axis, b is the length of semiminor axis, t is the thickness of the steel tube, and h is the height of the specimen. The specimen was named by the key parameters as follows: the aspect ratio-concrete cube strength-axial ratio. The letters m and l added at the end denote the medium (2050 mm) and the longest columns (2550 mm), and b for bending around the major axis. If there are no letters at the end, it means 1300 mm height and bending around the minor axis. The axial ratio was determined by equation (1), where N_d is the constant axial compression subjected by the specimen, A_c and A_s are the measured cross-sectional areas of the steel and concrete, respectively, and f_{co} and f_y are the cylinder strength, converted from the measured concrete cube strength [25] of concrete and yield strength of steel.

$$n = \frac{N_d}{(f_{co}A_c + f_yA_s)} \quad (1)$$

The elliptical steel tubes were cold-formed from the welded circular tubes (Figure 3). The material test of the steel tube was conducted according to [26], and the yield stress f_y and elastic modulus E_s of the steel tubes were obtained from the tensile coupon tests (Figure 4), as given in Table 1. Concrete grade C45, C60, C75, and C100 was used, and the mix proportions and tested cube strength are given in Table 2 and Table 1, respectively.

2.2. Instrument and Loading Procedure. As shown in Figure 5, the specimens were placed and tested within a reaction testing frame. The axial load was applied by a vertical hydraulic jack which is movable in the horizontal direction. The horizontal electrohydraulic servoactuator with a load capacity of 1000 kN and a stroke of 200 mm was used to apply the horizontal load. The push direction is defined as positive direction.

Eight LVDTs were used to measure the critical displacements. LVDT 1-2 were used to measure the translational movement of the foundation beam, LVDT 3-4 were used to measure the rotation of bottom end-plate. LVDT 5-6 were used to measure the columns end shortening within the 200 mm range. LVDT 7-8 were used to measure the translational displacement of the top of the column.

The loading procedure included three steps. A 30% of the designed vertical load was first preloaded to check the testing system. Then, the designed vertical load was applied and kept constant. Finally, the horizontal load was applied quasistatically following the JGJ/T standard loading protocol (JGJ/T 101-2015) [27], which is shown in Figure 6. Each of the first three levels of amplitude ($0.25 \Delta_y$, $0.5 \Delta_y$, and $0.75 \Delta_y$) was repeated only for one cycle, followed by three cycles at the rest levels of amplitude ($1 \Delta_y$, $2 \Delta_y$, $4 \Delta_y$, $6 \Delta_y$, $8 \Delta_y$, ...). The loading procedure was stopped when the horizontal load degraded to 85% of the peak load.

3. Test Results and Discussion

3.1. Failure Mode. Two typical failure modes were observed from the experimental results, namely, local buckling near the bottom end-plate and the fracture of the steel tube (Table 3 and Figure 7). For the local buckling failure mode, the outward bulges were observed at about 45 mm distance from the bottom end-plate. The bulges became more and more evident with the increase in the horizontal loading amplitude. Finally, the “elephant foot” failure mechanism was formed. For the fracture failure mode, the fracture occurred in the steel tube but not in the weld. It is mainly caused by stress concentration related to the heat-affected zone of the weld. The lack of stiffeners causes massive tension in the bottom of the steel tube, and it may be another reason for the fracture. More experiments or finite element analyses are needed to reveal the convinced reason.

In order to further investigate the damage condition of the concrete, end part of the steel tube was cut after the

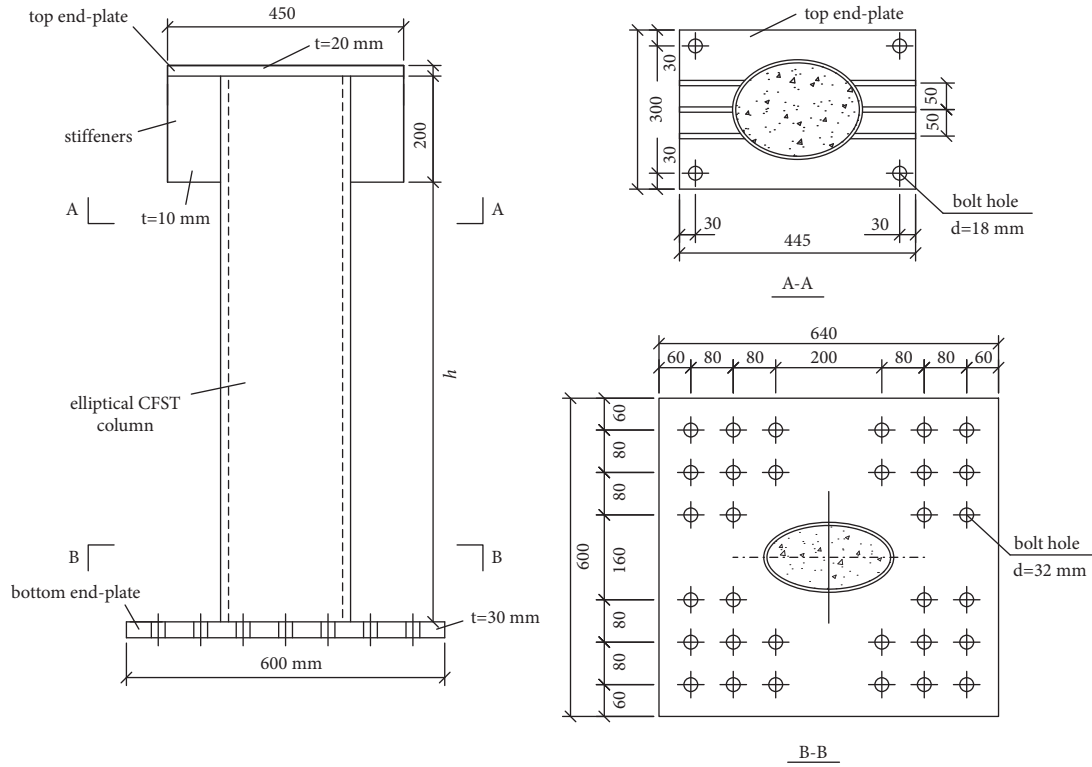


FIGURE 2: Details of the specimens.

TABLE 1: Measured information of the specimens.

Specimen	$2a$ (mm)	$2b$ (mm)	t (mm)	h (mm)	f_y (MPa)	E_s (MPa)	f_{cu} (MPa)
E1.0-C45-0.2	244.81	244.81	5.88	1300.00	334	190650	45.31
E1.3-C45-0.2	243.99	187.25	5.89	1300.00	370	214500	45.31
E1.8-C45-0.2	243.61	132.86	6.06	1300.00	389	214600	45.31
E2.3-C45-0.2	244.45	103.92	5.86	1300.87	409	203780	45.31
E1.8-C60-0.2	243.55	133.85	6.07	1300.57	389	214600	69.97
E1.8-C75-0.2	243.68	133.83	6.12	1300.63	389	214600	76.01
E1.8-C100-0.2	243.20	132.41	6.09	1302.67	389	214600	92.45
E1.8-C45-0.1	243.60	132.51	6.09	1305.50	389	214600	45.31
E1.8-C45-0.3	243.45	132.99	6.07	1300.27	389	214600	45.31
E1.8-C45-0.2m	243.52	133.04	6.04	2050.46	389	214600	45.31
E1.8-C45-0.2l	243.51	132.86	6.07	2552.31	389	214600	45.31
E1.8-C45-0.2b	243.73	132.37	6.08	1300.00	389	214600	45.31
E1.8-C45-0.3b	243.77	132.85	6.03	1300.33	389	214600	45.31

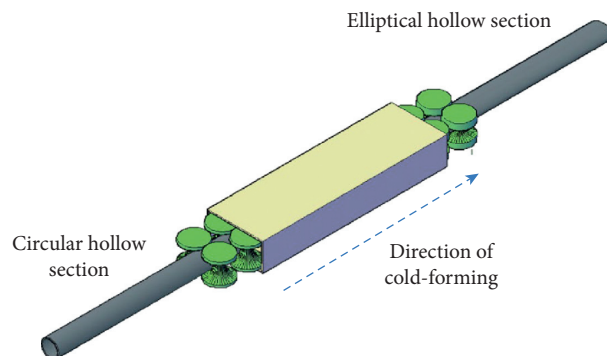


FIGURE 3: Cold-forming process (Chan et al. [6]).

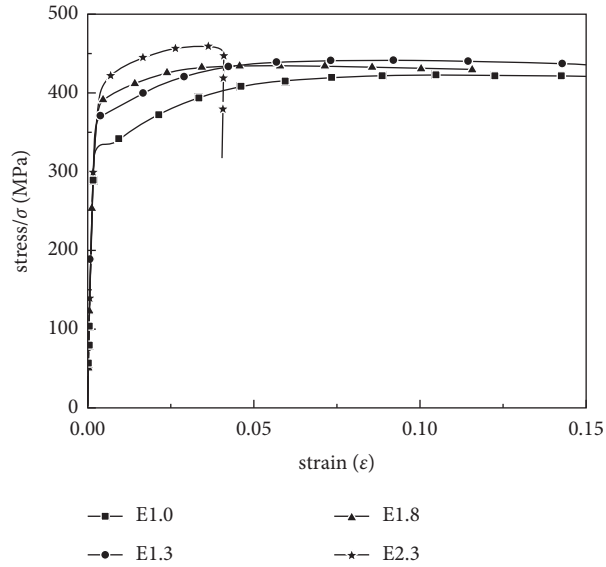


FIGURE 4: Stress-strain relationships of elliptical steel tubes.

TABLE 2: Mix proportions of the concrete (kg/m³).

Concrete grade	Cement	Water	Fines	Coarse	Fly ash	Water reducer	Expansion mixture
C45	363	191	790	851	176	0	55
C60	355	177	740	935	109	10	54
C75	375	150	720	1025	115	12	58
C100	390	132	700	1050	102	16	60

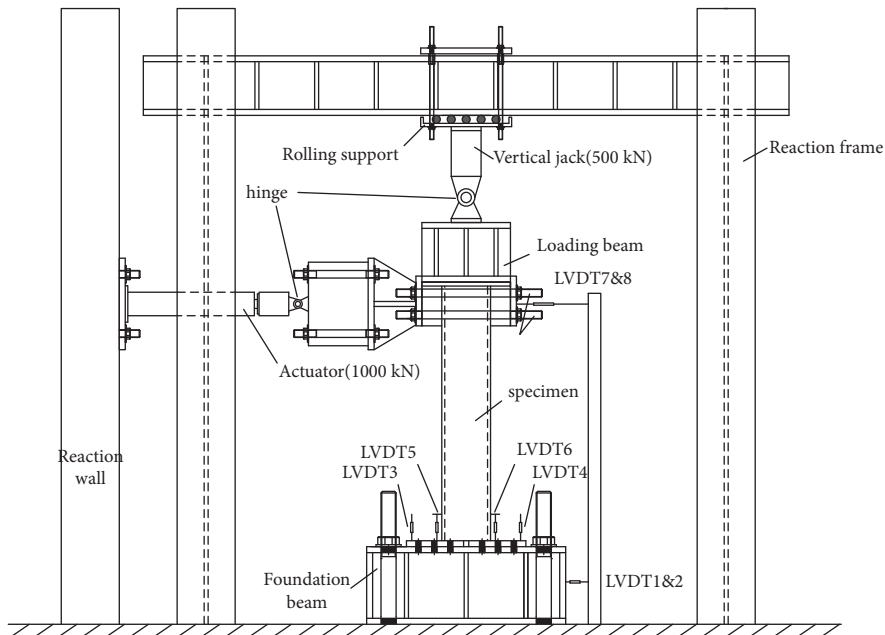


FIGURE 5: Test setup and instrumentation.

experiments, as shown in Figure 8. The concrete was crushed on both sides of the loading direction, and several minor cracks were observed.

3.2. *Hysteretic and Skeleton Curves.* The horizontal force-displacement responses of the ECFST beam-column specimens are shown in Figure 9. The test results showed that the

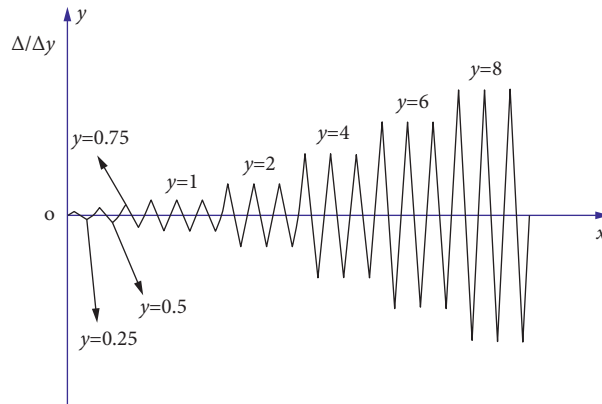


FIGURE 6: Horizontal loading procedure.

TABLE 3: Failure modes of the specimens.

Failure modes	Specimens
Local buckling	E1.3-C45-0.2, E1.8-C45-0.2, E1.8-C75-0.2, E1.8-C100-0.2, E1.8-C45-0.1, E1.8-C45-0.3, E1.8-C45-0.2m, E1.8-C45-0.2l, E1.8-C45-0.2b, E1.8-C45-0.3b
Fracture of the steel tube	E2.3-C45-0.2, E1.8-C60-0.2

*The loading procedure of E1.0-C45-0.2 was not completed due to the abrupt failure of the instrument.

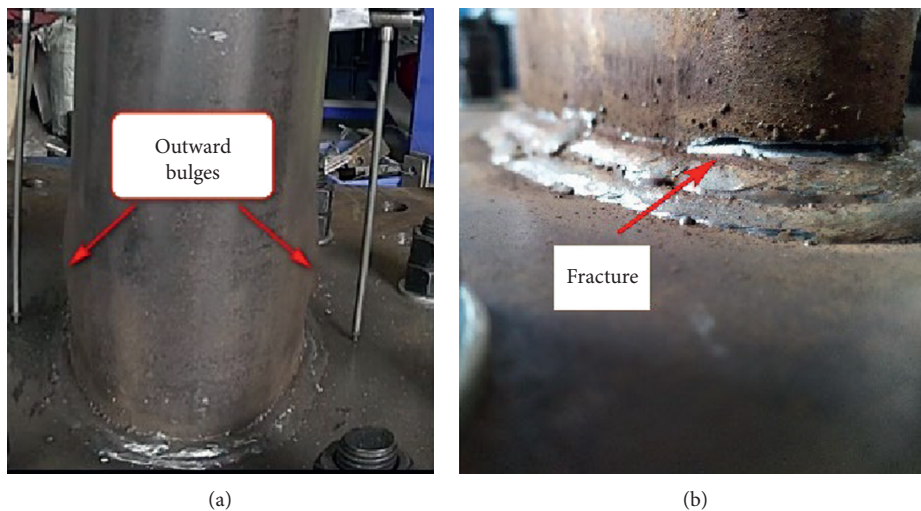


FIGURE 7: Typical failure modes of the specimens. (a) Local buckling. (b) Fracture of the steel tube.

hysteretic curves were chubbiness without pinching, which reveals the high-energy dissipation capacity. The hysteresis remains stable as the amplitude increase, and the three hysteresis loops at the same amplitude is almost the same at the earlier stage. When the applied load reaches the ultimate horizontal force P_{tw} , degradation of the hysteresis begins to be seen, in which case the loops became smaller as the cycle number increases.

Skeleton curves are shown in Figure 10 which were constructed by tracing the maximum loads at varying amplitudes. The skeleton curves consist of three stages, namely, the initial elastic ascending stage, nonlinear elastic-plastic ascending stage, and postpeak descending stage. As expected, concrete strength and axial compression ratio has a little effect on the initial stiffness, increasing the concrete strength tends to increase the ultimate load and speed up the



FIGURE 8: Typical damage mode of the concrete.

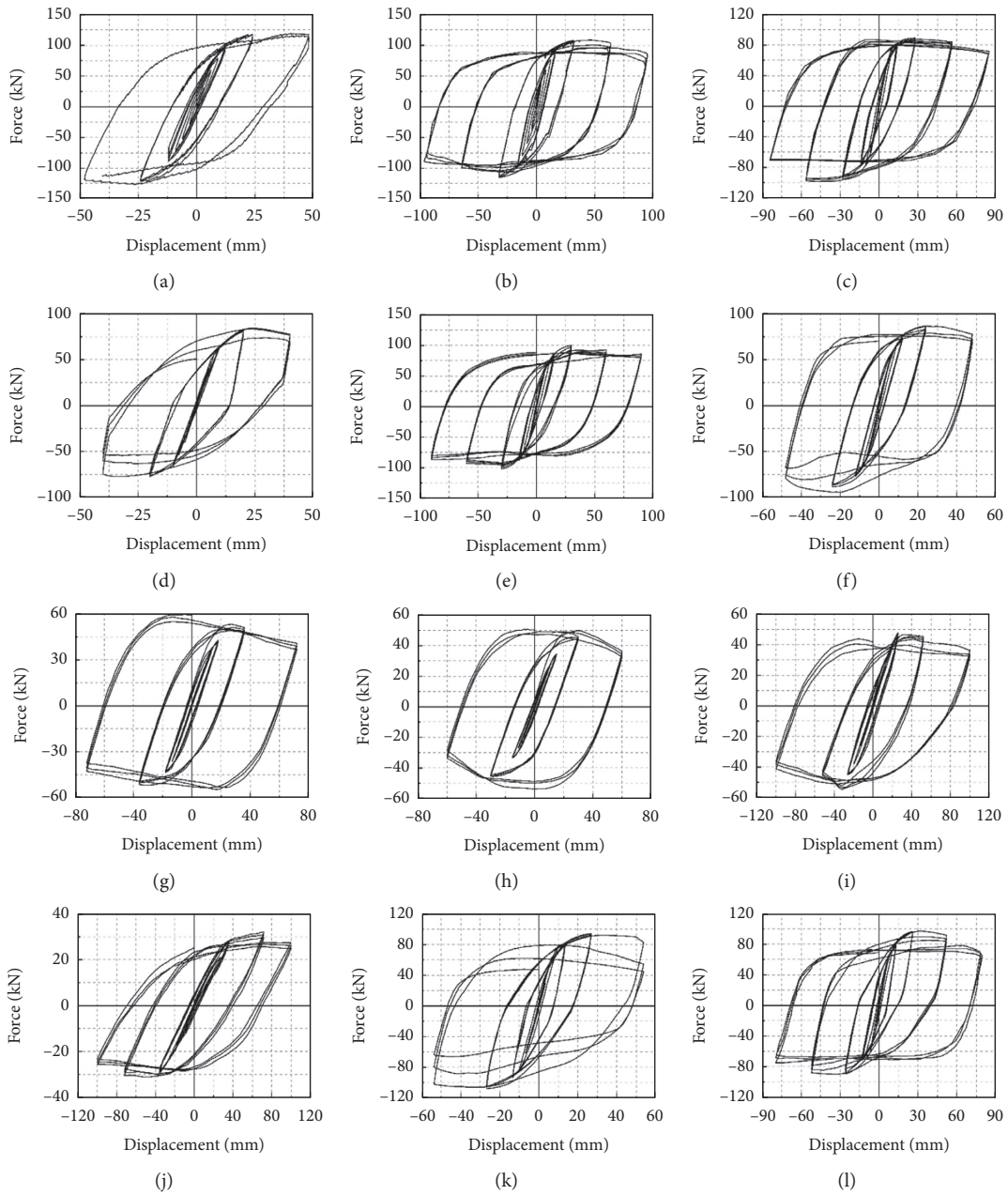


FIGURE 9: Continued.

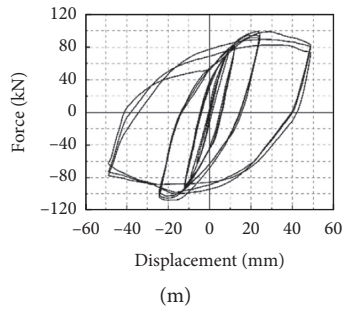


FIGURE 9: Horizontal force-displacement responses of the test specimens. (a) E1.0-c45-0.2. (b) E1.3-c45-0.2. (c) E1.8-c45-0.2. (d) E2.3-c45-0.2. (e) E1.8-c45-0.1. (f) E1.8-c45-0.3. (g) E1.8-c45-0.2b. (h) E1.8-c45-0.3b. (i) E1.8-c45-0.2m. (j) E1.8-c45-0.2l. (k) E1.8-c60-0.2. (l) E1.8-c75-0.2. (m) E1.8-c100-0.2.

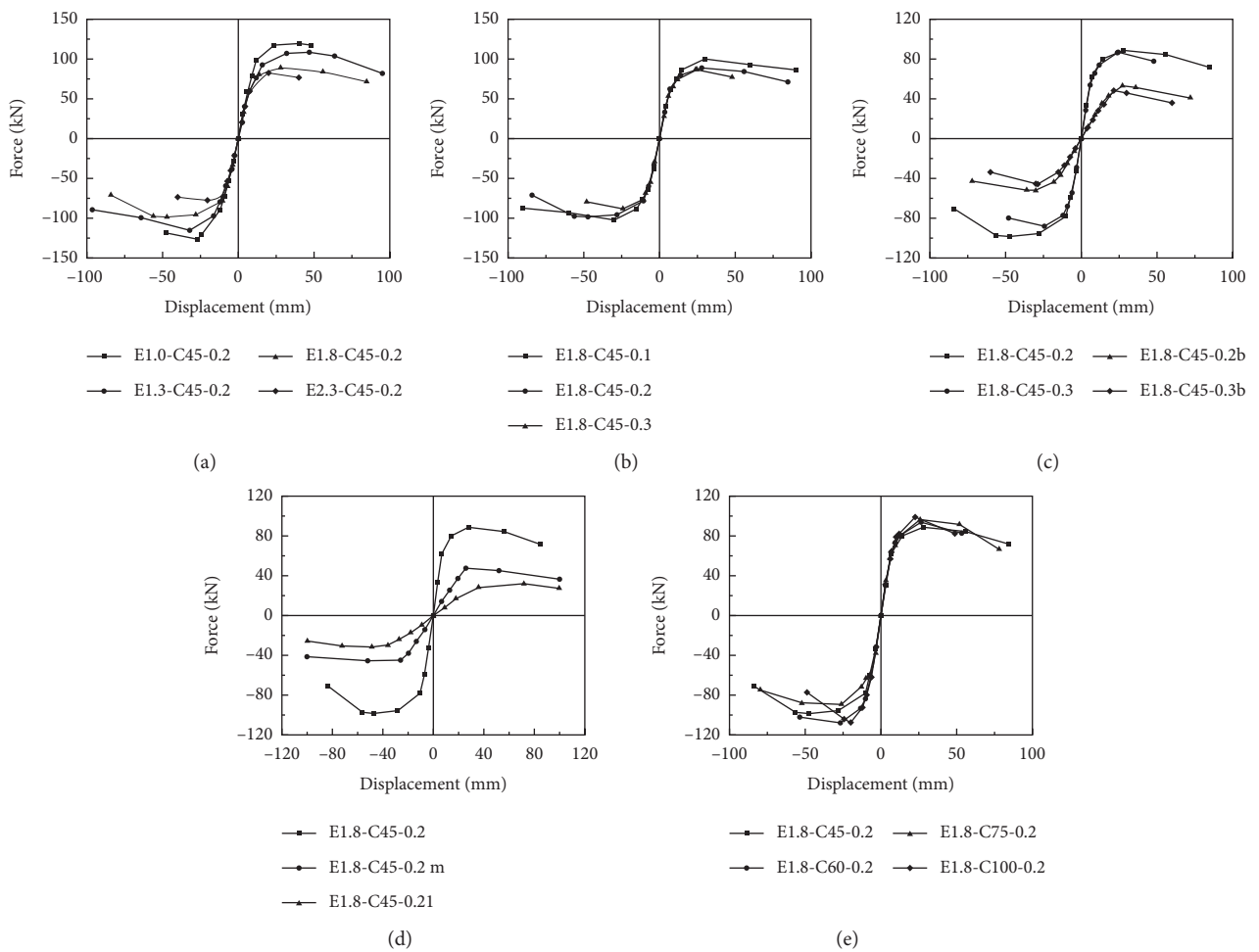


FIGURE 10: Skeleton curves of test specimens. (a) Variation of aspect ratio. (b) Variation of axial compression ratio. (c) Variation of bending axis. (d) Variation of slenderness ratio. (e) Variation of concrete strength.

degradation progress, and increasing the axial compression ratio is likely to decrease the ultimate load and speed up the degradation progress. The initial stiffness and ultimate load decreases with the increase of aspect ratio and slenderness

ratio, and the load drops faster as the aspect ratio increases and slenderness decreases. Major axis bending leads to the larger initial stiffness and ultimate load than minor axis bending, but it results in the more abrupt degradation.

3.3. Bearing Capacity and Ductility. The ductility of a beam-column is generally regarded as the deformation capacity which is defined as the ability to sustain plastic deformations before its failure. The most commonly used parameter is the ductility index μ and can be expressed as

$$\mu = \frac{\Delta_u}{\Delta_y}, \quad (2)$$

where Δ_{ul} and Δ_y are the ultimate displacement and yield displacement, respectively, Δ_{ul} is taken as the displacement at a 15% reduction in the ultimate load [28], and Δ_y is calculated from the skeleton curves using the average calculation of the geometric graphic method, equivalent elastoplastic energy method, and R. Park method [29], which are three common methods used to define the yield strength/load and yield displacement/drift. The ultimate load P_u , ultimate displacement Δ_{ul} obtained from the skeleton curves, and the calculated yield load P_y , yield displacement Δ_y are given in Table 4.

As given in Table 4, the ductility index of most specimens is greater than 3.0, indicating a highly ductile performance. The ductility index decreases with the increase of aspect ratio, axial compression ratio, slenderness ratio, and concrete strength. Major axis bending specimen has a greater ductility than that of minor axis bending specimen. The aspect ratio seems to have moderate influence on the ductility index.

3.4. Stiffness Degradation. As guided in the JGJ/T code (JGJ/T 101-2015, 2015), the average stiffness can be obtained from the horizontal load-displacement hysteretic curves, which can be expressed as

$$K_i = \frac{\sum_{j=1}^m (|(+P_{i,j})| + |(-P_{i,j})|)}{\sum_{j=1}^m (|(+\Delta_{i,j})| + |(-\Delta_{i,j})|)}, \quad (3)$$

where K_i is the average stiffness of the specimen at the i^{th} amplitude, $P_{i,j}$ is the maximum load of the j^{th} cycle at the i^{th} amplitude, $\Delta_{i,j}$ is the maximum displacement of the j^{th} cycle at the i^{th} amplitude, and (+) and (-) mean the positive and negative position, respectively.

Figure 11 shows the relationship of the average stiffness with horizontal displacement; it illustrates the stiffness degradation with increasing lateral displacement, which is highly correlated with the development concrete cracks. In all test specimens, the stiffness degradation is significant before the displacement reaches to $2\Delta_y$; as the displacement continues to increase, the stiffness degradation continues at a lower and continually decreasing rate. The aspect ratio, axial compression ratio, and concrete strength have a little effect on the stiffness degradation. The stiffness reduces faster when the specimen is less slender, and the stiffness degradation rate of minor axis bending specimen is lower than that of major axis bending specimen.

3.5. Energy Dissipation Capacity. The energy dissipation per cycle, E_i , is the area enveloped by each hysteretic loop [24, 30, 31]. Figure 12 shows the accumulated energy dissipation $\sum E_i$ of the 13 test specimens. As seen from the table, negligible energy dissipation is observed before the specimen reached the yield point, before which the specimens sustain limited plastic deformation. The energy dissipation starts to accumulate with the accumulated plastic deformation. The ultimate accumulated energy dissipation reflects the energy dissipation performance of the test specimens. As shown in Figure 12, specimens with a smaller aspect ratio, lower concrete strength, smaller axial compression ratio, and smaller slenderness ratio possess better energy dissipation capacity, and major axis bending specimens have a better performance on the energy dissipation quality than that of minor axis bending specimens.

4. Simplified Model of Force-Displacement Hysteretic Curve

4.1. Introduction of the Simplified Model. A kind of trilinear model is suggested by Han and Yang [32] and Han [2] to simplify the horizontal load P versus horizontal displacement Δ hysteretic relationship. A schematic view of the simplified force-displacement hysteretic relationship is shown in Figure 13. The key parameters of the model are listed as follows.

- (1) Elastic stiffness K_e is given by

$$K_e = \frac{3EI}{l_0^3}, \quad (4)$$

$$EI = E_s I_s + 0.6E_c I_c.$$

Here, l_0 is the effective length, E_c is the elastic modulus of concrete, which is expressed as $E_c = 4730\sqrt{f_{co}}$ [33], and I_s and I_c are the moment of inertia for the outer steel cross-section and inner concrete cross-section.

- (2) The ultimate strength P_u and corresponding displacement Δ_u can be given by

$$P_u = \begin{cases} \frac{1.05a_1 M_y}{h} & 1 < \xi_c \leq 4 \\ \frac{a_1(0.2\xi_c + 0.85)M_y}{h} & 0.2 < \xi_c \leq 1 \end{cases},$$

$$a_1 = \begin{cases} 0.96 - 0.002\xi_c & 0 \leq n \leq 0.3 \\ (1.4 - 0.34\xi_c)n + 0.1\xi_c + 0.54 & 0.3 < n < 1 \end{cases},$$

$$\Delta_u = \frac{6.74[(\ln r)^2 - 1.08 \ln r + 3.33]f_1(n)}{8.7 - s} \cdot \frac{P_u}{K_e},$$

$$f_1(n) = \begin{cases} 1.336n^2 - 0.044n + 0.8040 & 0 \leq n \leq 0.5 \\ 1.126 - 0.02n & 0.5 < n < 1 \end{cases} \quad (5)$$

TABLE 4: Load bearing capacity and ductility of test specimens.

Specimens		P_u (kN)	Δ_{ul} (mm)	P_y (kN)	Δ_y (mm)	μ
E1.0-C45-0.2	Positive direction	119.35	^a >48.05	103.02	14.78	>3.27
	Negative direction	126.49	^a >48.06	107.02	18.88	>2.55
	Average	122.92	^a >48.06	105.02	16.83	>2.91
E1.3-C45-0.2	Positive direction	108.43	80.30	94.17	17.47	>4.60
	Negative direction	115.05	69.00	99.65	18.15	3.81
	Average	111.74	74.65	96.91	17.81	4.21
E1.8-C45-0.2	Positive direction	89.03	75.72	75.95	12.37	6.14
	Negative direction	98.48	70.70	81.74	14.16	5.05
	Average	93.75	73.21	78.84	13.26	5.59
E2.3-C45-0.2	Positive direction	84.53	40.06	71.07	13.14	3.05
	Negative direction	77.35	40.08	67.73	11.59	3.46
	Average	80.94	40.07	69.40	12.37	3.26
E1.8-C60-0.2	Positive direction	94.22	53.66	80.44	12.35	4.38
	Negative direction	108.08	53.66	93.58	13.96	3.85
	Average	101.15	53.66	87.01	13.16	4.12
E1.8-C75-0.2	Positive direction	97.09	61.51	81.42	14.00	4.41
	Negative direction	89.78	76.72	72.22	13.87	5.61
	Average	93.44	69.11	76.82	13.93	5.01
E1.8-C100-0.2	Positive direction	99.32	45.88	84.14	13.18	3.48
	Negative direction	107.70	35.71	94.10	13.00	2.75
	Average	103.51	40.79	89.12	13.09	3.12
E1.8-C45-0.1	Positive direction	100.10	90.05	85.01	14.75	6.12
	Negative direction	102.10	90.01	86.94	14.77	6.11
	Average	101.10	90.03	85.97	14.76	6.11
E1.8-C45-0.3	Positive direction	86.70	48.01	74.22	12.27	3.92
	Negative direction	94.50	45.54	79.93	13.36	3.41
	Average	90.60	46.77	77.08	12.82	3.66
E1.8-C45-0.2m	Positive direction	47.58	78.14	45.97	25.00	3.13
	Negative direction	54.64	49.83	51.93	30.00	1.66
	Average	51.11	63.99	48.95	27.50	2.39
E1.8-C45-0.2l	Positive direction	32.00	99.78	28.82	40.19	2.48
	Negative direction	31.20	95.19	29.13	35.50	2.68
	Average	31.60	97.49	28.97	37.85	2.58
E1.8-C45-0.2b	Positive direction	54.70	56.68	48.00	22.57	2.51
	Negative direction	52.00	66.26	45.94	21.39	3.10
	Average	53.35	61.47	46.97	21.98	2.81
E1.8-C45-0.3b	Positive direction	48.50	44.35	47.08	21.00	2.11
	Negative direction	45.60	46.70	39.63	22.06	2.12
	Average	47.05	45.52	43.36	21.53	2.12

^aThe loading procedure of E1.0-C45-0.2 was not completed due to the abrupt failure of the instrument.

Here, $\xi_c = A_s f_y / A_c f_{ck} = \alpha \cdot f_y / f_{ck}$ is the steel confinement factor, in which f_{ck} is the prism compressive strength of concrete [25], $\alpha = A_s / A_c$ is the steel ratio, $r = \lambda_{sc} / 40$, and $s = f_y / 345$.

(3) Stiffness of the descending stage K_T is given by

$$K_T = \frac{0.03 \cdot f_2(n) \cdot f(r, \alpha) \cdot K_e}{c^2 - 3.39c + 5.41},$$

$$f_2(n) = \begin{cases} 3.043n - 0.21 & 0 \leq n \leq 0.7, \\ 1.57 + 0.5n & 0.7 < n < 1, \end{cases} \quad (6)$$

$$f(r, \alpha) = \begin{cases} (8\alpha - 8.6)r + 6\alpha + 0.9 & r \leq 1, \\ (15\alpha - 13.8)r + 6.1 - \alpha & r > 1, \end{cases}$$

where $c = f_{cu} / 60$.

4.2. Comparison of the Simplified Model with Tested Curve. To verify the validity of the above formulas, the force-displacement hysteretic relationships calculated with the simplified model were compared with those obtained from the experiment, as shown in Figure 14. It is proved that the simplified model predicts the force-displacement hysteretic relationship with reasonable accuracy. But discrepancies also exist; the main difference may be caused by residual stress and the lack of stiffeners; thus, more experimental and finite element research studies are needed to establish the more accurate formulas of the force-displacement hysteretic relationships.

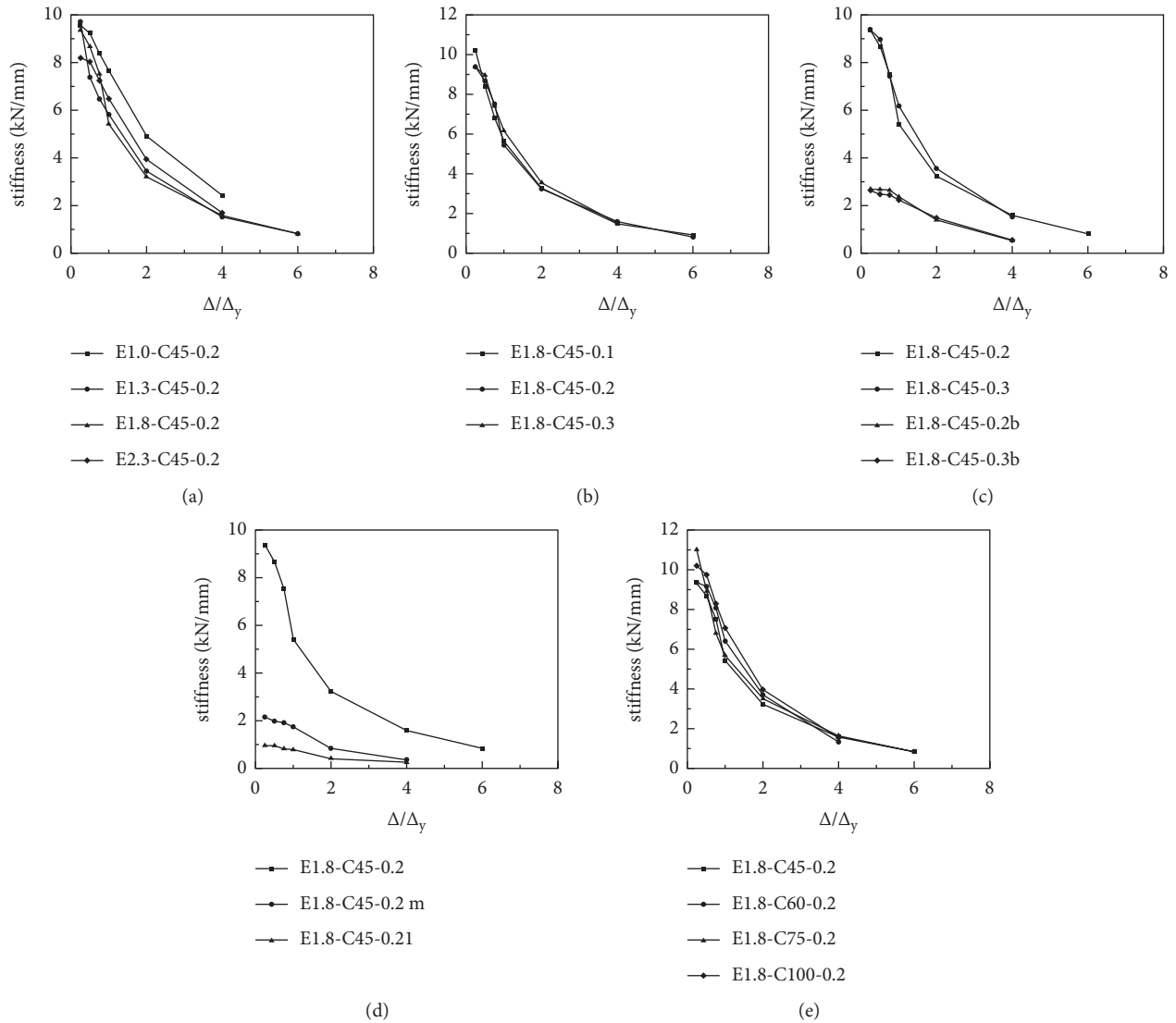


FIGURE 11: Stiffness of test specimens. (a) Variation of aspect ratio. (b) Variation of axial compression ratio. (c) Variation of bending axis. (d) Variation of slenderness ratio. (e) Variation of concrete strength.

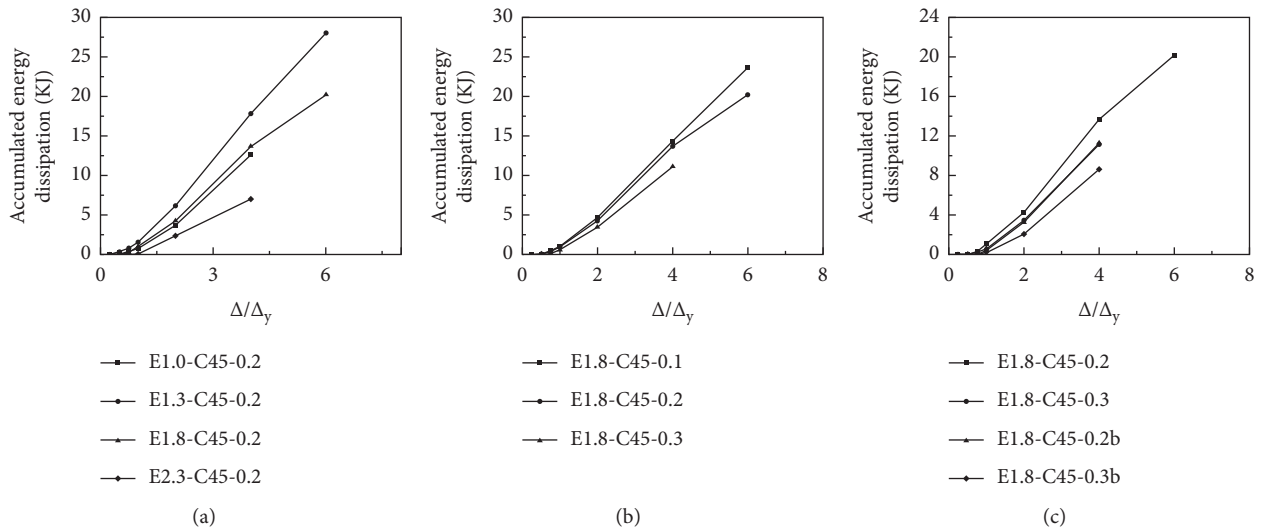


FIGURE 12: Continued.

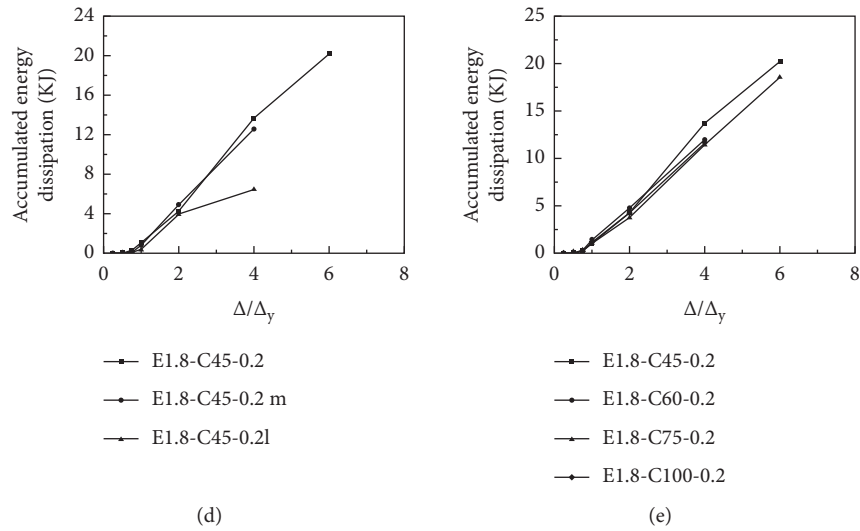


FIGURE 12: Accumulated energy dissipation of test specimens. (a) Variation of aspect ratio. (b) Variation of axial compression ratio. (c) Variation of bending axis. (d) Variation of slenderness ratio. (e) Variation of concrete strength.

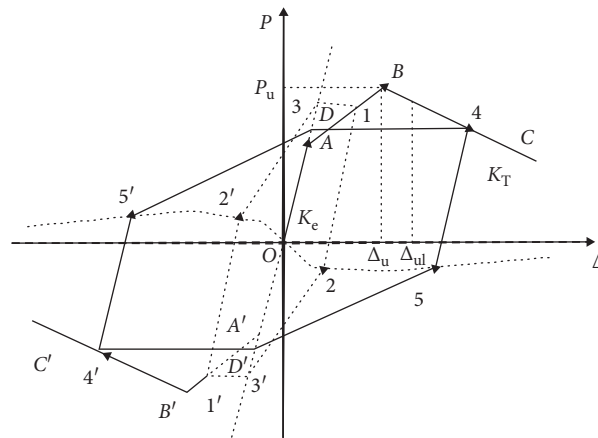


FIGURE 13: Simplified force-displacement relationship.

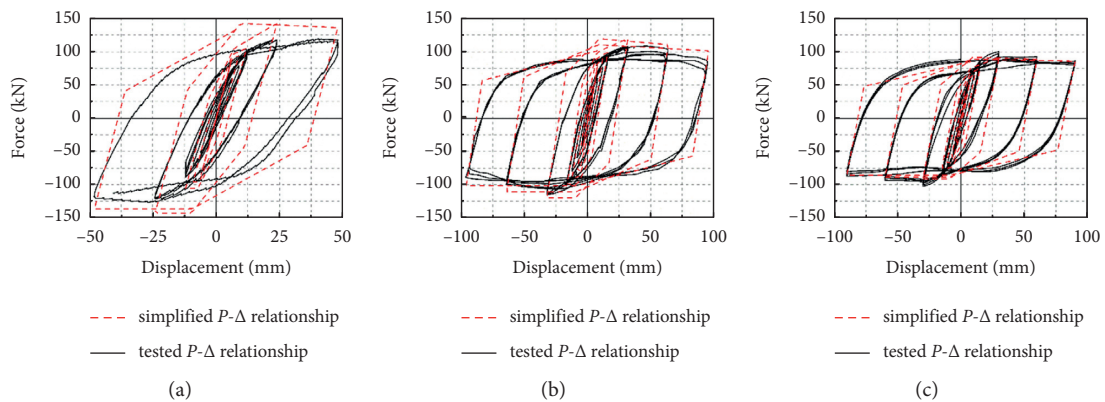


FIGURE 14: Continued.

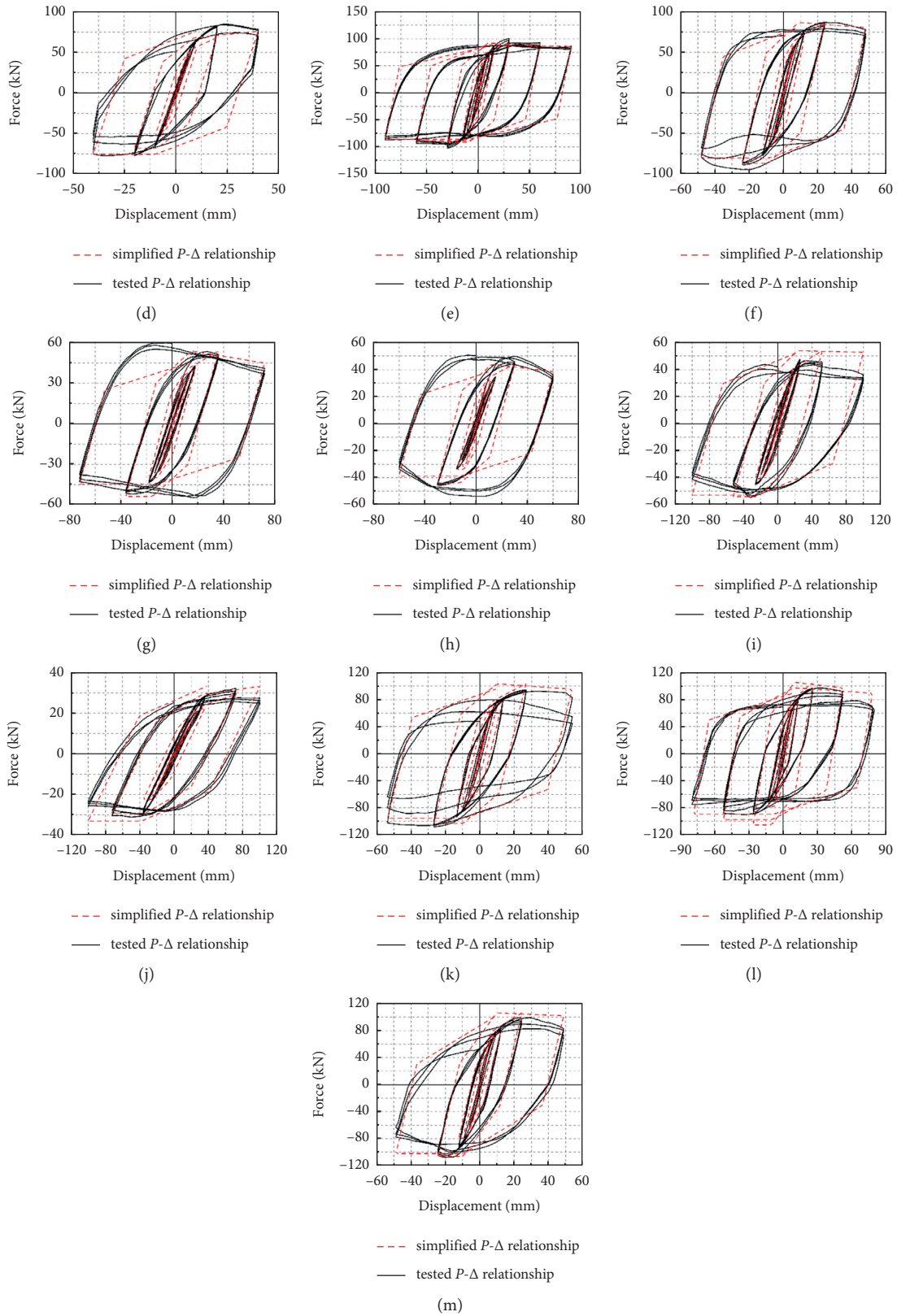


FIGURE 14: Comparison of simplified $P-\Delta$ relationship with tested $P-\Delta$ relationship. (a) E1.0-c45-0.2. (b) E1.3-c45-0.2. (c) E1.8-c45-0.2. (d) E2.3-c45-0.2. (e) E1.8-c45-0.1. (f) E1.8-c45-0.3. (g) E1.8-c45-0.2b. (h) E1.8-c45-0.3b. (i) E1.8-c45-0.2m. (j) E1.8-c45-0.2l. (k) E1.8-c60-0.2. (l) E1.8-c75-0.2. (m) E1.8-c100-0.2.

5. Conclusions

This study has focused on the seismic performance of elliptical CFST beam-columns under combined axial compression and cyclic lateral load. The main conclusions are summarized as follows:

- (1) Most of the specimens fail in local buckling, but there are individual specimens that failed in abrupt fracture of the steel tube, which reveals the stiffeners must be used at the column base.
- (2) The horizontal load and displacement hysteretic curves of all specimens are chubbiness without obvious pinching. Almost all specimens show good plastic deformation capacity and energy dissipation performance, which indicate that the elliptical CFST beam-column has good seismic performance, and it can be applied in the seismic area.
- (3) The ultimate loads increase with the increasing concrete strength, but decrease with the increasing aspect ratio, axial compression ratio, and slenderness ratio. The ultimate load of major axis bending specimens is notably larger than that of minor axis bending specimens.
- (4) The ductility index decreases with the increasing concrete strength, axial compression ratio, and slenderness ratio. The ductility index of major axis bending specimens is notably larger than that of minor axis bending specimens. The aspect ratio seems to have no markable influence on ductility index.
- (5) The energy dissipation capacity increases with the decreasing aspect ratio, concrete strength, axial compression ratio and slenderness ratio. The energy dissipation capacity of major axis bending specimens is significantly larger than that of minor axis bending specimens.
- (6) The simplified trilinear force-displacement model proposed by Han [2, 32] for rectangular and circular CFST beam-columns is also suitable for predicting the force-displacement hysteretic relationship of elliptical CFST beam-columns.
- (7) Further studies on the seismic performance of elliptical CFST should conduct for design and engineering practice, including the influence of residual stress, the modified force-displacement model, and detailed parametric analysis.

Data Availability

The data used to support the findings of this study are available from the corresponding author upon request.

Conflicts of Interest

The authors declare that they have no conflicts of interest.

Acknowledgments

This research was financially supported by the Fundamental Research Funds for Quzhou University (BSYJ202012) and the Zhejiang Provincial Natural Science Foundation (LY18E080014).

References

- [1] L.-H. Han, W. Li, and R. Bjorhovde, "Developments and advanced applications of concrete-filled steel tubular (CFST) structures: Members," *Journal of Constructional Steel Research*, vol. 100, pp. 211–228, 2014.
- [2] L. H. Han, *Concrete Filled Steel Tubular Structures—Theory and Practice*, China Science Publishing & Media Ltd, Beijing, China, 3th edition, 2016.
- [3] H. Yang, D. Lam, and L. Gardner, "Testing and analysis of concrete-filled elliptical hollow sections," *Engineering Structures*, vol. 30, no. 12, pp. 3771–3781, 2008.
- [4] X. L. Zhao and J. A. Packer, "Tests and design of concrete-filled elliptical hollow section stub columns," *Thin-Walled Structures*, vol. 47, no. 6-7, pp. 617–628, 2009.
- [5] N. Jamaluddin, D. Lam, X. H. Dai, and J. Ye, "An experimental study on elliptical concrete filled columns under axial compression," *Journal of Constructional Steel Research*, vol. 87, pp. 6–16, 2013.
- [6] T.-M. Chan, Y.-M. Huai, and W. Wang, "Experimental investigation on lightweight concrete-filled cold-formed elliptical hollow section stub columns," *Journal of Constructional Steel Research*, vol. 115, pp. 434–444, 2015.
- [7] Y. Cai, W.-M. Quach, M.-T. Chen, and B. Young, "Behavior and design of cold-formed and hot-finished steel elliptical tubular stub columns," *Journal of Constructional Steel Research*, vol. 156, pp. 252–265, 2019.
- [8] X. X. Zha, G. B. Gong, and X. C. Liu, "Study on behavior of concrete filled elliptical steel tube members part I: short and long columns under axial compression," *Adv. Steel Constr.* vol. 9, no. 2, pp. 90–107, 2013.
- [9] K. Uenaka, "Experimental study on concrete filled elliptical/oval steel tubular stub columns under compression," *Thin-Walled Structures*, vol. 78, pp. 131–137, 2014.
- [10] S. Yi and B. Young, "Experimental investigation of concrete-filled cold-formed steel elliptical stub columns," in *Proceedings of the 16th International Symposium for Tubular Structures*, Melbourne, Australia, December, March 2017.
- [11] F. Liu, Y. Wang, and T.-m. Chan, "Behaviour of concrete-filled cold-formed elliptical hollow sections with varying aspect ratios," *Thin-Walled Structures*, vol. 110, pp. 47–61, 2017.
- [12] Y. W. Xu, J. Yao, and X. Sun, "Cold-formed elliptical concrete-filled steel tubular columns subjected to monotonic and cyclic axial compression," *Advances in Structural Engineering*, vol. 23, no. 7, pp. 1383–1396, 2020.
- [13] T. Sheehan and X. H. Dai, T. M. Chan and T. M. Chan, "Structural response of concrete-filled elliptical steel hollow sections under eccentric compression," *Engineering Structures*, vol. 45, pp. 314–323, 2012.
- [14] X. X. Zha, G. B. Gong, and X. C. Liu, "Study on behavior of concrete filled elliptical steel tube members part 2: under bending and eccentric compression," *Adv. Steel Constr.* vol. 9, no. 2, pp. 108–123, 2013b.

- [15] Q.-X. Ren, L.-H. Han, D. Lam, and W. Li, "Tests on elliptical concrete filled steel tubular (CFST) beams and columns," *Journal of Constructional Steel Research*, vol. 99, pp. 149–160, 2014.
- [16] W. Qiu, *Beam-column behaviour of concrete-filled elliptical hollow sections*, Ph.D. Dissertation, Imperial College London, London, UK, 2017.
- [17] H. Yang, F. Q. Liu, T. M. Chan, and W. Wang, "Behaviours of concrete-filled cold-formed elliptical hollow section beam-columns with varying aspect ratios," *Thin-Walled Structures*, vol. 120, pp. 9–28, 2017.
- [18] X. Dai and D. Lam, "Numerical modelling of the axial compressive behaviour of short concrete-filled elliptical steel columns," *Journal of Constructional Steel Research*, vol. 66, no. 7, pp. 931–942, 2010.
- [19] X. H. Dai, D. Lam, N. Jamaluddin, and J. Ye, "Numerical analysis of slender elliptical concrete filled columns under axial compression," *Thin-Walled Structures*, vol. 77, pp. 26–35, 2014.
- [20] W. Qiu, F. McCann, A. Espinos, M. L. Romero, and L. Gardner, "Numerical analysis and design of slender concrete-filled elliptical hollow section columns and beam-columns," *Engineering Structures*, vol. 131, pp. 90–100, 2017.
- [21] J. F. Wang, Q. H. Shen, H. Jiang, and X. B. Pan, "Analysis and design of elliptical concrete-filled thin-walled steel stub columns under axial compression," *Int. J. Steel Struct.* vol. 18, no. 2, pp. 365–380, 2018.
- [22] M. Ahmed and Q. Q. Liang, "Computational simulation of elliptical concrete-filled steel tubular short columns including new confinement model," *Journal of Constructional Steel Research*, vol. 174, Article ID 106294, 2020.
- [23] X. F. Ma, "Research on seismic performance test and calculation methods of elliptical concrete filled steel tube," Master Dissertation, Hefei University of Technology, Hefei, China, 2019.
- [24] C. Fang, F. Zhou, Z. Y. Wu, and F. C. Wang, "Concrete-filled elliptical hollow section beam-columns under seismic loading," *Journal of Structural Engineering*, vol. 146, no. 8, Article ID 04020144, 2020.
- [25] Z. Y. Chen, J. Q. Zhu, and P. G. Wu, *High Strength concrete and its Application*, Tsinghua University Press Ltd, Beijing, China, 1992.
- [26] Gb/T. 228.1-2010, *Metallic Materials-Tensile Testing-Part 1: Method of Test at Room Temperature*, China Standard Press, Beijing, China, 2010.
- [27] Jgj/T 101, *Specification for Seismic Test of Buildings*, China Architecture & Building Press, Beijing, China, 2015.
- [28] X. Z. Zhao, F. P. Wen, Y. Y. Chen et al., "Experimental study on the static performance of steel reinforced concrete columns with high encased steel ratios," *Struct Des Tall Spec*, vol. 27, no. 15, p. e1536, 2018.
- [29] Y. B. Wu, "The experimental study of concealed bracings impact on seismic behavior of steel high-strength concrete low shear walls," Master Dissertation, Chongqing University, Chongqing, China, 2011.
- [30] C. Fang, F. Zhou, and W. Wu, "Performance of elliptical hollow sections under combined compression and cyclic bending," *Journal of Structural Engineering*, vol. 144, no. 8, Article ID 04018102, 2018.
- [31] C. Fang, F. Wang, C. Wang, and Y. Zheng, "Cyclic behavior of oval hollow section (OHS) beam-columns," *Thin-Walled Structures*, vol. 161, Article ID 107430, 2021.
- [32] L.-H. Han and Y.-F. Yang, "Cyclic performance of concrete-filled steel CHS columns under flexural loading," *Journal of Constructional Steel Research*, vol. 61, no. 4, pp. 423–452, 2005.
- [33] ACI, *Building code requirements for structural concrete and commentary*, American Concrete Institute, Farmington Hills, MI, USA, 2011.

Research Article

The Normal Force Characteristic of a Novel Magnetorheological Elastomer Based on Butadiene Rubber Matrix Compounded with the Self-Fabricated Silly Putty

Fei Guo,¹ Chengbin Du ,² and Guojun Yu³

¹School of Civil Engineering and Architecture, Anhui Polytechnic University, Wuhu 241000, China

²Department of Engineering Mechanics, Hohai University, Nanjing 210098, China

³Faculty of Civil Engineering and Mechanics, Jiangsu University, Zhenjiang 212013, China

Correspondence should be addressed to Chengbin Du; cbdu@hhu.edu.cn

Received 15 October 2021; Accepted 29 November 2021; Published 14 December 2021

Academic Editor: Rotana Hay

Copyright © 2021 Fei Guo et al. This is an open access article distributed under the Creative Commons Attribution License, which permits unrestricted use, distribution, and reproduction in any medium, provided the original work is properly cited.

In this paper, a novel magnetorheological elastomer (MRE) was prepared by dispersing carbonyl iron particles (CIPs) into a composite matrix compounded by butadiene rubber (BR) and self-fabricated Silly Putty. The rate-sensitive and magneto-induced characteristics of normal force were experimental investigated to discuss the working mechanism. The results demonstrated that the normal force increased with the compression rate and the mass fraction of boron-silicon copolymer added to the composite matrix due to the formation of the more and more B-O cross bonds which could be blocked in the C-C cross-linked network of BR. Meanwhile, the magneto-induced normal force was positively correlated with the applied magnetic field strength and the compression strain due to the decreased gap between the centers of soft magnetic particles and the increased particle intensity of magnetization. Moreover, the magneto-induced normal force continued to enhance with the increase of compression strain because the CIP chains fixed in the C-C cross-linked network could bend to a radian and CIP chains in B-O cross-linked network could rupture to form more stable and intensive short-chain structures. Besides, a simplified model was deduced to characterize the mechanism of the generation of the magneto-induced normal force. Furthermore, the normal force varied stably with the oscillatory shear strain (less than 9%) at different magnetic induction intensities and suddenly reduced when the applied oscillatory shear strain was more than 9%.

1. Introduction

Magnetorheological elastomer (MRE) is an intelligent material by dispersing micron-sized carbonyl iron particles (CIPs) into traditional rubber or thermoplastic matrix uniformly [1–3]. Different applied magnetic field strengths can control the dynamic mechanical properties such as the obtained MRE's storage modulus and damping factor [4, 5]. Because of the exhibited magnetorheological effect, this intelligent and safe material can be widely used in dampers [6, 7], soft armors [8], impact absorbers [9–12], and other applications such as shielding [13, 14], force sensing [15, 16], and medical systems [17, 18]. However, due to the contradiction between the magnetorheological effect and mechanical properties induced by cross-linking degree of

polymer rubber matrix [19], it is challenging to obtain MRE samples with excellent magnetorheological effect. Besides, MRE usually works in shear mode; the occurrence of shear behavior is perpendicular to the magnetic induction line direction, so the level of MRE shear modulus is far less than the vertical modulus. Furthermore, vertical extrusion deformation is limited; the tiny deformation can produce an excellent output strength. Therefore, it is essential to study the mechanical properties and magnetorheological effect of MRE in extrusion mode.

Silly Putty is a boron-silicon copolymer that can be stimulated to generate significant non-Newtonian behavior of shear stiffening performance. More nanocomposites based on Silly Putty have been intensively researched and discussed [20–22]. Xu et al. [23] fabricated a soft sandwich

structure consisting of two-layer Kevlar face sheets and a Silly Putty core. The results displayed that the storage modulus of Silly Putty, which was prepared by dispersing CaCO_3 particles into polyborodimethylsiloxane, increased by two to three orders of magnitude with the increasing shear frequency. The higher CaCO_3 content resulted in better shear-hardening behavior, which further enhanced the anti-impact performance of the sandwich structure. However, when micron-sized carbonyl iron particles (CIPs) are dispersed into Silly Putty, the properties of obtained magnetorheological Silly Putty (MRSP) can self-adapt to changes in the external stimuli environment and be controlled by different applied magnetic field strengths [24]. As a new kind of multifunctional material, it has aroused worldwide concern in recent years. Wang et al. [25] firstly prepared a novel multifunctional polymer composite (MPC) with different magnetic particles (CIP and Fe_3O_4), polydimethylsiloxane (PDMS), boric acid, and benzoyl peroxide (BPO). Besides, the mechanisms of “cross bonds” from the decomposition of cross-linking agent BPO and the magnetic particle chains induced by the magnetic field were introduced to describe the excellent multifunctional stimulus-response properties. Yao et al. [26] developed a novel magnet-induced aligning magnetorheological elastomer (MIMRE) based on ultrasoft polymeric matrix compounded of PDMS, boric acid, and chloroform to obtain the excellent magnetorheological effect and healing performance. Golinelli et al. [27] studied the behavior of magnetic Silly Putty first under a quasi-static compression and shear loading and second under dynamic shear loading; the results highlighted a strong dependence on the deformation rate the influence of the magnetic field was weak. However, in addition to applying single boron-silicon as the matrix, Wang [28] fabricated a novel magnetorheological shear-stiffening elastomer (MSTE) by dispersing CIPs into the shear-stiffening elastomer, which was synthesized by co-polymerization of shear-stiffening gel (STG) and methyl vinyl silicone rubber (VMQ). The results indicated that the content of STG could adjust the magnetic controllability and shear-stiffening performance of MSTE.

Besides, the influence factors and mechanisms of multifunctional properties for MRSP have also been extensively explored recently. Firstly, the rate-sensitive characteristic is mainly determined by the number of the B-O “cross bonds.” Liu et al. [29] prepared multifunctional magnetorheological gel (MMRG) samples with the mass ratio of pyroboric acid to PDMS varying from 0 to 0.6. The results demonstrated that the shear stiffening performance was positively correlated with the number of “cross bonds,” and when the numbers of molecular chains containing Si-O and Si-O-B were close (the mass ratio of pyroboric acid to PDMS reached 0.3), a substantial number of “cross bonds” were formed to result in excellent shear stiffening performance. Furthermore, the curing process, including temperature and time, were considered important factors influencing the shear stiffening performance [30]. In the study, curing temperature of 120°C and curing time of 30 min were selected to obtain the best shear stiffening performance. Moreover, additives such as CaCO_3 [31], graphene [32], and

carbon nanotubes [33, 34] were invested in the promotion of rate-sensitive characteristics. Simultaneously, the magnetorheological effect of MRSP induced by the externally imposed magnetic field is generally influenced by magnetic saturation of particles, magnetic particle size and dispersion, matrix properties, and additives similar to other magnetorheological materials [35–39]. The mechanism of formed chain or column structures [40–43] for magnetic particles along magnetic induction lines was usually employed to describe the magnetorheological effect.

Therefore, in this work, a novel MRE was prepared by dispersing CIPs into the BR matrix with the addition of self-fabricated Silly Putty. The rheometer testing system studied the normal force characteristic of the synthetic novel composite MRE. The testing results revealed that the developed novel MRE exhibited excellent magnetorheological effect and rate-dependent performance in extrusion mode. Furthermore, the content of Silly Putty played a pivotal role in improving the axial deformation ability of the novel MRE.

2. Experimental Methods

2.1. Materials. PDMS, boric acid, and absolute ethyl alcohol, purchased from Sinopharm Chemical Reagent Co. Ltd., Shanghai, China, were applied to fabricate the Silly Putty as well as the silicon-boron copolymer. Butadiene rubber (BR), vulcanization system including cross-linking agent benzoyl peroxide (BPO), zinc oxide (ZnO), stearic acid (SA), and accelerant, purchased from Sinopharm Chemical Reagent Co. Ltd., Shanghai, China, were applied to synthesize the composite matrix of MRE with Silly Putty. CIPs with different average particle sizes of 3.15, 3.5, and $3.65\ \mu\text{m}$ were purchased from Jiangsu Tianyi Ultra-fine Metal Powder Co. Ltd., Xuyi, China. Dioctyl phthalate (DOP), purchased from Sinopharm Chemical Reagent Co. Ltd., Shanghai, China, was used as the plasticizer. All the materials were analytically pure, and multifunctional properties were tested by MCR302 rheometer (Anton Paar Co., Austria).

MAT-3000S soft magnetic DC testing device was used to characterize the soft magnetic property of CIPs. The B - H magnetizing curves of different average particle sizes are displayed in Figure 1. It is shown that CIP with an average particle size of $3.5\ \mu\text{m}$ exhibits the best soft magnetic performance, which presents lower coercivity H_c (only $93.61\ \text{A/m}$ and testing magnetic field strength at $20,000\ \text{A/m}$) and the similar magnetization to CIP with an average size of $3.65\ \mu\text{m}$. Therefore, in this work, CIP with an average particle size of $3.5\ \mu\text{m}$ was selected as the filling particles of the novel MRE samples to obtain the apparent magneto-induced property and reduce the effect of remanent magnetism. The performance indexes of the selected CIP are shown in Table 1.

2.2. Preparation and Properties of the Novel MRE Samples. The process of preparing the novel MRE sample is shown in Figure 2. The first heating process led to the formation of Silly Putty as well as the silicon-boron copolymer. The second step generates the composite matrix by mixing BR and Silly Putty. The last step formed the novel MRE sample

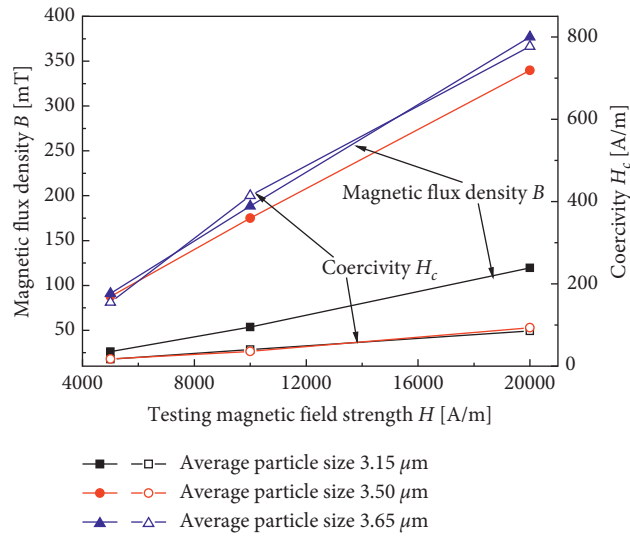


FIGURE 1: The testing B - H curve of CIPs with different average particle sizes.

TABLE 1: The major performance indexes of the CIP.

Fe content (%)	C content (%)	N content (%)	O content (%)	Average particle size (μm)	Apparent density	Tap density
98.10	0.74	0.90	0.26	3.5	$2.8 \text{ g}\cdot\text{cm}^{-3}$	$4.25 \text{ g}\cdot\text{cm}^{-3}$

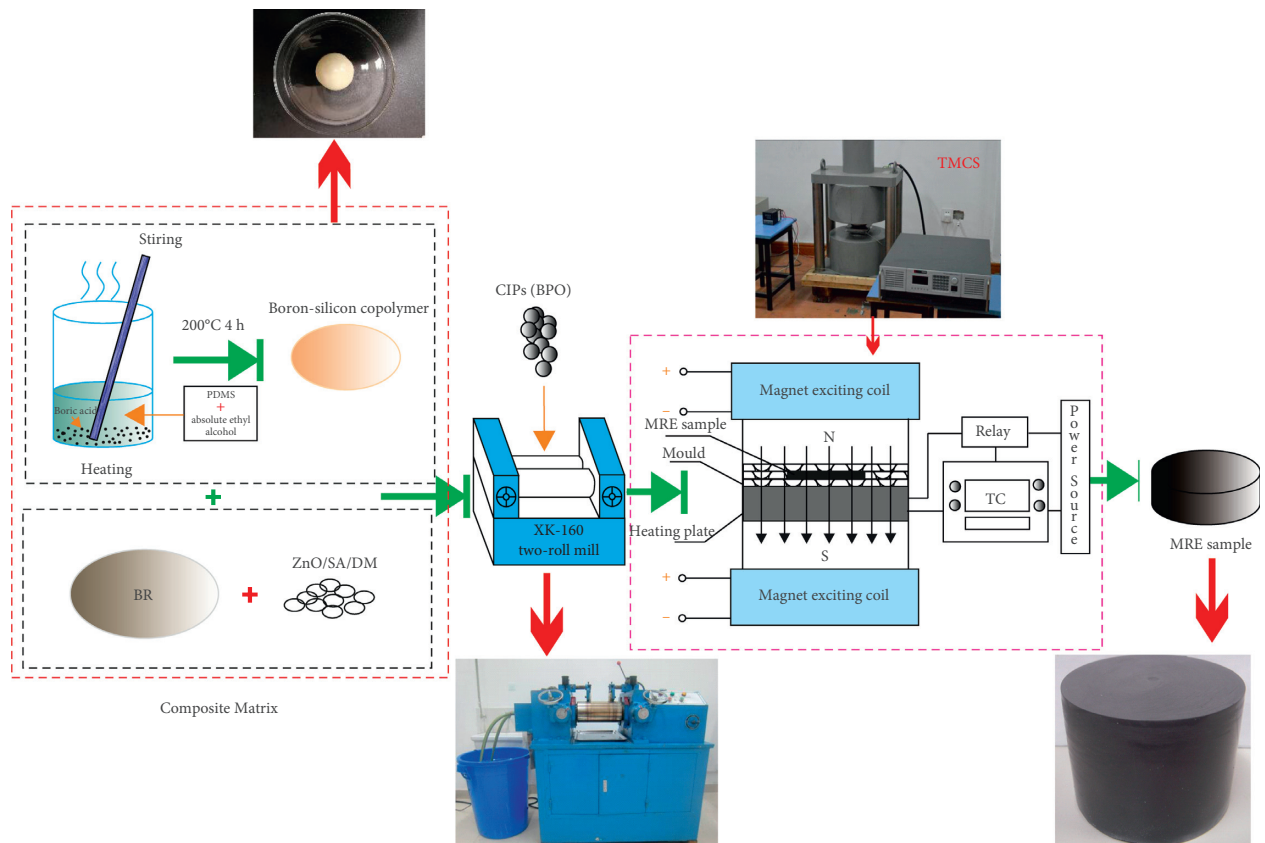


FIGURE 2: The preparation process of the novel MRE sample.

after the vulcanization process. The specific preparation steps were as follows:

- (1) Firstly, the mixture of a certain amount of PDMS, boric acid, and absolute ethyl alcohol was stirred in a beaker at room temperature until homogeneously. Then, the mixture was heated at 200°C for 4 hours and stirred every 15 min to keep the reaction adequate. During the process, the Si-O bond was broken, and the Si-O-B bond was formed. The boron-silicon copolymer was obtained after the viscous mixture was cooled to room temperature.
- (2) Next, the boron-silicon copolymer was mixed with BR in a two-roll mill (Nantong Hailite Rubber Machinery Inc., China; model XK-160) at room temperature. Additives such as ZnO, SA, accelerant, CIPs, and cross-linking agent BPO were added in sequence during the mechanical mixing method. Besides, plasticizer DOP was added in batches to improve the composite matrix plasticity.
- (3) Finally, the compound was vulcanized at 120°C for 20 min in the thermal-magnetic coupling system (TMCS) to form the novel MRE sample. The TMCS consisted of magnet exciting coils, temperature controller (TC), external power source, heating plate, and a relay. The mixed unvulcanized MRE sample in the mold was placed on the heating plate to be cured to form the novel MRE between the magnetic induction lines generated by the two magnet exciting coils when the external current was input. The previous research demonstrated that prestructured MRE exhibited anisotropic characteristics and a more excellent magnetorheological effect [44] due to an increasing number of particle chains and columns formed in the matrix under the applied magnetic field. During the curing process, the magnetic induction intensity was constant at 1 T. The MRE sample was prepared when the product cooled down to room temperature.

In the preparation process, the amount of CIPs added to the novel MRE is stationary. Before the magnetic saturation, the higher the mass ratio of CIPs to the matrix, the more pronounced the magnetorheological effect is, and the more sensitive the material is to a magnetic field. However, excessive CIPs will increase the initial modulus of the MRE, thus reducing the relative magnetorheological effect and the regulation range induced by the magnetic field. Therefore, in this work, the mass fraction of CIPs remains at 75%. Four groups of MRE samples are fabricated, and the compositions of the four groups of MRE samples are listed in Table 2. According to the proportioning principle of the traditional rubber process, the composite matrix is set to 100 phr. The percent of Silly Putty to the composite matrix from MRE-1 to MRE-4 is 0%, 10%, 25%, and 40% in sequence, respectively. Hence, MRE-1 is based on the pure BR matrix. Besides, to the boron-silicon copolymer, the mass fraction of PDMS, boric acid, and the absolute ethyl alcohol is 80%, 15%, and 5%, respectively.

In this work, the Hitachi S4800 scanning electron microscope (SEM) was used to observe the internal

microstructure of the MRE sample. The SEM images are displayed in Figures 3(a) and 3(b). It can be obtained from Figure 3(a) that CIPs are uniformly dispersed in composite matrix approximately, and the MRE sample presents isotropic feature when the prestructured magnetic field is in the close state. However, when the prestructured magnetic field is in the open state during the curing process, the CIPs are arranged in ordered chain structures along magnetic induction lines and MRE sample anisotropic feature from Figure 3(b).

The normal force characteristics of novel MRE samples were carried out by the MCR302 rheometer. During the testing procedure, a parallel plate PP20 with a diameter of 20 mm was used. The novel MRE sample was placed between the upper and lower plates. In this work, the normal force of each novel MRE sample was obtained by testing at quasi-static compression mode without magnetic field, quasi-static compression mode with the magnetic field, and dynamic oscillation shear mode. The rheological property of the fabricated boron-silicon copolymer is displayed in Figure 4. The fabricated Silly Putty exhibits apparent rate-sensitive performance. When the external rate-stimuli varies from 0 to 100 rad/s, the storage modulus of the boron-silicon copolymer generates the enhancement of three orders of magnitude.

3. Results and Discussion

3.1. The Normal Force at Quasi-Static Compression Mode without Magnetic Field. Under the condition of no external magnetic field and a constant compression rate, the normal force of the novel MRE samples on the rheometer plate can be detected. As for the fabricated four groups of the novel MRE samples from MRE-1 to MRE-4, Figure 5 shows the relationship between the normal force F_N and the gap h of parallel plates at the same compression rate of 100 $\mu\text{m/s}$. It is indicated that the normal force of all the MRE samples can reach the limit (50 N) of the rheometer when the samples are compressed to a specific state. Besides, as the mass fraction of the silicon-boron copolymer added in the matrix gradually increases, the compression deformation of the novel MRE samples gradually increases when it reaches the measurement limit of 50 N. For instance, the compression deformation of MRE-1 without the addition of silicon-boron copolymer is only 0.912 mm at the measured normal force limit of 50 N. However, the compression deformation of MRE-2 with the addition of 10% silicon-boron copolymer is 1.022 mm, while the compression of deformation of MRE-4 with the addition of silicon-boron copolymer exceeds 1.4 mm. It is because the modulus of the pure BR matrix is higher than the modulus of the silicon-boron copolymer. When the content of silicon-boron copolymer in the composite matrix is enhanced, the overall modulus of the novel MRE will reduce. Therefore, it depends on more significant compression deformation to achieve the same normal force. In addition, after each compression deformation, the novel MRE samples can generally recover to the initial deformation state. Hence, compared to the traditional MRE-1, it can improve the axial deformation capacity of the

TABLE 2: The composition of composite MRE samples (phr).

Samples	BR	Boron-silicon copolymer	CIPs	BPO	Vulcanization system, accelerant	ZnO	SA	DOP
MRE-1	100	0	645	5	5	3	2	100
MRE-2	90	10	645	5	5	3	2	100
MRE-3	75	25	645	5	5	3	2	100
MRE-4	60	40	645	5	5	3	2	100

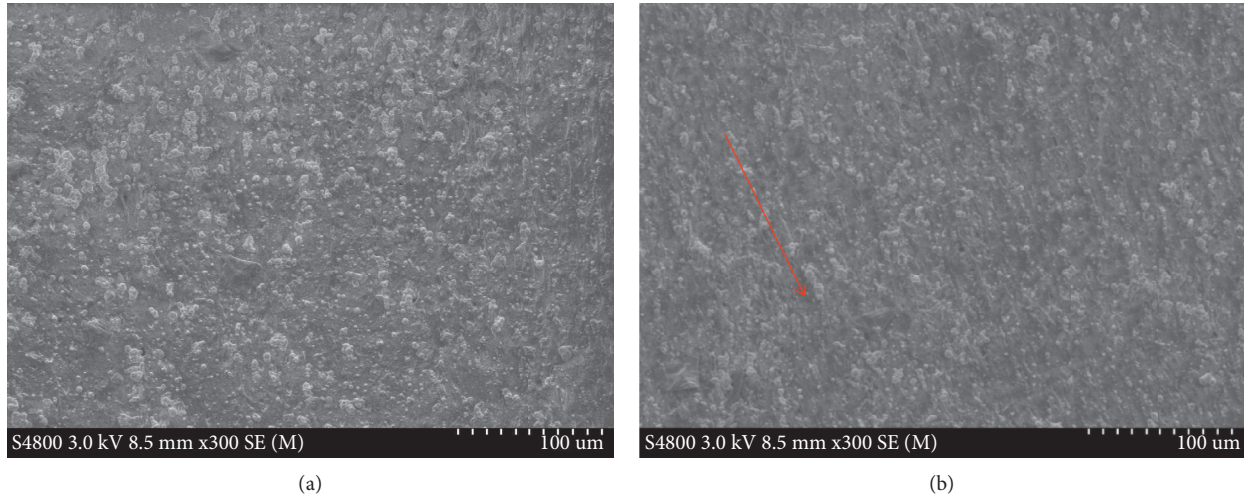


FIGURE 3: Prepared MRE sample and SEM image of internal microstructure: (a) the prestructured magnetic field is in the close state and (b) the prestructured magnetic field is in the open state.

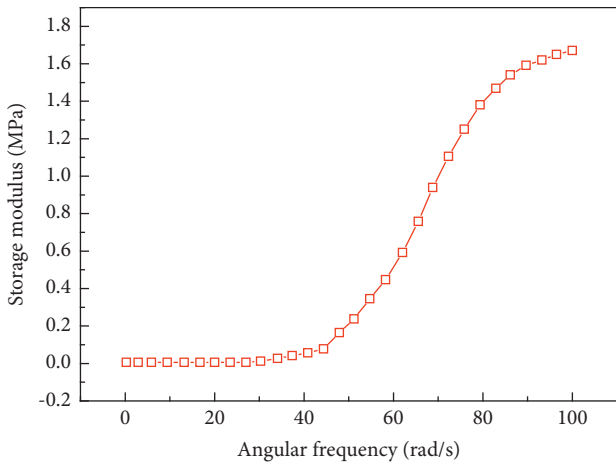


FIGURE 4: The rheological property of the fabricated boron-silicon copolymer.

novel MRE samples by adjusting the content of the silicon-boron copolymer in the composite matrix.

Figures 6(a) and 6(b) show the relationship between the normal force and the gap of parallel plates at different compression rates of MRE-1 and MRE-4, respectively. The compression rate of 100, 200, 300, and 400 $\mu\text{m/s}$ are applied separately in sequence, and the starting-ending positions of the compression range are the same. It can be observed from Figure 6(a) that the normal force curves of MRE-1 almost coincide under different compression rates. Furthermore, MRE-1 based on pure BR matrix exhibit no prominent rate-

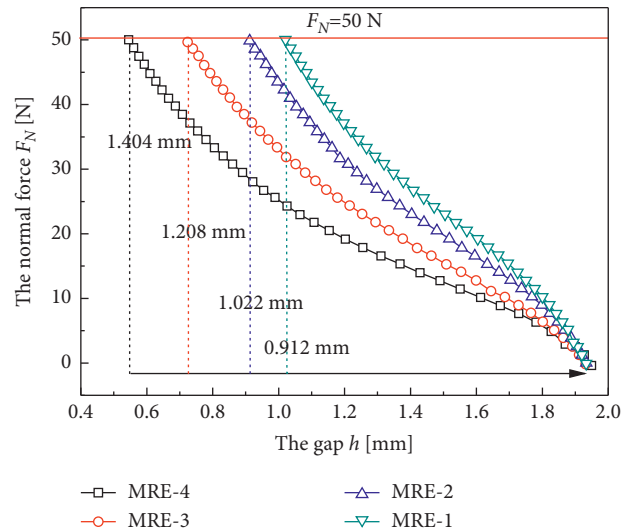


FIGURE 5: The normal force of the novel MRE samples as a function of the gap.

sensitive characteristic because the modulus of rubber only appears weak variation trend within an extensive exerted rate or frequency range. From Figure 6(b), MRE-4 exhibits prominent rate-sensitive property from the obtained normal force, increasing with the applied compression rate. When the compression deformation is 0.46 mm and the compression rate is 100 $\mu\text{m/s}$, the normal force of MRE-4 is only 12.7 N. However, when the compression rate reaches 400 $\mu\text{m/s}$, the normal force of MRE-4 can achieve 19.1 N,

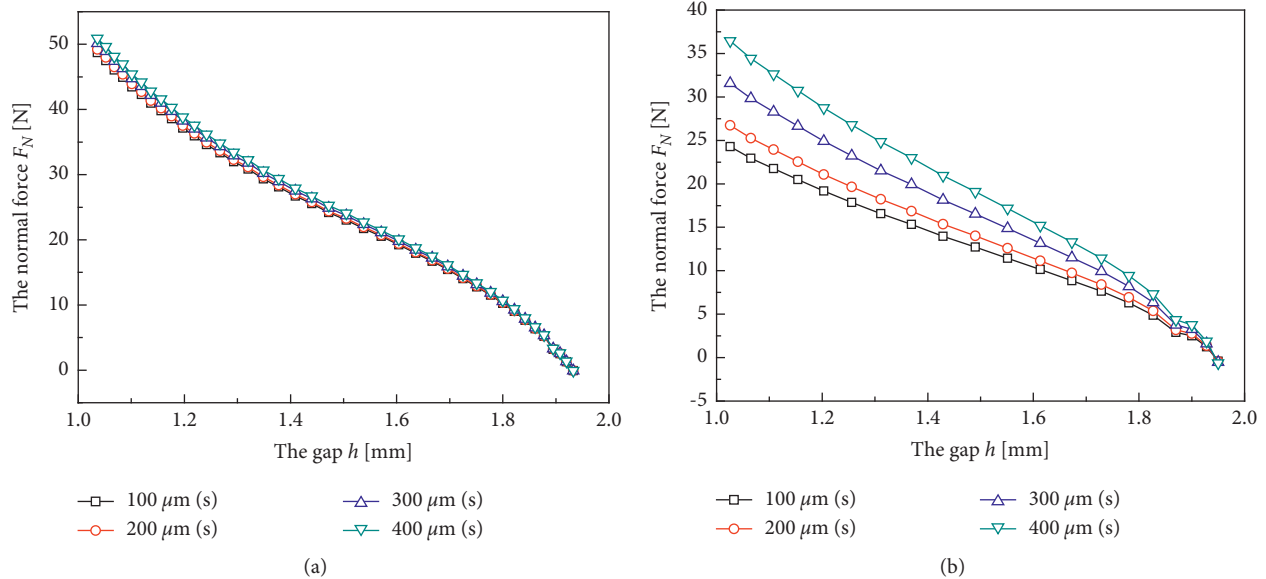


FIGURE 6: The normal force of the novel MRE samples as a function of the gap: (a) MRE-1 and (b) MRE-4.

which increases by 6.4 N dependently. While the compression deformation increases to 0.9 mm and the compression rate are $100 \mu\text{m/s}$, the normal force of MRE-4 is just 24.3 N. As the compression rate increases to $400 \mu\text{m/s}$, the normal force of MRE-4 can achieve 36.5 N, which increases 12.2 N dependently. Therefore, the novel MRE-4 sample with the addition of silicon-boron copolymer exhibits a more obvious rate-dependent performance of the normal force at more considerable compression deformation. Overall, the rate-sensitive property of the novel MRE can also reflect in the vertical normal force, not only in the horizontal shear performance based on the rheometer testing system.

From the working mechanism, the chain structure of PDMS has different polymerization degrees. When the PDMS reacts with boric acid, the Si-O bond breaks, and boron (atom B) is simultaneously introduced into the chains to form the silicon-boron copolymer with the Si-O-B bond. The molecular structure of the PDMS and the chains doped with atom B that can assume three forms [25, 45] are shown in Figure 7(a).

The electron-deficient p orbital of atom B obtains electrons from atom O in the Si-O bond [46] after forming the silicon-boron copolymer. Therefore, from Figure 7(b), the atom B from the Si-O-B bond in the chain structure of silicon-boron copolymer and the atom O from the Si-O bond in the chain structure of PDMS contribute to the formation of the B-O cross bond together that stimulate the rate-sensitive performance. In other words, the cross bond can be described as a slight damper, including a pair of piston and cylinder that can play an essential role in force output at different rate stimuli.

Furthermore, to the MRE sample based on pure BR matrix, the C-C cross bond can be formulated by adding cross-linking agent BPO, illustrated in Figure 8. The CIPs with chain structures are fixed in the cross-linked network

formed by C-C cross bonds. However, when the silicon-boron copolymer is added to the BR matrix, the B-O cross bond will be blocked in the cross-linked network of BR [47] due to the tremendous C-C bond energy exhibited in the cube cell. As for the B-O cross bond, the B and O come from the silicon-boron copolymer; therefore, the percent of silicon-boron copolymer determines the number of B-O cross bonds. From Figure 8, when the percent of silicon-boron copolymer increases gradually, the number of B-O cross bonds will enhance dependently, exhibiting more obvious rate-sensitive characteristics macroscopically. Besides, when the lower compression rate is applied, more “pistons” from atom O and “cylinders” from atom B are active freely concerning a small amount of the B-O connected “damper.” Therefore, the movement of chains is relatively free and flowing. When the compression rate increases, more and more “pistons” and “cylinders” are attracted to connect as “dampers,” which generate more B-O cross bonds. Furthermore, the movement of chains with Si-O-Si bond and Si-O-B bond will be restricted due to gradually forming the B-O cross-linked network. Hence, the axial modulus and normal force will be improved with the applied compression rate.

3.2. The Normal Force at Quasi-Static Compression Mode with the Magnetic Field. When there is an external magnetic field and a constant compression rate applied, the normal force of the novel MRE samples on the rheometer plate can be detected by adjusting the magnetic field strength. The variation of normal force with the external magnetic field strength is an essential indicator of the magnetorheological effect of the novel MRE samples.

Figure 9 reveals the relationship between the normal force and the magnetic induction intensity of MRE-1 and MRE-4. The compression strain of 10%, 20%, 30%, 40%, and 50% is applied, and the magnetic induction intensity varies

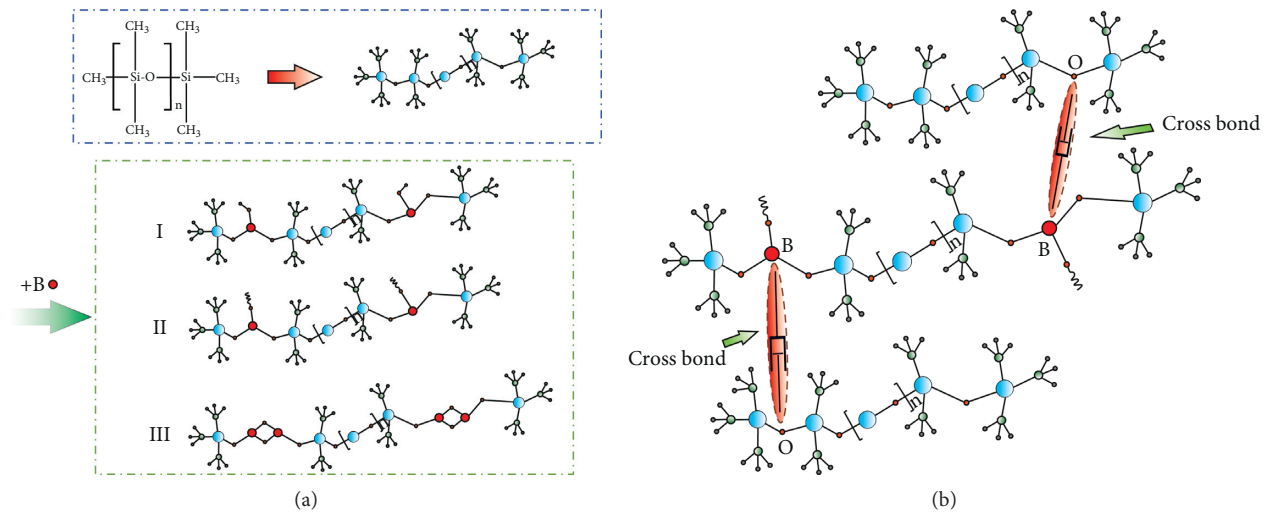


FIGURE 7: (a) Three possible structural forms of a molecular chain doped with atom B and (b) the mechanism to describe the formation of the cross bond.

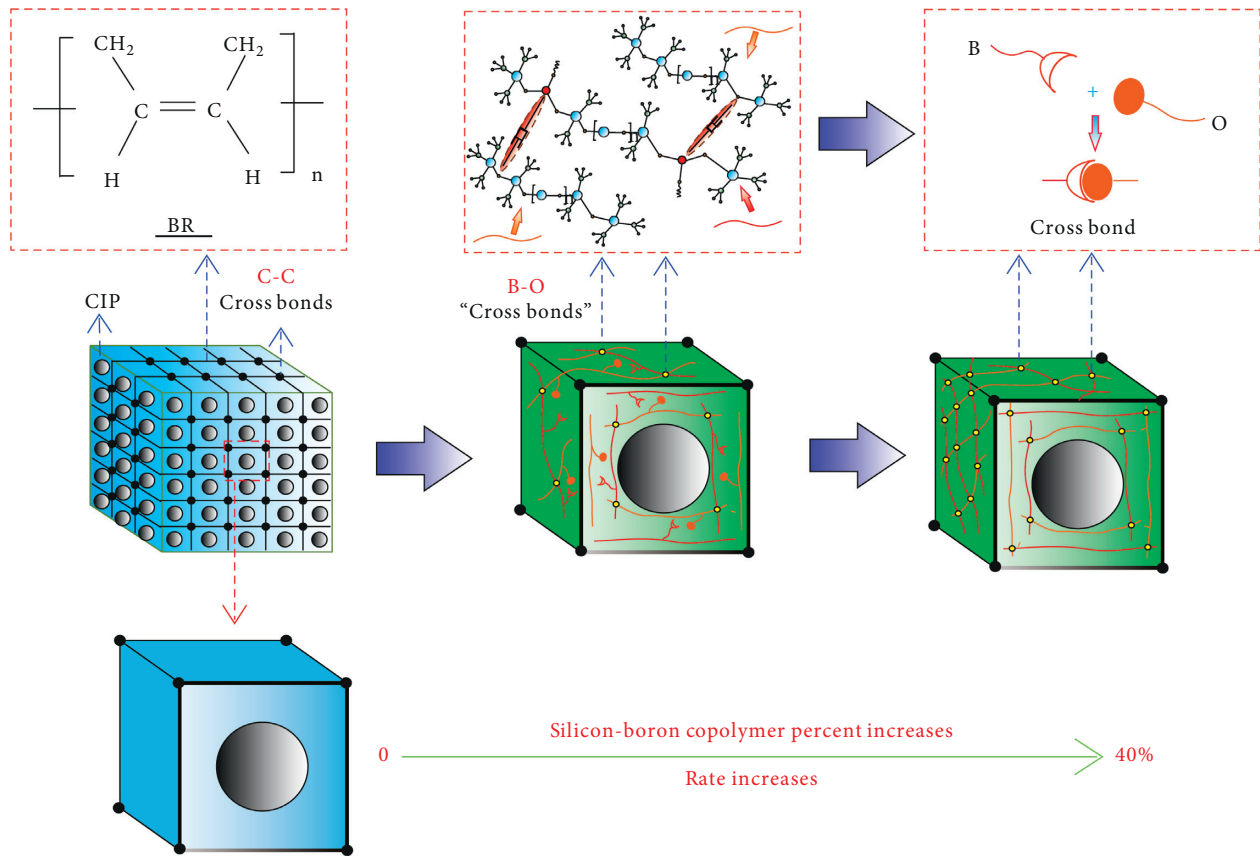


FIGURE 8: The mechanism of rate-sensitive characteristics and the molecular chain model when silicon-boron copolymer percent increases.

from 0 to 1.13 T continuously. It can be concluded that the normal force of each curve gradually increases with the enlargement of magnetic induction intensity, and when the magnetic induction intensity reaches 0.9 T, the normal force gradually tends to be stable due to magnetic saturation. Besides, compared with the traditional MRE-1 without the addition of Silly Putty, the overall normal force of MRE-4 at

each compression strain is lower. However, the adjustable range of normal force for MRE-4 is more comprehensive than MRE-1 due to the greater initial normal force of MRE-1. For instance, when the compression strain is 30% and the magnetic induction intensity varies from 0 to 1.13 T, the normal force of MRE-4 can change from 14.2 to 18.9 N, and the relative rate is 33%, which is greater than 21% of MRE-1.

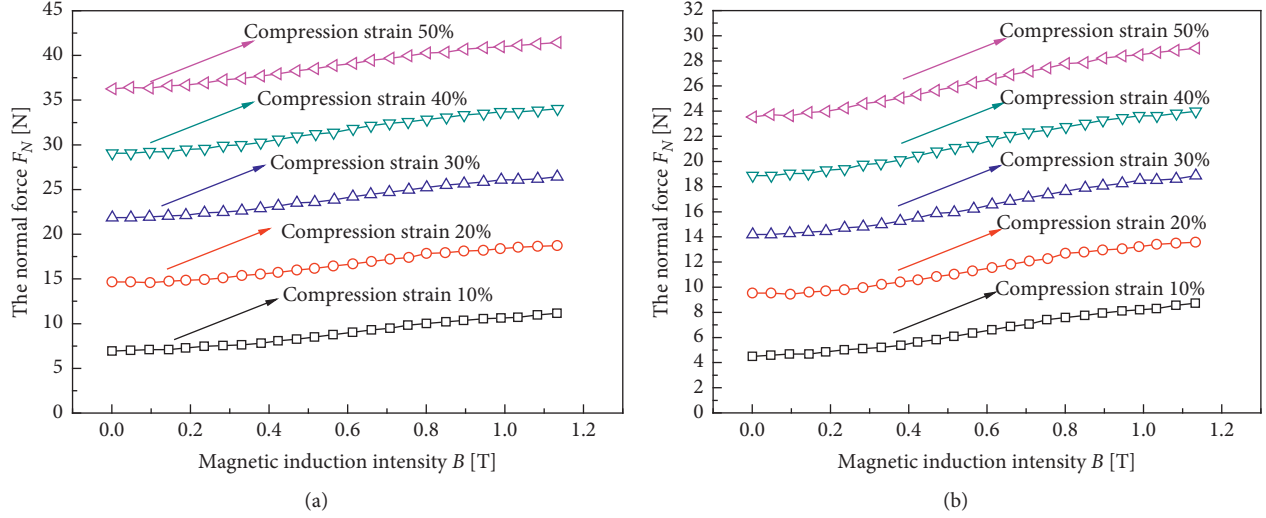


FIGURE 9: The normal force as a function of magnetic induction intensity at different compression strains: (a) MRE-1 and (b) MRE-4.

Therefore, it is explicit that the addition of Silly Putty can improve the adjustable range of normal force with magnetic field for MRE samples.

Figure 10 shows the relationship between the magneto-induced normal force ΔF_N and compression strain of MRE-4 at different magnetic induction intensities. Obviously, on the same compressive strain condition, the magneto-induced normal force increases with the magnetic induction intensity and tends to magnetic saturation when the magnetic induction intensity attains 0.997 T. Meanwhile, the variation trend between magneto-induced normal force and compression strain at different magnetic induction intensities is the same. When the compression strain is less than 20%, the magneto-induced normal force at different magnetic induction intensities is almost constant. Besides, when the compression strain is more than 20%, the magneto-induced normal force at different magnetic induction intensities increases with the increase of the compression strain. Furthermore, when the magnetic induction intensity attains to 1.03 T and the compression strain is 10%, the maximum magneto-induced normal force to magnetic saturation is 3.8 N. By comparison, the maximum magneto-induced normal force at the compression strain of 50% is more remarkable than 5 N.

Similar to the shear stress of MRE, the normal force is derived from the composite matrix and the interaction between the soft magnetic particles, which can be expressed as ΔF_N . The saturation magnetization intensity is the apparent property of soft magnetic particles. Therefore, when the magnetic induction intensity increases gradually, the soft magnetic particles are magnetized until they reach saturation. Due to the apparent nonlinear property of the magnetized process, the magneto-induced normal force of novel MRE samples exhibits evident nonlinear characteristics.

The magneto-induced mechanism can be described in Figure 11. To the prestructured MRE sample, the CIPs are arranged in chain structures along the magnetic induction

line fixed in the composite matrix compounded by BR and Silly Putty. When the external compression force F is applied, the composite matrix can be compressed to deformation. Meanwhile, the gap d between the centers of particles will reduce until the adjacent particles contact. However, when the compression deformation continues to increase to the particles fixed in the BR cross-linked network, the particle chains will bend to a possible radian due to compression force f . Still, to the particles in the Silly Putty, the long particle chains probably tend to rupture to form more intensive and stable short particle chains, which can generate more obvious magneto-induced normal force.

During the process of particle gap reduction, a simplified model based on the magnetic dipole and coupling field theory can be concluded to describe the magneto-induced normal force ΔF_N . In this model, CIPs are simplified to spheres with the same radius r . For a dipole i in a chain, its magnetic dipole moment can be expressed as follows [48]:

$$\vec{m}_i = \frac{4}{3} \pi r^3 \mu_0 \mu_1 M = \frac{4}{3} \pi r^3 \mu_0 \mu_1 \chi H_i, \quad (1)$$

where permeability of vacuum $\mu_0 = 4\pi * 10^{-7}$, μ_1 is the relative permeability of composite matrix, χ is the magnetic susceptibility, and M is the magnetization of a soft magnetic particle that can achieve magnetic saturation M_s during nonlinear magnetization.

The magnetic field strength at particle i can be expressed as follows [49]:

$$H_i = \vec{H}_0 + \sum_{j \neq i} H_j = \vec{H}_0 + 2 \sum_{j=1}^n \frac{3\hat{d}(\hat{d} \cdot \vec{m}_j) - \vec{m}_j}{4\pi\mu_0\mu_1(d_j)^3}, \quad (2)$$

where \vec{H}_0 is the external magnetic field strength, \hat{d}_j is the unit vector of \vec{d}_j , and $d_j = jd$. Substitute equation (1) into (2) to get

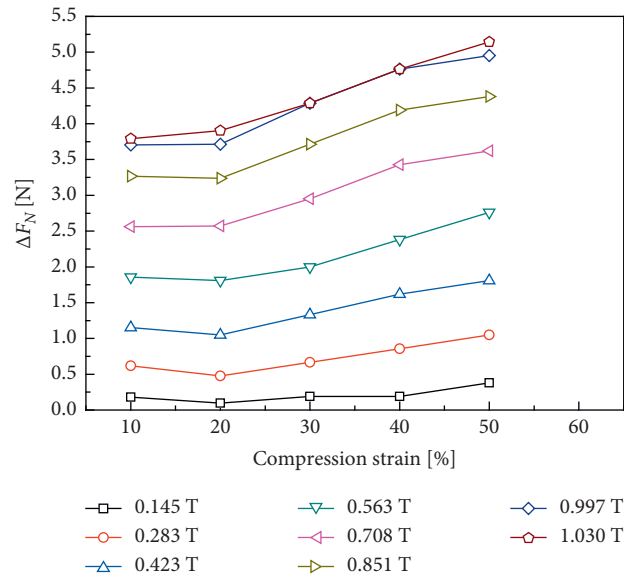


FIGURE 10: The magneto-induced normal force as a function of compression strain for MRE-4.

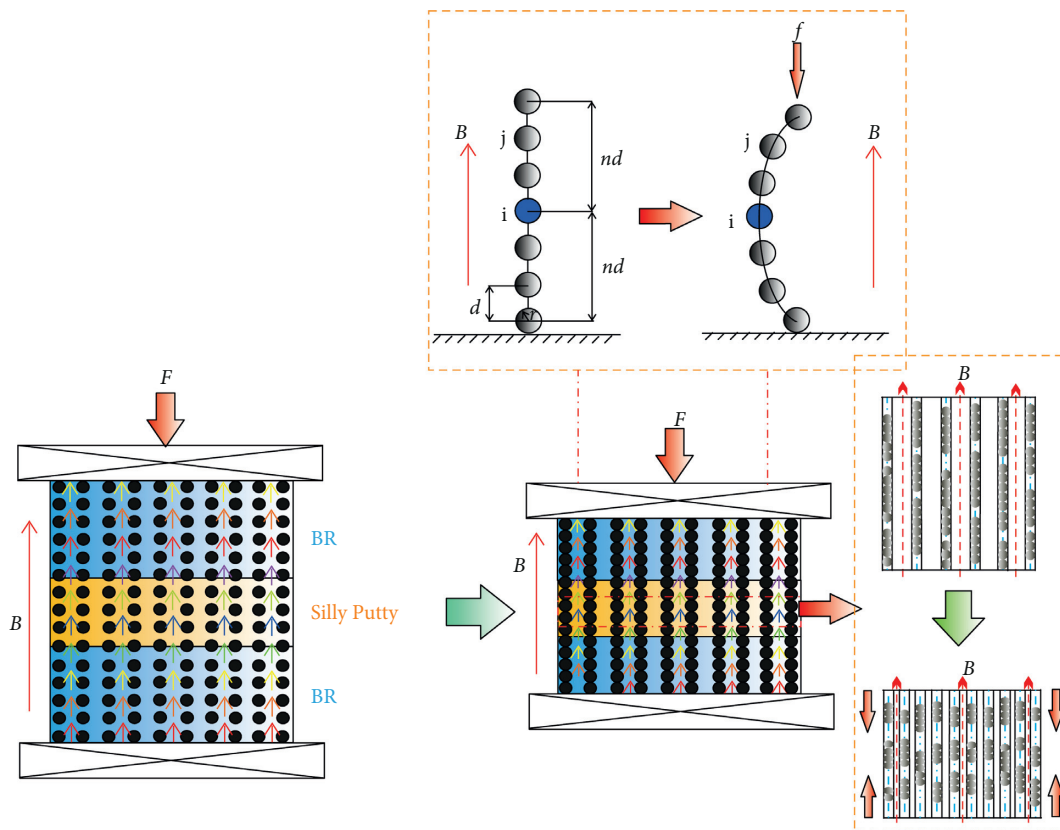


FIGURE 11: The magneto-induced mechanism of the novel MRE when compression is applied.

$$\vec{m}_i = \frac{4}{3} \pi r^3 \mu_0 \mu_1 \chi \left[H_0 + 2 \sum_{j=1}^n \frac{3\hat{d}(\hat{d} \cdot \vec{m}_j) - \vec{m}_j}{4\pi\mu_0\mu_1(jd)^3} \right], \quad (3)$$

where assume $A = \sum_{j=1}^n 1/j^3$; when n is large enough, $A \approx 1.202$.

Moreover, the compression strain can be expressed as follows:

$$\varepsilon = \frac{d - d_0}{d}, \quad (4)$$

where d_0 is the initial distance between adjacent particles. Because the stiffness of the soft magnetic particles is much larger than that of the composite matrix, the deformation of the particles can be ignored. Assume $m_i = m_j = m$, according to equation (3),

$$m = \frac{4}{3} \pi r^3 \mu_0 \mu_1 \chi H_0 \left[\frac{1}{1 - (4/3)\chi A (r/d)^3} \right]. \quad (5)$$

The magnetic interaction energy between the soft magnetic particle i and other soft magnetic particles in the same chain is

$$E = \frac{-1}{4\pi\mu_0\mu_1} \cdot \frac{4Am^2}{d^3}. \quad (6)$$

Therefore, the magnetic interaction energy per unit volume of the novel MRE can be expressed as follows:

$$E_d = \frac{3\phi}{8\pi r^3} E, \quad (7)$$

where ϕ is the volume fraction of the CIPs.

Hence, the magneto-induced normal stress can be expressed as follows:

$$\sigma = \frac{\partial E_d}{\partial \varepsilon} = \frac{\partial E_d}{\partial d} \frac{\partial d}{\partial \varepsilon} = d_0 \frac{\partial E_d}{\partial d}. \quad (8)$$

The magneto-induced normal force can be expressed as the product of the normal stress and the cross-sectional area S as follows:

$$\Delta F_N = \sigma S. \quad (9)$$

When the soft magnetic particles reach the magnetic saturation M_s , according to equations (6)–(9), the maximum magneto-induced normal force of the novel MRE based on the composite matrix can be obtained as follows:

$$\Delta F_N = \frac{2Sd_0\phi Ar^3 \mu_0 M_s^2}{\mu_1 d^4}. \quad (10)$$

From equation (10), the magneto-induced mechanism can be concluded that the magneto-induced normal force will enhance when the distance d between the centers of soft magnetic particles reduces with the increasing compression strain. Furthermore, the magneto-induced normal force will also enhance with the applied external magnetic field strength until the magnetic saturation of particles.

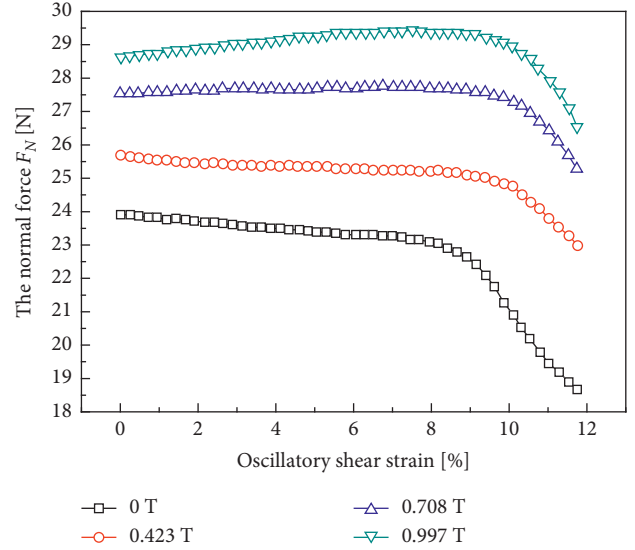


FIGURE 12: The normal force of MRE-4 at oscillatory shear mode.

3.3. The Normal Force at Dynamic Oscillation Shear Mode.

The magnetic interaction between CIPs fixed in the matrix is the source of generation for magneto-induced shear stress and magneto-induced normal force. The previous research results reveal that in the process of shear deformation, the elastic modulus in the direction of compression and the torque applied to particle chains are two important influence factors to the normal force of MRE [50, 51]. Besides, the variation trends of the normal force caused by the two influence factors are the opposite [52, 53]. On the low magnetic field condition, the influence of elastic modulus in compressive direction is more evident than the torque applied to particle chains, so the normal force decreases with the increase of shear strain. However, the torque applied to particle chains gradually increases with the enhancement of the external magnetic field. Meanwhile, the enhancement of normal force caused by the increase of the torque is higher than the decrease of the normal force caused by the decrease of the elastic modulus in the compressive direction. So the normal force gradually increases with the enhancement of the shear strain on the condition of a high magnetic field.

Figure 12 presents the relationship between the normal force and oscillatory shear strain of MRE-4 at different magnetic induction intensities when the angular frequency of 10 rad/s is applied. The normal force is stable at different magnetic induction intensities when the oscillatory shear strain is less than 9%. However, when the oscillatory shear strain is more than 9%, the normal force sharply reduces regardless of the magnetic induction intensity. Most particle chains in MRE rupture suddenly, which can be replaced by the failure of particle chains that is more likely to occur in the oscillatory shear mode. Furthermore, the normal force further decreases with the enhancement of oscillatory shear strain due to the continuous fracture of particle chain structures.

4. Conclusions

A novel MRE based on composite matrix compounded by BR and self-fabricated Silly Putty was prepared. The normal force of MRE samples at quasi-static compression mode without magnetic field, quasi-static compression mode with the magnetic field, and dynamic oscillation shear mode were tested.

- (1) The novel MRE samples with the addition of Silly Putty exhibited greater axial deformation capacity than traditional MRE-1. It could improve the novel MRE samples' axial deformation capacity by adjusting the silicon-boron copolymer's content in the composite matrix. Moreover, the normal force varied stably with the oscillatory shear strain (less than 9%) at different magnetic induction intensities and suddenly reduced when the applied oscillatory shear strain was more than 9%.
- (2) The fabricated novel MRE-4 exhibited prominent rate-sensitive characteristics, indicating that normal force F_N enhanced with the increased compression rate than traditional MRE-1. The B-O cross bonds were formulated and blocked in the C-C cross-linked network of BR with the addition of silicon-boron copolymer. The more and more B-O cross bonds allowed the linear molecular chains to form a B-O cross-linked network structure that restricted the movement of molecular chains, including Si-O and Si-O-B bonds, resulting in an increase in the normal force the compression rate and the mass fraction of silicon-boron copolymer addition increased.
- (3) Furthermore, compared to the traditional MRE-1, the addition of Silly Putty to the novel MRE samples could improve the adjustable range of normal force with the applied magnetic field. The magneto-induced normal force ΔF_N was obtained and increased with the magnetic induction intensity until magnetic saturation. Due to the prestructured CIP chains fixed in the composite matrix, the magneto-induced normal force was obtained under the applied external magnetic field. The gap d between the centers of soft magnetic particles reduced with the compression deformation, resulting in a slight increase of magneto-induced normal force. Moreover, when the compression deformation continued to increase, the CIP chains fixed in the C-C cross-linked network possibly bent to a radian, and the CIP chains in the B-O cross-linked network tended to rupture to form more intensive and stable short particle chains; therefore, the magneto-induced normal force increased. Besides, a simplified model was deduced to characterize the magneto-induced mechanism during the process of particles gap reduction. Furthermore, external magnetic field strength, gap d between the centers of soft magnetic particles, and magnetic

saturation M_s were the key factors influencing the magneto-induced normal force ΔF_N .

Data Availability

The experimental data used to support the findings of this study are included within the article.

Conflicts of Interest

The authors declare that there are no conflicts of interest regarding the publication of this paper.

Acknowledgments

This work was supported by the Ph.D. Research Startup Foundation of Anhui Polytechnic University (Grant no. S022020069), the Key Research Foundation of Anhui Polytechnic University (Grant no. KZ42020240), and the Jiangsu Province Key R&D Project (Grant no. BE2017167).

References

- [1] X. L. Gong, X. Z. Zhang, and P. Q. Zhang, "Fabrication and characterization of isotropic magnetorheological elastomers," *Polymer Testing*, vol. 24, no. 5, pp. 669–676, 2005.
- [2] M. Cvek, M. Kralcik, M. Sedlacik, M. Mrlik, and V. Sedlarik, "Reprocessing of injection-molded magnetorheological elastomers based on TPE matrix," *Composites Part B: Engineering*, vol. 172, pp. 253–261, 2019.
- [3] X. Qiao, X. Lu, X. Gong, T. Yang, K. Sun, and X. Chen, "Effect of carbonyl iron concentration and processing conditions on the structure and properties of the thermoplastic magnetorheological elastomer composites based on poly (styrene-*b*-ethylene-co-butylene-*b*-styrene) (SEBS)," *Polymer Testing*, vol. 47, pp. 51–58, 2015.
- [4] Q. Shu, L. Ding, and T. Hu, "High performance magnetorheological elastomers strengthened by perpendicularly interacted flax fiber and carbonyl iron chains," *Smart Materials and Structures*, vol. 29, no. 2, pp. 25010–25013, 2020.
- [5] F. Guo, C. B. Du, and R. P. Li, "Viscoelastic parameter model of magnetorheological elastomers based on abel dashpot," *Advances in Mechanical Engineering*, vol. 6, Article ID 629386, 2014.
- [6] S. Sun, J. Yang, T. Yildirim et al., "A magnetorheological elastomer rail damper for wideband attenuation of rail noise and vibration," *Journal of Intelligent Material Systems and Structures*, vol. 31, no. 2, pp. 220–228, 2019.
- [7] Q. Wang, X. F. Dong, L. Y. Li, and Q. Yang, "Wind-induced vibration control of a constructing bridge tower with MRE variable stiffness tuned mass damper," *Smart Materials and Structures*, vol. 29, no. 4, Article ID 045043, 2020.
- [8] T. J. Kang, K. H. Hong, and H. Jeong, "Preparation and properties of a p-aramid fabric composite impregnated with a magnetorheological fluid for body armor applications," *Polymer Engineering & Science*, vol. 55, no. 4, pp. 729–734, 2015.
- [9] Y. Wen, Q. Sun, Y. Zou, and H. You, "Study on the vibration suppression of a flexible carbody for urban railway vehicles with a magnetorheological elastomer-based dynamic vibration absorber," *Proceedings of the Institution of Mechanical Engineers, Part F: Journal of Rail and Rapid Transit*, vol. 234, no. 7, pp. 749–764, 2019.

- [10] S. Sun, J. Yang, T. Yildirim et al., "Development of a nonlinear adaptive absorber based on magnetorheological elastomer," *Journal of Intelligent Material Systems and Structures*, vol. 29, no. 2, pp. 194–204, 2018.
- [11] D. I. Jang, J. E. Park, and Y. K. Kim, "Designing a compact module of vibration absorber based on magnetorheological elastomer with a novel magnetic field generator," *Transactions of the Korean Society of Mechanical Engineers - A*, vol. 43, no. 3, pp. 177–183, 2019.
- [12] A. Rasooli, R. Sedaghati, and M. Hemmatian, "A novel magnetorheological elastomer-based adaptive tuned vibration absorber: design, analysis and experimental characterization," *Smart Materials and Structures*, vol. 29, no. 11, Article ID 115042, 2020.
- [13] M. Sedlacik, M. Mrlik, V. Babayan, and V. Pavlinek, "Magnetorheological elastomers with efficient electromagnetic shielding," *Composite Structures*, vol. 135, pp. 199–204, 2016.
- [14] I. E. Kuznetsova, V. V. Kolesov, A. S. Fionov, and E. Y. Kramarenko, "Magnetoactive elastomers with controllable radio-absorbing properties," *Materials Today Communications*, vol. 21, Article ID 100610, 2019.
- [15] M. Cvek, M. Mrlik, M. Ilčíková, J. Mosnáček, L. Münster, and V. Pavlínek, "Synthesis of silicone elastomers containing silyl-based polymer-grafted carbonyl iron particles: an efficient way to improve magnetorheological, damping, and sensing performances," *Macromolecules*, vol. 50, no. 5, pp. 2189–2200, 2017.
- [16] B. Sapiński and P. Orkisz, "Real-time sensing action of the electromagnetic vibration-based energy harvester for a magnetorheological damper control," *Energies*, vol. 14, no. 10, Article ID 2845, 2021.
- [17] M. Cvek, A. Zahoranova, M. Mrlik, P. Sramkova, A. Minarik, and M. Sedlacik, "Poly (2-oxazoline)-based magnetic hydrogels: synthesis, performance and cytotoxicity," *Colloids and Surfaces B: Biointerfaces*, vol. 190, Article ID 110912, 2020.
- [18] N. M. Hapipi, S. A. Mazlan, U. Ubaidillah et al., "Solvent dependence of the rheological properties in hydrogel magnetorheological elastomer," *International Journal of Molecular Sciences*, vol. 21, no. 5, Article ID 1793, 2020.
- [19] L. Chen, X. L. Gong, W. Q. Jiang, J. J. Yao, H. X. Deng, and W.H Li, "Investigation on magnetorheological elastomers based on natural rubber," *Journal of Materials Science*, vol. 42, no. 14, pp. 5483–5489, 2007.
- [20] Z. Chang, Y. He, H. Deng et al., "A multifunctional silly-putty nanocomposite spontaneously repairs cathode composite for advanced Li-S batteries," *Advanced Functional Materials*, vol. 28, no. 50, Article ID 1804777, 2018.
- [21] M. Hébert, J. P. Huissoon, and C. L. Ren, "A silicone-based soft matrix nanocomposite strain-like sensor fabricated using graphene and silly putty," *Sensors and Actuators A Physical*, vol. 305, no. 11, Article ID 111917, 2020.
- [22] Y. Chen, X. Pu, M. Liu et al., "Shape-Adaptive, self-healable triboelectric nanogenerator with enhanced performances by soft solid-solid contact electrification," *ACS Nano*, vol. 13, no. 8, pp. 8936–8945, 2019.
- [23] C. Xu, Y. Wang, J. Wu et al., "Anti-impact response of Kevlar sandwich structure with silly putty core," *Composites Science and Technology*, vol. 153, pp. 168–177, 2017.
- [24] F. Guo, C. B. Du, G. J. Yu, and L. P. Run, "The static and dynamic mechanical properties of magnetorheological silly putty," *Advances in Materials Science and Engineering*, vol. 2016, Article ID 7079698, 11 pages, 2016.
- [25] S. Wang, W. Jiang, W. Jiang et al., "Multifunctional polymer composite with excellent shear stiffening performance and magnetorheological effect," *Journal of Materials Chemistry C*, vol. 2, no. 34, pp. 7133–7140, 2014.
- [26] J. Yao, Y. Sun, Y. Wang, Q. Fu, Z. Xiong, and Y. Liu, "Magnet-induced aligning magnetorheological elastomer based on ultra-soft matrix," *Composites Science and Technology*, vol. 162, no. 7, pp. 170–179, 2018.
- [27] N. Golinelli, A. Spaggiari, and E. Dragoni, "Mechanical behaviour of magnetic Silly Putty: viscoelastic and magnetorheological properties," *Journal of Intelligent Material Systems and Structures*, vol. 28, no. 8, pp. 953–960, 2017.
- [28] Y. Wang, L. Ding, C. Zhao et al., "A novel magnetorheological shear-stiffening elastomer with self-healing ability," *Composites Science and Technology*, vol. 168, no. 10, pp. 303–311, 2018.
- [29] B. Liu, C. Du, G. Yu, and Y. Fu, "Shear thickening effect of a multifunctional magnetorheological gel: the influence of cross-linked bonds and solid particles," *Smart Materials and Structures*, vol. 29, no. 1, Article ID 015004, 2020.
- [30] B. Liu, C. Du, S. Jiang, G. Zhou, and J. Sun, "The influence of the curing process on the shear thickening performance of RMG and property optimization," *RSC Advances*, vol. 10, no. 21, Article ID 12197, 2020.
- [31] W. Jiang, X. Gong, S. Wang et al., "Strain rate-induced phase transitions in an impact-hardening polymer composite," *Applied Physics Letters*, vol. 104, no. 12, Article ID 121915, 2014.
- [32] C. S. Bolland, U. Khan, G. Ryan et al., "Sensitive electromechanical sensors using viscoelastic graphene-polymer nanocomposites," *Science*, vol. 354, no. 6317, pp. 1257–1260, 2016.
- [33] X. Fan, S. Wang, S. Zhang, Y. Wang, and X. Gong, "Magnetically sensitive nanocomposites based on the conductive shear-stiffening gel," *Journal of Materials Science*, vol. 54, no. 9, pp. 6971–6981, 2019.
- [34] M. Liu, S. Zhang, S. Liu et al., "CNT/STF/Kevlar-based wearable electronic textile with excellent anti-impact and sensing performance," *Composites Part A: Applied Science and Manufacturing*, vol. 126, no. 11, Article ID 105612, 2019.
- [35] X. L. Gong, X. Z. Zhang, and P. Q. Zhang, "Study of mechanical behavior and microstructure of magnetorheological elastomers," *International Journal of Modern Physics B*, vol. 19, no. 7–9, pp. 1304–1310, 2005.
- [36] Y. Wang, Y. Hu, L. Chen et al., "Effects of rubber/magnetic particle interactions on the performance of magnetorheological elastomers," *Polymer Testing*, vol. 25, no. 2, pp. 262–267, 2006.
- [37] L. Pei, H. Pang, X. Ruan, X. Gong, and S. Xuan, "Magnetorheology of a magnetic fluid based on Fe₃O₄ immobilized SiO₂ core-shell nanospheres: experiments and molecular dynamics simulations," *RSC Advances*, vol. 7, no. 14, pp. 8142–8150, 2017.
- [38] Q. Wen, Y. Wang, and X. Gong, "The magnetic field dependent dynamic properties of magnetorheological elastomers based on hard magnetic particles," *Smart Materials and Structures*, vol. 26, no. 7, Article ID 075012, 2017.
- [39] W. Zhao, H. Pang, and X. Gong, "Novel magnetorheological elastomer filled with NdFeB particles: preparation, characterization, and magnetic-mechanic coupling properties," *Industrial & Engineering Chemistry Research*, vol. 56, no. 31, pp. 8857–8863, 2017.
- [40] F. H. Xu, Z. D. Xu, X. C. Zhang, G. Q. Ying, and Y. Lu, "A compact experimentally validated model of magnetorheological fluids," *Journal of Vibration and Acoustics-Transactions of the ASME*, vol. 138, no. 1, Article ID 011017, 2016.

- [41] W. H. Li, X. Z. Zhang, and T. F. Tian, "Fabrication and characterisation of patterned magnetorheological elastomers," *AIP Conference Proceedings*, vol. 1542, no. 1, pp. 129–132, 2013.
- [42] W. Zhang, X. L. Gong, and L. Chen, "A Gaussian distribution model of anisotropic magnetorheological elastomers," *Journal of Magnetism and Magnetic Materials*, vol. 322, no. 23, pp. 3797–3801, 2010.
- [43] Y. S. Zhu, X. L. Gong, H. Dang, X. Z. Zhang, and P. Q. Zhang, "Numerical analysis on magnetic-induced shear modulus of magnetorheological elastomers based on multi-chain model," *Chinese Journal of Chemical Physics*, vol. 19, no. 2, pp. 126–130, 2006.
- [44] L. Chen, X. L. Gong, and W. H. Li, "Microstructures and viscoelastic properties of anisotropic magnetorheological elastomers," *Smart Materials and Structures*, vol. 16, no. 6, pp. 2645–2650, 2007.
- [45] T. I. Zatssepina, M. L. Brodskii, Y. A. Frolova, A. A. Trapeznikov, V. N. Gruber, and G. A. Kruglova, "Rheological behaviour of polyheterosiloxanes," *Polymer Science U.S.S.R.* vol. 12, no. 11, pp. 2899–2905, 1970.
- [46] M. P. Goertz, X.-Y. Zhu, and J. E. Houston, "Temperature dependent relaxation of a "solid-liquid"," *Journal of Polymer Science Part B: Polymer Physics*, vol. 47, no. 13, pp. 1285–1290, 2009.
- [47] W. L. Wu and G. Cheng, "Study on silicone rubber/BR/EPDM blend," *China Elastomerics*, vol. 16, no. 1, pp. 43–46, 2006.
- [48] M. R. Jolly, J. D. Carlson, and B. C. Muñoz, "A model of the behaviour of magnetorheological materials," *Smart Materials and Structures*, vol. 5, no. 5, pp. 607–614, 1996.
- [49] Y. Shen, M. F. Golnaraghi, and G. R. Heppler, "Experimental research and modeling of magnetorheological elastomers," *Journal of Intelligent Material Systems and Structures*, vol. 15, no. 1, pp. 27–35, 2004.
- [50] E. M. James and A. A. Robert, "Chain model of electro-rheology," *The Journal of Chemical Physics*, vol. 104, no. 12, p. 4814, 1996.
- [51] J. D. Vicente, F. C. González, G. Bossis, and O. Volkova, "Normal force study in concentrated carbonyl iron magnetorheological suspensions," *Journal of Rheology*, vol. 46, no. 5, pp. 1295–1303, 2002.
- [52] G. Liao, X. Gong, and S. Xuan, "Influence of shear deformation on the normal force of magnetorheological elastomer," *Materials Letters*, vol. 106, no. 9, pp. 270–272, 2013.
- [53] G. Liao, X. Gong, S. Xuan, C. Guo, and L. Zong, "Magnetic-field-induced normal force of magnetorheological elastomer under compression status," *Industrial and Engineering Chemistry Research*, vol. 51, no. 8, pp. 3322–3328, 2012.

Research Article

Mechanical Properties of Full-Scale Prestressed Concrete Beams with Thin Slab after Exposure to Actual Fire

Chaowei Hao ¹, Yanjiang Chen ², Yu Tang,¹ and Laiyong Wang¹

¹Research Institute of Highway, Ministry of Transport, Beijing 100088, China

²Beijing Laboratory of Earthquake Engineering and Structural, Beijing University of Technology, Beijing 100124, China

Correspondence should be addressed to Chaowei Hao; cw.hao@rioh.cn

Received 20 August 2021; Revised 18 October 2021; Accepted 23 November 2021; Published 10 December 2021

Academic Editor: Antonio Caggiano

Copyright © 2021 Chaowei Hao et al. This is an open access article distributed under the Creative Commons Attribution License, which permits unrestricted use, distribution, and reproduction in any medium, provided the original work is properly cited.

To provide an effective basis and reference for applications of prestressed concrete thin-slab beams after a bridge fire, methods and principles of fire-resistant design, repair, and reinforcement of such beams were discussed. Taking a simple supported and continuous girder bridge of an expressway in service as a sample, appearance testing and nondestructive testing of the internal structure were carried out. Four representative full-scale prestressed concrete beams were selected. Through the comparative test of the ultimate bearing capacity of such beams, the laws of the deflection deformation, strain distribution, crack formation, and crack development were obtained. By combining with the finite element simulation and theoretical analysis, the ultimate bearing capacity, complex mechanical characteristics, and breakage feature and failure mechanism of such beams were studied. It was indicated by the results the following: (1) Prestress loss will cause height reduction of the concrete shear zone, which is one of the main reasons why the bending-shearing failure of such beams happened before the pure bending failure. (2) Under certain operating loads, brittle fracture is more likely to occur on the bottom surface of such beams when directly exposed to fire. (3) The bursting and spalling depth of concrete after being exposed to fire can be used as the characteristic parameters for the rapid identification of the bottom surface of such after-fire beams.

1. Introduction

With the vigorous development of highway traffic in China, more and more inflammable and explosive goods are transported by road and the number of bridge fires is increasing. The fire, which affects the bridges, not only causes economic losses for the country but also brings potential safety hazards to the service of the bridge, affecting the normal operation of the highway. In China, prestressed concrete bridges account for a large proportion of the completed bridges in service [1]. Hollow slab beams are the most common form of medium- and small-span highway bridge superstructures, and about 35% of concrete girder bridges adopt hollow slab structures [2].

The floor thickness of the hollow slab beam is generally between 8 cm and 15 cm, which is relatively thin. Once exposed to fire, its effective prestress will decrease, and the overall rigidity of the beam and slab will drop, affecting the normal service of the whole bridge. When conflagration

happened, the failure of the complete bonding between steel strand and concrete will lead to structural failure along with the brittle damage of the beam and plate, which will seriously threaten the traffic safety and arouse pernicious social impact. Hence, it is necessary to examine and further study the mechanical properties of those beams from fire-damaged bridges.

Many scholars researched on the mechanical properties of prestressed concrete beams after the fire from different perspectives, including material properties, fire resistance calculation method, evaluation of postdisaster bearing capacity, and new fireproof technologies. Zheng et al. [3] carried out fire resistance tests on 15 prestressed concrete simply supported slabs and 9 two-span unbonded prestressed concrete continuous slabs. The results have shown that concrete spalls more easily when the stress is greater on the surface exposed to fire. Wang et al. [4] have experimented on the creep of high-strength prestressed rebars under high-temperature conditions, establishing a high-

temperature creep model of those rebars. The necessity of considering the creep of the concrete when analyzing the fire resistance performance of the prestressed concrete structures was verified. Ding et al. [5] studied the temperature field and relaxation of prestressed tendons of concrete beams and slabs through numerical simulation and model tests when underbridge space encountered fire. It turned out that, after the fire, the prestress loss of the steel strands from such beams and slabs has occurred. The higher the fire field temperature, the greater the prestress loss. Based on the investigation of the firing time and its temperature, after-fire prestress loss is analyzed. And the foundation for post-disaster assessment of bridge performance was laid. Dwaikat and Kodur [6] established a monolithic model of high-strength concrete bursting and spalling based on the influence of concrete pore water pressure, pointed out that the axial constraint has an obvious influence on the bursting and spalling performance of concrete beams, and concluded that high-strength concrete has lower fire resistance performance than ordinary concrete due to the effect of its surface concrete bursting and lower permeability. Kodur and Dwaikat [7] studied the influence of the stress-temperature path on the prestressed concrete beams and slabs. A numerical method considered the thermal-mechanical coupling effect that was proposed. By combining with experimental data, the fire resistance performance of prestressed concrete beams and slabs was learned. Yun and Jeon [8] proposed a method to evaluate the fire damage of bridge structures based on the thermal-structure interaction then applied this method to prestressed concrete bridges, respectively. It was founded that the temperature distribution, deflection, and its standard fit well with the standard fire test results. Zhang et al. [9] used the thermal field coupling calculation method to explore the failure mode of T-section prestressed concrete beam bridges under different fire modes. The beam rib and flange plate deformation of such beams were tracked under different fire modes. As for the long-span prestressed concrete box girder bridges (PC box girder bridges). Yanagisawa et al. [10] discovered a method that can identify the failure mode of the after-fire bridge and reduce the fire damage by adding a fire protection panel (FFP). And the effectiveness of the method through real practice was forwardly testified. Taking into account the geometric nonlinearity, material nonlinearity, and nonlinear thermal gradient, and combining the bidirectional coupling between thermal analysis and structural analysis, Prakash and Srivastava [11] proposed a nonlinear thermal analysis method for RC beam fire based on the direct stiffness method. The results show that the framework can predict the response of RC structure well. Alos-Moya et al. [12] calibrated the fire model by using the temperature results of Valencia bridge fire test conducted by Valencia Polytechnic University in Valencia (Spain). The results show that some of the fire stability models are only suitable for scale bridge fire test, not for actual bridge fire analysis. Beneberu and Yazdani [13] carried out a full-scale single-span prestressed concrete bridge that was tested under a combined hydrocarbon fire and simulated AASHTO live load. The results show that without fire prevention measures, the carbon fiber cloth will

degum rapidly, resulting in serious spalling of concrete and loss of some prestressed steel strands. Kodur et al. [14] studied the fire resistance of composite box girder with transverse and longitudinal stiffeners and proposed a method to predict the failure time of arch bending moment zone of continuous composite box girder based on deflection ratio. The results show that the fire resistance of continuous composite box girder can be significantly improved by preventing the negative bending moment zone of continuous composite box girder from fire.

As mentioned above, the studies about the mechanical properties of prestressed concrete girder bridges after the fire were mainly focused on five aspects, including material properties, thermal performance, effective prestress loss mechanism, fire resistance performance tests of reduced-scale components, and numerical simulation analysis of the entire bridge. However, research based on the mechanical properties of full-scale beams after the fire is still lacking. After experiencing different high-temperature burning, the failure criteria and morphology of prestressed concrete thin-slab beams have not been studied in depth. In this paper, to obtain the law of deformation, strain, and crack development, a full-scale failure test of such beams is carried out. Combined with theoretical and numerical analysis, several properties are studied, including the ultimate bearing capacity, force characteristics, and failure mechanism of such beams. These results can serve as a decision-making foundation for the practical fire-resistant design, maintenance, and reinforcement of similar beams.

2. Method

2.1. Source and Classification of Test Components. A precast 9×20 m prestressed concrete hollow bridge in-service on provincial expressway is designed in split width, and each width contains 16 hollow slab beams [15]. The minimum floor thickness of this bridge is 15 cm, the net protection layer thickness of steel strands is 3.6 cm, and the designed value of standard cube compressive strength of concrete is 50 MPa. Each middle beam of this bridge is equipped with 14 steel strands, and the effective length of these steel strands is shown in Table 1. Each prestressed steel bundle is composed of $6 \times \Phi_s 15.2$, whose standard tensile strength of prestressing tendons is 1860 MPa and the tension control stress is 1395 MPa. The reinforcement of elevation and middle plate are shown in Figure 1.

All reliable samples in this study come from the hollow slab removed from the bridge above after exposure to fire due to the oil tank truck at its bottom. The tank truck rolled over under the sixth hole of that bridge, causing the fuel tank to rupture and burn. The fuel flowed along the road to the seventh hole and then burned a large area. As a result, the bottom surface of the girder slab near the 6th and 7th holes was directly burned by the fire nearly two hours (the side face was not directly overfired).

According to the appearance test results, the web of the hollow slab girder was not directly burned by the fire source, suffering little influence on the shear bearing capacity. Thus, little web plate damage was found. In addition, after multiple

TABLE 1: Effective length of strand (unit: m).

No.	1	2	3	4	5	6
L	19.9	16.8	15.2	13.2	11.0	7.8

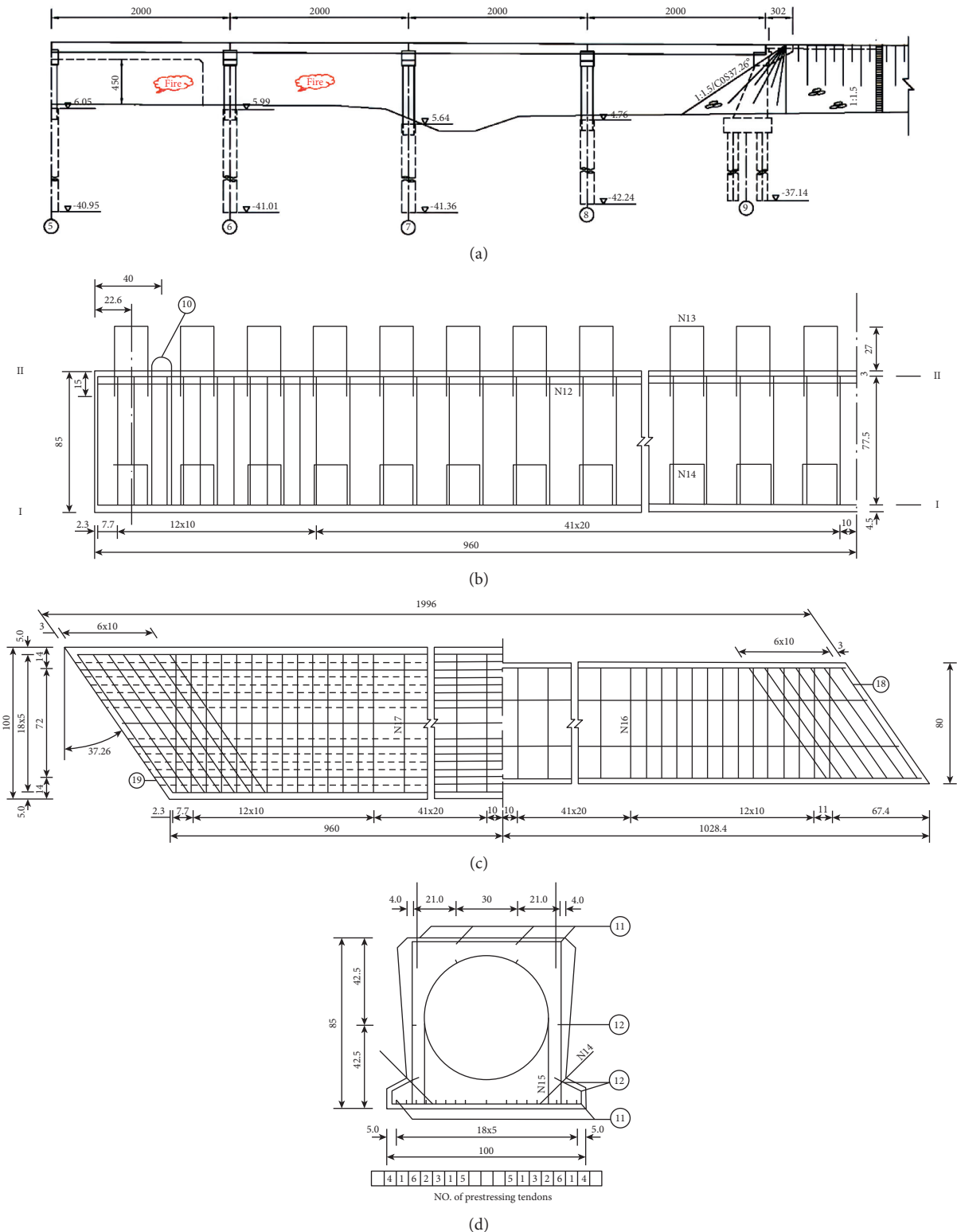


FIGURE 1: The elevation and reinforcement diagram. (a) Elevation (the unit of elevation is m, and the unit of span is cm). (b) Medium plate reinforcement diagram.

hoisting and transportation, most of the beams and slabs have varying degrees of damage near the fulcrum. Therefore, it is very important to carry out the bending bearing capacity test, which is our main test. The hollow slabs are divided into four categories differentiated by the degree of after-fire damage for the later experiment. See Table 2 and Figure 2. Among them, beam 2# is the reference beam, which is nearly unaffected by the fire. The proving process will be discussed in Section 3 as follows, through numerical simulation and experimental comparison of these beams.

2.2. Loading Device. Loading devices include ultra-high-pressure jack, rubber-bearing, welded H-type steel beam and counterforce beam, number display pressure ring, $\Phi 32$ fine-rolled rebar, and gravity ground anchor device. The pressure generated by the jack is applied to the longitudinal loading beam in the form of a reaction force through the ground anchor device. Then, the force is transferred from the longitudinal beam to the hollow slab structure through a rubber bearing (steel pad). The maximum bending moment in the normal section and the maximum shear force from one-third to two-thirds of the span length has been considered simultaneously in the test loading arrangement. The loading arrangement layout is detailed in Figure 3, and the on-site loading situation is shown in Figure 4.

2.3. Process of the Loading Test. The test of each beam is divided into two loading conditions. The first condition means loading until each cross section reaches or is close to the design value of an ultimate bending moment, and the second condition means loading to the actual ultimate failure state or the loading to the test termination conditions. The loading process is shown in Table 3. Refer to the relevant specifications for test termination conditions.

2.4. Items and Methods for the Test

2.4.1. Beam Deflection and Pier Settlement Measurement. The deflection of the beam and the test bench under various loading conditions is measured by using AL-ML32 high-precision leveling instrument shown in Figure 5. Numbers of deflection and settlement at one-quarter of the span length, three-quarters of the span length, and the midspan can be read through the preembedded indium steel ruler.

2.4.2. Strain Measurement of the Key Sections. On both sides of the hollow slab beams, along the height direction of the webs, bridge strain gauges were arranged for measurement, especially at one quarter, three quarters, one-eighth, three-eighths of the span length, and the midspan.

The detailed arrangement of measuring points is shown in Figure 6.

2.4.3. Crack Observation and Damage Pattern Recording. Before the test, the initial conditions of the selected beams were carefully checked, the original cracks were marked,

and the original crack diagram was drawn in detail. The two sides of the hollow slab girder web are divided into 20 cm square grids at equal intervals as the reference coordinate system for recording cracks on the concrete surface. During the test, the appearing cracks were drawn on the beam and recorded, and the corresponding load size when the cracks appeared was marked. At the same time, several representative cracks were selected to track and measure their width changes.

2.5. Numerical Simulation. According to Chaowei et al. [15], after obtaining the material's mechanical performance parameters, the ultimate bearing capacity of the prestressed concrete beam was analyzed. And the finite element analysis method was applied during this process to meet the required engineering accuracy. The comparison between numerical simulation and the experiment proves that the beam 2# is almost unaffected by the fire and thus can be used as the reference beam [15]. The general large-scale finite element software ANSYS is used for modeling. SOLID65 elements should be selected for concrete. The stress-strain relationship model of concrete is an important part of the nonlinear analysis of after-fire concrete hollow slabs. And the dynamic hardening model is used for this simulation. In the concrete failure criterion, the shear-transfer coefficient of open cracks is set to 0.7 after trial calculations based on relevant experience, and the shear-transfer coefficient of closed cracks is set to 0.95. The uniaxial stress-strain of concrete can be found in [15]. Steel strands are simulated by the LINK8 unit, without considering the bond-slip between steel and concrete, and steel strands are simulated by the bilinear isotropic strengthening model BISO considering strengthening. To consider the exact effects, ordinary steel bars are dispersed into concrete elements in a way of defining real constants (reinforcement ratios of stirrups and longitudinal and transverse steel bars). In order to prevent stress concentration from causing the in-advance jumping out of the calculation, a unit with an elastic modulus 100 times that of concrete is set at the loading position and the bridge bearing. When dividing elements, a hexahedral mapping grid is used. The number of bridge elements is 5918 in total, and the number of nodes is 8266. The finite element model is shown in Figure 7.

3. Result and Discussion

Due to the requirements for keeping the bridge appearance and the nondestructive inspection in the early stage, the test bench bed has a clear height of 1.2 m. Because of the safety considerations and limited working stroke of the jack, the loading test stopped in advance before the hollow slab beam was completely destroyed. So, there was no complete destruction of the structure, such as concrete crushing, beam fracture, and beam slab collapse. The main reaction of the structure during the test was learned: (1) As the load increases, the deflection of the beam continues to increase, and deformation

TABLE 2: The appearance of test beam.

No.	The appearance of the floor (the floor is divided into 70 areas)
2#	The concrete was fumigated and blackened in partial areas without any other damage
3#	The color of the concrete remains unchanged. The sound of hammering in 6% of the concrete area is dull. 30% of the concrete area falls off with a characteristic depth of 2.1 cm, mostly locating at the end of the beam. And a small part of the beam-end steel strand is exposed, distributed from the fulcrum to quarter of the span
4#	6% of the concrete area is pink. Micro-crack and coarse-crack networks appear in partial areas. The sound of hammering in 76% of the concrete area is dull. 97% of the concrete area falls off with a characteristic depth of 2.6 cm. And the steel strands are exposed in some areas
5#	98% of the concrete area is pink or khaki. The sound of hammering in 96% of the concrete area is dull. 100% of the concrete area falls off with a characteristic depth of 3.6 cm. And steel strands in 25% of the concrete area have been exposed, which distributes from the fulcrum to a half of the span

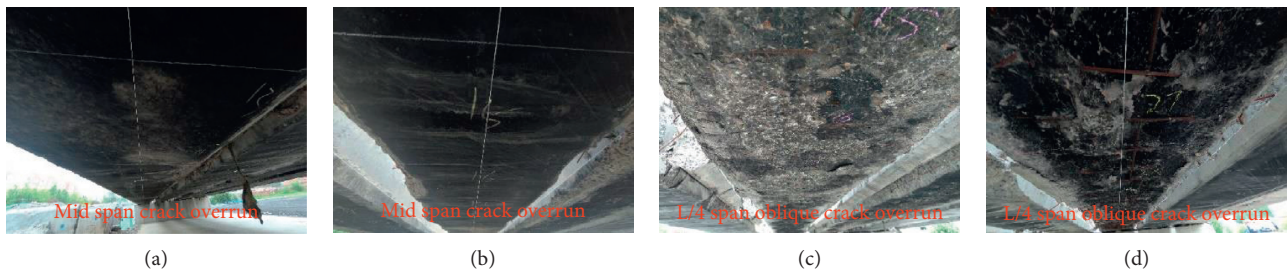


FIGURE 2: The appearance of test beam. (a) No. 2#. (b) No. 3#. (c) No. 4#. (d) No. 5#.

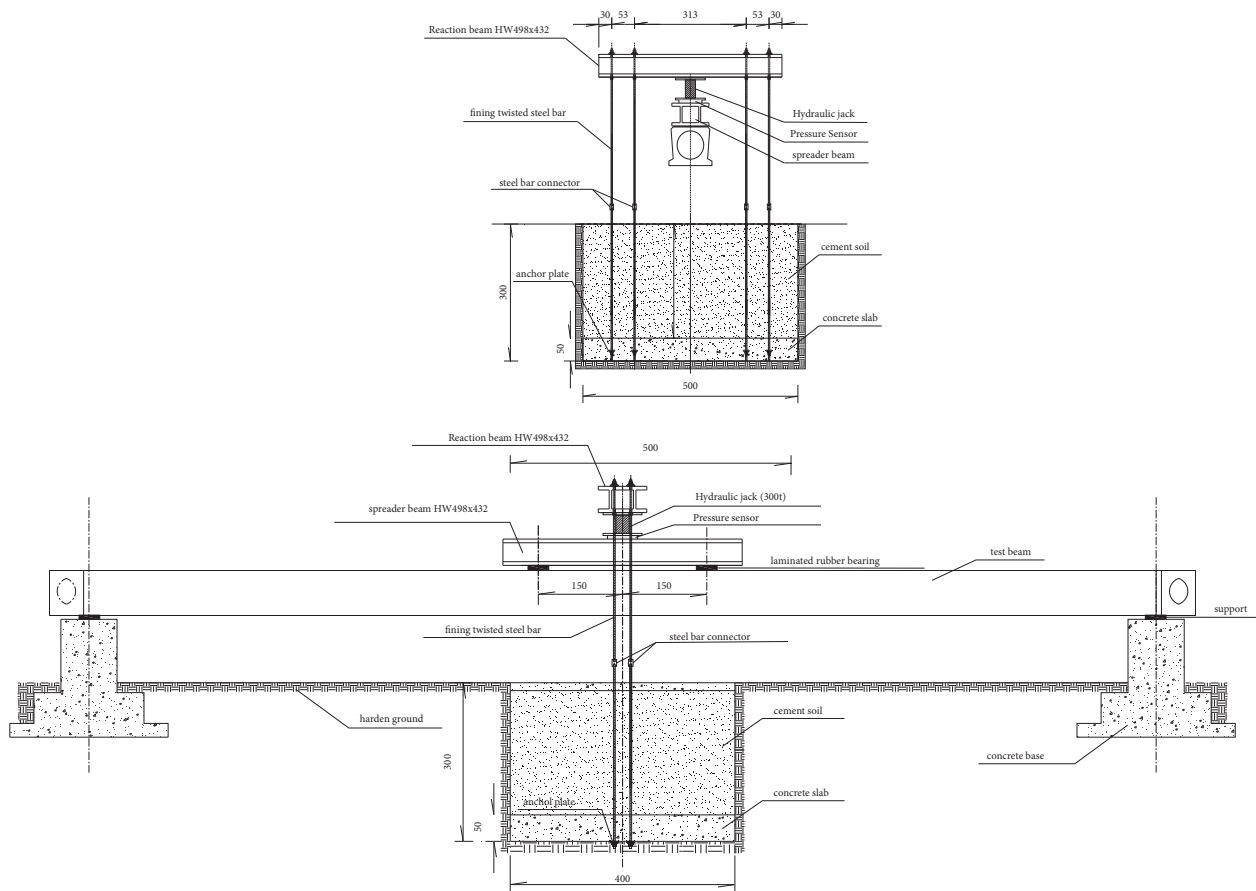


FIGURE 3: The loading arrangement (unit: cm).



FIGURE 4: The on-site loading situation.

TABLE 3: Loading process for hollow slab beams.

Step	Description
1	Deadweight (including distributing beam and jack deadweight). The load will last for 15 minutes to eliminate the inelastic deformation of the beam end support
2	Preload, load directly to 30% of the calculated ultimate load, last for 5 minutes, and then unload to zero. Force-control mode is adopted. The main purpose is to further eliminate the inelastic deformation of the loading system and verify the reliability of the loading system
3	Under formal loading, the ultimate load of hollow slab beams is calculated by 10 stages, and the ultimate load of hollow slab beams is calculated by 10% for each stage. Each step loading lasts for 5 minutes and force-control mode will be adopted.
4	After 100% ultimate load, unloading is carried out, and then four stages of secondary loading to 100%. Finally, the hollow slab beam is destroyed by intensive loading. The ultimate load of each stage is calculated by 5% ultimate load. Each step loading lasts for 5 minutes and force-control mode will be adopted
5	If the deformation of all hollow slab beams cannot converge with time, that is, the deformation cannot stop, it means that they have entered the ultimate load-bearing state, immediately stop loading, record the corresponding data and unload



FIGURE 5: The AL-ML32 high-precision leveling instrument.

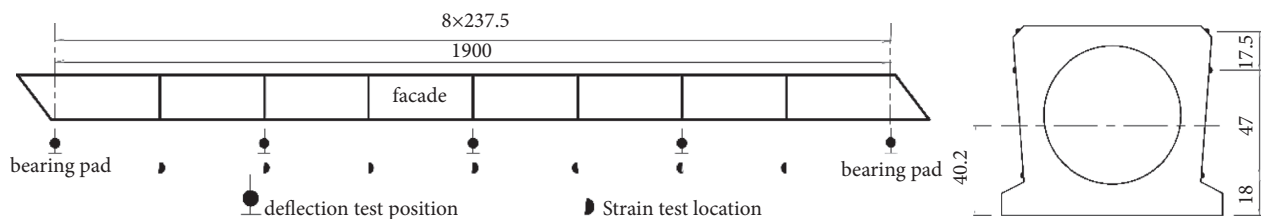


FIGURE 6: The strain location and deflection measuring points.

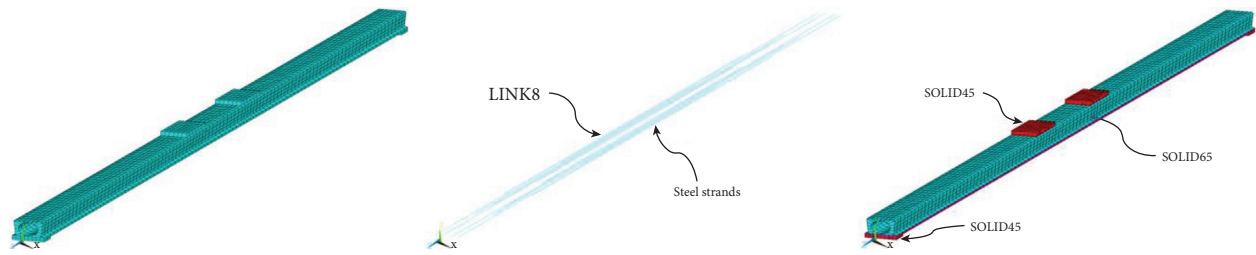


FIGURE 7: Finite element model.

gradually develops from linear to nonlinear when the total load is greater than 16 tons. (2) The original cracks gradually widened, and the area where new cracks first appeared was within 5 m of the longitudinal distance from the midspan and gradually extended toward the fulcrum as the loading progressed. The average crack spacing gradually decreased when load increases.

Cracks were spotted at the midspan where the longitudinal distance is 5.5 m. When these oblique cracks at the oblique cracks at the main tendon under tension firstly exceeded the vertical width of 1.5 mm, the loading was stopped. Typical failure mode is shown in Figure 8 and Table 4. It can be seen from the table that as the degree of beam damage increases, the failure mode of the test beam changes; that is, the shear failure will occur before the pure bending failure. The main reason was founded after careful considerations. As the fire temperature increases, the effective prestress of the bottom plate at one-quarter of the span length will decrease gradually, and the axial pressure that prevents the appearance and development of oblique cracks will decrease. Besides, due to the reduced strength of steel strands and concrete materials, the damage mode of such beams finally changes.

4. Analysis

4.1. Analysis of the Displacement

4.1.1. Normal Loaded Displacement. The normal-loaded deflection-load curve of midspan is shown in Figure 9. From the figure, the displacement-load relationship of the beam 2#, beam 3#, and beam 4# is linear when the total load distributes from 0 to 16 tons (just call it “0–16t stage” in the following passage). The displacement-load of the beam 4# in the “0–8t stage” is linear. In the “15~32t” stage, the measured stiffness of the hollow slab beam 2#, 3#, and 4# has decreased, and the downward deflection value of the midspan has accelerated. In the “5~32t” stage, the stiffness of the hollow slab beam 4# has decreased. While before the “5t stage,” the reduction of the stiffness was obvious but not too sharp during the loading process.

After the fire of hollow slab beams, due to the appearance and development of microcracks or cracks, as well as the loss of the prestress, the structural rigidity of the hollow slab section will be degraded. This phenomenon is defined as the stiffness degradation for convenience. By

comparing this stiffness degradation, the precise performances of those 4 beams will be learned. The hollow slab beam 2# is basically not affected by the fire and thus can be used as our benchmark for the stiffness. Under the same level of load, the deflection ratio of the remaining beams to the beam 2# is defined as the relative after-fire degradation stiffness K_f , and the calculation formula is shown as follows:

$$K_f = \frac{\delta_0}{\delta_i} \quad (1)$$

where δ_0 is midspan deflection of the unfired beam and δ_i is midspan deflection of beam i # under the same load.

When the maximum total load under normal loading is $32t$, it can be seen from Table 5 that the maximum bending moment of the corresponding pure bending section in the midspan is 1906 kN m, which has reached the design limit. It is calculated using the material-design values for calculation, according to the regulation “JTJ D62-2004 Code for Design of Highway Reinforced Concrete and Prestressed Concrete Bridges and Culverts” [16]. The relative after-fire degradation stiffness K_f of beams 3#, 4#, and 5# is, respectively, 89.4%, 81.5%, and 76.1%. Since those four selected beams were originally located in two adjacent holes of the same bridge, the stiffness of the 4 beams before the fire can be considered equal, and the mass distribution of those beams after the fire is supposed to be unchanged. The K_f value is consistent with the 3, 4, 5 boundaries of the bridge natural frequency assessment scale, which is from the regulations called “JGJ/T J21-2011, Specification for inspection and evaluation of the load-bearing capacity of highway bridges” [17], which means that the test of those four beams is very typical.

The mechanical properties of concrete and steel reinforcement materials will decrease to varying degrees after a bridge fire. When the overfire temperature exceeds 300°C, the elastic modulus (E) of the concrete after natural cooling is only 0.75 times that before the overfire. The higher the overfire temperature, the greater the reduction coefficient of elastic modulus. When the overfire temperature exceeds 800°C, the reduction coefficient of concrete elastic modulus after natural cooling is only 0.03. Fire will cause the elastic modulus of the steel bar to decrease after cooling, but its reduction coefficient is less than that of concrete under the same overfire temperature. And that coefficient is 0.9 when the overfire temperature is 400°C. Although the elastic modulus of the steel strand is hardly reduced after the fire,



FIGURE 8: The typical failure pattern. (a) No. 2#. (b) No. 3#. (c) No. 4#. (d) No. 5#.

TABLE 4: The failure mode of test beams.

Beam no.	Failure form
2#	The cracks in the tensioned main steel bars near the middle of the span first exceed the width of 1 mm
3#	The cracks in the tensioned main steel bars near the middle of the span first exceed the width of 1 mm
4#	The width of the crack at the tensioned main steel bar at the diagonal crack near 6.5 m from the middle span exceeds 1 mm
5#	The width of the crack at the tensioned main steel bar at the diagonal crack near 5.5 m from the middle span exceeds 1 mm

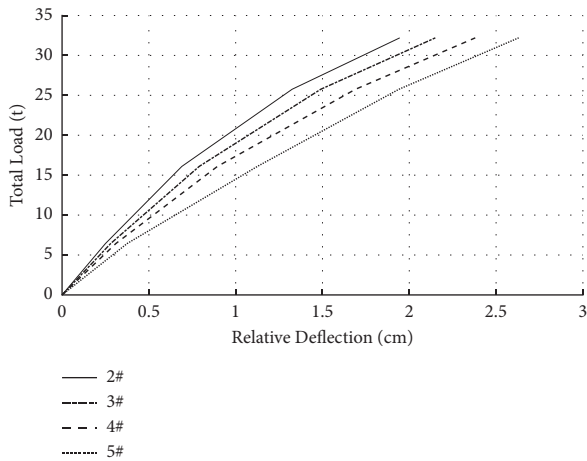


FIGURE 9: Midspan deflection-load curve of normal loading.

the effective prestress of the steel strand will decrease anyway, which will cause the overall rigidity of the beam to decrease too. As a result, when the fire temperature increases, the stiffness of the bridge after cooling decreases gradually.

4.1.2. Displacement under Ultimate Loading Condition.

The ultimate load results are summarized in Table 6 and Figure 10. From the table, the ultimate bending moments of beams 2#, 3#, 4#, and 5# are reduced successively. And the ultimate bending moment of beam 5# is only 76.4% compared to beams not exposed to fire, which is reduced by 23.6%. The corresponding deflection values of the limit bending moment of beams 2#, 3#, 4#, and 5# are gradually increased. Consequently, as the fire damage becomes more and more serious, the ultimate damage mode gradually changes from ductile failure to brittle failure, especially for beam 5#. The ultimate failure deflection of beam 5# after the fire is only 28.5% of that before the fire.

TABLE 5: Maximum deflection and relative overfire degradation stiffness in midspan under normal loading.

Beam no.	Maximum deflection (cm)	Relative stiffness/ K_f (%)
2#	1.94	100.0
3#	2.17	89.4
4#	2.38	81.5
5#	2.65	76.1

TABLE 6: Limit loading displacement results.

Beam no.	2#	3#	4#	5#
Total loading weight (t)	69.7	65.1	63.7	49.4
Limit moment (kN·m)	3429	3247	3191	2619
Relative value of the unburned beam (%)	100	94.7	93.1	76.4
Limit midspan deflection (cm)	37.2	26.55	15.95	10.62

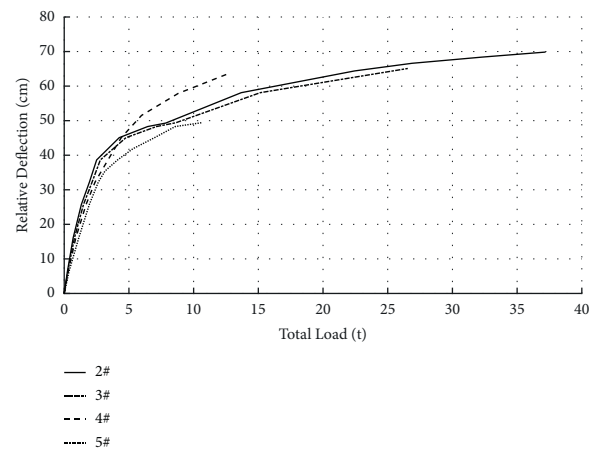


FIGURE 10: Deflection-load curves of beam 2# and beam 5# in midspan.

Figure 11 is the contrast diagram of finite element simulation values between beam 2# and the unfired beam. The midspan deflection of beam 2# was almost equal to the

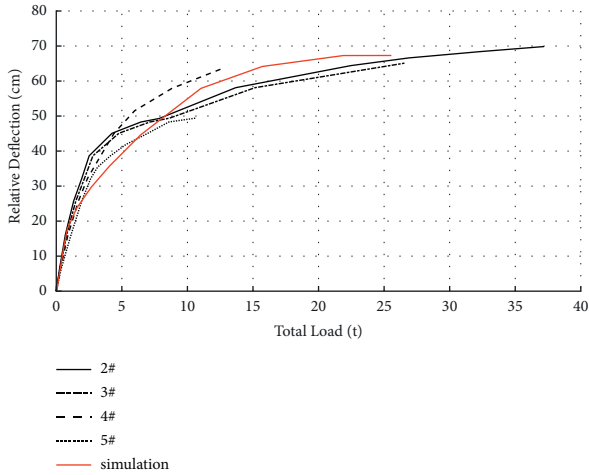


FIGURE 11: Contrast diagram of midspan deflection (simulated value of beam 2# and the unfired beam).

simulated value before cracking. And there is only a slight difference of the deflection before and after cracking, which can furtherly prove that beam 2# is unaffected by the fire and can be used as the reference beam. The mechanical properties of concrete and steel reinforcement materials will decrease to varying degrees after a bridge fire. The reduction coefficient of concrete compressive strength after natural cooling is only 0.8 times of the strength before the fire, when the overfire temperature exceeds 300°C [18, 19]. The strength reduction coefficient grows when the overfire temperature increases. And that coefficient reaches 0.2 under an overfire temperature beyond 800°C. Fire will cause the yield strength of the steel bar to decrease after cooling, but its reduction coefficient is less than that of concrete under the same overfire temperature. And that coefficient is 0.95 at around 400°C (which is the overfire temperature). After high temperature, the yield strength of prestressed steel bars has a certain relationship with the highest temperature and the initial stress level [20]. The ultimate strength and yield strength generally decrease with the increase of temperature. Also, the fire not only causes the physical properties of steel bars and steel strands to decrease, but also reduces the bonding force between them and its wrapping concrete [21]. As the overfire temperature increases, the concrete spalling becomes more serious, and the effective stress of the steel strands is distributed more unevenly along the longitudinal direction [22, 23]. With the gradual increase of the load, this phenomenon becomes far more obvious, which will cause the steel bar (steel strand) to yield before the concrete compression crashing. And the phenomenon is quite similar to the failure of under-reinforced beams. The following test results of full-scale compressive strain and diagrams of crack distribution can furtherly prove it. (1) When beam 2# fails, the cracks that appeared are relatively short and dense. The crack spacing and the average width of beam 2# is much smaller than that of beam 5#. (2) The compressive strain exceeds 0.002 for beam 2#, being 0.0008 for beam 5# when fails. Based

TABLE 7: Strain result of tensile side (measuring points 4–6#) under normal loading.

Beam no.	2#	3#	4#	5#
Strain/ $\mu\epsilon$	140	163	196	285
Q_f (%)	100.	85.9	71.4	49.1
Residual strain/ $\mu\epsilon$	0	3	7	17
Relative residual strain (%)	0	1.8	3.6	6

on the above two reasons, the failure mode of beams 2~5# gradually changed from ductile failure to brittle failure.

4.2. Strain Analysis

4.2.1. Normal Load Strain. The normal loading strain results are shown in Tables 7 and 8 and Figures 12 and 13. From the figure, at the preliminary stage of loading (when the total loading weight is less than 7t), the strain-load relationship is linear. The tensile test concrete strain-load curve is obviously nonlinear when loading weight is bigger than 7t, indicating that invisible microcracks on the tensile side will gradually appear at the middle and late loading process. At the last loading process, when the total loading weight is 32.2t, the strain on the tension side of beams 2#, 3#, 4#, and 5# gradually increases. In other words, the strength of beams 2#, 3#, 4#, and 5# decrease in sequence. After unloading, the residual strains of all selected beams are less than 20%.

In a hollow slab beam fire, the concrete strength of the hollow slab section will degrade accordingly. For simplicity, this phenomenon is referred to as the overfire degradation strength in later parts of this article. As mentioned before, beam 2# is the reference beam, and its concrete strength can be regarded as the benchmark. Thus, relative overfire-degradation strength (Q_f) can be defined by the following formula:

$$Q_f = \frac{\epsilon_0}{\epsilon_i} \quad (2)$$

in the formula, ϵ_0 is the midspan deflection of the unfired beam and ϵ_i is the midspan deflection of beam i# under the same load.

From Table 8, when the maximum total load under normal loading is 32t, the corresponding maximum bending moment of the pure bending section in the midspan is 1906 kN m. And the design value of ultimate bending moment of this section has been reached. The relative overfire degradation strength Q_f of beams 3#, 4#, and 5# is, respectively, 85.7%, 71.5%, and 49.1%. Considering the increase of the tensile strain caused by the concrete microcracks during the later loading process, this value of the corresponding beam is less than the relative degradation stiffness after being exposed to fire K_f .

4.2.2. Ultimate Load Strain. The compressive strain results of each beam at the end condition of the ultimate loading process are shown in Table 9. In ultimate failure, the compressive strain on the compression side of beams 2# and 3# exceeds 0.002, while the compressive strain of beam 5#, which was most seriously damaged by the fire, was only

TABLE 8: Tensile strain measurements under normal loading (32.2t).

Measuring point	Bridge deck position	Strain for the point/ $\mu\epsilon$			
		Beam 2#	Beam 3#	Beam 4#	Beam 5#
1-6#	One-eighth of the span	40	50	60	96.4
2-6#	Quarter of the span	48	59	73	119.5
3-6#	Three-eighths of the span	117	126	138	161.9
4-6#	A half of the span	140	182	226	284.5
5-6#	Five-eighths of the span	122	128	139	185.4
6-6#	Three-fourths of the span	51	62	77	129.8
7-6#	Seven-eighths of the span	42	51	63	69.7

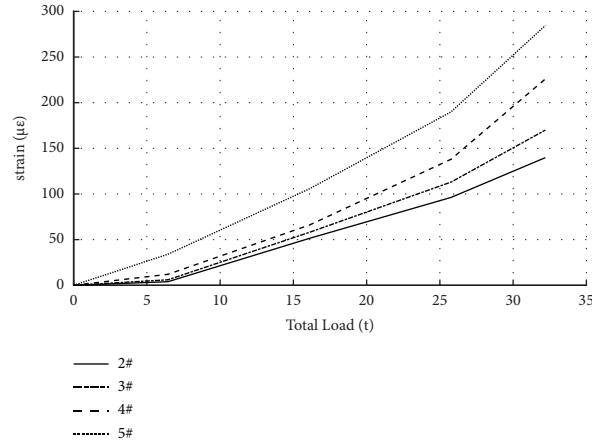


FIGURE 12: Strain history of normal loading tension side (measuring points 4-6#).

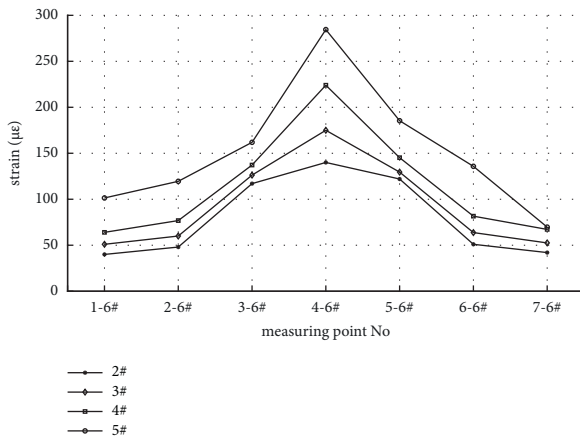


FIGURE 13: Strain distribution diagram of each section (tension side).

814 $\mu\epsilon$. And the strength of concrete materials is far from being fully utilized. The strain loading history of concrete on the compression side of a typical beam is shown in Figure 14.

4.3. Fracture Development Analysis

4.3.1. *Crack Development under Normal Loading.* During the normal loading process, no visible cracks appear in the beam bodies.

TABLE 9: Stress and strain measurements under ultimate loading.

Beam no.	2#	3#	4#	5#
Compressive strain/ $\mu\epsilon$	2021	1843	1429	814

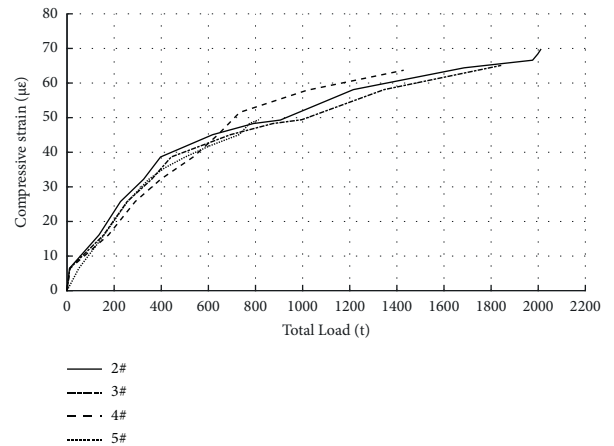


FIGURE 14: Strain distribution of typical beam section (tension side).

4.3.2. *Crack Development under Ultimate Loading.* Check Table 10 for the loading force when visible cracks occurred in the beam body. When visible cracks appear, the loading tonnage of beams 2#, 3#, 4#, and 5# decreases sequentially. Several reasons are shown as follows: (1) The bridge bottom plates are directly burned when caught fire, resulting in the

TABLE 10: Loads of beams with visible cracks.

No.	Load tonnage when cracked/t	Remarks
Beam 2#	48.3	—
Beam 3#	46.8	—
Beam 4#	45.1	The floor starts to seep
Beam 5#	38.6	Unusual noise from the steel strand

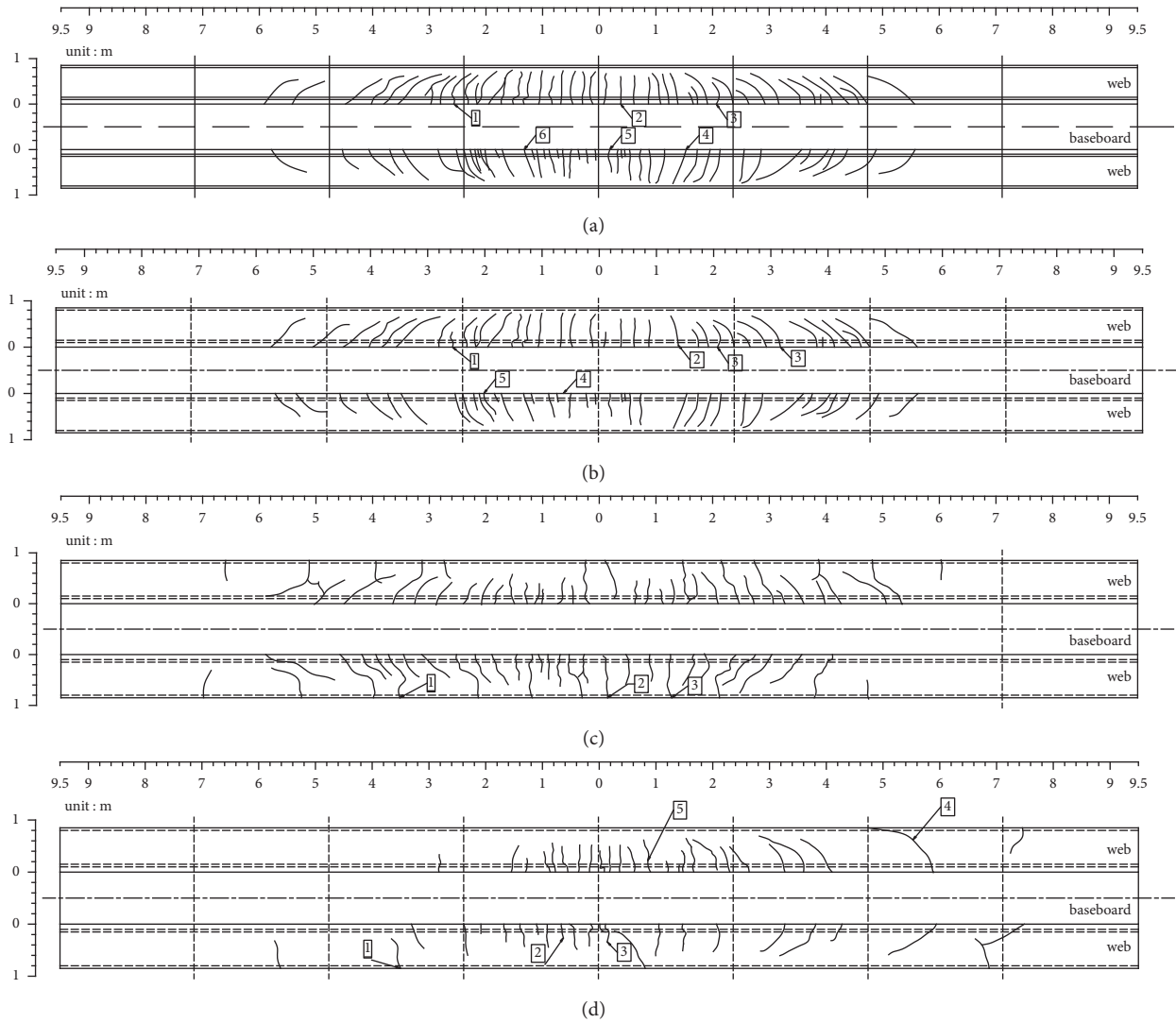


FIGURE 15: Schematic diagram of cracks at the end of limit loading. (a) Beam 2#. (b) Beam 3#. (c) Beam 4#. (d) Beam 5#.

loss of effective prestress and the reduction of the decompression moment. (2) The tensile performance of concrete will decrease after cooling when the overfire temperature exceeds 300°C. (3) Other reasons, such as the reduction of the bonding strength between the steel bar and the concrete, will also cause the bending moment to decrease for the beams and slabs after being exposed to fire reduce.

After the ultimate load is terminated, the cracks of the test beam are shown in Figure 15. When the ultimate failure occurs, the average cracks' spacing of the 2#, 3#, 4#, and 5# beam webs increases successively. And the proportion of long and wide cracks increases. The average crack spacing of

beam 5# is about two times the distance of beam 2# when destroyed.

5. Conclusion

In this paper, the appearance inspection and classification of prestressed concrete thin slab beams removed after a fire in an operating expressway are carried out. On this basis, four typical full-scale beams are selected for flexural failure test research. And the regular patterns of the mechanical properties of such thin-slab beams after a bridge fire are obtained. To a certain extent, these results make up for the

insufficiency of the numerical calculation method of thermal field coupling, and the following conclusions were initially obtained:

- (1) The drop-off depth and area of concrete after exposure to fire can be used as the characteristic parameters for the rapid identification of the bottom surface from prestressed concrete thin-slab beams after a bridge fire.
- (2) Brittle failure is the main mode of beams that slab concrete falling off in 97% area with a characteristic depth more than 2.6 cm on the bottom surface when directly exposed to fire. Thus, it is not appropriate to use thin-slab beams for busy road networks transporting hazardous chemicals.
- (3) Prestress loss will cause height reduction of the concrete shear zone, which is one of the main reasons why the bending-shearing failure of such beams happened before the pure bending failure.
- (4) Only the bottom surface of the hollow slab is directly exposed to the fire in this study. Thus, when the typical depth of the concrete spalling of the bottom plate after a fire is close to the net protective layer of the steel strand, the flexural bearing capacity is only 76% of that before the fire.
- (5) The mechanical properties of the prestressed concrete thin-slab beams whose bottom plate and web are simultaneously burned at high temperatures need further studies.

Data Availability

Some or all data, models, or code that support the findings of this study are available from the corresponding author upon reasonable request.

Conflicts of Interest

The authors declare that they have no conflicts of interest regarding the publication of this paper.

Acknowledgments

Financial support from Transportation Science and Technology Project of Shandong Province (Grant no. 2017B62) was gratefully acknowledged by the first and the second authors, respectively.


References

- [1] Ke Zhang, *Numerical Simulation Analysis of Fire Cracking of concrete Beam Bridge*, Chongqing Jiaotong University, Chongqing, China, 2018, in Chinese.
- [2] H. He, *The Experiment of Monolithic Reinforcement for Hollow Slab of Reinforced Concrete*, Chongqing Jiaotong University, Chongqing, China, 2013, in Chinese.
- [3] W. Z. Zheng, X. M. Hou, D. S. Shi, and M. X. Xu, "Experimental study on concrete spalling in prestressed slabs subjected to fire," *Fire Safety Journal*, vol. 45, no. 5, pp. 283–297, 2010.
- [4] J. Wang, Y. Cai, and D. Huang, "Testing research on thermal creep strain model of prestressing tendons and application of FEM analysis," *China Civil Engineering Journal*, vol. 32, no. 11, pp. 1–5, 2004, in Chinese.
- [5] Y. Ding, W. Zhang, X. Han, and X. Shi, "Study on the temperature field of prestressed concrete beam-plate in underbridge fire hazard and the prestress loss of tendon," *China Civil Engineering Journal*, vol. 48, no. S1, pp. 42–47, 2015.
- [6] M. B. Dwaikat and V. K. R. Kodur, "Hydrothermal model for predicting fire-induced spalling in concrete structural systems," *Fire Safety Journal*, vol. 44, no. 3, pp. 425–434, 2009.
- [7] V. K. R. Kodur and M. Dwaikat, "A numerical model for predicting the fire resistance of reinforced concrete beams," *Cement and Concrete Composites*, vol. 30, no. 5, pp. 431–443, 2008.
- [8] S.-H. Yun and J.-S. Jeon, "Post-fire damage assessment of Korean bridges using thermal-structure interaction fire analysis," *Magazine of Concrete Research*, vol. 70, no. 18, pp. 938–953, 2018.
- [9] G. Zhang, M. Zhu, S. He, and C. J. Wang, "Failure model analysis of prestressed concrete girder exposed to fire," *China Journal of Highway and Transport*, vol. 30, no. 2, pp. 77–85, 2017.
- [10] N. Yanagisawa, Y. Imagawa, O. Ohyama, M. Rutner, and A. Kurita, "Fire safety of bridges-methodology supporting design and forensic evaluation," *Steel Construction*, vol. 10, no. 1, pp. 2–9, 2017.
- [11] P. R. Prakash and G. Srivastava, "Nonlinear analysis of reinforced concrete plane frames exposed to fire using direct stiffness method," *Advances in Structural Engineering*, vol. 21, no. 7, pp. 1036–1050, 2018.
- [12] J. Alos-Moya, I. Paya-Zaforteza, A. Hospitaler, and E. L. Ossori, "Valencia bridge fire tests: validation of simplified and advanced numerical approaches to model bridge fire scenarios," *Advances in Engineering Software*, vol. 128, pp. 55–68, 2018.
- [13] E. Beneberu and N. Yazdani, "Residual strength of CFRP strengthened prestressed concrete bridge girders after hydrocarbon fire exposure," *Engineering Structures*, vol. 184, no. APR.1, pp. 1–14, 2019.
- [14] G. Zhang, V. Kodur, W. Yao, and Q. Huang, "Behavior of composite box bridge girders under localized fire exposure conditions," *Structural Engineering & Mechanics*, vol. 69, no. 2, pp. 193–204, 2019.
- [15] H. Chaowei, L. Kang, L. Hongyin, and W. Laiyong, "Research on the material properties of prestressed concrete girder bridge after exposed to fire," *IOP Conference Series: Earth and Environmental Science*, vol. 371, no. 4, Article ID 042027, 2019.
- [16] China Communication Press, *Jtj D62-2004 Code for Design of Highway Reinforced Concrete and Prestressed Concrete Bridges and Culverts*, China Communication Press, Beijing, China, 2004, In Chinese.
- [17] China Communication Press, *Jgj/T J21-2011 Specification for Inspection and Evaluation of Load-Bearing Capacity of Highway Bridges*, Communications Press of China, Beijing, China, 2014, in Chinese.
- [18] China Communication Press, *Cecs 252:2009, Standard for Building Structural Assessment after the Fire*, Planning Press of China, Beijing, China, (in Chinese), 2009.
- [19] S.-A. Li, *Mechanical Performance Process and post-disaster Evaluation Method of Pre-stressed concrete Girder Bridge*, Chang'an University, Xian, China, 2012.

- [20] M. F. Day, E. A. Jenkinson, and A. I. Smith, "Effect of elevated temperatures on high-tensile-steel wires for prestressed concrete," *Proceedings Instituting of civil Engineers*, vol. 16, no. 5, pp. 55–70, 1960.
- [21] C. T. Davie, H. L. Zhang, and A. Gibson, "Investigation of a continuum damage model as an indicator for the prediction of spalling in fire exposed concrete," *Computers & Structures*, vol. 94-95, no. 3, pp. 54–69, 2012.
- [22] J. D. Glassman and M. E. M. Garlock, "High temperatures and bridges: transverse stiffeners in steel girder fire performance," *Bridge Structures*, vol. 10, no. 1, pp. 43–52, 2014.
- [23] T. Liu, *Study on Decay Mechanism of Effective Prestress of concrete Bridges Exposed to fire*, Chang'an University, Xian, China, 2016, in Chinese.

Research Article

Pretreatment of Crumb Rubber with a Silane Coupling Agent to Improve Asphalt Rubber Performance

Li Liu ^{1,2}, Zhaohui Liu,² and Chengcheng Yang²

¹National Engineering Laboratory for Highway Maintenance Technology, School of Traffic and Transportation Engineering, Changsha University of Science & Technology, Changsha 410114, China

²School of Traffic and Transportation Engineering, Changsha University of Science & Technology, Changsha 410114, China

Correspondence should be addressed to Li Liu; 805296712@qq.com

Received 12 June 2021; Revised 22 September 2021; Accepted 23 September 2021; Published 12 October 2021

Academic Editor: Rotana Hay

Copyright © 2021 Li Liu et al. This is an open access article distributed under the Creative Commons Attribution License, which permits unrestricted use, distribution, and reproduction in any medium, provided the original work is properly cited.

There are known problems of dissolution, consistency of performance, segregation, and instability with the crumb rubber currently used in asphalt for road engineering. A silane coupling agent (KH550) solution was therefore used to pretreat the crumb rubber so as to improve its interfacial characteristics. The effects of KH550 on the properties of asphalt rubber were studied using high- and low-temperature performance tests, temperature sensitivity test, and compatibility test. On the basis of these tests, the optimum concentration of KH550 pretreated crumb rubber is 1.0%. The surface properties and micromodifications of the treated crumb rubber were analyzed using scanning electron microscopy and an infrared spectrometer. The performance and economic benefit of the modified asphalt rubber was compared to styrene-butadiene-styrene (SBS) modified asphalt, and it was found that KH550 pretreated crumb rubber is able to significantly improve the high-temperature performance of asphalt rubber, thus offering notable potential economic benefits.

1. Introduction

In recent years, a growing concern with saving energy, reducing emissions, recycling, and environmental protection has led to a stronger emphasis upon environmentally and socially responsible highway construction, encapsulated in the idea of the “Green Highway” and the work of the Green Highways Partnership (GHP), which is dedicated to transforming the relationship between the environment and transportation infrastructure.

Waste tires were once considered “black pollution,” which are not only damaging to the environment, but also a waste of resources [1–3]. Developments in industry have made it possible to turn waste tires into crumb rubber for highway engineering. This not only deals with the black pollution problem in a “one-step” and harmless way but also improves the quality of asphalt pavements and prolongs their service life [4–6].

Asphalt rubber has been applied in road engineering for nearly 50 years. It is widely used in the production of asphalt

rubber concrete, stress absorbing layers (Sam), stress absorbing intermediate layers (Sami), crushed stone seals (CHIP SEAL), waterproof pavement materials (TRCK COAT), and filling materials. Years of research and engineering practice have underscored the obvious advantages of asphalt rubber concrete in reducing road noise, delaying reflection cracks, and reducing the thickness of asphalt pavements and resistance to heavy traffic and bad weather [7, 8].

Crumb rubber is a macromolecular compound and its preparation and use in asphalt rubber involves a complex physical-chemical reaction with asphalt. It is difficult to completely dissolve crumb rubber in the asphalt matrix, making it easy for segregation to occur during transportation and use and diminishing the quality of asphalt rubber pavements [9–11].

While crumb rubber is an organic compound, asphalt is a mixture containing organic and inorganic compounds. The molecular structure of the silane coupling agent, KH550, can act as a “molecular bridge” in the form of Y-R-Si(OR)₃, in

which Y is an organic functional group and $\text{Si}(\text{OR})_3$ is a siloxane group. The siloxane group can react with the inorganic compounds, and the organic functional group can react with the organic compounds. When KH550 is interposed between the inorganic and organic interfaces, an organic matrix-silane coupling agent-inorganic matrix combination can be formed. Thus, the crumb rubber and the asphalt can be connected using the silane coupling agent to promote their mutual compatibility and effectively improve the road performance of the asphalt rubber [12–15].

This paper reports on a study of the technology involved in pretreating the surface of crumb rubber with the silane coupling agent, KH550, and the subsequent process of preparing asphalt rubber. The high-temperature performance, low-temperature performance, temperature sensitivity, and segregation performance of asphalt rubber before and after the addition of KH550 pretreated crumb rubber are compared and analyzed, and the optimum concentration of KH550 pretreated crumb rubber is determined. The mechanism by which crumb rubber pretreated with KH550 is modified is revealed and discussed through the use of scanning electron microscopy and an infrared spectrum test. The performance and economic benefit of using this kind of asphalt rubber is compared with that of SBS modified asphalt [16–19].

2. Materials and Methods

2.1. Materials. The base asphalt used in our tests was 70# asphalt and its performance indices are shown in Table 1. The molecular formula of KH550 is $\text{NH}_2(\text{CH}_2)_3\text{Si}(\text{OC}_2\text{H}_5)_3$, wherein $\text{NH}_2(\text{CH}_2)_3-$ is an organic functional group and $-(\text{OC}_2\text{H}_5)_3$ is a siloxy group. Its physical properties (provided by the manufacturer) are shown in Table 2. The particle size of the crumb rubber was 40 mesh, and its performance indices are shown in Table 3.

2.2. Technology for Pretreating Crumb Rubber with KH550. KH550 was added to an ethanol solution prepared with m (water) : m (anhydrous ethanol) = 1 : 20, where the different concentrations of KH550 at room temperature were 0.7%, 1.0%, and 1.3%. The three different concentrations of KH550 were used to treat crumb rubber by adding them to the crumb rubber in a solid blender. The rotational speed of the solid blender was 200 r/min, and the treatment was conducted for 30 min. As crumb rubber is granular and has a large specific surface area, the treatment time was controlled at about 30 min to ensure there was enough time for it to react fully with the KH550 solution. The treated crumb rubber was dried in an oven at about 100°C. The standard used to assess when the drying was complete was that the crumb rubber modifier was able to be completely dispersed without agglomeration, and after weighing separately for two times, the weight difference was less than 0.1%. Adding crumb rubber modifier that has not completely dried into asphalt can result in a large number of bubbles and may even lead to the asphalt rubber swelling and overflowing because of the presence of

ethanol and water. Once this process was complete, the asphalt rubber could be prepared by adding the crumb rubber modifier. For the sake of convenience, the asphalt rubber incorporating the crumb rubber modifier after surface treatment will be called “modified asphalt rubber” from now on. The process flow for pretreating CRM with KH550 solution is shown in Figure 1.

2.3. Preparation of the Modified Asphalt Rubber. With the drying of the crumb rubber modifier complete, the matrix asphalt was heated to 170~180°C in an oven and kept at constant temperature for about 1 h. Then, the weighed crumb rubber modifier was added and the mixture was sheared for 30 min at 5000 r/min using a high-speed shearing apparatus. After this, the mixture was put back into the oven at 170~180°C for 30 min. Finally, the developed mixture was sheared again for 15~20 min at 5000 r/min and then was allowed to swell for 1 h. When this process finished, the modified asphalt rubber was ready for testing. The process of preparing the modified asphalt rubber is shown in Figure 2.

2.4. High-Temperature Performance Test. The high-temperature performance of asphalt is directly related to the resistance of an asphalt pavement to deformation under temperature and load. In this paper, a softening point test and DSR complex shear viscosity test were used to evaluate the high-temperature performance of the modified asphalt rubber. The softening point of two kinds of asphalt rubber was measured by an automatic softening point meter. A dynamic shear rheometer (DSR) was used to measure the viscosity of the two kinds of asphalt rubber at 50~175°C. Their complex shear viscosities at 60°C were used as evaluation indexes. Both specimens had a diameter of 25 mm and a thickness of 1 mm. The test frequency was 10 rad/s, in accordance with AASHTO T315-05 [20].

2.5. Low-Temperature Performance Test. Low temperatures are one of the most important causes of the cracking of asphalt pavements, so the low-temperature performance of the asphalt directly affects a pavement’s resistance to cold conditions. Low-temperature ductility tests and low-temperature bending beam rheological tests were therefore used to evaluate the low-temperature performance of the modified asphalt rubber. The 5°C ductility of the two kinds of asphalt rubber was measured by an automatic ductility tester. The values for the creep stiffness modulus, S , and creep rate, m , were measured at -6°C by a low-temperature bending beam rheometer (BBR). The size of the specimens was $6.25 \text{ mm}^{\text{H}} \times 12.5 \text{ mm}^{\text{W}} \times 127 \text{ mm}^{\text{L}}$, and the specimens were loaded at $980 \text{ mN} \pm 50 \text{ mN}$ for 240 s, in accordance with AASHTO T313-12 [21].

2.6. Temperature Sensitivity Test. Asphalt is a temperature-sensitive material. Its temperature sensitivity is an important indicator for determining its workability and serviceability on the road surface. In this paper, we have used a penetration

TABLE 1: Performance indices of 70# asphalt.

Design index		Unit	Detected result
Penetration (25°C, 100 g, 5 s)		0.1 mm	70
Penetration index PI		—	-0.87
Softening point R and B		°C	49
Dynamic viscosity (60°C)		Pa.s	230
Ductility (10°C, 5 cm/min)		cm	37
Ductility (15°C, 5 cm/min)		cm	>100
Density		g/cm ³	1.040
Aging of rotating thin films (RTFOT)	Mass loss	%	-0.328
	Ductility (10°C, 5 cm/min)	cm	6.2
	Penetration ratio	%	63.8

TABLE 2: Physical properties of KH550.

Item	Property
Appearance	Colorless transparent liquid
Proportion (25°C/25°C)	0.946
Boiling point/°C	217
n_D^{25}	1.420
Solubility	Water-soluble
Acid-base property	Alkalinity

TABLE 3: 40-mesh crumb rubber performance indices.

Technical index	Detected result	Technical index (%)	Detected result
Relative density	1.2576	Acetone extractives	12.4
Water (%)	0.1	Carbon black content	34.8
Metal content (%)	0.002	Rubber hydrocarbon content	48.6
Fiber content (%)	0.3	Ash	3.1

index to evaluate the temperature sensitivity of the modified asphalt rubber. The penetration index was calculated according to formulas (1) and (2) when testing the penetration of the modified asphalt rubber at 15°C, 25°C, and 30°C.

$$\lg P = K + A \bullet T, \quad (1)$$

$$PI = \frac{20 - 500A}{1 + 50A}, \quad (2)$$

where PI is the penetration index; $\lg P$ is the logarithm of the penetration value measured at different temperatures; T is the test temperature; and K and A are regression coefficients.

2.7. Storage Stability Performance Test. As crumb rubber is a polymer material, it needs to undergo high-speed shearing, swelling, and development. However, it is difficult to ensure that it is completely dissolved in the asphalt. This can easily result in segregation during storage and transportation, thus affecting its performance. To evaluate the storage stability properties of the modified asphalt rubber and analyze the compatibility of the crumb rubber with the asphalt, tests were carried out in accordance with JTG E-20-2011, *Standard Test Methods of Bitumen and Bituminous Mixtures for Highway Engineering* [22]. The specific process was as

follows: the two kinds of modified asphalt rubber were heated to ensure they were fully irrigated. After uniform stirring, about 50 g of the modified asphalt rubber was slowly injected into a vertical aluminum tube. The opening of the tube was then closed with tweezers, and the tube was placed in an oven at $165^\circ\text{C} \pm 1^\circ\text{C}$ for $48\text{ h} \pm 1\text{ h}$. After heating, the aluminum tube was put in a freezer for 4 h to solidify the asphalt rubber. Then, the tube was cut into three sections with scissors. The upper and lower sections were put into sample boxes and heated until the asphalt rubber had melted. After mixing, the softening point test samples were poured, and their softening point was tested. It was then possible to evaluate the storage stability performance of the modified asphalt rubber by comparing the difference between the upper and lower sample's softening points.

2.8. Scanning Electron Microscopy Test. Scanning electron microscopy is an important tool for studying the micro-morphology and microstructure of materials. In order to evaluate the modification effect of KH550 on the crumb rubber and analyze the changes in the crumb rubber micro-morphology from before to after its modification, microobservations of the crumb rubber were carried out using scanning electron microscopy equipment. The specific test process was as follows: 2 g each of the treated and untreated crumb rubber modifier were weighed and placed

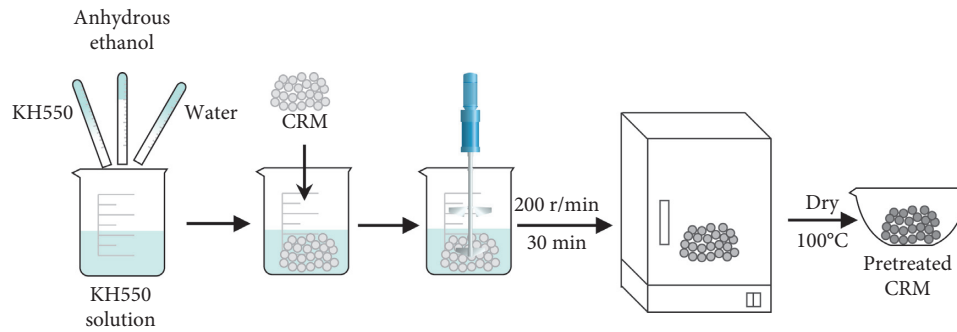


FIGURE 1: The process flow for pretreating CRM with KH550 solution.

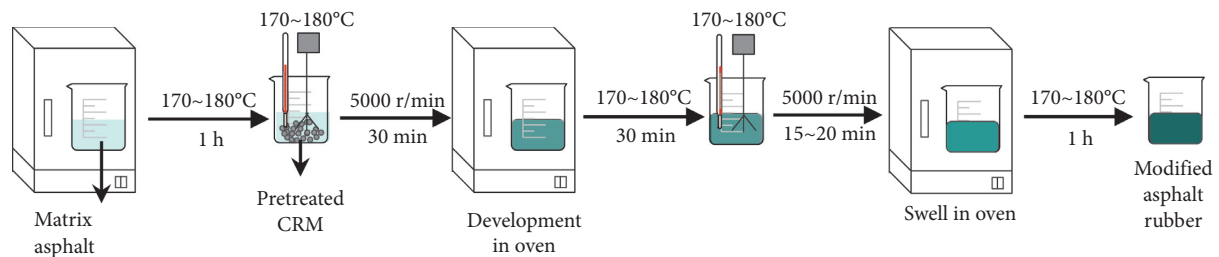


FIGURE 2: The process of preparing the modified asphalt rubber.

on a loading platform. A metal conductive film was evaporated on the surface of each sample using a vacuum membrane plate machine. Then, the loading platform was put into the scanning electron microscopy equipment for testing.

2.9. Infrared Spectrum Test. Infrared spectrum testing provides both a quantitative and qualitative method for analyzing functional group changes in materials. In order to analyze the changes in the asphalt rubber treated with KH550, it was subjected to infrared spectrum testing. The specific test process was as follows: 1 g of each of the two kinds of asphalt rubber was weighed and put into a test tube containing a carbon tetra-chloride solution. This was fully stirred until the asphalt rubber had completely dissolved. Two to three drops of the liquid samples were squeezed between two KBr crystal windows to form a thin liquid film. This was gently clamped with a fixture and put into an infrared spectrometer to determine the spectrogram.

3. Results and Discussion

3.1. Test Results of the High-Temperature Performance. The softening points of four kinds of asphalt rubber were tested using a ring and ball method, and the viscosities of the asphalt rubber were measured by a dynamic shear rheometer (DSR). The 60°C complex shear viscosities were selected as evaluation indices. The test results are shown in Figure 3.

It can be seen from Figure 3 that as the KH550 concentration increased, the softening point and 60°C complex shear viscosity of the modified asphalt rubber also gradually increased, with the growth trend for both being basically the same. This indicates that pretreating the crumb rubber with

KH550 effectively improves the high-temperature performance of asphalt rubber. It specifically suggests that KH550 improves the surface activity of the crumb rubber, enhances its wettability and dispersibility in asphalt, and promotes the compatibility of the crumb rubber and the asphalt.

When the concentration of the KH550 solution was between 0 and 1.0%, the high-temperature performance of the asphalt rubber increased at a continuous rate. However, when the concentration of the KH550 solution was between 1.0% and 1.3%, the growth rate decreased significantly. This suggests that there is a certain concentration at which a KH550 solution will most effectively treat crumb rubber, with the optimum value being about 1.0%.

3.2. Test Results of the Low-Temperature Performance. Values for the 5°C ductility, creep stiffness modulus, S , and creep rate, m , were acquired using -6°C low-temperature bending beam rheological tests, to evaluate the low-temperature performance of the four kinds of asphalt rubber. As the purpose of these tests was to determine the influence of the KH550 concentration on the performance of the asphalt rubber, the tests were also carried out using unmodified asphalt rubber (asphalt aged without being put in the rotating film oven or subjected to pressure aging). The test results are shown in Table 4.

Table 4 shows that treating crumb rubber with different concentrations of KH550 has little effect on the low-temperature performance of the asphalt rubber. The effect on the 5°C ductility was no more than 6.7%, and the effect on the creep modulus S and m values was only 5.6% and 5.1%. Crumb rubber is an elastic material that reacts with asphalt to enhance its elasticity. However, after the KH550 treatment, the rubber powder is coupled with the asphalt and

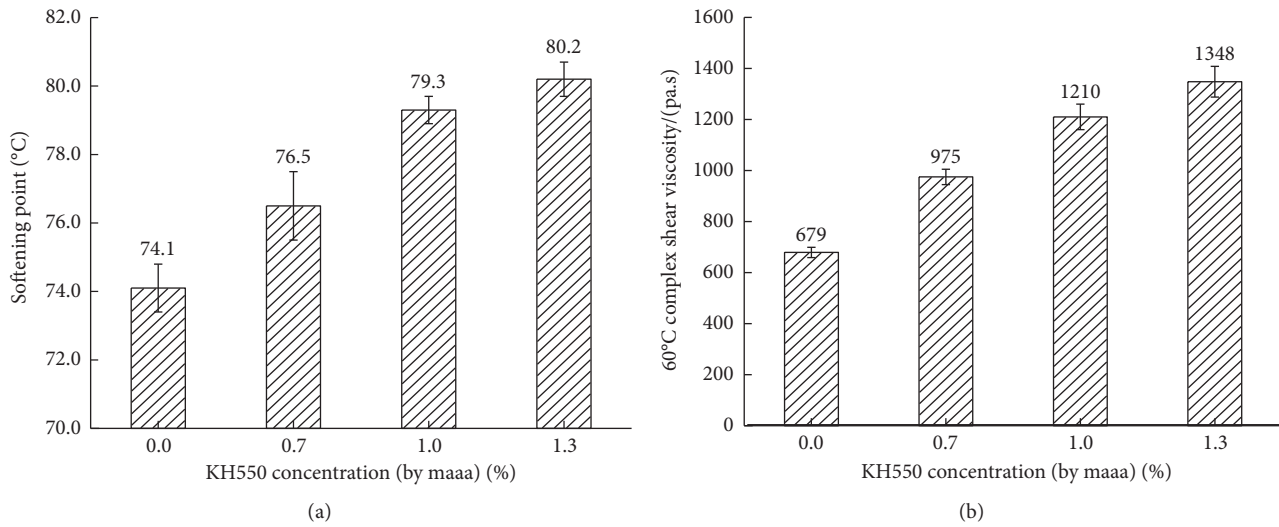


FIGURE 3: Effect of KH550 concentration on the asphalt rubber's high-temperature performance: (a) softening point; (b) 60°C complex shear viscosity.

TABLE 4: Test results of the low-temperature performance of the asphalt rubber.

Modified asphalt rubber	5°C ductility/cm		-6°C	
			S/MPa	<i>m</i>
MAR ₀	10.3		125	0.454
MAR _{0.7}	10.2		131	0.431
MAR _{1.0}	10.6		129	0.443
MAR _{1.3}	11.0		132	0.448

other complex reactions occur, the crumb rubber absorbs the lighter components of the asphalt to produce swelling, penetrating into the asphalt to form a gel layer, but at the same time, the lighter components of the asphalt are reduced, the deformation capacity of low temperature is weakened, and the low-temperature performance of asphalt rubber appears slightly reduced. However, after treatment with KH550 solution, the organic functional groups grafted onto the crumb rubber can react with the asphalt to produce stable covalent bonds, which can significantly improve the performance of asphalt rubber. However, as the crumb rubber can never be completely dissolved in the asphalt, the location of the crumb rubber is prone to stress concentration during the low-temperature stressing process, resulting in premature damage to the specimen.

3.3. Test Results of the Temperature Sensitivity. A penetration index, PI, was used to evaluate the temperature sensitivity of the modified asphalt rubber. The bigger the PI value, the lower the temperature sensitivity of the asphalt, that is, the better its temperature sensitivity performance. The PI value was calculated from penetration tests conducted at 15°C, 25°C, and 30°C. The results are shown in Table 5.

Table 5 shows that as the KH550 concentration increased, the PI value also increased, which indicates that KH550 improves the surface properties of the crumb rubber, improving the elasticity and thixotropy of the asphalt

rubber, transforming it from sol-type to gel-type, enhancing its compatibility with the asphalt and thereby reducing and significantly improving the temperature sensitivity of the modified asphalt rubber.

3.4. Test Results of the Storage Stability Performance. Storage stability performance tests confirmed the compatibility between the crumb rubber modifier treated with KH550 and the asphalt. The results are shown in Table 6.

Table 6 shows that the difference in softening point for the original asphalt rubber MAR₀ was 6.9°C, which is much larger than the 2.5°C maximum specified in JTG F40-2004 [23]. As the KH500 concentration increased, the softening point difference of the modified asphalt rubber gradually decreased. The main reason is that the crumb rubber and asphalt undergo a complex physical and chemical reaction at the high temperature. Although some of the crumb rubbers swell after the reacting with asphalt, they cannot be completely dissolved in asphalt. During the storage process of the asphalt rubber, segregation occurs under the action of gravity, which affects the storage stability of asphalt rubber. After the surface treatment with KH550, the surface of the crumb rubber is grafted with functional groups that react with inorganic and organic substances, which can react with inorganic and organic substances in asphalt and form stable covalent bonds, promoting the compatibility and cross-linking of crumb rubber and asphalt, enhancing the stability

TABLE 5: Asphalt rubber PI index.

Modified asphalt rubber	Penetration/(0.1 mm)			PI index
	15°C	25°C	30°C	
MAR ₀	18.9	35.8	54.3	1.95
MAR _{0.7}	18.4	34.5	52.0	2.07
MAR _{1.0}	18.3	33.5	51.2	2.17
MAR _{1.3}	17.8	32.1	49.2	2.26

TABLE 6: Asphalt rubber segregation test results.

Modified asphalt rubber	Softening point/°C		Difference
	Upper	Lower	
MAR ₀	68.8	75.7	6.9
MAR _{0.7}	75.2	77.8	2.6
MAR _{1.0}	78.1	79.9	1.8
MAR _{1.3}	79.3	81.0	1.7

of asphalt rubber, reducing the generation of segregation at the high temperature, and improving the storage stability of asphalt rubber.

According to the high-temperature test, low-temperature test, temperature sensitivity test, and segregation and dispersion performance test, the optimum concentration of KH550 pretreated crumb rubber is about 1.0%.

3.5. Test Results of the Scanning Electron Microscopy. In order to study the surface modification effects of KH550 on the crumb rubber, scanning electron microscopy (SEM) was used to examine and compare the surface characteristics of ordinary crumb rubber and modified crumb rubber. The SEM results are shown in Figure 4.

The following can be seen from Figure 4.

After treating the surface with KH550, the crumb rubber was noticeably changed, with a prismatic rather than a smooth surface, indicating that the coupling groups in the KH550 reacted with the crumb rubber surface, forming stable chemical bonds and changing the previously disconnected surface to a continuous surface.

A silane coupling film was formed on the surface of the modified crumb rubber. This film can form a solid chemical bond with the black carbon in the crumb rubber, also helping to connect the crumb rubber with the asphalt to form a stable continuous system.

The surface properties of the crumb rubber were significantly changed after treatment. At a high temperature, the silane coupling film in the crumb rubber has a strong reaction with the asphalt and forms a stable structure. This can improve the performance of the asphalt rubber in relation to high temperatures, temperature sensitivity, storage stability, and segregation. The low-temperature performance of the modified crumb rubber, however, is limited because of the slowing down of intermolecular activity.

3.6. Test Results of the Infrared Spectrum. Changes in the configuration and functional groups of the modified asphalt rubber were analyzed by comparing it with the original

asphalt rubber using infrared spectroscopy. The location of the infrared spectral band of the asphalt rubber and its attributions are shown in Table 7. The results are shown in Figure 5.

The following can be seen from Figure 5.

The saturated C-H bond in the main absorption peak of the modified asphalt rubber was significantly lower than it was in the original asphalt rubber. This shows where the saturated C-H bond breaks to form an unsaturated bond. It therefore appears to be the case that the strong chemical reaction between the modified crumb rubber modifier and the asphalt is more productive of breaks in chemical bonds and the formation of other stable chemical bonds. This makes the bonding between the modified crumb rubber and the asphalt better and increases its capacitance.

The treatment applied to the modified asphalt rubber increased the C≡C bond vibration zone. So, the treated crumb rubber and the asphalt had greater internal cross-linking, leading to the further formation of chemical bonds. This improved the compatibility of the two materials, resulting in an increase of viscosity at high temperatures.

The increase in the methylene C-H bond shear vibration absorption peak for the modified asphalt rubber indicates that the internal crosslinking of the treated crumb rubber decreased while the reaction with the asphalt increased, promoting bonding and further reaction between the treated crumb rubber and the asphalt. This resulted in a reduction in the degree of segregation.

3.7. Comparative Road Performance Analysis. At present, SBS modified asphalt is the most widely used product for high-grade highways. This kind of asphalt generally performs well, but it has high production costs, so it is difficult to justify its use for lower-grade roads or ones where there is high traffic volume. The treated crumb rubber in modified asphalt rubber can improve the road performance of asphalt and has a very broad range of possible applications. To undertake a cost-benefit analysis of using modified asphalt rubber, 20% modified asphalt rubber (with a KH550 concentration of 1.0%) and 4.5% SBS modified asphalt (the

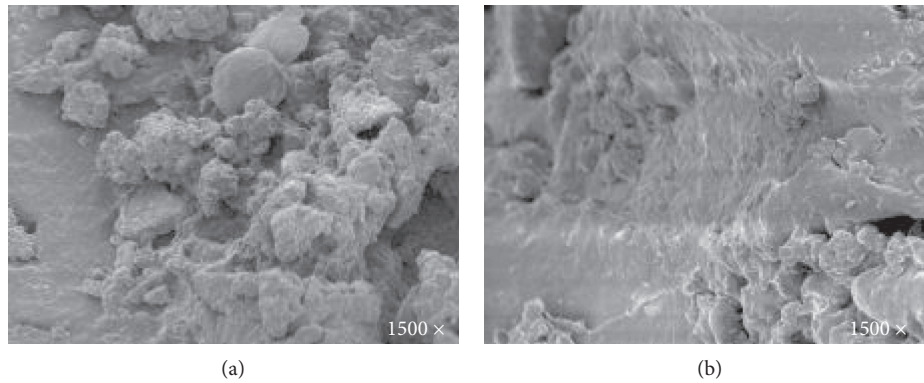


FIGURE 4: SEM photos of ordinary and modified crumb rubber: (a) ordinary crumb rubber (1500x); (b) modified crumb rubber (1500x).

TABLE 7: The asphalt rubber’s position and home form in the infrared spectrum.

Absorption peak	Absorption peak position/cm ⁻¹
Saturated C—H bond stretching vibration	2 924
C = C bond stretching vibration	1 599
Methylene C—H bond shear vibration	1 458
C≡C bond vibration area	2 360

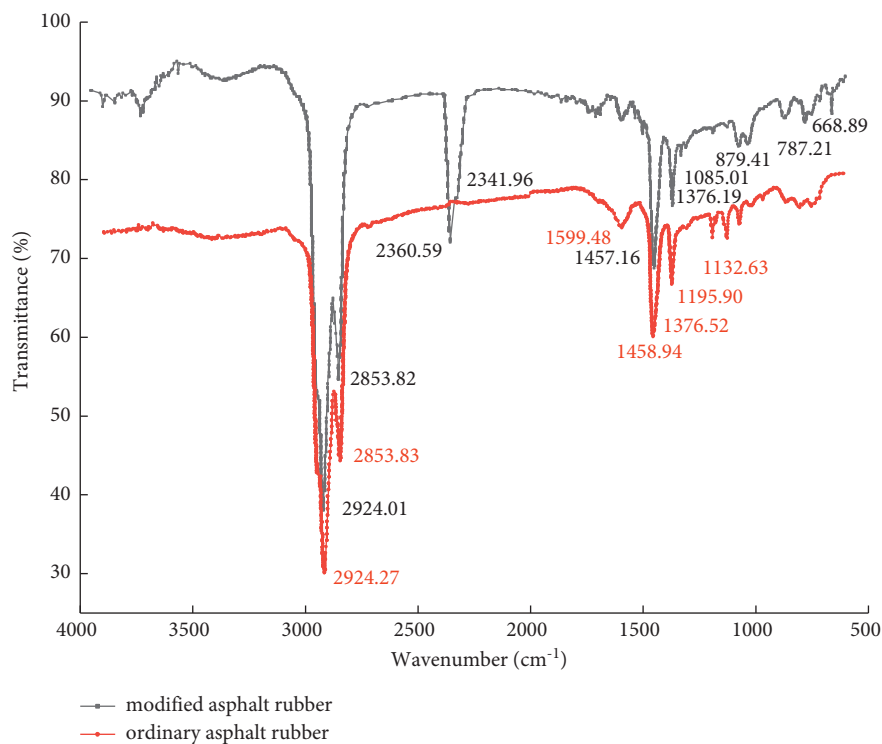


FIGURE 5: Infrared spectrum test results.

current content for SBG modified asphalt is generally between 4.0% and 5.0%) were subjected to a cost comparison. A comparison of the performance indices of the two types of modified asphalt is shown in Table 8. The results of the economic benefit comparison are shown in Table 9.

Table 8 shows that after surface modification by KH550, the high-temperature performance of the crumb rubber

modifier was significantly improved, with its performance index exceeding that of SBS modified asphalt. Although the low-temperature ductility of the crumb rubber modifier was clearly lower than that of SBS modified asphalt, according to recent research, the presence of crumb rubber modifier particles in asphalt rubber can make it easier for a concentration of stress to occur during tensile processes,

TABLE 8: Comparison of the performance indices of modified asphalt rubber and SBS modified asphalt.

Performance index	Modified asphalt rubber	SBS modified asphalt
Penetration (25°C, 100 g, 5 s)/(0.1 mm)	33.5	51.4
Ductility (5°C, 5 cm·min ⁻¹) (cm)	10.6	25.8
Softening point (R&B) (C)	79.3	76.1
Elastic restitution (25°C) (%)	85	87
PG standard	PG82-28	PG76-28

TABLE 9: Analysis of the economic benefit of modified asphalt rubber.

Asphalt type	Modified asphalt rubber					SBS modified asphalt	
Raw material	70# asphalt	CRM	KH550	Water	Ethanol	70# asphalt	SBS
Proportion (t)	1.000	0.200	0.002	0.002	0.040	1.000	0.045
Unit price/(CHY·t ⁻¹)	3 200	2 800	38 000	3	850	3 200	18 000
Material price/CHY	3 200.000	560.000	76.000	0.006	34.000	3 200.000	810.000
Material mass (t)			1.200				1.045
Total material price/CHY			3 870				4 010
Price per ton/CHY			3 225				3 837
Processing price/(CHY·t ⁻¹)			350				200
Finished product price/(CHY·t ⁻¹)			3 575				4 037

affecting test results. In addition, the low-temperature PG standard for modified asphalt rubber and SBS modified asphalt is the same, indicating that their low-temperature performance is similar.

Table 9 shows that the product price of modified asphalt rubber is 462 CHY·t⁻¹(12.9%) lower than that of SBS modified asphalt. In the production process, only needing a device to treat the surface of the crumb rubber can produce obvious economic benefits. In addition, the preparation of modified asphalt rubber using just a surface treatment of the crumb rubber can also reduce the amount of solid waste pollution. This has resulted in the process receiving extensive support from the state in terms of both investment and policy, with what promises to be good economic and social outcomes.

4. Conclusions

The consumption of crumb rubber, as a processed product of waste tires, can deal with the problem that crumb rubber is difficult to handle in the natural environment, and also by adding crumb rubber to asphalt, modified asphalt rubber can be prepared, which improves the performance of asphalt pavement. The paper uses KH550 solution to pretreat the surface of crumb rubber and prepare the modified asphalt rubber. Through a series of tests to study the performance of coupled surface modified asphalt rubber, the main conclusions were as follows.

As the concentration of KH550 solution increases, the softening point and viscosity of the modified asphalt rubber show a rising trend, with small changes in 5°C ductility and bending stiffness modulus S and m , indicating that KH550 solution can improve the high-temperature performance of asphalt rubber, while KH550 solution has little effect on the low-temperature performance of asphalt rubber.

After the surface pretreatment of the crumb rubber with KH550 solution, the penetration index PI of the modified

asphalt rubber gradually increases and the softening point difference gradually decreases, indicating that the pretreatment of the crumb rubber with KH550 solution can promote the compatibility of the crumb rubber and asphalt and enhance the temperature sensitivity and storage stability of the asphalt rubber.

Through high-temperature performance test, low-temperature performance test, temperature sensitivity test, and segregation performance test, the optimum concentration of KH550 for the surface treatment of crumb rubber was determined to be 1.0%.

The results of the scanning electron microscope test show that KH550 solution reacts with the crumb rubber and forms a silane coupling film on the surface of the crumb rubber, which can promote the chemical reaction between the crumb rubber asphalt to form a stable structure.

The results of infrared spectroscopy tests showed that the reaction between KH550 surface pretreatment and the crumb rubber and asphalt resulted in a new C≡C bond, which promoted the crosslinking and compatibility of the crumb rubber with the asphalt and enhanced the performance of the asphalt rubber.

Data Availability

The data used to support the findings of this study are available from the corresponding author upon request.

Conflicts of Interest

The authors declare that there are no conflicts of interest regarding the publication of this paper.

Acknowledgments

This work was supported by National Key R&D Program Projects of China (2018YFB1600200); Natural Science

Foundation of Hunan Province (2020JJ5578); Excellent Youth Project of Education Department of Hunan Province (20B033); Open Fund (kfj180101) of the National Engineering Laboratory of Highway Maintenance Technology (Changsha University of Science and Technology); and Foundation for Application of Steel Slag and Nickle Slag in Highway of Coastal Area (KJ-2020ZU01XM-001).

References

- [1] X. Yang, Z. You, D. Perram et al., "Emission analysis of recycled tire rubber modified asphalt in hot and warm mix conditions," *Journal of Hazardous Materials*, vol. 365, pp. 942–951, 2019.
- [2] J. Tang, C. Zhu, H. Zhang, G. Xu, F. Xiao, and S. Amirkhani, "Effect of liquid ASAs on the rheological properties of crumb rubber modified asphalt," *Construction and Building Materials*, vol. 194, pp. 238–246, 2019.
- [3] P. Li, X. Jiang, Z. Ding, J. Zhao, and M. Shen, "Analysis of viscosity and composition properties for crumb rubber modified asphalt," *Construction and Building Materials*, vol. 169, pp. 638–647, 2019.
- [4] A. P. Vilela, D. W. Silva, L. M. Mendes, M. A. Martins, L. E. V. D. B. Vaz, and R. F. Mendes, "Surface modification of tire rubber waste by air plasma for application in wood-cement panels," *Bioresources*, vol. 13, pp. 6409–6427, 2018.
- [5] X. Ding, T. Ma, W. Zhang, and D. Zhang, "Experimental study of stable crumb rubber asphalt and asphalt mixture," *Construction and Building Materials*, vol. 157, pp. 975–981, 2017.
- [6] Z. Chen, J. Pei, T. Wang, and S. Amirkhani, "High temperature rheological characteristics of activated crumb rubber modified asphalts," *Construction and Building Materials*, vol. 194, pp. 122–131, 2019.
- [7] M. Bueno, J. Luong, F. Terán, U. Viñuela, and S. E. Paje, "Macrotecture influence on vibrational mechanisms of the tyre-road noise of an asphalt rubber pavement," *International Journal of Pavement Engineering*, vol. 15, no. 7, pp. 606–613, 2014.
- [8] L. Liu, Z. H. Liu, C. C. Yang, H. You, and W. Li, "Effect of the binary compound method of TOR promoting dissolution and NaOH solution surface treatment on the performance of rubber asphalt," *Construction and Building Materials*, vol. 305, 2021.
- [9] Z. Ding, J. Jiang, S. Y. He, and C. Shen, "Research on physical and chemical behavior of crumb rubber in asphalt rubber," *Advanced Materials Research*, vol. 255-260, pp. 3411–3415, 2011.
- [10] K. Egami, M. Kimura, and T. Hamaguchi, "Effect of crumb rubber modifier dissolution on storage stability of crumb rubber-modified asphalt," *Transportation Research Record Journal of the Transportation Research Board*, vol. 2370, pp. 109–115, 2013.
- [11] A. Ghavibazoo, M. Abdelrahman, and M. Ragab, "Changes in composition and molecular structure of asphalt in mixing with crumb rubber modifier," *Road Materials and Pavement Design*, vol. 17, pp. 1–14, 2016.
- [12] M. Provost, K. Raulin, T. Maindron, and V. Gaud, "Influence of silane coupling agent on the properties of UV curable SiO₂-PMMA hybrid nanocomposite," *Journal of Sol-Gel Science and Technology*, vol. 89, no. 3, pp. 796–806, 2019.
- [13] Z. Li, J. Wan, Y. Li, Y. Li, F. Zhao, and S. Zhao, "Effects of coupling agents on the properties of an NR/SBR matrix and its adhesion to continuous basalt fiber cords," *Journal of Applied Polymer Science*, vol. 136, no. 8, Article ID 47098, 2019.
- [14] J. Song, M. Xu, W. Liu et al., "Thermoplastic rubber (TPR) modified by a silane coupling agent and its influence on the mechanical properties of oil well cement pastes," *Advances in Materials Science and Engineering*, vol. 2019, Article ID 3587081, 11 pages, 2019.
- [15] M. Raj, S. Joshi, R. Savaliya, and L. Raj, "Studies on the effects of cenosphere on polypropylene matrix using silane coupling agent," *Journal of Thermoplastic Composite Materials*, vol. 31, no. 11, pp. 1510–1528, 2018.
- [16] Z. Wang, Y. Liu, H. Lv, and B. Yang, "Enhancement of interface performance between shape memory alloy fiber and polymer matrix using silane coupling agent KH550 and Al₂O₃ nanoparticles," *Polymer Composites*, vol. 39, no. 9, pp. 3040–3047, 2018.
- [17] W. K. Choi, G. Y. Park, B. S. Kim, and M. K. Seo, "Effect of silane coupling agent on the creep behavior and mechanical properties of carbon fibers/acrylonitrile butadiene rubber composites," *Journal of Nanoscience and Nanotechnology*, vol. 18, no. 9, pp. 6220–6227, 2018.
- [18] Y. Xiang, Y. Xie, and G. Long, "Effect of basalt fiber surface silane coupling agent coating on fiber-reinforced asphalt: from macro-mechanical performance to micro-interfacial mechanism," *Construction and Building Materials*, vol. 179, pp. 107–116, 2018.
- [19] Q. Wei and W. H. Wang, "Properties of phenol formaldehyde resin modified with silane coupling agent (KH550)," *International Journal of Adhesion and Adhesives*, vol. 84, pp. 166–172, 2018.
- [20] AASHTO T315-05, *Standard Method of Test for Determining the Rheological Properties of Asphalt Binder Using a Dynamic Shear Rheometer*, American Association of State Highway and Transportation Officials, Washington, DC, USA, 2005.
- [21] AASHTO T313-12, *Determining the Flexural Creep Stiffness of Asphalt Binder Using the Bending Beam Rheometer (BBR)*, American Association of State Highway and Transportation Officials, Washington, DC, USA, 2012.
- [22] China, MoT.PsRo, *Standard Test Methods of Bitumen and Bituminous Mixtures for Highway Engineering, JTG E20-2011*, China Communications Press Co., Ltd., Beijing, China, 2011.
- [23] China, MoT.PsRo, *Technical Specifications for Construction Highway Asphalt Pavement. JTG F40-2004*, China Communications Press Co., Ltd., Beijing, China, 2004.

Research Article

Early Age Hydration Characteristics of Calcium Sulphoaluminate Cement Mortar Cured at a Temperature Range from -10 to 20°C

Zhongyu Chen,¹ Jianhong Fang ,² Feng Ming ,³ and Yuhang Liu³

¹Qinghai Communications Holding Group Co. Ltd., Xining 810000, China

²Qinghai Research Institute of Transportation, Xining 810016, China

³State Key Laboratory of Frozen Soil Engineering, Northwest Institute of Eco-Environment and Resources, Chinese Academy of Sciences, Lanzhou 730000, China

Correspondence should be addressed to Feng Ming; mf0329@163.com

Received 22 July 2021; Accepted 11 September 2021; Published 8 October 2021

Academic Editor: Rotana Hay

Copyright © 2021 Zhongyu Chen et al. This is an open access article distributed under the Creative Commons Attribution License, which permits unrestricted use, distribution, and reproduction in any medium, provided the original work is properly cited.

With the increasing number of infrastructures constructed in marine and cold regions, research on and applications of calcium sulphoaluminate (CSA) cement have been flourished, but the hydration process of CSA at low temperature has not been systematically investigated. To characterize the influence of low temperature on the hydration characteristics, freshly mixed CSA mortars were cured at -10 , -5 , 0 , 5 , and 20°C , respectively. The hydration process was investigated by electrical resistivity, compressive strength, and microstructure analyses. Results show that the hydration process (especially the induction period) is lengthened by low curing temperature. Both the electrical resistivity and compressive strength increase with an increase in the curing temperature. The compressive strength was reduced at a low curing temperature. Among these five curing temperatures, 5°C is the optimal curing temperature. Low temperatures do not change the kinds of hydrates, but reduce their amount. The scanning electron microscopy results illustrate that fewer hydrates fill the pores in specimens cured at low temperatures, while more hydrates form at higher temperatures. Moreover, low curing temperature contributes to the formation of coarse ettringite crystals. For the cement used at low temperature, the induction period should be reduced by adjusting the calcining process and composition proportion.

1. Introduction

Over nearly three decades, many infrastructures have been constructed in China, which has greatly promoted the development of concrete structures and cements [1]. The future development of cold and polar regions has become a trend. However, traditional Portland cement cannot meet the needs of engineering constructions in these low temperature areas, such as high-early strength and better expansion fill performance. Compared with other types of cement, calcium sulphoaluminate (CSA) cement has the advantages of fast setting, high early strength, and short construction period [2]. CSA cement is not only suitable for projects with high resistance to erosion, but is also very suitable for projects in cold regions. Moreover, CSA cement is one of the most economical rapid hardening cements with an annual output about approximately 1.3 million tons [3]. Motivated by the

demand for environment protection and other special requirements, research on and applications of CSA have received increasing attention [4–6]. However, the hydration process of CSA at low temperatures is not well characterized.

To date, many methods have been used to quantify the hydration degree of cement [7–11]. During the hydration process, with the consumption of free water, the resistivity of mortar exhibits a large change. Therefore, the hydration process can be indirectly reflected by measuring its resistivity [12]. Moreover, resistivity can combine the chemical reaction with the changes in physical properties. Thus, it has been used to describe the hydration characteristics of cement at an early age [13]. Tamas noted out that two maxima appeared in the resistivity curves: the first one occurred at 1–3 hours, and the second one occurred at 6–10 hours [14]. Furthermore, the time of the first maxima is close to the initial setting time [15, 16]. Because the plasma impedance

can accurately reflect the variation in the ion concentration and structure [17], the electrical resistivity method has been adopted as a standard method in cement engineering [18]. Based on the electrical resistivity and its differential curves, the hydration process was first divided into three stages [12] and then four stages [19].

The hydration process is accompanied by the variation in the pore structure. The resistivity is an effective parameter for describing the formation of the pore structure [20]. It is found that the diffusion coefficient of ions in porous media has a proportional relationship to their resistivity, and that their permeabilities can be evaluated by their resistivities [21]. However, results have indicated that the diffusivity measured by the resistivity method is larger than that measured by other methods. Moreover, there is no significant association between the diffusivity and porosity when the admixtures are added [22]. As an improvement, on the basis of the Nernst–Einstein equation, the resistivity has been adopted as a rapid test method for determining the permeability of concrete. This method can be applied only when the pores are saturated with saltwater. Even so, this has not prevented the resistivity method from becoming the standard method for determining the permeability of concrete [23, 24]. Moreover, there is a quantitative relationship between the electrical resistivity and pore structure during the hydration process [20]. Because the porosity and pore structure are closely related to strength, the compressive strength can be predicted through resistivity [25, 26]. In addition, studies have demonstrated that resistivity can not only describe the evolution of the pore structure, but also can be used to evaluate the damage degree [27]. In other words, the resistivity is a key parameter for the evaluation of the pore structure and durability of concrete [28, 29].

Because ettringite (AFt)/monosulphoaluminate (AFm) has an obvious influence on compressive strength, many laboratory tests have been conducted to investigate the formation conditions of AFt/AFm. It is found that temperature has a great influence on the hydration process of cement paste. However, some researchers have found that the amount of AFt and AFm reaches the maximum at 20°C and 40°C [30], while some researchers have noted out that the stable product is AFt at 80°C, while AFm at 120°C, respectively [31]. Researchers believe that ettringite starts to dehydrate rapidly at approximately 50°C under normal humidity conditions [32]. These results indicate that an elevated temperature can accelerate the formation of AFm [33]. It can be seen that temperature not only influences the hydration process, but also influences the kinds of hydration products. At present, there are few studies on the hydration mechanism of CSA cement at low (subzero) temperatures. Furthermore, the influence of temperature on the hydration process is not uniform, which provides an opportunity to study the hydration mechanism of CSA cement cured at low (subzero) temperatures.

It can be concluded that the resistivity method has been widely used to characterize the hydration behavior of cement in the early stage. However, few studies have focused on the resistivity of CSA cement cured at low temperatures, especially at subzero temperatures. The lack of data on the CSA

cement cured at low temperatures has hampered the further application of CSA cement in cold regions. Therefore, a series of macro- and microtests were conducted. In this study, the hydration characteristics at low temperatures were investigated, and the variations in resistivity, compressive strength, and hydration products were analyzed.

2. Materials and Methods

2.1. Raw Materials. A rapid hardening calcium sulphoaluminate cement, which was taken from Tangshan, China, was used in this study. Tables 1 and 2 show the chemical components and the physical properties of the CSA cement, respectively. Figure 1 presents the X-ray diffraction pattern.

A commercial standard sand was used, and its particle size distribution is shown in Table 3.

The antifreeze was ethanediol (C₂H₅OH, analytical pure, with a mass fraction greater than 99.7% and a density of 0.789~0.791 g/ml at 20°C), with a mass fraction of 10% of water (this content can keep the water from freezing at -10°C). Tap water was used to mix the mortar.

2.2. Specimen Preparation. According to the national standards (methods of testing cement-determination of strength (GB/T 17671)), the cement-sand ratio was determined as 1 : 3. Two water-cement ratios (w/c = 0.4 : 1 and w/c = 0.5 : 1) were adopted in the laboratory tests. The raw material was stirred uniformly by a planetary-type mixer. First, the cement, ethanediol, and water were mixed for 30 s at 60 rpm. Second, sand was added and mixed for 30 s at 60 rpm. Third, mixing was stopped 90 s and further mixing was continued for 90 s at 120 rpm. Then, the mortars were ready for electrical resistivity and compressive strength tests. These sample preparation steps were conducted at room temperature (approximately 25°C).

2.3. Curing Conditions. A thermostat (temperature range -30~60°C with an accuracy of 0.1°C) was used to provide the required temperature. Before the electrical resistivity test, the thermostat's temperature was set at the required value for at least 12 hours. Later, specimens were placed into the thermostat, and the temperature remained unchanged until the resistivity test was completed. The specimens were wrapped with plastic bag, so they were cured under airtight conditions.

2.4. Testing Procedure. The samples were only prepared for electrical resistivity and compressive strength tests. The samples used for scanning electron microscopy (SEM), X-ray diffraction (XRD), and Mercury intrusion porosimetry (MIP) tests were selected from the crushed samples (after the compressive strength test). The flow chart is shown in Figure 2.

2.4.1. Electrical Resistivity. The electrical resistivity test methods included two phase electrodes, four phase electrodes, and noncontact test techniques. Here, to reduce the

TABLE 1: Chemical components of the CSA cement (wt%).

Material	Al ₂ O ₃	CaO	SiO ₂	SO ₃	Fe ₂ O ₃	MgO	TiO ₂	LOI
CSA cement	33.36	43.01	8.28	7.90	1.95	1.69	1.35	0.89

TABLE 2: Physical properties of the CSA cement.

Material	Specific surface area (m ² /kg)	Density (kg/m ³)	Setting time (min)	
			Initial setting	Final setting
CSA cement	460	2900	26	43

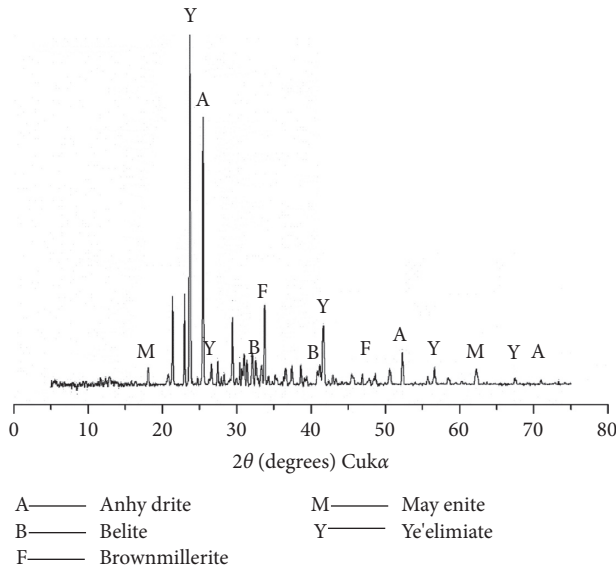


FIGURE 1: X-ray diffraction pattern of the tested cement.

TABLE 3: Particle size distribution of the sand.

Size (mm)	2.0	1.6	1.0	0.5	0.16	0.08
Accumulated retained (%)	0	7 ± 3	32 ± 3	65 ± 3	87 ± 3	99 ± 1

disturbance caused by the electrodes, the two phase electrode method was used in the resistivity test. A content of 500 g of mortar was placed into a plastic bucket (with a diameter of 65 mm and the length was measured after the test), and, then, one copper plate was fixed at each sidewall of the specimen. The copper plates and the resistivity testing equipment (type: TH 2830) were connected by a conducting wire. After sample preparation, the specimens for the resistivity test were placed into the thermostat. The resistance was automatically recorded by TH 2830 resistivity testing equipment at an interval of 5 min. The testing frequency is 10 kHz. The schematic diagram of the resistivity test is shown in Figure 3. The resistivity can be calculated as follows:

$$\rho = R \frac{A}{L} \tag{1}$$

where ρ is the resistivity, R is the resistance, A and L are the area and length of the sample, respectively.

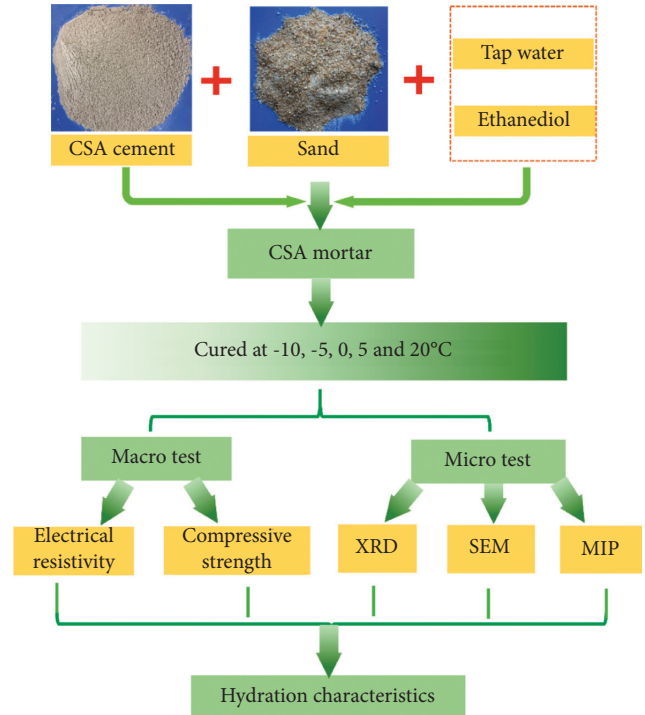


FIGURE 2: Flow chart of the laboratory tests.

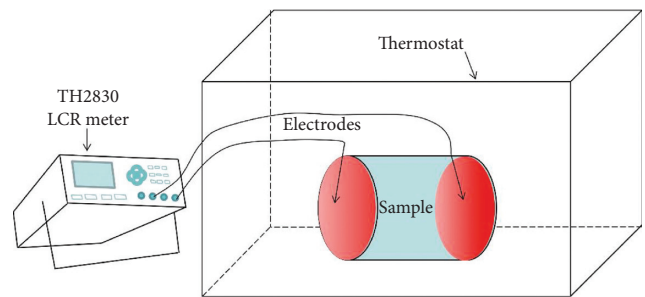


FIGURE 3: Schematic diagram of the electrical resistivity test at different temperatures.

2.4.2. Compressive Strength Tests. The mortar was poured in a steel mold (with a size of 40 mm × 40 mm × 40 mm), and the mold was vibrated. Then, the mold was wrapped in a plastic bag. Finally, the specimens were cured at constant temperatures of -10, -5, 0, 5, and 20°C for 24 hours, and then demolded and kept at the required temperature. The compressive strength tests were carried out at days 1, 3, and 7 on a universal testing machine with a loading rate of 2.4 kN/

s. The average value of the three specimens was used to determine the compressive strength. If the range was more than 30% of the average value, the value with the largest deviation was eliminated, and the average of the other two values was taken as the compressive strength.

2.4.3. SEM, XRD, and MIP Tests. After the compressive strength, the crushed specimens with a size of 10–20 mm were selected and immersed in ethyl alcohol for 7 d to stop hydration and then dehydrated in a drying oven at 45°C for 24 hours. After that, the specimens were crushed again, and the specimens with a size of 5–10 mm were selected. A fresh fractured surface was scanned by using the field emission scanning electron microscope (ESEM, QUANTA FEG 450). Phase analysis was conducted by using X-ray diffraction (type: Bruker D8A). The diffraction patterns were recorded within 10°–75° (2θ) with 0.01°/step. Finally, the pore structure characteristics were investigated by using the MIP tests (type: Autopore IV 9500).

3. Results

3.1. Electrical Resistivity. Figure 4 presents the development of the electrical resistivity of the mortars cured at different temperatures. The laboratory results indicate that the resistivity of mortar increases with curing time. The resistivity method actually tests ion migration in cementitious materials [11]. After water was added to the cement, the amount of ions released by the cement particles in the liquid phase continuously changed. In the dissolution and induction stages, less water and ions were consumed, and there was little change in the resistivity. At the acceleration stage, the fast consumption of ions and water led to the formation of a large amount of hydrates and gradually reduce the liquid phase space. This results in poor water connection. Therefore, the resistivity gradually increased [19]. However, there is the same difference between the results of two water-cement ratios. As presented in Figure 4(a), at the same cured age and temperature, the samples with low water-cement ratio (0.4) have a larger resistivity than the samples with a high water-cement ratio (0.5).

CSA cement is a rapid hardening cement, it enters the acceleration stage quickly at 20°C, and thus the resistivity rapidly increases from 2 hours [11]. However, low temperatures delay the hydration process. As shown in Figure 4(b), the electrical resistivity is relatively large at 30 hours when the samples are cured at 5 and 20°C. The electrical resistivity is relatively small before 60 hours when the samples are cured at –10 and –5°C. Compared with the samples cured at a low temperature, the samples cured at a high temperature have larger changes in the resistivity rate, no matter the water-cement ratio. Moreover, when the curing temperature is above 5°C, the resistivity curves have a consistent trend and include four parts: a slight increase, a decrease, stabilization, and then an increase followed by a gradual stabilization. With the decreasing curing temperature (at –10°C), the stabilization part does not appear on the resistivity curve. It is evident that the acceleration stage

appears significantly earlier with an increasing curing temperature, and this indicates that a lower temperature lengthens the induction stage and delays the hydration process.

Previous studies have indicated that ions released by cement cause a decrease in electrical resistivity [11, 16]. As shown in Figures 4 and 5, there is a slight increase in electrical resistivity and the increment increases gradually with the decrease in the curing temperature. There are two reasons for the change in resistivity in the dissolution stage. One reason is the temperature decrease (from room temperature 25°C to the tested temperature), and the other reason is the dissolution of soluble ions from cement particles. The former increases resistivity, and the later decreases resistivity. The diminution of resistivity is not apparent, and resistivity shows an increasing trend. The result shows little difference from the results presented by literature [11]. This can be explained by the fact that (1) low temperatures impede the dissolution of ions and (2) the decrease in resistivity has little change (less than 0.5 Ω m) [11, 16]. Furthermore, the hydration process gradually reaches the acceleration stage. However, the hydration process is significantly delayed by the low curing temperature (–10°C and –5°C). As seen in Figures 5(a) and 5(b), the curves of variation rate of resistivity have similar change trends: there are two peaks in the curves of the variation rate of resistivity when the samples are cured at 20°C, 5°C, and 0°C. Only one peak is observed at –5°C and –10°C. However, the node time is different for different water-cement ratios. For the sample with low water-cement ratio cured at 0°C and 5°C, the acceleration stages start from 30 hours to 8.6 hours, respectively (Figure 5(a)). For the sample with high water-cement ratio cured at 0°C and 5°C, the acceleration stages start from 15.7 hours to 7.5 hours, respectively (Figure 5(b)). As shown in Figure 4, the horizontal segment (induction stage) is extended with the decreasing temperature, especially at –10°C and –5°C. In the acceleration stage, the hydrates are continuously formed [34]. The length of the conducting path increased, which caused the increase in resistivity. In addition, the rate of electrical resistivity decreases with decreasing curing temperature, which can be explained by the fact that a higher temperature can improve the activity of the raw materials and promote the hydration process.

3.2. Compressive Strength. The compressive strength of CSA mortars cured at different temperatures was measured in 1 d, 3 d, and 7 d. The compressive strength of CSA mortar increases with increasing curing age, regardless of the curing temperature and water-cement ratio. As shown in Figure 6(a), the compressive strength of the sample cured at –10°C is about 3.23 MPa at day 1, which is only approximately 10% of that of the specimens cured at 20°C (28.83 MPa). The similar result can be found in Figure 6(b). The test results indicate that the compressive strength decreases sharply at low curing temperature, especially from 0 to 1 d. Although the low temperature slows the hydration rate, the compressive strength continuously increases with the curing time. Moreover, at a water-cement ratio of 0.5, the

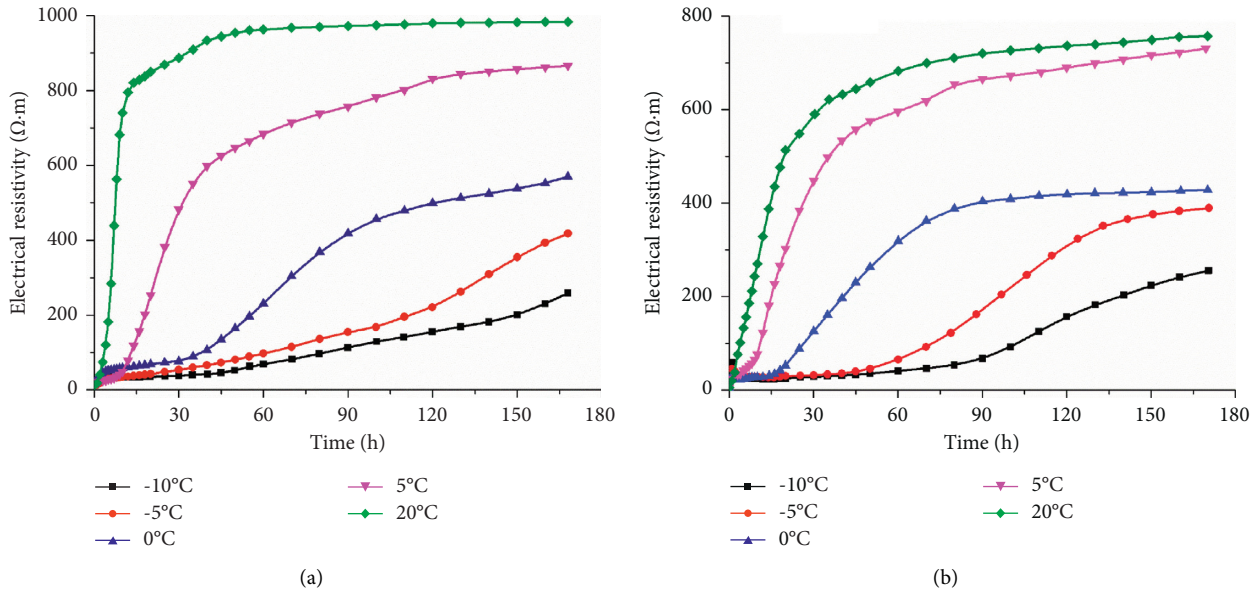


FIGURE 4: Electrical resistivity of the mortar at different curing temperatures during 0–7 d. (a) $w/c = 0.4$; (b) $w/c = 0.5$.

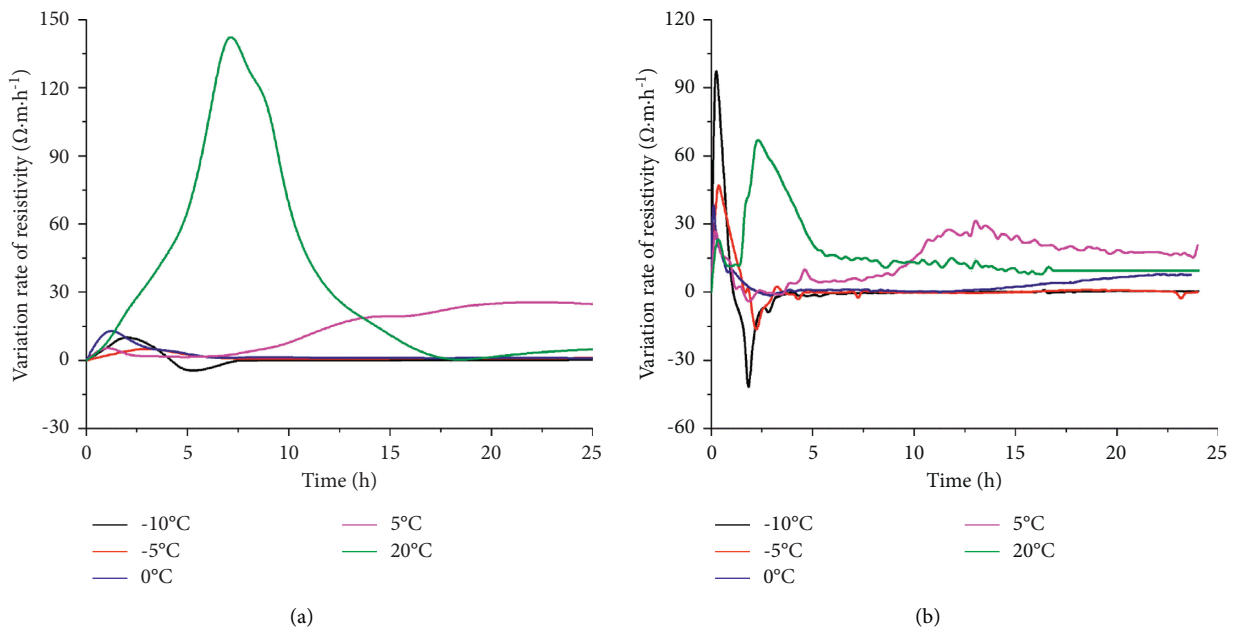


FIGURE 5: Rate of electrical resistivity of the mortar at different curing temperatures for 0–1 d. (a) $w/c = 0.4$. (b) $w/c = 0.5$.

compressive strength of the specimen cured at -5°C for 7 d is only approximately 2 MPa lower than that of the sample cured at 0°C . The sample cured at 5°C has a compressive strength of 46.4 MPa, while the sample cured at 20°C has a compressive strength of 43.6 MPa. This trend is similar to the results presented by Xu et al. [33]. It can be concluded that there is an optimal curing temperature for CSA cement cured at temperatures ranging from -10°C to 20°C .

As shown in Figure 6, at these two water-cement ratios, the early strength of the mortars decreased significantly at low curing temperature. This is because a lower curing temperature delays the hydration process and decreases the

hydration rate, which leads to a decrease in the amount of hydrates. It is known that the strength of the CSA mortar is controlled by the amount of AFt crystals and its microstructure. When samples have the same hydration degree, the connection between the hydration products and the microstructure controls the strength [35]. As mentioned above, a low curing temperature slows the hydration rate. Therefore, the sample cured at a lower temperature has a lower hydration degree than that cured at a high temperature [36]. In other words, a lower curing temperature decreases the hydration degree and reduces the amount of hydrates. Consequently, an unstable microstructure is

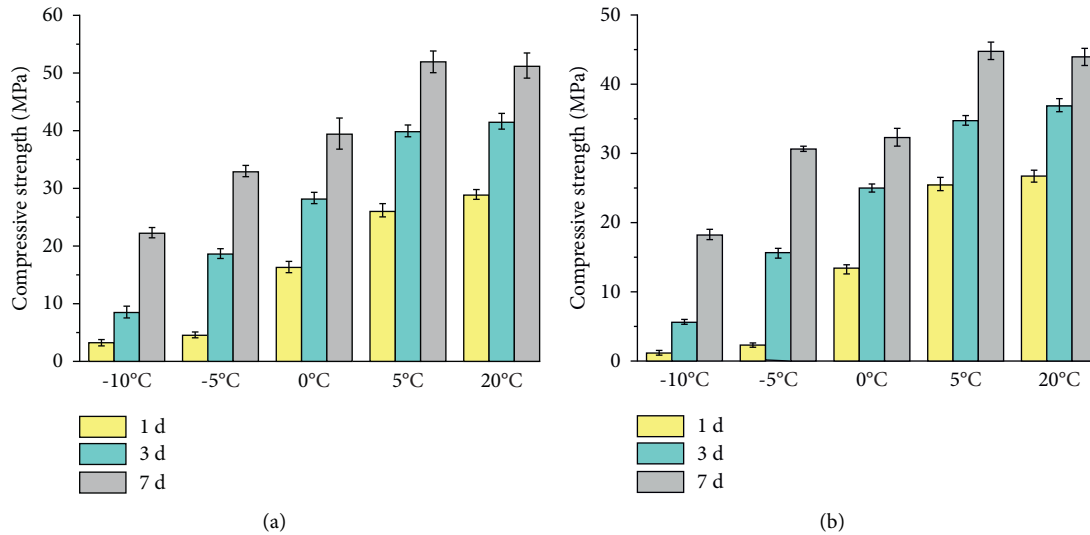


FIGURE 6: Compressive strength of mortar cured at -10 , -5 , 0 , 5 , and 20°C . (a) $w/c=0.4$. (b) $w/c=0.5$.

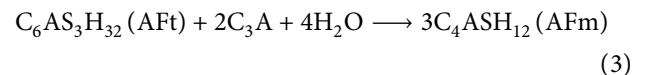
formed in the mortars without the connection provided by the hydration production. Therefore, the compressive strength decreases at low curing temperatures, no matter the water-cement ratio.

3.3. X-Ray Diffraction (XRD). Figure 7 shows the XRD patterns of CSA mortars cured under different conditions. Previous study indicates that the main hydration products of CSA cement are ettringite (AFt), monosulphoaluminate (AFm), and alumina gel (AH_3) [3]. This can be verified by the microanalysis (Figures 7 and 8). However, the main hydration product of the samples cured at -10 , -5 , and 0°C is AFt, almost without AFm and AH_3 (Figure 8). For the sample cured at 5 and 20°C , the dominant hydrates are AH_3 and AFm. This can explain the fact that the formation of hydrates is determined by the hydration degree, as reflected by the consumption of gypsum. When calcium sulfate is completely consumed, hydrates of AFm and AH_3 will gradually form according to (2) [3]. As noted by Wang et al., the AFm will form in the middle of the hydration process. The XRD results show that the specimens cured at 20°C have early access to the middle of the hydration process, which illustrates that the hydration process is delayed by low curing temperature [35].



As shown in Figure 7(b), with prolonged hydration time, the diffraction peak of AFt increases gradually and the diffraction peak of Ye'eliminate decreases. In addition, because the hydration product AH_3 has poor crystallinity, it is difficult to characterize AH_3 by using XRD. From the details mentioned above, we can conclude that a low curing temperature only suppresses the hydration reaction and does not change the kinds of hydrates, but the amount of hydrates obviously decreases. Moreover, because the lower curing temperature delays the hydration process, the appearance time of AH_3 is postponed.

3.4. Scanning Electron Microscope (SEM). Figure 8 shows the microstructure of a hydrated paste cured at different temperatures for 3 d. For the sample cured at 20°C , the hydration products contain more plate-shaped AFm and pompon-shaped AH_3 , almost without AFt (Figure 8(a)). With the decrease in curing temperature, small, short, and fine needle AFt gradually appears. At -10°C , more acicular ettringite can be observed in the specimens. In total, as the curing temperature drops from 20°C to -10°C , the AFm and AH_3 gradually disappear, and the AFt becomes coarser (Figure 8(e)). This finding can be explained by the fact that the solubility of ettringite at 20°C is larger than that at -10°C , so it is easy to form ettringite at low temperature [37]. In addition, the formation of hydrated calcium silicate gel at -10°C is slower than that at 20°C , and there is a large residual space between particles, which promotes the growth of ettringite [35]. Moreover, when gypsum is completely consumed, AFm will form according to equation (3) [3]. Therefore, the content of AFt at -10°C is higher than that at 20°C . In addition, a higher curing temperature results in faster conversion from AFt to AFm,



As shown in Figure 8, with the elevated curing temperature, the amount of AH_3 gradually increases. Combined with the compressive strength results, it is found that the compressive strength increases with increasing curing temperature. This conclusion agrees well with the previous results [38]. During the hydration process, AFt forms first, but its structure is relatively loose and the compressive strength is low. By increasing the hydration time, the hydration degree increases and AH_3 is formed. Because AH_3 has a high cohesion and large specific surface area of approximately $285 \text{ m}^2/\text{g}$ [39], the connection between components strengthened by AH_3 . Moreover, as the AH_3 phase fills the pore spaces, the structure becomes relatively dense.

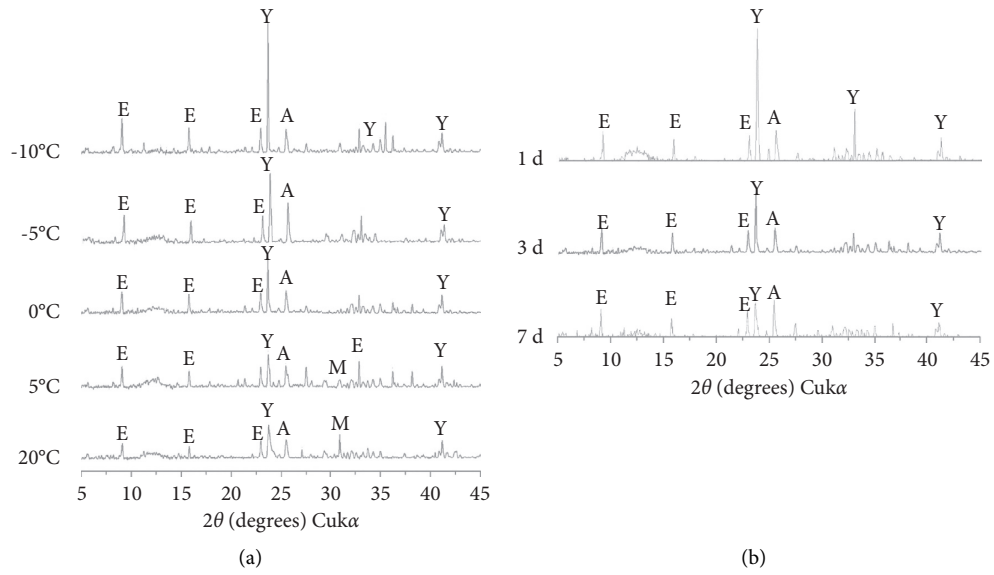


FIGURE 7: XRD patterns of mortars (E: ettringite, M: monosulphoaluminate, Y: Ye'eliminate, and A: anhydrite). (a) Samples cured at -10°C , -5°C , 0°C , 5°C , and 20°C for 3 d. (b) Samples cured at 0°C for 1 d, 3 d, and 7 d.

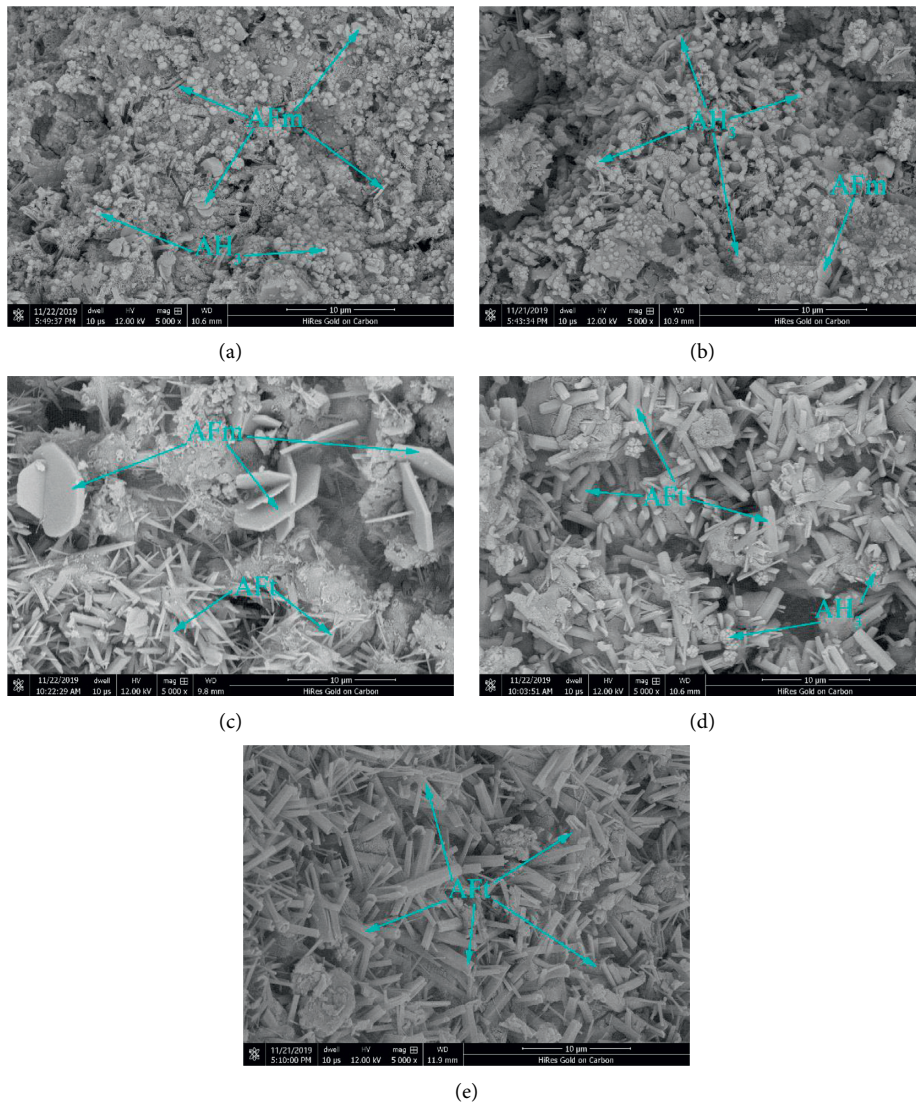


FIGURE 8: SEM images of CSA cement mortars cured at different curing temperatures for 3 d. (a) 20°C ; (b) 5°C ; (c) 0°C ; (d) -5°C ; (e) -10°C .

Therefore, the compressive strength increases with hydration time, and the elevated curing temperature can enhance the compressive strength.

3.5. Pore Sizes. The pore structure can be treated as one of the external manifestations of cement hydration. Figure 9 shows the pore size distribution of the specimens cured at different temperatures ($w/c=0.5$). At day 3, the pore volumes of the samples cured at -10 , -5 , 0 , 5 , and 20°C are 0.288 , 0.229 , 0.213 , 0.178 , and 0.182 mL/g, respectively. The porosity results show that the curing temperature has a noticeable effect on the total porosity, and that 5°C is the optimum curing temperature to obtain a minimum porosity. Li et al. [40] pointed out that increasing the amount of hydration products will decrease the total porosity. As the temperature decreases, the hydration process is delayed. Consequently, the amount of the hydration product is reduced. Therefore, with less hydrates filling the pore space, porosity increases with the decreasing curing temperature. Moreover, the results show that the pore size distribution shows little difference at different curing temperatures. As shown in Figure 9, the volume of a pore with a diameter larger than $0.1\ \mu\text{m}$ is 0.098 mL/g at -10°C and 0.031 mL/g at 20°C . Compared with the sample cured at 20°C , the number of coarse pores noticeably increases when the sample is cured at -10°C . The change law is consistent with the influence of high-temperature curing on the pore structure of the silicate cement [41, 42].

Because pores with different sizes have different effects on the physical-mechanical properties of concrete, the pores are divided into four classes depending on the endanger degree (Table 4) [43]. Total porosity varies little at 5°C and 20°C . However, the proportion of harmful pores is larger at 20°C than that at 5°C . As a result, the specimen cured at 5°C has a large compressive strength. This indicates that the optimal curing temperature can reduce the number of harmful pores.

4. Discussion

4.1. Influence of Temperature on the Formation of Strength.

The experimental results indicate that an elevated temperature results in the compressive strength first increasing (cured at $-10^\circ\text{C}\sim 5^\circ\text{C}$) and then decreasing (cured at $5^\circ\text{C}\sim 20^\circ\text{C}$). This changing trend does not completely agree with the results presented by Li et al., which showed that the strength tends to decrease with increasing curing temperature (samples were cured at $5^\circ\text{C}\sim 40^\circ\text{C}$) [40]. It is well known that concrete has a resistant freezing critical strength [44]. The compressive strength of the specimens cured at -10°C and -5°C for 1 d is lower than the resistant freezing critical strength of 2.5 MPa (the resistant freezing critical strength is determined by the literature [45]). Therefore, frost heaving stress, induced by pore water migration and freezing, will destroy the structure of the mortars cured at -10°C and -5°C and lead to a decrease in strength. Moreover, the specimens cured at -5°C and -10°C are still in the deceleration stage at day 7. This means that fewer hydrates

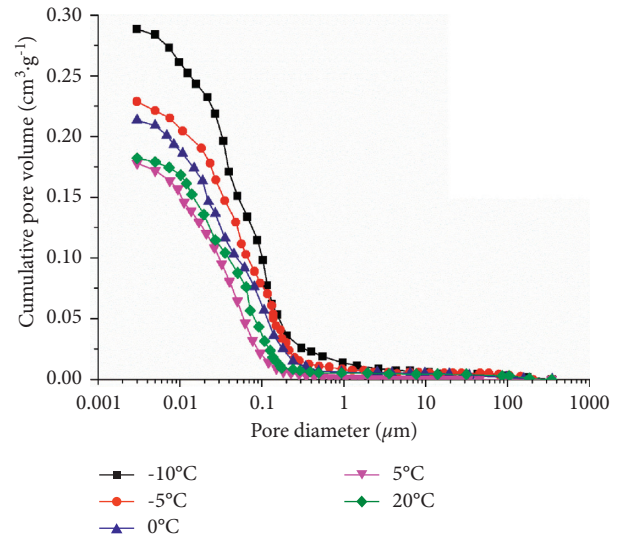


FIGURE 9: Pore structure of the CSA mortar at different curing temperatures for 3 d.

TABLE 4: Pore-class classification [43].

Pore size/nm	<20	20–100	100–200	>200
Hazard ranking	Harmless	Less harmful	Harmful	More harmful

form and the components in the mortar have a poor connection, which does not benefit in developing strength. For curing temperature over 5°C , there is no frost heaving stress. Under this condition, low temperatures are beneficial to the formation of ettringite and increase in strength [35]. Moreover, the specimens cured at 20°C and 5°C have reached the stable stage in 7 d. Many hydrates are formed, and the components are strengthened by the hydrates. Consequently, the mortar has a denser structure and a larger compressive strength. At a high temperature (20°C), due to the large hydration rate, more harmful pores will be formed. Results show that higher and lower curing temperatures result in an increase in the number of harmful pores. Thus, there is a critical curing temperature for obtaining the largest compressive strength and lowest porosity. Moreover, as shown in Table 5, the low temperature increases the total porosity and results in a decrease in the proportion of harmless pores.

4.2. Influence of Temperature on Electrical Resistivity.

Previous results indicated that the liquid phase played a key role in determining the electrical resistivity [46]. After the mortar was mixed, the hardening of mortar occurs in three states: flow state, plastic state, and solid state. At the early time, both the ion concentration and the volume of the liquid phase were large. Sands are surrounded by pore water in the mortar. All the pores were connected with each other, and the length of the conducting path was short (Figure 10(a)). Consequently, the electrical resistivity was small. Due to the formation of hydration products, the porosity and free water content were reduced continually.

TABLE 5: Proportions of hazard ranking of pores.

Test condition	Hazard ranking				Porosity (mL/g)
	Harmless (%)	Less harmful (%)	Harmful (%)	More harmful (%)	
5°C, w/c = 0.4	51.28	21.60	8.38	18.74	0.110
5°C, w/c = 0.5	32.45	54.37	10.36	2.83	0.178
-5°C, w/c = 0.4	39.37	27.70	10.22	22.71	0.163
-5°C, w/c = 0.5	22.23	43.16	21.43	13.17	0.229

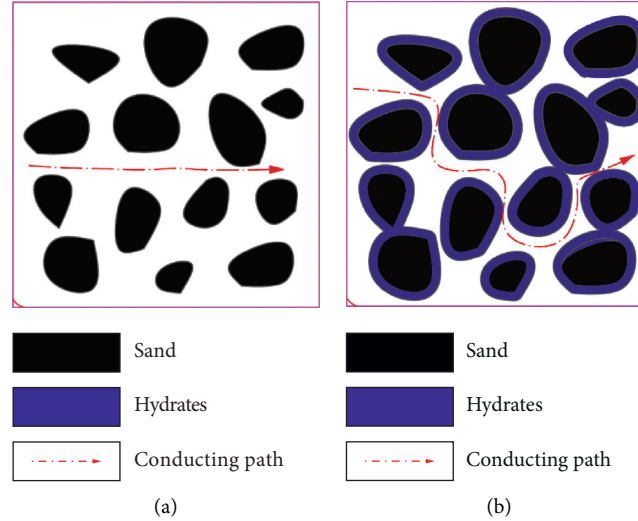


FIGURE 10: Schematic presentation of the conduction paths in the mortar (a) fresh mortar and (b) mortar hydrated for some time.

With time going on, the volume of the solid phase increases and the volume of the liquid phase decreases. Consequently, the hydration products broke the conduction path and lengthened the conducting path (Figure 10(b)). Moreover, the formation of hydrates consumed many ions. The decrease in ion concentration and the increase in the length of the conducting path led to a dramatic increase in resistivity.

Actually, the variation in electrical resistivity reflects the evolution of the pore structure. Here, the formation factor was used for describing the pore structure, which can be calculated as follows [24]:

$$F = \frac{\rho}{\rho_0}, \quad (4)$$

where ρ is the resistivity of the mortar and ρ_0 is the resistivity of the pore water in the mortar. All the ions were dissolved in water in the induction stage, and the minimum electrical resistivity was treated as ρ_0 .

Based on the tested resistivity, the formation factor can be calculated, as shown in Figure 11. The results indicate that at these two water-cement ratios, the formation factor increases with prolonged hydration time. Moreover, as seen in Figure 6, at the same curing age and temperature, the sample with a low water-cement ratio has a larger electrical resistivity. With the hydration process going on, free water is gradually consumed and more hydrated cement is generated. This results in a decrease in the volume of the liquid phase and an increase in the volume of the solid phase [13]. As a result, the resistivity increases. Therefore, the formation factors increase with hydration time. Moreover, at the same

age, specimens cured at high temperatures have a larger formation factor. This can be explained that a higher hydration degree indicates more free water and ions have been consumed. Therefore, compared with the specimens cured at lower temperatures, the sample cured at 20°C has the minimal volume for the liquid phase. A poor connection between pore water results in the longest conducting path formed in the sample cured at 20°C. Consequently, this sample has the largest resistivity and formation factor. Because the hydration rate is decelerated by low temperature, more free water exists in the pores, resulting in an increase in the volume of the liquid phase. Better pore water connection causes the decrease in resistivity. To some degree, the change in the formation factor can reflect the hydration degree. In addition, the sample with low water-cement ratio has a smaller change rate in the formation factor. A low water-cement ratio means that less water is added in the cement, and the pore water connection is poor, so the minimum electrical resistivity is larger in the low water-cement ratio. When the resistivity of the mortar has little difference, the formation factor was determined by the minimum electrical resistivity ρ_0 .

4.3. Influencing Mechanism of Temperature on the Hydration Process. The hydration process can be summarized in three steps: dissolution of cement particles, consumption of free water, and formation of hydration products [3]. As seen, the low curing temperature did not change the final hydration products [47], but lengthened the hydration process (Table 6).

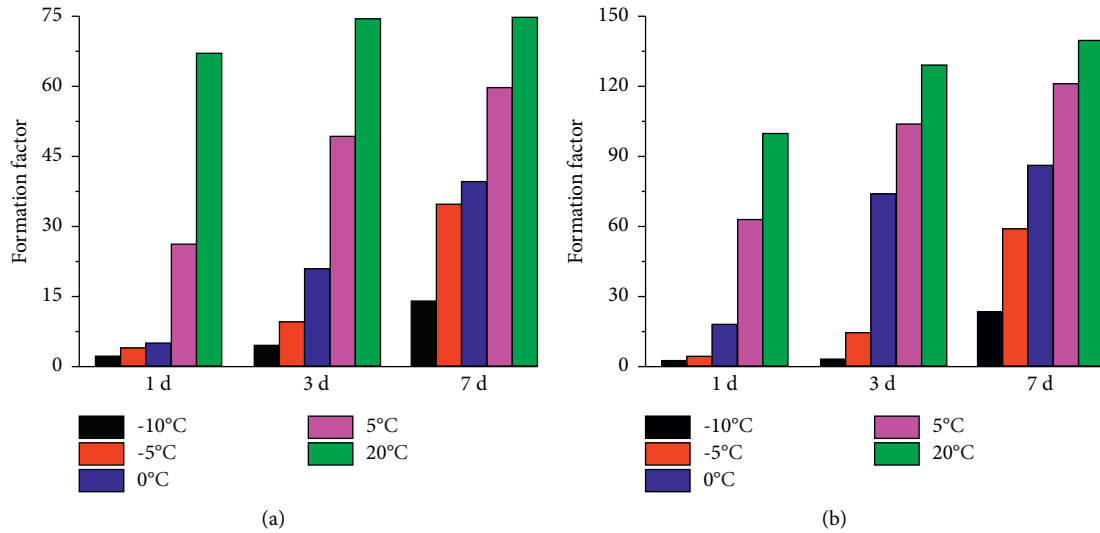


FIGURE 11: Variation in the formation factor at different curing temperatures for 1 d, 3 d, and 7 d. (a) $w/c=0.4$; (b) $w/c=0.5$.

TABLE 6: The initial time of the mortar access to different hydration stages (unit: hour).

Hydration stages	Curing temperature				
	20°C	5°C	0°C	-5°C	-10°C
Dissolution stage	0.0	0.0	0.0	0.0	0.0
Induction stage	0.8	2.4	3.5	4.2	4.8
Acceleration stage	1.4	7.5	15.7	28.6	80.2
Deceleration stage	2.5	12.5	24.5	77.4	118.1
Stabilization stage	16.2	48.4	101.3	—	—

Notes: The symbol “—” means does not appear. Water-cement ratio is 0.5.

Taking the age of 1 d, for example, the specimens with a water-cement ratio 0.5 cured at 20°C and 5°C have access to the deceleration stage, the specimens cured at 0°C have access to the acceleration stage, but the specimens cured at -5°C and -10°C are still in the induction stage. Moreover, the specimens cured at -5°C and -10°C still did not enter the stable stage even at 7 d.

The results indicate that the hydration process was lengthened by the low temperature. The key piece of evidence is that both compressive strength and electrical resistivity decreased with decreased curing temperature at the same age. Therefore, in some degree, we can conclude that the low curing temperature decreases the hydration rate. In this section, we will discuss how the temperature decreases the hydration rate.

The hardening of cement is accompanied by chemical reactions. Therefore, we will analyze the influencing mechanism from the perspective of chemical reactions. The “collision theory” in chemical reaction indicates that a reaction may occur when reactant molecules collide with each other [48, 49]. However, not every collision can result in a reaction, and only an “effective collision” can result in a reaction. An effective collision must meet two basic conditions: (1) the molecules have high energy and (2) the molecules collide with each other in a certain direction [49].

The collision theory also noted that both increasing the number of activation molecules and increasing the effective collision times can speed up the reaction rate. At a lower temperature, the molecules have lower energy and may not meet the required activation energy compared to that at a higher temperature, which means that a lower temperature will reduce the number of activation molecules (Figure 12(a)). Meanwhile, water is sticky at low temperatures, and ions encounter more resistance during the moving process. Therefore, the effective collision frequency is reduced by lower temperature (Figure 12(b)). As a result, the decrease in the number of activation molecules and the decrease in the effective collision frequency lead to a decrease in the hydration rate (Figure 12(c)). Thus, at the same age, the specimens cured at high temperature have a high hydration degree. In other words, the hydration process is lengthened by a lower curing temperature, as listed in Table 4. Moreover, the Arrhenius theorem indicates that the constant of the reaction rate decreases with decreasing temperature. Because the hydration process is suppressed by the low temperature, the amount of hydration products is reduced. In turn, the compressive strength decreases. In short, the low temperature decreases the hydration rate. Therefore, when designing the cement for low temperature, the induction period should be reduced.

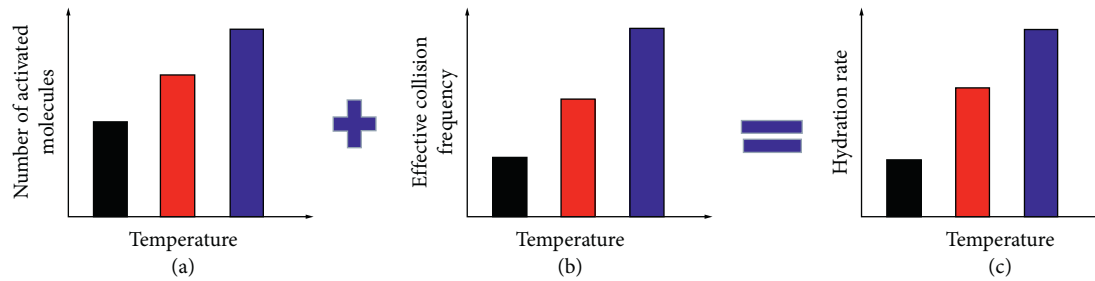


FIGURE 12: Schematic of the function of temperature on the hydration of CSA cement. (a) The elevated temperature can increase the number of activated molecules; (b) the elevated temperature can enhance the effective collision frequency, (c) With the increase in the number of activated molecules and the effective collision frequency, the hydration rate is accelerated by the elevated temperature.

5. Conclusion

A series of laboratory tests were conducted to investigate the influence of low temperatures on the hydration characteristics of CSA cement. Through systematic analyses, the following conclusions can be obtained:

- (1) Temperature has a significant effect on the macro-properties of mortar. The influence degree of the temperature decreases with the increase in curing time. The hydration rate determines the early strength, but the later strength is controlled by the amount of hydrates and the microstructure.
- (2) Low curing temperatures slows the hydration rate, lengthens the hydration process, and delays the transformation of AFt to AFm. The types of hydration products are not changed by low curing temperature, but their quantity decreases sharply with decreasing temperature, especially at the early stage.
- (3) For the tested CSA cement, the optimum curing temperature is around 5°C. An appropriate hydration rate can decrease the number of harmful pores and increase the compressive strength. Therefore, in the engineering application, an appropriate curing temperature should be provided.

Data Availability

The datasets generated during and/or analyzed during the current study are available from the corresponding author on reasonable request.

Conflicts of Interest

The authors declare that they have no conflicts of interest.

Acknowledgments

This work was supported by the Basic Research Projects of Qinghai (grant number 2021-ZJ-908).

References

- [1] W. Wang, "Analysis of the state of Chinese NSP cement industry technology development and reflection on its future," *Cement Engineering*, vol. 5, pp. 17–21, 2003.
- [2] J. Péra and J. Ambroise, "New applications of calcium sulfoaluminate cement," *Cement and Concrete Research*, vol. 34, no. 4, pp. 671–676, 2004.
- [3] Y. M. Wang, M. Z. Su, and L. Zhang, *Sulphoaluminate Cement*, Beijing University of Technology Press, Beijing, China, 1999.
- [4] Z. He, H. Yang, and M. Liu, "Hydration mechanism of sulphoaluminate cement," *Journal of Wuhan University of Technology-Materials Science Edition*, vol. 29, no. 1, pp. 70–74, 2014.
- [5] L. Coppola, D. Coffetti, E. Crotti, and T. Pastore, "CSA-based Portland-free binders to manufacture sustainable concretes for jointless slabs on ground," *Construction and Building Materials*, vol. 187, pp. 691–698, 2018.
- [6] C. Liu, J. Luo, Q. Li et al., "Calcination of green high-belite sulphoaluminate cement (GHSC) and performance optimizations of GHSC-based foamed concrete," *Materials and Design*, vol. 182, Article ID 107986, 2019.
- [7] J.-B. Champenois, C. Cau Dit Coumes, A. Poulesquen, P. Le Bescom, and D. Damidot, "Beneficial use of a cell coupling rheometry, conductivity, and calorimetry to investigate the early age hydration of calcium sulfoaluminate cement," *Rheologica Acta*, vol. 52, no. 2, pp. 177–187, 2013.
- [8] D. Gastaldi, F. Canonico, and E. Boccaleri, "Ettringite and calcium sulfoaluminate cement: investigation of water content by near-infrared spectroscopy," *Journal of Materials Science*, vol. 44, no. 21, pp. 5788–5794, 2009.
- [9] D. Gastaldi, E. Boccaleri, F. Canonico, and M. Bianchi, "The use of Raman spectroscopy as a versatile characterization tool for calcium sulphoaluminate cements: a compositional and hydration study," *Journal of Materials Science*, vol. 42, no. 20, pp. 8426–8432, 2007.
- [10] N. Singh and S. P. Singh, "Electrical resistivity of self consolidating concretes prepared with reused concrete aggregates and blended cements," *Journal of Building Engineering*, vol. 25, Article ID 100780, 2019.
- [11] Y. Liao, X. Wei, and G. Li, "Early hydration of calcium sulfoaluminate cement through electrical resistivity measurement and microstructure investigations," *Construction and Building Materials*, vol. 25, no. 4, pp. 1572–1579, 2011.
- [12] X. S. Wei and L. Z. Xiao, "Study on hydration of Portland cement using an electrical resistivity method," *Journal of the Chinese Ceramic Society*, vol. 32, no. 1, pp. 34–38, 2004.
- [13] Y. S. Liao, P. F. Xu, H. M. Yang, G. S. Liao, and X. Zhong, "Hydration process of calcium aluminate cement at early age investigated by electrical resistivity method," *Journal of the Chinese Ceramic Society*, vol. 46, no. 5, pp. 657–661, 2018.
- [14] F. D. Tamás, "Electrical conductivity of cement pastes," *Cement and Concrete Research*, vol. 12, no. 1, pp. 115–120, 1982.

- [15] Z. Li, L. Xiao, and X. Wei, "Determination of concrete setting time using electrical resistivity measurement," *Journal of Materials in Civil Engineering*, vol. 19, no. 5, pp. 423–427, 2007.
- [16] B. Dong, J. Zhang, Y. Wang, G. Fang, Y. Liu, and F. Xing, "Evolutionary trace for early hydration of cement paste using electrical resistivity method," *Construction and Building Materials*, vol. 119, pp. 16–20, 2016.
- [17] P. Gu, Y. Fu, and J. J. Beaudoin, "A study of the hydration and setting behaviour of OPC-HAC pastes," *Cement and Concrete Research*, vol. 24, no. 4, pp. 682–694, 1994.
- [18] W. J. Mccarter, T. M. Chrisp, G. Starrs, and J. Blewett, "Characterization and monitoring of cement-based systems using intrinsic electrical property measurements," *Cement and Concrete Research*, vol. 33, no. 2, pp. 197–206, 2003.
- [19] T. B. Sui, X. H. Zeng, Y. J. Xie et al., "Early age cement hydration behavior by resistivity method," *Journal of the Chinese Ceramic Society*, vol. 36, no. 4, pp. 431–435, 2008.
- [20] Z. Y. Liu, Y. S. Zhang, G. W. Sun, Q. Jiang, and W. H. Zhang, "Resistivity method for monitoring the early age pore structure evolution of cement paste," *Journal of Civil, Architectural and Environmental Engineering*, vol. 34, no. 5, pp. 148–153, 2012.
- [21] J. S. Qian, L. Zhang, X. W. Jia, and Y. D. Dang, "Progress and prospect of testing method based on electric field in evaluation concrete permeability," *Materials Review*, vol. 25, no. 21, pp. 124–128, 2011.
- [22] A. A. Kyi and B. Batchelor, "An electrical conductivity method for measuring the effects of additives on effective diffusivities in Portland cement pastes," *Cement and Concrete Research*, vol. 24, no. 4, pp. 752–764, 1994.
- [23] ASTM C1202, *Standard Test Method for Electrical Indication of Concrete's Ability to Resist Chloride Ion Penetration*, ASTM International, West Conshohocken, PA, USA, 2007.
- [24] L. Z. Xiao, Z. Ren, W. C. Shi, and X. S. Wei, "Experimental study on chloride permeability in concrete by non-contact electrical resistivity measurement and RCM," *Construction and Building Materials*, vol. 123, pp. 27–34, 2018.
- [25] X. Wei, L. Xiao, and Z. Li, "Prediction of standard compressive strength of cement by the electrical resistivity measurement," *Construction and Building Materials*, vol. 31, pp. 341–346, 2012.
- [26] N. Singh and S. P. Singh, "Evaluating the performance of self compacting concretes made with recycled coarse and fine aggregates using non destructive testing techniques," *Construction and Building Materials*, vol. 181, pp. 73–84, 2018.
- [27] K. Hornbostel, C. K. Larsen, and M. R. Geiker, "Relationship between concrete resistivity and corrosion rate—a literature review," *Cement and Concrete Composites*, vol. 39, pp. 60–72, 2013.
- [28] R. A. Medeiros-Junior and M. G. Lima, "Electrical resistivity of unsaturated concrete using different types of cement," *Construction and Building Materials*, vol. 107, pp. 11–16, 2016.
- [29] S. E. S. Mendes, R. L. N. Oliveira, C. Cremonez, E. Pereira, E. Pereira, and R. A. Medeiros-Junior, "Electrical resistivity as a durability parameter for concrete design: experimental data versus estimation by mathematical model," *Construction and Building Materials*, vol. 192, pp. 610–620, 2018.
- [30] P. M. Wang, N. Li, L. L. Xu, and G. F. Zhang, "Hydration characteristics and strength development of sulphoaluminate cement cured at low temperature," *Journal of the Chinese Ceramic Society*, vol. 45, no. 2, pp. 242–248, 2017.
- [31] Z. Xu, W. L. Zhou, and M. Deng, "Stability of hardened sulphoaluminate cement paste treated at high temperature," *Journal of the Chinese Ceramic Society*, vol. 29, no. 2, pp. 104–108, 2001.
- [32] H. F. W. Taylor, *Cement Chemistry*, Thomas Telford Publishing, London, UK, 2nd edition, 1997.
- [33] L. L. Xu, X. J. Yang, P. M. Wang, and K. Wu, "Influences of curing temperature on the microstructure evolution of calcium sulfoaluminate cement based on ternary blends," *Journal of Building Materials*, vol. 19, no. 6, pp. 983–998, 2016.
- [34] L. Pelletier-chaignat, F. Winnefeld, B. Lothenbach, and C. J. Müller, "Beneficial use of limestone filler with calcium sulfoaluminate cement," *Construction and Building Materials*, vol. 26, no. 1, pp. 619–627, 2012.
- [35] L. Xu, S. Liu, N. Li, Y. Peng, K. Wu, and P. Wang, "Retardation effect of elevated temperature on the setting of calcium sulfoaluminate cement clinker," *Construction and Building Materials*, vol. 178, pp. 112–119, 2018.
- [36] P. Wang, N. Li, and L. Xu, "Hydration evolution and compressive strength of calcium sulfoaluminate cement constantly cured over the temperature range of 0 to 80°C," *Cement and Concrete Research*, vol. 100, pp. 203–213, 2017.
- [37] R. B. Perkins and C. D. Palmer, "Solubility of ettringite (Ca₆[Al(OH)₆]2(SO₄)₃•26H₂O) at 5–75°C," *Geochimica et Cosmochimica Acta*, vol. 63, no. 13/14, pp. 1969–1980, 1999.
- [38] J. Chang, Y. Y. Zhang, X. P. Shang, J. Y. Zhao, and X. Yu, "Effect of AH3 phase content and hydration degree on the strength of calcium sulfoaluminate cement," *Journal of Building Materials*, vol. 19, no. 6, pp. 1028–1032, 2016.
- [39] K. Kaiser and G. Guggenberger, "Mineral surfaces and soil organic matter," *European Journal of Soil Science*, vol. 54, no. 2, pp. 219–236, 2003.
- [40] L. Li, R. Wang, and S. Zhang, "Effect of curing temperature and relative humidity on the hydrates and porosity of calcium sulfoaluminate cement," *Construction and Building Materials*, vol. 213, pp. 627–636, 2019.
- [41] B. Lothenbach, F. Winnefeld, C. Alder, E. Wieland, and P. Lunk, "Effect of temperature on the pore solution, microstructure and hydration products of Portland cement pastes," *Cement and Concrete Research*, vol. 37, no. 4, pp. 483–491, 2007.
- [42] S. A. Abo-El-Enain, F. I. El-Hosiny, S. M. A. El-Gamal, M. S. Amin, and M. Ramadan, "Gamma radiation shielding, fire resistance and physicochemical characteristics of Portland cement pastes modified with synthesized Fe₂O₃ and ZnO nanoparticles," *Construction and Building Materials*, vol. 173, pp. 687–706, 2018.
- [43] Z. W. Wu, "An approach to the recent trends of concrete science and technology," *Journal of the Chinese Ceramic Society*, vol. 7, no. 3, pp. 262–270, 1979.
- [44] T. C. Powers, "A working hypothesis for further studies of frost resistance of concrete," *ACI Journal Proceedings*, vol. 41, no. 1, pp. 245–272, 1945.
- [45] X. F. Li, *Anti-Frost Design Method and Preventive Measures for Concrete Structure in the Qinghai-Tibet Plateau (Dissertation)*, Southeast University, Nanjing, China, 2015.
- [46] Q. Li, S. Xu, and Q. Zeng, "The effect of water saturation degree on the electrical properties of cement-based porous material," *Cement and Concrete Composites*, vol. 70, pp. 35–47, 2016.
- [47] L. L. Xu, S. H. Fan, G. F. Zhang, and P. M. Wang, "Temperature sensitivity of hydration properties of calcium sulfoaluminate cement based blends," *Journal of the Chinese Ceramic Society*, vol. 45, no. 11, pp. 1613–1620, 2017.

- [48] L. Arnaut, S. Formosinho, and H. Burrows, *Chemical Kinetics: From Molecular Structure to Chemical Reactivity*, Elsevier Science, Amsterdam, Netherland, 2007.
- [49] Z. A. Zhu and W. J. Ruan, *Physical Chemistry*, Science Press, Beijing, China, 2018.

Research Article

Damage Evolution of Sandstone under Constant-Amplitude Cyclic Loading Based on Acoustic Emission Parameters and Resistivity

Kui Wang ¹, Zhengting Xia ¹, Zhen Huang ², and Xue Li ¹

¹Engineering Research Center of Diagnosis Technology of Hydro-Construction, Chongqing Jiaotong University, Chongqing 400074, China

²Chongqing Panlong Pumped Storage Power Station Co. Ltd., Chongqing 401420, China

Correspondence should be addressed to Kui Wang; anhuiwk@163.com

Received 26 May 2021; Revised 2 July 2021; Accepted 6 August 2021; Published 12 August 2021

Academic Editor: Rotana Hay

Copyright © 2021 Kui Wang et al. This is an open access article distributed under the Creative Commons Attribution License, which permits unrestricted use, distribution, and reproduction in any medium, provided the original work is properly cited.

In the real environment, besides static load, rock is more affected by cyclic load. There is a large difference in the mechanical properties exhibited by rocks under cyclic and static loading. Therefore, it is particularly necessary to investigate the mechanical characteristics of rock subjected to cyclic loading. These parameters of rock, acoustic emission (AE) and resistivity, are both sensitive to the failure process of rock, and they are complementary to the different stages of rock damage. Therefore, in this paper, the AE characteristics and resistivity properties of sandstone subjected to constant-amplitude cyclic loading and unloading were experimentally investigated using a typical sandstone in Chongqing. The same three-stage pattern was found for the AE evolution of sandstones during constant-amplitude cyclic loading. Initial evolution stage: the rock deformation is fast with strong changes in the AE signal. The rock deformation developed slowly while the changes of the AE signal were stable in the constant velocity evolution stage. The rock deformation developed dramatically while the AE signal became more intense in accelerated evolution stage. The change in resistivity is characterized by a rapid decrease during the loading stage and a rapid rebound during the unloading stage. Overall, from the beginning of the cycle to the end of the cycle, the resistivity of the sandstone showed a general trend of gradual decrease, until the sudden increase in resistivity at the time of damage. Finally, a damage model based on AE parameters and resistivity was constructed by combining damage mechanics.

1. Introduction

Rock mass is a discontinuous medium with a complex internal structure. Many studies [1, 2] have shown that the phenomenon of particle crushing often occurs in conjunction with rock particle compaction, and a number of experimental methods have been carried out to analyze the crushing behaviour of rock particles. Ma et al. [3, 4] used laboratory, theoretical, and field studies followed by experimental data to calculate and analyze the evolution of the deformation behaviour of gangue grains during compression tests. Alnedawi et al. [5] monitored the effect of loading frequency on rock deformation characteristics by using repeated loading triaxial tests.

In addition, there are also a series of studies on the evolution of rock damage. Hu et al. [6] performed triaxial

tests on granular rocks under cyclic stress paths and discussed the linear evolution of the plastic work with respect to the critical state. Ghebi and Hedaya [7] investigated the ultrasonic properties, such as longitudinal velocity, principal frequency, and transmission amplitude, during compressional deformation of granular quartzitic rocks. Rock's stability is affected by many natural conditions and human factors. Furthermore, in practical engineering applications, the rock mass is often subject to cyclic loading, for example, coal rock exhibits different damage patterns under cyclic disturbance and early backfill liquefaction due to cyclic loading conditions such as far-field mine blasting, rock blasting, and earthquakes. Under the action of cyclic loading, rock damage gradually accumulates until the final appearance of fatigue degradation characteristics, which have a negative impact on the stability of the project and increase

the risk of engineering safety. Therefore, the study of rock damage law under constant-amplitude cyclic loading has important practical value in engineering.

As an elastic wave, AE is produced by the damage of rock itself, and the rock is bound to be accompanied by the closure of pores and the initiation and propagation of microcracks in the process of loading. Therefore, the damage and failure process of rock is bound to be accompanied by the generation of AE signals, which can represent the damage evolution of rocks. The phenomenon of AE activity in rock during compression was first found in the 1930s [8]. After years of research by scholars [9–12], the application of the AE method in rock materials is becoming more and more mature. Rodríguez et al. [13] characterized the fracture mode of marble and granite in a radial compression test by AE experiment and lithofacies analysis, so that the main cracking areas in rock samples and their changes in the test process can be visualized. Lei et al. [14] researched the damage evolution of several common lithologies under differential compression using detailed AE data. Ou et al. [15] conducted graded loading tests on marble under different stress paths and investigated the AE characteristics and the changing trend of loading-unloading response ratio in the deformation and failure process of marble under variable stress paths. Zhao et al. [16] used the AE system to study the uniaxial compression process of red sandstone specimens under different water contents and analyzed the characteristics of special stress and the evolution of AE (wide and narrowband) parameters in the deformation and failure process of specimens. Jiang et al. [17] analyzed the properties of AE during fatigue injuries of red sandstone, divided the axial deformation process into three stages and the transverse deformation process into two stages, and discussed the rationality of the damage variable theory according to axial strain.

As one of the inherent characteristics of rock, the resistivity is a necessary condition to study its microstructure and engineering mechanical properties, which can usually reflect the basic physical characteristics of rock. In practical engineering, people usually detected the geological conditions of engineering rock based on resistivity characteristics [18]. It was not until 1942 that the study of the resistivity properties of rocks was gradually developed on the basis of Archie's law [19–22]. Brace and Orange [23] analyzed the variation law of resistivity during rock failure through an indoor resistivity test and believed that the change of rock volume and porosity was the fundamental factor for the change of resistivity. Zhang et al. [24] studied sandstone under different thermal damage and tested the resistivity of sandstone at different temperatures, indicating that monitoring resistivity is a good method for detecting thermal damage to rocks. Wang et al. [25] explained the variation characteristics of rock resistivity from the theoretical level combined with the typical rock expansion phenomenon. At the same time, the damage variable based on resistivity was established by the analogy method, and the resistivity ratio coefficient was introduced to characterize the damage degree of overburden in coal mine goaf. In addition, Wu et al. [26] obtained the

theoretical relationship between porosity and rock resistivity based on Archie's formula. In general, the closure of pores in rock materials, changes in volume, and the expansion of microcracks in response to external forces affect the electrical conductivity of rocks. Therefore, it is possible to judge the evolution of damage to rocks by the pattern of changes in resistivity and thus infer the mechanical properties of rocks for engineering construction.

To sum up, although some studies had been conducted on the correlation between AE characteristics and rock resistivity, there has been relatively little research into the parameters of wave-electric characteristics of rocks under cyclic stress and the integrated use of the wave-electric test to investigate the evolution of damage deformation in rocks. In a previous study [27], under different test conditions, the two characteristics of AE and resistivity of sandstone were investigated, such as different stress amplitudes and different loading frequencies, using sandstone as the object of study. Furthermore, different saturation levels were tested and the evolution law of AE was found. Based on existing studies of the AE and resistivity evolution of sandstones, this paper further studies the damage evolution process of sandstone under constant-amplitude cyclic loading and deeply analyzes the relationship among sandstone AE parameters and resistivity parameters and damage accumulation. Therefore, according to the AE parameters and the resistivity parameters, the damage evolution model of sandstone under cyclic loading was established.

2. Test Device and Method

Figure 1 shows the self-designed synchronous testing device of AE, resistivity, and stress employed in the tests. The loaded test system used the RMT-301 rock mechanics test system, and a fixed device of the AE sensor was designed. The four sensors had been installed on the surrounding surface of the sandstone specimens, and the coupling agent was applied to ensure that the sandstone specimen is in good contact with the sensor. Finally, the position of the AE sensor was fixed by tightening the screws. In the experiment, as shown in Figure 2, the M300 data acquisition system was used for the resistivity test, and the SAEU2S AE system was used for the AE test.

2.1. Sandstone Sample Preparation. The samples used in this experiment were all derived from the same area of Chongqing sandstone rock samples. The sandstone specimens were obtained by the wet processing method and drilling, accurately processing into $\Phi 50 \text{ mm} \times 100 \text{ mm}$ standard cylindrical specimens, and the flatness error of the two bottom surfaces was not more than 0.02 mm, as shown in Figure 3. The height, wave velocity, mass, and diameter of the specimens are measured. Furthermore, the sandstone specimens with the closest density, geometry, and wave speed were grouped and numbered to reduce the dispersion of test results due to individual differences. For each working condition, three samples were tested to ensure the accuracy of the results.

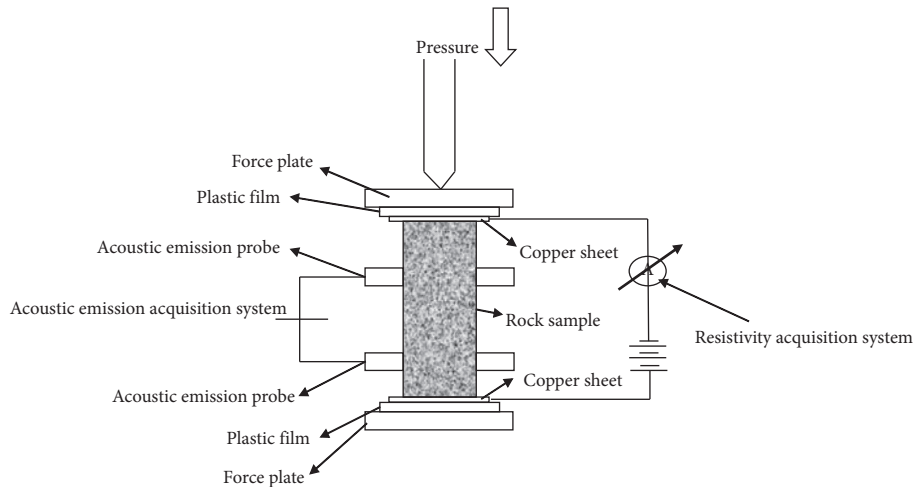


FIGURE 1: Test system design.

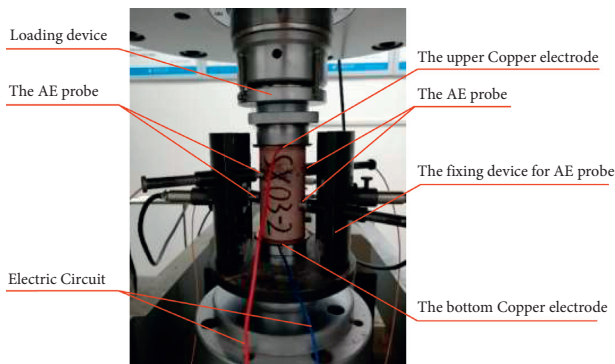


FIGURE 2: Stress-AE-resistivity synchronous testing device.



FIGURE 3: Sandstone specimen.

Through the analysis of the sandstone composition, the sandstone studied in the thesis was mainly made up of quartz, plagioclase, and potash feldspar, with mica, calcareous, and iron cuttings as minor components. The cement is mainly made up of argillaceous minerals, calcite, and dolomite with the least content of pyrite. The specific component content is shown in Table 1.

2.2. Loading Equipment. The rock mechanical test system, RMT-301, developed by Wuhan Institute of Geotechnical Mechanics, Chinese Academy of Sciences, was used in this rock loading test. The system is a multifunctional electro-hydraulic servo testing machine that can be controlled by a

computer. It is a unique four-in-one function system, which has the advantages of convenient operation, good control performance, high automation, and high stiffness. It can be used for uniaxial, triaxial, shear, and tensile tests.

2.3. Measuring Equipment and Parameters

2.3.1. Acoustic Emission Test Instrument. AE test adopts the SAEU2S multichannel AE signal measurement system manufactured by Beijing Shenghua Science and Technology Co., Ltd., which had 24 parallel detection channels and can simultaneously measure multichannel signals, as shown in Figure 4. In the process of signal acquisition, the waveform of each channel AE signal and various AE characteristic parameters could be displayed in real time, which could meet the needs of various field detection and scientific research. The main amplifier of the AE test device is 40 dB, the voltage threshold was set to 45 dB, the resonant frequency of the sensor was 20 ~ 400 kHz, and the sampling frequency was 1×10^7 times/s. At the same time, the ambient noise is needed to be standardized before the experiment to minimize the influence of noise on the test data.

2.3.2. Resistivity Test Instrument. Resistivity test adopted M300 series data acquisition/switching system produced by Beijing Puyuan Precision Electric Technology Co., Ltd, as shown in Figure 5. This system combined precise measurement function with flexible signal connection function, which could collect voltage, current, resistance, temperature, and various sensor signals and provide long-term measurement and recording of multiple test points and various signals. In this experiment, the bipolar method was carried out to measure the resistance of the sandstone specimen. Then, the resistivity ρ of the sandstone specimen was indirectly obtained according to the formula $\rho = R (S/L)$. To ensure the dependability of the measurement data, copper sheets with good conductivity should be placed on both ends of the specimen. At the same time, a plastic gasket should be placed on both ends of the end face to play the role of

TABLE 1: Sand rock composition.

Debris (%)		Cement (%)			Cementation type	Granularity (mm)		
Quartz	Plagioclase/potassium feldspar	Schist/mica	Calcareous/iron	Argillaceous	Dolomite	Pyrite	Porosity	0.01–0.15
57	23	3	6	8	2	1		



FIGURE 4: SAEU2S multichannel acoustic emission signal measurement system.



FIGURE 5: M300 series data acquisition/switching system.

insulation, and a certain amount of graphite powder should be applied to the ends of the sandstone specimen to increase the conductivity of the rock.

2.4. Test Method. Firstly, uniaxial compression tests of sandstone samples all take axial force as the control parameter. To maintain the consistency before and after the test, in the uniaxial compression test, the same axial force as the constant-amplitude cyclic loading test was used as the control parameter with 0.5 kN/s of the average loading rate. Finally, six specimens were selected for the test. According to the test results, the compressive strength and variance of specimens are shown in Table 2.

The lower limit stress value $\sigma_{\min} = 12.554$ MPa and the upper limit stress value $\sigma_{\max} = 53.355$ MPa for the cyclic load used in this study, so the average stress and amplitude are, respectively, 32.955 MPa and 20.401 MPa.

As shown in Figure 6, the equal amplitude cyclic test uses axial force as the control variable and the test was conducted in two stages. In the first stage, the axial stress was loaded continuously from zero to the average stress value $(\sigma_{\max} + \sigma_{\min})/2$ at a rate of 0.5 kN/s. In the second stage, the

cyclic loading was applied from the average stress value until the fatigue damage occurred in the sandstone specimen. Because the AE characteristics of sandstone specimens under the action of different stress amplitudes are relatively similar, the yield strength of sandstone will not be exceeded when the stress magnitude is below 85% of the compressive strength. So, the loading waveform was sinusoidal, and the frequency was 0.2 Hz, of which the upper-stress limit σ_{\max} was 85% of the uniaxial compressive strength, and the lower-stress limit σ_{\min} was 20% of the uniaxial compressive strength. The cyclic loading tests of 3 specimens were carried out under this condition.

3. Test Results and Analysis

The number of AE ringing refers to the number of oscillations caused by the oscillating wave generated by the AE signal crossing the voltage threshold, which has been widely used in the activity evaluation of AE. The number of acoustic emission rings produced per unit time in a rock sample can reflect the state of damage and deformation of the internal structure of the sample when subjected to cyclic stress. The more the number of AE ringing counts in unit time, the more serious the damage of the rock sample. On the contrary, the damage degree of rock samples was lighter.

Therefore, this paper mainly explores the AE characteristics of sandstone specimens by AE ring number. Based on the experimental results, as shown in Figure 7, the axial force and ring number-time curves of two representative sandstone specimens were plotted.

At present, the characteristic parameter method is widely used in processing AE signals [28]. The AE characteristic parameters contain a lot of information about the material damage evolution process, and the characteristic parameter method is to reflect the characteristics of AE signals by analyzing and processing several simplified waveform characteristic parameters. From the AE evolution diagram of sandstone damage evolution process under constant-amplitude cyclic loading, it is possible to find that the AE intensity of two sandstone specimens was different under the same stress level based on cyclic loading. The AE intensity of specimen 1 was greater than that of specimen 2, which was due to the heterogeneity of the specimen. Rock was heterogeneous material, its internal structure characteristics of different rocks were different, and the mechanical properties were different.

During the cyclic loading phases, the evolution pattern of the AE signal closely matches the three-stage law of rock fatigue deformation proposed by Ge et al. [29, 30]. During the first few cycles, the original cracks and weak structural surfaces in the specimen were destroyed, the degree of

TABLE 2: Results of uniaxial compression test.

No.	Compressive strength (kN)	Average compressive strength (kN)	Variance
DZ01	116.880		
DZ02	123.600		
DZ03	127.050		
DZ04	125.100	120.245	43.089
DZ05	119.670		
DZ06	109.170		

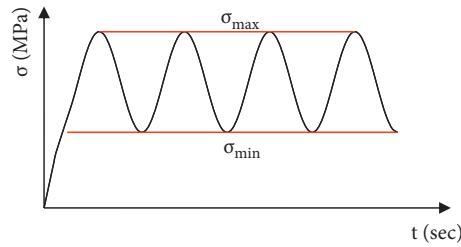


FIGURE 6: Loading loop path.

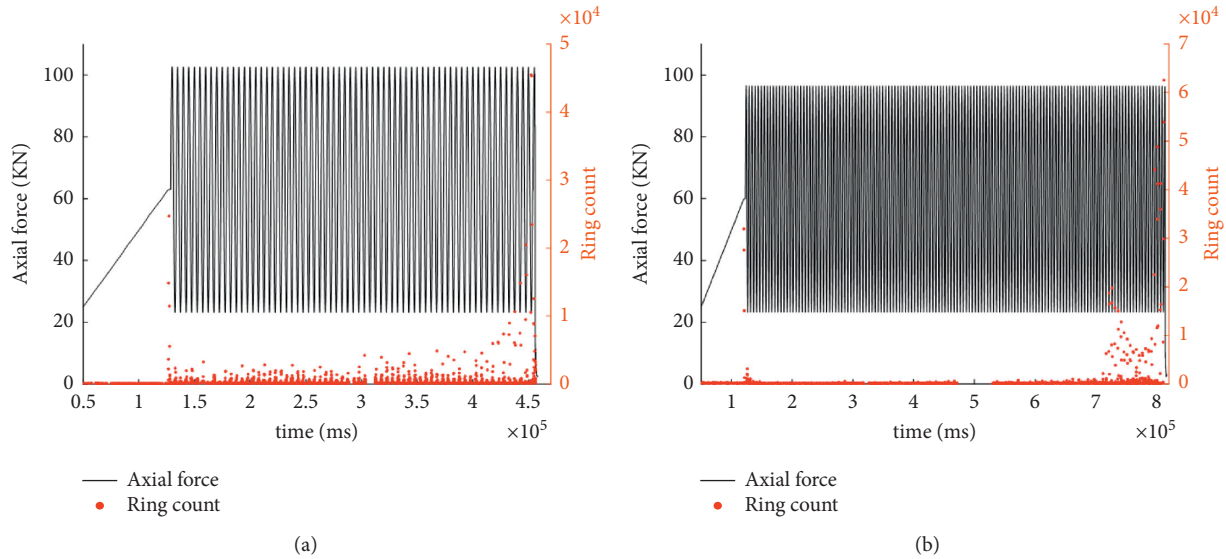


FIGURE 7: Evolution law of acoustic emission: (a) acoustic emission evolution law of specimen 1; (b) acoustic emission evolution law of specimen 2.

sandstone deformation was rapid, the AE activity evolved strongly, and the number of AE vibrations was high. Then, entering the stage of constant velocity development, as can be seen from the AE local magnification diagram, where the AE signal of essentially the same magnitude is present in each cycle, the evolution of the AE activity diminishes and the number of rings decreases, indicating that the upper stress had reached the yield strength of the rock and therefore a small amount of plastic damage occurs in each cycle. Finally, in the accelerated damage phase, the degree of deformation of the rock suddenly increases and its strain reaches the ultimate deformation of the rock in a few cycles. The macroscopic fracture was penetrated, and the rock was destroyed. It can be seen that the evolution of AE activity was suddenly enhanced, and the number of ringing counts

increased exponentially, which well reflects the destruction process of the rock material during cyclic loading. Furthermore, most of the AE signals occur near the upper-stress limit, indicating that the upper-stress limit was more sensitive to the AE signals from the rock [31].

At the same time, the force-time and resistivity-time curves of specimens were drawn, respectively, according to the test results, as shown in Figure 8, to investigate the variation law of sandstone resistivity under constant-amplitude cyclic loading.

The resistivity of the sandstone loaded in equal amplitude cycles follows a basically similar pattern to the loading path as can be seen from Figure 6. During the loading stage, due to the heterogeneity of rock specimens, there were many microcracks and pores in the rock specimen, the stress

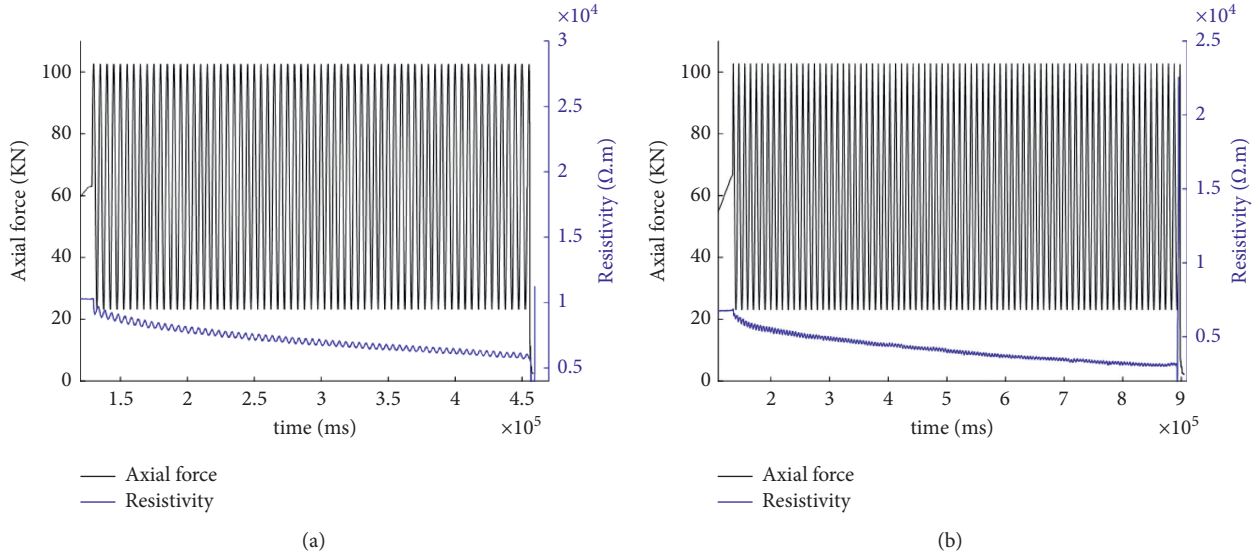


FIGURE 8: Resistivity evolution law: (a) evolution law of resistivity of specimen 1; (b) resistivity evolution law of specimen 2.

increased, and the pores closed rapidly, which made the resistivity decrease rapidly. On the other hand, due to the decrease of stress, the compacted pores and microcracks gradually opened, the air entered, and the resistivity increased in the unloading stage. During the unloading stage, the compacted pores and microcracks gradually open up due to the stress reduction, leading to the entry of air and an increase in resistivity.

In general, the change rules of the two specimens were consistent. Due to the high level of load stress, after each cyclic loading and unloading, the specimen yielded and produced plastic residual deformation, including the plastic deformation caused by the pressure sealing of microcracks and the loose particles generated by the convex failure of the microcrack surface. This results in better contact between the mineral particles, between the skeleton and the pore water, and better connectivity of the hydraulic channels after each loading cycle than after the previous cycle. Therefore, the resistivity of the rock specimen tends to decrease as the cyclic loading proceeds. By the last couple of cycles, when the sandstone specimen is on the verge of destruction, the internal cracking accelerates and the contact between the skeletal particles deteriorates, and the rock resistivity shows a gradual increase. By the time the fatigue life of the specimen was reached, the extended microcracks have been penetrated into large macroscopic cracks, the specimen was damaged, and the resistivity increased suddenly [26, 32].

4. Analysis of Sandstone Damage Evolution Law

Under the action of cyclic loading, the essence of rock damage is the damage process of continuous sprouting, expansion, and penetration of internal cracks. The resistivity and AE parameters were very sensitive to the changes of crack closure, initiation, and coalescence, but the sensitivity of the two parameters to different loading stages was different. Two kinds of parameters played a complementary

role, so it is feasible to combine the two parameters to comprehensively determine the failure process of rock. In this paper, damage mechanics was used to defining the damage variable based on wave-electric field parameters. On this basis, the damage evolution model based on wave-electric field parameters was constructed to analyze the fatigue damage evolution law of sandstone.

4.1. Damage Variables Based on AE Parameters. Yang et al. [33] researched the damage evolution law of rock by triaxial compression test and established a rock damage model based on the cumulative ringing count of AE. The formula was used to define the damage variable D as the ratio of the defect area A_d on the material cross section to the total area A of the material cross section [34], and the damage variable D reflected the degree of material degradation.

$$D = \frac{A_d}{A}. \quad (1)$$

When $D = 0$, it was equivalent to the nondestructive state of the material; when $D = 1$, it was equivalent to the complete failure state of the material. The larger the D value was, the more serious the material was damaged.

If the cumulative ringing count of AE was assumed to be ϕ_m when the whole section area A of the material was completely destroyed, the AE rate per unit area was

$$n_v = \frac{\phi_m}{A}. \quad (2)$$

When the damaged area of the section reached A_d , the cumulative ringing count is

$$\begin{aligned} \phi &= n_v A_d \\ &= \frac{\phi_m}{A} A_d. \end{aligned} \quad (3)$$

According to equations (1) and (3), the damage variable based on cumulative ringing count can be obtained:

$$D_c = \frac{\phi}{\phi_m}. \quad (4)$$

Boundary conditions: $N = 0, D = 0; N = N_F, D = 1$, where N represents the cycle period and N_F represents the total cycle period of rock failure.

4.2. Damage Variable Based on Resistivity. The damage process of rock was always accompanied by the closure and propagation of cracks, which were the factors that cause the change of resistivity. Based on Dai's definition of damage variable by porosity, Li et al. [35] firstly creatively established damage variable based on resistivity by porosity.

We defined damage variable D_ρ based on rock porosity:

$$D_\rho = \frac{\phi_0 - \phi}{\phi_0 - \phi_s}, \quad (5)$$

where ϕ_0 is the initial porosity of unloaded rock and ϕ_s is the porosity of rock failure.

According to Archie formula [8], the resistivity of rock is as follows:

$$\rho = \frac{ab\rho_w}{\phi^m} Sr^{-n}, \quad (6)$$

where a, b are coefficients related to rock; ρ_w is the resistivity of stratigraphic water; ϕ is the porosity of the rock materials; Sr is the saturability; m is the index of rock cementation; and n is the index of rock saturation.

Based on the definition of saturation,

$$Sr = \frac{V_w}{V_v}. \quad (7)$$

For dry rock, unsaturated, its natural water content was very small. Then, assume that the volume of water has not changed during the loading process. The saturation can be defined, after correction, as

$$Sr = \frac{V_w}{\phi V}, \quad (8)$$

where $\phi = (V_v/V)$.

Then, the resistivity is

$$\rho = \frac{ab\rho_w}{\phi^m} \left(\frac{V_w}{\phi V} \right)^{-n}. \quad (9)$$

In order to increase the applicability of Archie's equation, the trend of rock resistivity evolution is expressed as the ratio of resistivity to initial resistivity:

$$\frac{\rho}{\rho_0} = \left(\frac{\phi_0}{\phi} \right)^{m-n}. \quad (10)$$

Therefore, we can get the resistivity of rock at any time in the loading process by measuring the porosity of rock. The damage variable D_ρ defined on the basis of resistivity

ratio can be obtained by adding formula (5) to formula (10):

$$D_\rho = \frac{1 - (\rho/\rho_0)^{-(1/m-n)}}{1 - (\rho_s/\rho_0)^{-(1/m-n)}}, \quad (11)$$

where ρ_0 is the initial resistivity of the material; ρ_s is the resistivity when material is damaged; m is the bond index (parameter inversion m is 2.0); and n is the saturation index (the parameter inversion n is 1.33).

In this way, through formulas (5) and (10), the damage variable D_ρ based on resistivity was established.

4.3. Comprehensive Damage Variables. First of all, the damage variable-cycle number relationship according to the resistivity and AE from above was established, respectively, by taking specimen 1 as an example, as shown in Figure 9.

Then, a comprehensive damage variable D was defined according to the complementarity of D_ρ and D_c in different stages of rock failure, as shown in Figure 10. In the initial cycle stage, D_ρ can better characterize the damage deformation process of sandstone, and D_ρ was selected to define the comprehensive damage variable D . In the accelerated failure stage, D_c can better reflect the failure process of sandstone, and D_c was selected to define comprehensive damage variable D . In fatigue stability stage, the part between the two was taken to define comprehensive damage variable. In this way, comprehensive damage variables D can better reflect the failure process of sandstone under constant-amplitude cyclic loading.

Then, through data fitting, the piecewise expression of the comprehensive damage variable can be obtained as equations (12)–(17):

$$AA_1: D = a_0 \left(\frac{N}{N_F} \right)^4 + b_0 \left(\frac{N}{N_F} \right)^3 + c_0 \left(\frac{N}{N_F} \right)^2 + d_0 \frac{N}{N_F} + e_0, \quad (12)$$

$$\begin{aligned} a_0 &= -3596, \\ b_0 &= 1304.5, \\ c_0 &= -164.56, \\ d_0 &= 9.4655, \\ e_0 &= 0.0088, \\ (R^2 &= 0.9877), \end{aligned} \quad (13)$$

$$A_1B: D = a_1 \frac{N}{N_F} + b_1, \quad (14)$$

$$\begin{aligned} a_1 &= 0.5538, \\ b_1 &= 0.2242, \\ (R^2 &= 0.9999), \end{aligned} \quad (15)$$

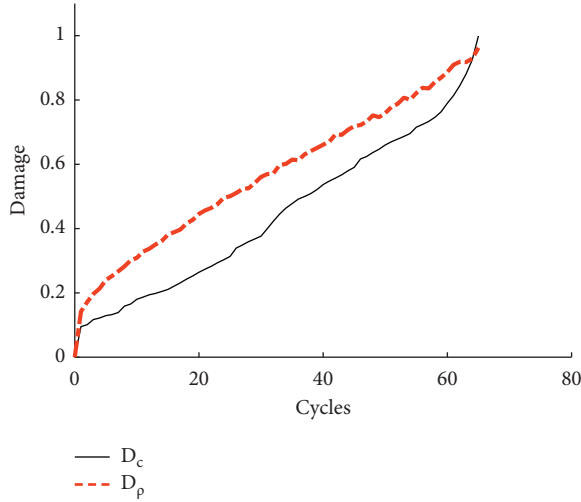


FIGURE 9: Rock's damage variables based on resistivity and AE.

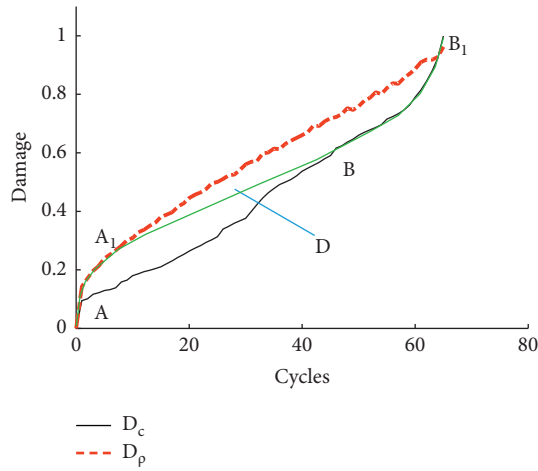


FIGURE 10: Comprehensive damage variables.

$$B_1B: D = a_2 \left(\frac{N}{N_F} \right)^3 + b_2 \left(\frac{N}{N_F} \right)^2 + c_2 \frac{N}{N_F} + d_2, \quad (16)$$

$$\begin{aligned} a_2 &= 26.795, \\ b_2 &= -64.637, \\ c_2 &= 52.49, \\ d_2 &= -13.664, \\ (R^2 &= 0.9968), \end{aligned} \quad (17)$$

where N/N_F is the cycle ratio.

4.4. *Damage Evolution Model.* Damage evolution equation based on low cycle fatigue:

$$D = 1 - \left[1 - \left(\frac{N}{N_F} \right)^{1-c} \right]^{1/b+1}. \quad (18)$$

The damage evolution equation of sandstone can be obtained by using the comprehensive damage variable proposed above and equation (18) fitted by Origin software:

$$D = 1 - \left[1 - \left(\frac{N}{N_F} \right)^{0.29} \right]^{0.41},$$

$$b = 1.437, \quad (19)$$

$$c = 0.710,$$

$$R^2 = 0.9988.$$

The damage constitutive relation of rock under uniaxial compression based on existing studies is

$$\sigma = E(1 - D)\varepsilon. \quad (20)$$

Under uniaxial constant-amplitude cyclic loading, the damage model of sandstone can be obtained as follows:

$$\sigma = E \left[1 - \left(\frac{N}{N_F} \right)^{0.29} \right]^{0.41} \varepsilon. \quad (21)$$

It can be seen that the comprehensive damage model established by the combination of resistivity and AE parameters can well describe the damage process of rock.

5. Conclusions

In this paper, an experimental study of sandstone under constant-amplitude cyclic loading was carried out. Under different loading conditions, the two characteristics of AE and resistivity of sandstone were analyzed, and the damage model was established by combining the two parameters. The research contents of this paper are summarized as follows:

- (1) The three stages of fatigue deformation correspond to the evolution of AE under constant-amplitude cyclic loading conditions: the deformation developed faster and AE activity was stronger in the initial stage. Then, in the fatigue stabilization stage, the deformation developed at a low rate and AE activity weakened. And cracks expand rapidly and AE activity increases suddenly until the rock is damaged in accelerated damage stage. At the same time, most of the AE signals occur near the upper-stress limit.
- (2) The evolution trend of rock resistivity with load shows that, on the one hand, the resistivity drops rapidly in the loading stage, and on the other hand, in the unloading stage, it rises rapidly. Overall, the resistivity of sandstone under cyclic loading gradually decreased, until resistivity instantaneously increased when the failure occurs.
- (3) Based on the existing theoretical basis, mainly the relationship between rock porosity and resistivity, the damage variable based on resistivity was deduced. Combined with the damage variable established by the cumulative AE number proposed by

predecessors, a comprehensive damage variable based on AE parameters and resistivity was established by fitting test data. The comprehensive damage variable can better reflect the damage process of rock. Based on this, under constant-amplitude cyclic loading, the damage model of sandstone was constructed.

Data Availability

The experimental data used in this study are available from the corresponding author upon request.

Conflicts of Interest

The authors declare that they have no conflicts of interest.

Acknowledgments

The authors gratefully acknowledge the financial support from the Natural Science Foundation Project of China (grant no. 51609027), Science and Technology Projects of Department of Transportation of Jiangxi Province (grant no. 2019Q0027), and Chongqing Postgraduate Research Innovation Project, University Level (project no. 2021S0023).

References

- [1] J. Li, Y. Huang, Z. Chen, M. Li, M. Qiao, and M. Kizil, "Particle-crushing characteristics and acoustic-emission patterns of crushing gangue backfilling material under cyclic loading," *Minerals*, vol. 8, no. 6, p. 244, 2018.
- [2] S. Y. Liu, L. Y. Tong, Q. Yu, and L. C. Miao, "Crushable effects on engineering mechanical properties of colliery wastes," *Chinese Journal of Geotechnical Engineering*, vol. 27, pp. 505–510, 2005.
- [3] D. Ma, J. Zhang, H. Duan et al., "Reutilization of gangue wastes in underground backfilling mining: overburden aquifer protection," *Chemosphere*, vol. 264, no. 1, Article ID 128400, 2021.
- [4] D. Ma, H. Duan, J. Liu, X. Li, and Z. Zhou, "The role of gangue on the mitigation of mining-induced hazards and environmental pollution: an experimental investigation," *The Science of the Total Environment*, vol. 664, pp. 436–448, 2019.
- [5] A. Alnedawi, K. P. Nepal, and R. Al-Ameri, "Effect of loading frequencies on permanent deformation of unbound granular materials," *International Journal of Pavement Engineering*, vol. 22, pp. 1–9, 2019.
- [6] W. Hu, Z.-Y. Yin, G. Scaringi, C. Dano, and P.-Y. Hicher, "Relating fragmentation, plastic work and critical state in crushable rock clasts," *Engineering Geology*, vol. 246, pp. 326–336, 2018.
- [7] A. Gheibi and A. Hedayat, "Ultrasonic investigation of granular materials subjected to compression and crushing," *Ultrasonics*, vol. 87, pp. 112–125, 2018.
- [8] L. Obert and W. I. Duvall, "Micro-seismic method of determining the stability of underground openings," Department of the Interior, Washington, DC, USA, 1957.
- [9] X. Lei, S. Ma, and S. Ma, "Laboratory acoustic emission study for earthquake generation process," *Earthquake Science*, vol. 27, no. 6, pp. 627–646, 2014.
- [10] L. Yi and D. Feng, "A review of experimental and theoretical research on the deformation and failure behavior of rocks subjected to cyclic loading," *Journal of Rock Mechanics and Geotechnical Engineering*, 2021.
- [11] M. Gernot, C. Denis, and O. Dani, "Sources and characteristics of acoustic emissions from mechanically stressed geologic granular media — a review," *Earth-Science Reviews*, vol. 112, pp. 97–114, 2012.
- [12] X. Lei, "Laboratory acoustic emission study review," in *Rock Mechanics and Engineering* Vol. 2, CRC Press, Boca Raton, FL, USA, 2017.
- [13] P. Rodríguez, P. B. Arab, and T. B. Celestino, "Characterization of rock cracking patterns in diametral compression tests by acoustic emission and petrographic analysis," *International Journal of Rock Mechanics and Mining Sciences*, vol. 83, pp. 73–85, 2016.
- [14] X. Lei, T. Satoh, and O. Nishizawa, "Experimental study on stress-induced pre-failure damage in rocks and its applications to earthquake source-process research based on AE," in *Proceedings of the The National Seminar on Non-Destructive Evaluation (NDE)*, Hyderabad, India, December 2006.
- [15] J. Ou, Z. Zhou, Y. Wang et al., "Mechanics and acoustic emission characteristics of marble under uniaxial cyclic loading and unloading conditions," *China tungsten industry*, vol. 32, no. 6, pp. 34–39, 2017.
- [16] K. R. Zhao, Z. Peng, S. H. Ran, D. X. Yang, and T. Y. Teng, "Effect of moisture content on characteristic stress and acoustic emission characteristics of red sandstone," *Rock and Soil Mechanics*, vol. 42, no. 4, pp. 1–10, 2021.
- [17] Y. Jiang, X. Ge, and J. Ren, "Deformation rules and acoustic emission characteristics of rocks in process of fatigue failure," *Chinese Journal of Rock Mechanics and Engineering*, vol. 23, no. 11, pp. 1810–1814, 2004.
- [18] J. Z. Wang, M. Su, and C. Research, "Review of resistivity variation characteristics under load conditions on rock," *Journal of Chongqing Jianzhu University: Natural Science Edition*, vol. 30, no. 3, pp. 419–423, 2011.
- [19] G. E. Archie, "The electrical resistivity log as an aid in determining some reservoir characteristics," *Transactions of the AIME*, vol. 146, no. 1, pp. 54–62, 1942.
- [20] O. A. L. Lima, B. C. Michael, G. N. Geraldo, and N. Sri, "A volumetric approach for the resistivity response of freshwater shaly sandstones," *The Journal Geophysics*, vol. 70, no. 1, pp. F1–F10, 2005.
- [21] T. Masao, Y. Isao, and F. Yoshio, "Anomalous electrical resistivity of almost dry marble and granite under axial compression," *Journal of Physics of the Earth*, vol. 41, no. 6, pp. 337–346, 1993.
- [22] G. Chen and Y. Lin, "Stress-strain-electrical resistance effects and associated state equations for uniaxial rock compression," *International Journal of Rock Mechanics and Mining Sciences*, vol. 41, no. 2, pp. 223–236, 2004.
- [23] W. F. Brace and A. S. Orange, "Electrical resistivity changes in saturated rock under stress," *Science*, vol. 153, no. 3 743, pp. 1 525–531 526, 1966.
- [24] W. Zhang, Q. Sun, S. Zhu, and S. Hao, "The effect of thermal damage on the electrical resistivity of sandstone," *Journal of Geophysics and Engineering*, vol. 14, no. 2, pp. 255–261, 2017.
- [25] C. Wang, Y. Xu, and X. Gao, "Electrical resistivity variation of compressed rock and damage evolution of overburden in coal mine goaf," *Coal Engineering*, vol. 53, no. 2, pp. 117–121, 2021.
- [26] G. Wu, K. Wang, M. Zhao, Z. Nie, and Z. Huang, "Analysis of damage evolution of sandstone under uniaxial loading and unloading conditions based on resistivity characteristics," *Advances in Civil Engineering*, vol. 2019, Article ID 9286819, 12 pages, 2019.

- [27] K. Wang, X. Li, Z. Huang, and M. Zhao, "Experimental study on acoustic emission and resistivity response of sandstone under constant amplitude cyclic loading," *Advances in Materials Science and Engineering*, vol. 2021, Article ID 6637200, 13 pages, 2021.
- [28] Z. Lin, G. Li, T. Dong et al., "Overview on development of acoustic emission signal analysis technique and processing," *Materials Reports*, vol. 28, no. 9, pp. 56–60+73, 2014.
- [29] X. Ge, Y. Jiang, Y. Lu, and J. Ren, "Testing study on fatigue deformation law of rock under cyclic loading," *Chinese Journal of Rock Mechanics and Engineering*, vol. 22, no. 10, pp. 1581–1585, 2003.
- [30] Q. Zhang, X. Ge, M. Huang, and H. Sun, "Testing study on fatigue deformation law of red-sandstone under triaxial compression with cyclic loading," *Chinese Journal of Rock Mechanics and Engineering*, vol. 25, no. 3, pp. 473–478, 2006.
- [31] Y. Bai, *Experimental Research on the Fatigue Property of Salt Rock under Cyclic loading*, Chongqing University, Chongqing, China, 2012.
- [32] J. Wang, C. Su, and M. Zhao, "Experimental study on resistivity properties of rocks under loading," *Geotechnical Investigation & Surveying*, vol. 41, no. 3, pp. 23–26, 2013.
- [33] Y. Yang, D. Wang, M. Guo, and B. Li, "Study of rock damage characteristics based on acoustic emission tests under triaxial compression," *Chinese Journal of Rock Mechanics and Engineering*, vol. 3, no. 1, 104 pages, 2014.
- [34] X. Tang, J. Xu, and B. Yan, "A description of rock fatigue evolution using acoustic emission damage variables," *Soil Engineering and Foundation*, vol. 27, no. 6, pp. 81–83+110, 2013.
- [35] S. Li, X. Xu, Z. Liu et al., "Electrical resistivity and acoustic emission response characteristics and damage evolution of sandstone during whole process of uniaxial compression," *Chinese Journal of Rock Mechanics and Engineering*, vol. 33, no. 1, pp. 14–23, 2014.